

© 2014 by Ryan Arthur Fontaine. All rights reserved.

VERY NEAR-NOZZLE SHEAR-LAYER TURBULENCE AND JET NOISE

BY

RYAN ARTHUR FONTAINE

DISSERTATION

Submitted in partial fulfillment of the requirements
for the degree of Doctor of Philosophy in Theoretical and Applied Mechanics
in the Graduate College of the
University of Illinois at Urbana-Champaign, 2014

Urbana, Illinois

Doctoral Committee:

Professor Jonathan B. Freund, Chair and Co-Director of Research
Professor Joanna M. Austin, Co-Director of Research
Professor Gregory S. Elliott
Professor Kenneth T. Christensen

Abstract

Jet noise is sensitive to nozzle configurations and most current aircraft operate close to Federal Aviation Administration (FAA) and other noise restriction levels, with more stringent requirements expected in the future. At the current time, however, prediction capabilities lack the fidelity to accurately model the noise production from a high-Reynolds-number turbulent jet, which impedes progress toward quieter designs. A small-scale anechoic facility has been designed, constructed, and validated which allows for nozzle testing. Both axisymmetric and complex nozzle geometries have been investigated utilizing traditional machining and rapid prototyping capabilities. In addition to noise measurements, a number of flow diagnostic techniques have been implemented allowing the very-near-nozzle region to be studied in detail. The facility construction, validation, and capabilities are described in detail. Flow and noise studies are performed on two separate passive nozzle control methods. The first is a parametric study of how nozzle lip perturbations affect far-field noise through the use of chevron-style nozzles. The second is a family of clamshell style nozzles where the source of an unwanted tone is identified. It is found that designs must consider flow separation from the clamshell surface.

The central scientific contribution of this work is a fundamental investigation of the influence of the initial shear layer thickness to answer some long-standing questions regarding the role of turbulence inflow conditions on jet noise. These are important both for predictive simulation and lab-scale experiments. One of the principal challenges in the prediction and design of low-noise nozzles is resolving the near-nozzle mixing layers at the high Reynolds numbers of engineering conditions. Faithfully representing the near-nozzle dynamics in a

large-eddy simulation is a challenge because the locally largest scales are so small. Model-scale experiments will likewise typically have relatively thick near-nozzle shear layers, which can hamper their applicability to high-Reynolds-number design. To quantify the sensitivity of the far-field sound to nozzle turbulent shear layer conditions, a family of nozzles is constructed and studied in which the exit turbulent boundary layer thickness is varied from momentum thickness $0.0042 D$ up to $0.021 D$ for otherwise identical flow conditions. Measurements include particle image velocimetry (PIV) to within 0.04 nozzle diameters of the exit plane and far-field acoustic spectra. The influence of the initial turbulent shear layer thickness is pronounced, though less significant than the well-known sensitivity of the far-field sound to laminar versus turbulent shear layer exit conditions. For thicker shear layers, the nominally missing region where the corresponding thinner shear layer develops is the principal factor that leads to the noise difference. The nozzle-exit momentum thickness successfully scales the high-frequency component of the spectra for nozzles of different sizes and exhaust conditions. Despite the success of this single parameter on the far-field acoustic spectra, detailed turbulence statistics show distinct signatures of both the nozzle boundary layer, which varies significantly from nozzle to nozzle, and the growing shear layer, which seems to develop surprisingly similarly for all the nozzles. An analysis of the mean exit velocity profiles suggest that their linear stability is indeed insensitive to their thickness by $x = 0.04 D$.

To my family.

Acknowledgments

First, I would like to thank my advisors, Professors Jonathan Freund and Joanna Austin for their support, encouragement, and insight through the years. They have helped me progress as both a researcher and a scholar. I could not have asked for better mentors. Professor Freund, thank you specifically for all the time you have put in helping organize ideas, editing drafts, and in the development of this document. I would also like to thank Professor Gregory Elliott for his essential advice, especially with the diagnostics used throughout my studies, serving very much as my unofficial third advisor. I also would like to thank Professor Christensen for our discussions on PIV processing, as well as for serving on my committee. Additionally, I would like to thank Professor Lawrence Ukeily for providing data to benchmark my initial PIV results and Professor Mo Samimy, Dr. James Bridges, and Dr. Peter Jordan for their discussions and observations during the design and construction phase of the facility.

I am grateful to my colleagues Bill Flaherty, Andrew Swantek, Andrew Knisely, Todd Reedy, Tommy Herges, Bradley Deblauw, and Manu Sharma for help in the lab over the past 6 years, making the time both enjoyable and educational. Also, David Buchta for his patience when I was first learning about linear stability codes. I am also thankful for the many other graduate students and friends I have interacted with in my time in Illinois. Also, thank you to Shweta Sharma for her initial research into facility designs and the undergraduate students who help with chamber construction and data acquisition, Brock Bobbitt (specifically for helping with figures A.1, A.2, and A.3) and Heath Reising.

I would also like acknowledge the agencies who have funded various aspects of this work

including Rolls-Royce, Gulfstream, and the Office of Naval Research.

Most of all I would like to thank my family who laid the foundation of who I am today. Mom, thank you for always believing in me no matter what I did and answering all those questions I always had when I was young. I can't imagine they didn't eventually get annoying, but by answering them you encouraged me to never stop asking. Dad, thank you for working multiple jobs throughout my childhood to provide everything I could ever need while still being there for me and encouraging me to get an education so I would never have to work so hard. Aunty Cyndy, thank you for encouraging reading and taking me to all those library sales when I was young. It fueled my desire to keep exploring no matter the topic. Last but not least, Dani, thank you for being a great sister and friend. Best of luck, and you'll be finished with yours before you know it.

Table of Contents

List of Tables	x
List of Figures	xi
List of Abbreviations	xviii
List of Symbols	xix
Chapter 1 Introduction	1
1.1 A Fundamental Challenge for Full-scale Jet Design	2
1.2 Nozzle Conditions Affect Sound	3
1.3 Statistical Representation and Modeling	5
1.4 Scale Experiments and Sensitivity to Nozzle Conditions	9
1.5 Simulation-based Prediction	11
1.6 Control	12
1.6.1 Passive Control	12
1.6.2 Active Control	13
1.7 Goal and Organization	14
Chapter 2 Experimental Facility and Procedures	16
2.1 Facility Design	16
2.1.1 Anechoic Chamber	16
2.1.2 Facility Improvements	18
2.1.3 Air Supply	20
2.1.4 Make-up Air	21
2.1.5 Exhaust	22
2.2 Control and Measurement	23
2.2.1 Flow Rate Control	23
2.2.2 Microphones	23
2.2.3 Other Hardware	25
2.2.4 Signal Processing	26
2.2.5 Atmospheric Absorption	27
2.3 Facility Characterization	28
2.4 Complex Nozzle Capabilities	30
2.5 Facility Validation	31

2.5.1	Acoustics	31
2.5.2	Particle Image Velocimetry	32
Chapter 3	Passive Nozzle Control and Noise	37
3.1	Motivation	37
3.2	Chevrans	38
3.2.1	Experimental Setup	39
3.2.2	Results	43
3.3	Small Perturbation Acoustics	47
3.4	Clamshell Nozzles	51
3.5	Center Body Nozzle	54
Chapter 4	Nozzle Boundary Layer Influence on Far-Field Sound	62
4.1	Motivation	62
4.2	Nozzles	62
4.3	Results	64
4.3.1	Nozzle-Exit Boundary-Layer Properties	64
4.3.2	Velocity and Turbulence Profiles	66
4.3.3	Nozzle-lip Thickness	67
4.3.4	Far-field Sound	79
4.3.5	The Turbulent State of the Initial Boundary Layer	82
4.3.6	Near-nozzle Shear-layer Development	86
4.3.7	Downstream Evolution	91
4.3.8	Noise Reduction	96
Chapter 5	Linear Stability of the Near-nozzle Shear Layers	98
5.1	Motivation	98
5.2	Governing Equations	99
5.3	Numerical Solution	103
5.4	Results	106
Chapter 6	Summary and Conclusions	111
Appendix A	Additional Facility Information	115
A.1	Additional Facility Characterization	115
A.2	Heated Jet	115
A.2.1	Helium	118
A.2.2	Validity of Helium Tests	118
A.2.3	Heater	119
A.3	Conclusion	119
Appendix B	Measurement Error Analysis	120
B.1	Acoustics	120
B.2	PIV	121
Appendix C	Detailed Facility Specification (CAD Drawings)	122

Appendix D List of Tests Conducted in the Facility	179
References	183







List of Tables

2.1	Parameters for the atmospheric absorption equations defined in (2.2). . . .	28
4.1	Parameters for nozzles used in exit boundary-layer influence investigation. Refer to figures 4.1 and 4.2 for the contraction schematic.	64
4.2	Exhaust values for nozzles used in exit boundary-layer influence investigation. Refer to figure 4.1 for the corresponding schematic.	66
4.3	Nozzles with various exit-lip thickness, d . In all cases, the long nozzle was used. For the thin and thinnest cases, a 12.7 mm long plastic addition was used to reduce the lip thickness.	78
4.4	The 5-95% momentum thickness calculated for both the short and long nozzle with run conditions ranging from Mach 0.2-0.9.	86

List of Figures

1.1	Schematic of mean boundary and shear layers for both thin and thick initial conditions.	3
1.2	Schematic of the near-nozzle exhaust region. Depicted is the wave-packet representation in the turbulent shear layer to illustrate an anticipated relation between large turbulence scales and sound.	8
2.1	The anechoic jet noise facility.	17
2.2	Sideline, $\theta = 90^\circ$, 1/3-octave band spectra showing spurious peaks from preliminary tests.	18
2.3	Upstream acoustic conditioning: (a) staggered baffles in the upstream muffler section and (b) foam lining and tapered transition piece in the upstream piping.	19
2.4	(a) Foam baffles in the upstream piping and (b) the resulting improvements in noise measurements at Mach 0.74.	20
2.5	Exhaust collector improvement: \circ before; \blacksquare after.	21
2.6	Anechoic facility overview.	23
2.7	Typical free-field response of a type 4939 microphone at 0 degrees incident angle. Response data from Brüel & Kjær.	24
2.8	Microphone response testing importance of microphone support. The data have been offset for clarity.	25
2.9	Typical microphone configuration.	26
2.10	Experimental measurements of sound field spherical divergence in chamber \blacksquare and $\text{---} 1/R^2$: (a) sideline 90° at individual frequencies; (b) downstream 30° OASPL.	29
2.11	Comparison of OASPL with $\text{---} U_j^8$ and $\text{---} U_j^4$ visual fits at both $\theta = \bullet 30^\circ$ and $\blacksquare 90^\circ$	30
2.12	Nozzles manufactured with rapid prototyping.	31
2.13	Typical 1/3-octave far-field response corrected to lossless conditions at $72D$: $\blacksquare D = 19$ mm rapid prototyped; $\blacktriangle D = 26.9$ mm machined metal; \square Brown & Bridges (2006); and \triangle Viswanathan (2004).	32
2.14	In chamber PIV equipment set-up.	33
2.15	Mean velocity field normalized by centerline velocity $\left(\frac{U}{U_j}\right)$ of a Mach 0.98 jet.	34
2.16	Comparison of PIV data by $\frac{u'v'}{U_j^2}$ in a Mach 0.98 flow.	34

2.17	Radial velocity (m/s) for the underexpanded jet.	35
2.18	Streamwise velocity (m/s) for the underexpanded jet.	36
2.19	Acoustic spectra for the underexpanded jets: (A) $p_j/p_\infty = 3.65$; (B) $p_j/p_\infty = 4.94$	36
3.1	Boeing 787 “Dreamliner” showing the use of chevrons for noise mitigation in practice. Photo from www.boeing.com	39
3.2	Sample far-field sound response to a nozzle geometry (G) alteration: - - step response and a — smoother change in sound produced with geometry modification.	40
3.3	Baseline geometry for chevron nozzle studies.	41
3.4	Chevron nozzle geometry for 5° testing.	41
3.5	Array of nozzles with 5° chevron taper.	42
3.6	Comparison of third-octave acoustic response to Bridges & Brown (2004). The UIUC data are taken at Mach 0.9 while the Bridges & Brown (2004) data were acquired at Mach 0.98 and rescaled to Mach 0.9 using U^8 scaling.	42
3.7	Chevron nozzle geometry for 18.2° testing.	43
3.8	Array of nozzles with 18.2° chevron taper.	43
3.9	Change in overall sound pressure level as a function of the chevron length for both sideline and downstream measurement angles.	44
3.10	Third-octave response for the 5° chevrons at different lengths at both sideline and downstream measurement locations.	45
3.11	Third-octave sound pressure level change from baseline for the 5° chevrons at different lengths at both sideline and downstream measurement locations.	46
3.12	Third-octave sound pressure level change from baseline for the 5° chevrons at different measurement locations for the two longest chevrons studied which had similar Δ OASPL.	46
3.13	Third-octave response for the 18.2° chevrons at different lengths at both sideline and downstream measurement locations.	47
3.14	Third-octave sound pressure level change from baseline for the 5° chevrons at different lengths at both sideline and downstream measurement locations.	48
3.15	CAD depiction of the small perturbation set-up. Machine drawings are provided in appendix C.	49
3.16	Noise measurements for six different chevron penetrations tested.	50
3.17	Third-octave noise change from the baseline penetration: — 0.4 mm; - - - 0.8 mm; - - - - 1.2 mm; - 1.6 mm; - - - - 2.4 mm.	50
3.18	Change from baseline in the overall sound pressure level.	51
3.19	Narrowband sound spectra for circular and elliptical clamshell geometries normalized to $72 D_h$: (A) circular exhaust; (B) elliptical exhaust; (C) axisymmetric baseline.	53
3.20	Overview of a clamshell style nozzle with surface flow visualization view identified. Image from Thirumurthy <i>et al.</i> (2010).	54
3.21	Nozzle exit velocity normalized by centerline velocity.	55

3.22	Front view of the four nozzles used in the parametric study of a class of clamshell nozzles. The major and minor diameter of the nozzle exits are shown along with the vertical distance between the exit and the nearest point on the clamshell tip. All dimensions are in mm.	56
3.23	Instantaneous surface flow results for a class of clamshell nozzles.	57
3.24	High-speed schlieren snapshots with exposure time of $20 \mu\text{s}$	58
3.25	Shedding frequency for each nozzle.	58
3.26	Center body installed in facility.	59
3.27	View of plug nozzle and supporting hardware.	59
3.28	Figure continued on next page.	60
3.28	Noise from plug nozzle at various exhaust conditions normalized to $72 D_h$: Nozzle pressure ratio = (A) 6.20; (B) 4.94; (C) 3.67; (D) 2.77; (E) 2.14; (F) 1.69; (G) 1.39; (H) 1.19.	61
3.29	Center body nozzle far-field sound at Mach 0.9 compared with an axisymmetric baseline.	61
4.1	(a) Contraction shape: $r(x) = \frac{D}{2} + (\frac{D_u}{2} - \frac{D}{2}) \left[10 \left(\frac{L-x}{L} \right)^3 - 15 \left(\frac{L-x}{L} \right)^4 + 6 \left(\frac{L-x}{L} \right)^5 \right]$, where $D_u = 101.6 \text{ mm}$ is the inlet diameter and $L = 50.8 \text{ mm}$ is the length of the contraction. (b) The $D = 26.8 \text{ mm}$ family of straight-walled nozzles, with the short $\ell = 63.5 \text{ mm}$ nozzle shown. The medium $\ell = 292.1 \text{ mm}$ and long $\ell = 508 \text{ mm}$ nozzles are not shown.	63
4.2	(a) Small and (b) large diameter alternate configuration nozzles. Nozzle (a) is inserted into the contraction in figure 4.1a and nozzle (b) has a contraction that follows a similar polynomial reduction.	64
4.3	Measured momentum thickness for the  short,  medium, and  long nozzles and the linear fits used to extrapolate to nominal nozzle values.	65
4.4	Streamwise velocity statistics at $x = 0.04D$:  short;  medium; and  long nozzles. The horizontal line at $u_{\text{rms}}/U_j = 0.08$ is for reference.	67
4.5	Near-nozzle streamwise velocity (U/U_j) for the short nozzle (see table 4.1).	68
4.6	Near-nozzle streamwise velocity fluctuation (u_{rms}/U_j) for the short nozzle (see table 4.1).	69
4.7	Near-nozzle streamwise velocity (U/U_j) for the medium nozzle (see table 4.1).	70
4.8	Near-nozzle streamwise velocity fluctuation (u_{rms}/U_j) for the medium nozzle (see table 4.1).	71
4.9	Near-nozzle streamwise velocity (U/U_j) for the long nozzle (see table 4.1).	72
4.10	Near-nozzle streamwise velocity fluctuation (u_{rms}/U_j) for the long nozzle (see table 4.1).	73
4.11	Near-nozzle streamwise velocity (U/U_j) for the small nozzle (see table 4.1).	74
4.12	Near-nozzle streamwise velocity fluctuation (u_{rms}/U_j) for the small nozzle (see table 4.1).	75
4.13	Near-nozzle streamwise velocity (U/U_j) for the large nozzle (table 4.1).	76
4.14	Near-nozzle streamwise velocity fluctuation (u_{rms}/U_j) for the large nozzle (see table 4.1).	77

4.15	Mean flow and streamwise turbulence intensity for different nozzle-lip thicknesses: $d = 0.0332D$; $d = 0.0172D$; and $d \lesssim 0.0093D$.	78
4.16	Low-frequency scaling improvement using displacement thickness. (a) Baseline third-octave spectra at 30° scaled with nozzle diameter, D . (b) The same data as (a) but now scaled using an equivalent diameter of $D - 2\delta^*$, where δ^* is the experimentally measured displacement thickness. Lines indicate the --- short and --- long nozzles.	80
4.17	Sideline ($\theta = 90^\circ$) and downstream ($\theta = 30^\circ$) noise measurements for the (A) short, (B) medium, (C) long, (D) small D and (E) large D nozzles.	81
4.18	Sideline momentum thickness scaling using a least squares fit of the form $\text{SPL} = a + b \log f$ for the last half-decade of the experimental spectrum and extending to higher frequency.	82
4.19	$\theta = 75^\circ$ noise measurements for the (A) short, (B) medium, (C) long, (D) small D and (E) large D nozzles.	83
4.20	$\theta = 60^\circ$ noise measurements for the (A) short, (B) medium, (C) long, (D) small D and (E) large D nozzles.	83
4.21	$\theta = 45^\circ$ noise measurements for the (A) short, (B) medium, (C) long, (D) small D and (E) large D nozzles.	84
4.22	Momentum thickness scaling for various Mach numbers.	84
4.23	Downstream evolution of the peak (a) streamwise and (b) radial turbulence intensity for the (A) short, (B) medium, and (C) long nozzles.	85
4.24	Nozzle momentum thickness sensitivity to Re_D with fits $\text{---} Re^{1/7}$ and $\text{---} Re^{1/2}$.	87
4.25	Streamwise fluctuations versus $\tilde{r} = r - D/2$ subject to different scaling factors as labeled. The plot lines are lighter in tone for larger x in the downstream direction. (a,b) The short-nozzle data equally spaced from $107\theta_o$ to $240\theta_o$. (c,d) The long-nozzle data equally spaced from $110\theta_o$ to $230\theta_o$.	88
4.26	Near-nozzle streamwise turbulence intensity from $x = 0\theta_o$ to $100\theta_o$: (a,b) the short nozzle with equally spaced profiles from $x = 9\theta_o$ to $84\theta_o$; and (c,d) the long nozzle with equally spaced profiles from $x = 5\theta_o$ to $95\theta_o$.	89
4.27	The near nozzle streamwise fluctuations normalized by both momentum thickness and downstream distance. Left: Short nozzle data equally spaced from $9\theta_o$ to $84\theta_o$ downstream. Right: Long nozzle data equally spaced from $5\theta_o$ to $95\theta_o$ downstream.	90
4.28	Mean downstream (approximately self-similar region) fluctuation profiles for both the --- short and --- long exhaust profiles.	90
4.29	Near-nozzle fluctuations plotted with the background contour the jet velocity. Data shown is for the short nozzle. The streamwise fluctuation profiles are from $0.038 D$, $0.113 D$, $0.184 D$, $0.259 D$, $0.335 D$, and $0.411 D$ downstream of the nozzle exit. The \times symbol designates the $U(r)/U_j = 0.05, 0.95$ points.	91
4.30	Downstream streamwise velocity (U/U_j) for the short nozzle (table 4.1).	92
4.31	Downstream streamwise velocity (U/U_j) for the long nozzle (table 4.1).	93
4.32	Downstream streamwise velocity fluctuation (u_{rms}/U_j) for the short nozzle (table 4.1).	94

4.33	Downstream streamwise velocity fluctuation (u_{rms}/U_j) for the long nozzle (table 4.1).	95
5.1	Comparison of using the experimentally determined initial momentum thickness as a parameter in (5.22) (----) with the corresponding experimentally determined initial profile.	104
5.2	Comparison of experimental streamwise velocity data to fits described by (5.23) (----) with the corresponding experimentally determined initial profile for the — short and ---- long nozzles.	105
5.3	Comparison with previous results of Bodony (2004) (symbols) and the current results (lines): mode $m = 0$ ■ (—); $m = 1$ ▲ (---); $m = 2$ ▼ (---); $m = 3$ ● (.....).	106
5.4	Stability analysis with growth rate normalized by the layer thickness: --- tanh baseline; — short; ---- long.	107
5.5	Axisymmetric mode $n = 0$ amplification (a) and phase speed (b) for $e^{i\alpha x + i\omega t}$ modes with $\alpha = \alpha_r + i\alpha_i$ linear amplification: --- baseline; — short nozzle; and ---- long nozzle.	107
5.6	Linear instability growth rates as a function of Strouhal number: mode — $n = 0$; ---- $n = 5$; ---- $n = 10$; ---- $n = 15$; ---- $n = 20$; and — $n = 25$.	108
5.7	Streamwise velocity eigenfunction solution for the $n = 0$ most unstable frequency: --- baseline; — short; ---- long.	109
5.8	Radial velocity eigenfunction solution for the $n = 0$ most unstable frequency: --- baseline — short; ---- long.	109
5.9	Density eigenfunction solution for the $n = 0$ most unstable frequency: --- baseline; — short; ---- long.	110
5.10	Pressure eigenfunction solution for the $n = 0$ most unstable frequency: --- baseline; — short; ---- long.	110
A.1	Far-field measurements at 30° before in chamber reflections were minimized.	116
A.2	Far-field measurements at 12° before in chamber reflections were minimized.	116
A.3	Far-field measurements at 35° after in chamber reflections were minimized.	117
A.4	Laser sheet thickness measurement. The FWHM is 0.19 mm.	117
C.1	Aero Lab A overview	123
C.2	Aero Lab A general floor plan	124
C.3	North wall outside structure. This wall contains the door to the facility as well as the large optical access window.	125
C.4	West wall outside structure. This wall contains the exhaust.	126
C.5	South wall outside structure.	127
C.6	East wall outside structure. This wall houses the opening for the jet to enter the facility.	128
C.7	Roof - outside structure. The 8 in support spacing allows for more load in the facility.	129
C.8	Floor outside structure.	130
C.9	North wall interior wedge layout.	131

C.10 West wall interior wedge layout.	132
C.11 South wall interior wedge layout.	133
C.12 East wall interior wedge layout.	134
C.13 Roof interior wedge layout.	135
C.14 Floor interior wedge layout.	136
C.15 Overview of the piping before entering the chamber	137
C.16 Baffled section of the upstream piping	138
C.17 Honeycomb dimensions	139
C.18 8 inch to 4 inch aluminum contraction	140
C.19 8 inch to 4 inch aluminum contraction	141
C.20 In chamber piping for the short copper nozzle	142
C.21 In chamber piping for the medium copper nozzle	143
C.22 In chamber piping for the long copper nozzle	144
C.23 Contraction from 4 inches to 1 inch used for many nozzles in the facility	145
C.24 Support to fit between floor wedges	146
C.25 Support to fit between floor wedges	147
C.26 Exhaust collector	148
C.27 Smooth, acoustically treated exhaust transition from round to square cross section	149
C.28 Smooth, acoustically treated exhaust transition from round to square cross section	150
C.29 Exhaust from facility constructed by Spiral Manufacturing	151
C.30 Exhaust vanes designed by ELD	152
C.31 Subsonic nozzle with a 0.5 inch diameter exhaust	153
C.32 Subsonic nozzle with a 0.75 inch diameter exhaust	154
C.33 Subsonic nozzle with a 1.375 inch diameter exhaust	155
C.34 Nozzle designed for perfect expansion at Mach 2 using the method of characteristics	156
C.35 Attachment ring which is soldered to the copper tubing to form nozzles	157
C.36 Short copper nozzle	158
C.37 Medium copper nozzle	159
C.38 Long copper nozzle	160
C.39 For testing the effect of the nozzle lip thickness	161
C.40 Baseline axisymmetric nozzle which had all chevrons “cut” into it	162
C.41 Sample 5° penetration four chevron nozzle	163
C.42 Sample 18.2° penetration six chevron nozzle	164
C.43 Aerodynamic center body used to hold the plug at the nozzle exit	165
C.44 Cross support to hold the center body in place	166
C.45 Plug geometry	167
C.46 Plug geometry coordinates in inches	168
C.47 Mach 3 jet back plate	169
C.48 Mach 3 jet mounting plate	170
C.49 Metal retaining ring to reinforce nozzle mounting	171
C.50 Spacer to put jet at the center of the tunnel	172

C.51 Stagnation chamber	173
C.52 Mach 3 nozzle designed using the method of characteristics	174
C.53 Overview of the Mach 3 jet	175
C.54 Full support structure overview of the Mach 3 jet	176
C.55 Mounting bracket for linear actuators for chevron perturbation study	177
C.56 Nozzle used for the small perturbation experiments with a 5° baseline penetration angle	178

List of Abbreviations

CFD	Computational Fluid Dynamics
DEHS	Bis(2-ethylhexyl) sebacate
EPNL	Effective Perceived Noise Level
FAA	Federal Aviation Administration
FWHM	Full Width at Half Maximum
LES	Large-eddy Simulatoin
NPR	Nozzle Pressure Ratio
OASPL	Overall Sound Pressure Level
PIV	Particle Image Velocimetry
RPT	Rapid Prototype
SLS	Selective Laser Sintering

List of Symbols

c	Speed of Sound
d	Nozzle Lip Thickness
D	Nozzle Diameter
f	Frequency (Hz)
f_{rN}	Relaxation Frequency for Nitrogen
f_{rO}	Relaxation Frequency for Oxygen
G	Representative Geometric Value
g_i	Gravitational Acceleration
h	Absolute Humidity (%)
h_{rel}	Relative Humidity (%)
I_n	Modified Bessel Function of the First Kind
ℓ	Length of Nozzle Straight Section
L	Chevron Length, Nozzle Contraction Length
k	Constant
K_n	Modified Bessel Function of the Second Kind
M	Gas Dynamic Mach Number(U/c_j)
M_a	Acoustic Mach Number (U/c_∞)
n	Azimuthal Wave-Number (integer valued)
p_r	Reference Pressure (101,325 Pa)
p_{sat}	Saturated Vapor Pressure

Pr	Prandtl Number
r	Distance along the Radial Direction
R	Jet Radius, Distance from Sound Source
R_u	Radius In Upstream Stagnation Region
Re	Reynolds Number
St	Strouhal Number
T	Temperature
T_r	Reference Temperature (293.15 K)
T_{tp}	Triple-Point Isotherm Temperature for Water (273.16 K)
u'	Streamwise Velocity Fluctuation
U	Streamwise Velocity
v_r	Radial Velocity
v'	Radial Velocity Fluctuation
V	Radial Velocity
x	Distance along the Streamwise Direction

Greek

α	Axial Eigenvalue, Atmospheric Attenuation Coefficient (dB/m)
δ	Boundary Layer Thickness
δ^*	Displacement Thickness
γ	Ratio of Specific Heat Capacities
θ	Momentum Thickness, Microphone Angle
ρ	Density
τ_{ij}	Viscous Stress
ω	Temporal Eigenvalue

Superscripts

$()'$	Fluctuating Quantity
--------	----------------------

$\overline{(\)}$ Base Flow
 $\widetilde{(\)}$ Linear Stability Eigenfunction

Subscripts

$(\)_0$ Initial Value
 $(\)_f$ Fluid Value
 $(\)_j$ Centerline Value
 $(\)_\infty$ Ambient Value
 $(\)_p$ Particle Value
 $(\)_{\text{rms}}$ Root-Mean-Squared Value

Chapter 1

Introduction

Since the advent of the commercial jet airplane, noise from the exhaust has polluted nearby communities. As planes have become larger, flights more frequent, and they service more regions, noise regulations have limited air travel options and made low noise an essential design goal for aircraft. Even after more than sixty years of progress, noise prediction, a step toward mitigation, is lacking with a better understanding and modeling of the flow-to-noise link required.

The goal of this dissertation is to study this problem at a fundamental level. First, a small scale anechoic facility has been constructed for jet noise testing at the University of Illinois. In this facility, demonstrations are made with scale models of complex geometries, including chevron and clamshells. We quantify sensitivity by showing how small changes at the exhaust have a measurable effect on the far-field sound. A detailed understanding of the turbulent shear layer emanating from the exhausts is essential to understand these effects, representing them in simulations, and studying them in small-scale experiments. To this end, a study of the effect of the turbulent boundary layer on the sound from an axisymmetric nozzle is designed and completed. Improved knowledge of the role of the exhausting turbulent boundary layer on far-field sound will allow for enhanced predictions and models, resulting in nozzles designed for noise control.

1.1 A Fundamental Challenge for Full-scale Jet Design

High-Reynolds-number jet exhaust, like those from full-scale jet engines, can have remarkably thin shear-layers between the relatively uniform exhaust plume and the slower ambient flow. The thickness depends on the flow conditions, but typically we expect that the jet leaving the nozzle will have a nozzle-diameter Reynolds numbers of over 10^6 at application scales (Janardan *et al.*, 2000). Even for scale models with nozzle diameter $D = 90$ mm, the momentum thickness can be as small as $\theta/D = 0.0009$ and is expected to be even smaller at full-scale (Viswanathan & Clark, 2004a). This presents a challenge for both numerical simulations and testing in a model-scale facility where nozzles will typically have relatively thicker shear-layers δ/D . As a result of the relatively thick initial conditions, a missing region of noisy turbulence (see figure 1.1), between $\delta_{o,thin}$ and $\delta_{o,thick}$, of locally large, and noisy (Lilley, 1993), but globally small organized structures result in missing contributions to high Strouhal number sound. Furthermore, altering jet exit conditions is understood to affect flow development and noise (Maestrello & McDaid, 1971; Hill *et al.*, 1976; Hussain & Clark, 1977; Hussain & Zedan, 1978b,a; Husain & Hussain, 1979; Zaman, 1985b,a; Bridges & Hussain, 1987; Stanley & Sarkar, 2000; Viswanathan & Clark, 2004b; Bogey & Bailly, 2005; Kleinmann & Freund, 2008; Bogey & Bailly, 2010; Bogey *et al.*, 2011; Zaman, 2012; Bogey *et al.*, 2012; Bogey & Marsden, 2013), which will in general also involve the dynamics in this thin region. These issues motivate this study. In addition, characterization of thick nozzle boundary layer jets will enable accounting for this region when it cannot be explicitly represented in simulations or model-scale experiments. The near-nozzle flow is also particularly important because of its central role in noise suppression designs.

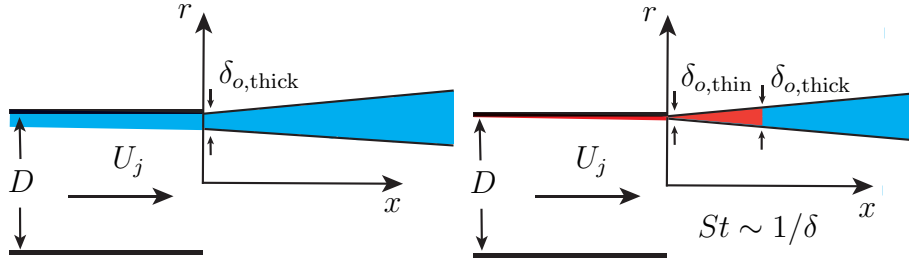


Figure 1.1: Schematic of mean boundary and shear layers for both thin and thick initial conditions.

1.2 Nozzle Conditions Affect Sound

The thinness of the turbulent boundary layer leaving the nozzle presents a challenge in its explicit representation in detailed simulation models because it requires a high number of mesh points to represent in detail. Early direct numerical simulation (DNS), designed to investigate sound generation mechanisms, focused on low-Reynolds-number turbulent jets (Freund, 2001) with essentially laminar near-nozzle shear layers. Though numerical simulations, usually large-eddy simulations (LES), can nominally be run at sufficiently high Reynolds numbers, matching the realistic dynamics of the near nozzle region challenges resolution. Bodony & Lele (2008) emphasize the influence of the jet exhaust conditions and suggest that it is the “dominant parameter in determining the accuracy of the prediction.” While large-eddy simulation (LES) has improved in its ability for prediction in high-Reynolds-number flows, much of this research has been done in an *ad hoc* manner (Bodony & Lele, 2008) and not for the general problem of flow-generated sound. Often, numerical viscosity will end up making the simulated jet have artificially thick near-nozzle shear layers, with unclear consequences. Not being able to match inflow conditions, either from lack of availability or computational restrictions, causes uncertainty in the predictions.

Beginning with the experimental visualizations of Mollo-Christensen (1967), there has been evidence of relatively large-scale energetic structures contained in the shear layer of

a jet which may be responsible for sound production and Fuchs (1972) was able to show the presence of structures which were spatially correlated over distances much larger than the turbulent length scales and on the order of the mixing layer thickness. Using acoustic excitation to enhance the organization in the flow has since confirmed their presence (Crow & Champagne, 1971; Zaman & Hussain, 1980; Hussain & Zaman, 1980; Zaman, 1985*b*; Bridges & Hussain, 1992). Source localization techniques have shown direct sound radiation from the near jet shear layer in addition to the sound produced at the end of the potential core (Laufer *et al.*, 1976; Chu & Kaplan, 1976; Narayanan *et al.*, 2002; Panda & Seasholtz, 2002; Panda, 2007; Tam *et al.*, 2008). Narayanan *et al.* (2002) uses this to observe the main contribution to low-frequency sound occurs at the close of the potential core, $5 \lesssim x/D \lesssim 10$, and high-frequency sound is primarily produced in the region near the nozzle exit $0 \lesssim x/D \lesssim 3$ with x measured in the downstream direction.

This general behavior reflects expectations based upon the largest turbulence scales, which will roughly match the jet diameter D near the end of the potential core and the smaller shear-layer thickness δ near the nozzle. Given that these locally largest scales carry most of the turbulence energy, it can be anticipated that they will generate most of the acoustic energy from their respective regions of the flow. Statistical analysis of theoretical turbulence sound sources supports this (Lilley, 1993). The single length-scale of self-similar mixing layers, which can be expected to be at least approximately realized near the nozzle exit, simplifies this perspective, and motivates in part the empirical similarity spectra of Tam *et al.* (1996). In addition to setting the smallest shear length scale, the nozzle boundary layer thickness at its exit will also limit the onset of shear-layer self-similarity, the deviation from which should similarly disrupt self-similarity of the sound spectrum. We therefore also investigate the initial shear-layer development in our studies.

1.3 Statistical Representation and Modeling

Early models sought to use statistical methods to represent the production of sound by flow and more recently incorporate the link between the largest turbulent scales and δ . The first acoustic analogy was developed by Lighthill (1952) by modeling aerodynamically generated sound generated by quadrupole sources, essentially a low-Mach number approximation. Building on this, Lighthill (1954) made an early attempt to predict jet sound in a homogeneous base flow and was able to predict the overall behavior of the spectra but with insufficient fidelity. Other attempts have since followed using either this basic or improved acoustic analogies. Ribner (1969) included refraction to better estimate the directional pattern of the broad band turbulence sound emission. The Ribner (1969) model was generalized by Goldstein & Rosenbaum (1973) who replaced the assumption of isotropic turbulence by axisymmetric turbulence, which is presumably more realistic for jet flows.

Lilley (1974) explicitly modeled refraction in parallel shear flows to include flow-acoustic interaction effects. Colonius *et al.* (1997) applied this acoustic analogy and found the acoustic field predicted was sensitive to small changes in the description of the source, possibly making evaluation difficult. The Lilley along with the Lighthill analogy was generalized by Goldstein (2003), who demonstrated that the linearization could be performed about any base flow and used this to model a spreading base flow which damps instabilities from growing unrealistically downstream. Goldstein & Leib (2005) proposed incorporating these instabilities to help explain turbulent jet sound and Gudmundsson & Colonius (2011) showed linearized disturbances to a turbulent mean flow field can predict the average evolution of large-scale structures in turbulent jets. Recently, Khavaran & Bridges (2005) improved the Lilley (1974) model using a non-compact source with an exponential two-point correlation distribution instead of a Gaussian distribution which improved agreement with experimental data at sideline measurement angles. This was particularly important in the high-frequency region where previous models would suffer from a fall-off in intensity of predicted sound.

Many of the analytic models do not account for the shear layer length scale explicitly and will miss the dependence upon this term. If they do account for it, the prediction will need accurate inflow conditions. The potential importance of this region is illustrated in the appendix of Lilley (1993), Lighthill was able to estimate the covariance of T_{xx} , the acoustic source strength in the streamwise direction, and has shown the majority of acoustic radiation is generated by eddies of comparable size to the main energy bearing eddies. Michalke (1984) used a hyperbolic tangent axisymmetric velocity profile to theoretically show the growth of an instability was induced by the vorticity contained in the jet shear layer. In a self-similar turbulent mixing layer, the scale of these structures will be proportional to the local mixing layer thickness. This relationship motivated the similarity spectra of Tam *et al.* (1996) who suggested that the lack of characteristic length and time scales in the near nozzle mixing region should result in self-similarity for the radiated sound. He proposed two separate sound sources in the flow, one from the large-scale structures primarily responsible for the sound in the downstream direction and another from the fine-scale turbulence of the jet which was quieter than the large-scale sound but radiated in all directions and found empirical fits for each.

The relation between δ and the largest turbulence scales also underlies models that attempt to represent sound-producing dynamics more explicitly. These have commonly involved a wave-packet representation of the largest turbulence structures, based upon linear stability models (Huerre & Crighton, 1983; Merkine & Liu, 1975) or phenomenologically similar wave-like model sources (Crighton & Huerre, 1990; Ffowcs Williams & Kempton, 1978). Ffowcs Williams & Kempton (1978) were among the first to analytically show the large-scale structure of the jet turbulence could provide a dominant contribution to jet noise and others followed, including Mankbadi & Liu (1984) and Crighton & Huerre (1990).

Recent attempts to capture the underlying physics in the flow through a wave-packet model are discussed by Guitton *et al.* (2008), Kerhervé *et al.* (2008), and Jordan & Colonius (2013). In this representation, structures with correlation sizes much larger than the integral

scales of the turbulence advect downstream in the vortical region of the jet. The varied amplitude of a wave packet type source allows for a portion of the energy to leak into the far-field, (Crighton & Huerre, 1990), which would not be possible for homogeneous subsonic advection. Sound in all directions is attributed to radiation from these organized structures along with high-frequency broadband sound from the turbulence. This single source can be shown to produce the noise measured in both the downstream and sideline directions, even with their different spectral shapes (Papamoschou, 2011; Obrist, 2009). The aspect ratio of a Gaussian wave packet with a subsonic convective velocity is shown to affect the direction of preferential sound emission, with superdirectivity in the downstream direction possible, agreeing well with observation.

The instability mode character of these wave-packet structures implies an approximate relation between the local shear layer thickness and their streamwise wavelength. Since it is expected that the wave packets will travel with a convection velocity U_c that is approximately half the jet velocity U_j , their Strouhal number will depend upon the local shear-layer thickness, $St \propto U_c/\delta$, which, in turn links the the local thickness to the Strouhal number of the radiated sound (Jordan & Colonius, 2013) (see figure 1.2).

Another perspective is the presence of large, irregular events which are responsible for sound production. Hileman *et al.* (2005) observed the rapid breakdown of flow structures in a $M = 1.28$ jet correlated to loud time windows, and Juvé *et al.* (1980) found approximately 50% of the sound emission occurred in just 10%-20% of the time window. Cavalieri *et al.* (2011) performed an analysis of an LES of a $M = 0.9$, $Re_D = 4 \times 10^5$ jet with a momentum thickness $\theta = 0.025D$ to investigate the important flow structure features for sound production. By developing a wave-packet line source model, they are able to match the LES data within 1.5 dB if they included space-time “jitter” to account for high-amplitude spatiotemporally localized events. By using time-averaged wave-packets, error increased to 12 dB, highlighting the importance of including high-amplitude events on the sound production in a flow, a feature present in wave-packet models described in section 1.3.

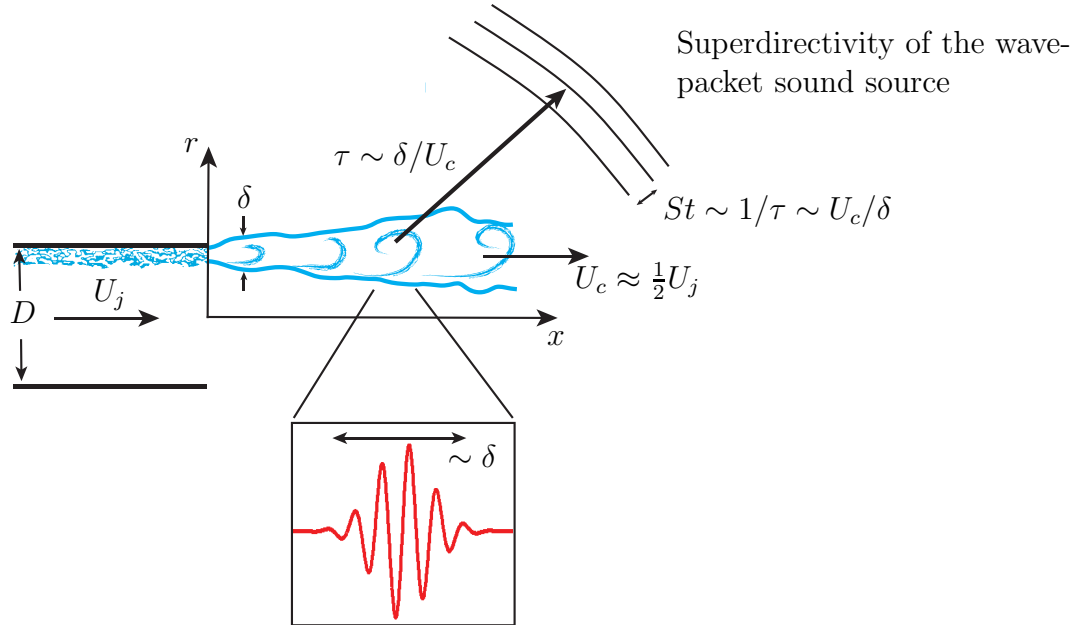


Figure 1.2: Schematic of the near-nozzle exhaust region. Depicted is the wave-packet representation in the turbulent shear layer to illustrate an anticipated relation between large turbulence scales and sound.

There is still some debate whether the more regular wave packet behavior or the event based structures are a more accurate representation of the sound production dynamics, with researchers differing on their interpretation and analysis of even the same data set. Wei & Freund (2006) applied an adjoint based control to a direct numerical simulation of a randomly excited two-dimensional mixing layer which regularizes the turbulent structures and reduces noise, favoring a wave packet sound production model. This same two-dimensional mixing layer has been investigated where a triple vortex interaction which radiates high-amplitude pressure waves to the far field (Cavaleri *et al.*, 2010) was observed. Elimination of this merging accounted for 70% of the noise reduction through control, suggesting that intermittency must be explicitly modeled.

Of course, there is no expectation of perfect self-similarity or an ideal wave-packet character, and in general anticipating the connection between turbulence and its radiated sound is even more challenging away from these quasi-equilibrium conditions. The nozzle will affect the turbulence for a distance downstream, delaying the onset of these better characterized

regimes. For example, the transition region between a turbulent boundary layer of momentum thickness θ to self-similar shear layer, spans 150θ downstream (Morris & Foss, 2003; Bradshaw, 1966). For the thicker initial shear layers of model-scale experiments and some simulations, this 150θ might extend far downstream, perhaps even the length of the potential core. Starting very close to the nozzle, we will quantify the developing shear layers of our high-speed jets.

1.4 Scale Experiments and Sensitivity to Nozzle Conditions

For simple round nozzles, the radiated sound is well-known to be sensitive to the laminar versus turbulent character of the nozzle boundary layers. We emphasize that the present studies considers only turbulent shear layers, but briefly review these results. Even when comparing sound between small-scale facilities, significant differences exist in experimental subsonic jet databases as a result of differences in the initial jet exhaust state. Husain & Hussain (1979) showed a strong dependence of the streamwise evolution of an axisymmetric low-speed mixing layer based on the initial state of the jet. The peak fluctuation intensity increased exponentially to a peak for laminar jets and then fell to an asymptotic value of $u'_p/U_j = 0.159$ while the turbulent jet increased monotonically to $u'_p/U_j = 0.166$. This overshoot is attributed to a linear instability in the laminar jet which is damped by the turbulence for the initially turbulent cases. Zaman (1985*a*) showed up to a 4 dB increase in sound intensity in an untripped, laminar jet at Mach 0.2 compared to a similar tripped jet case. The excess noise was attributed to a shear layer instability observed previously by Zaman & Hussain (1981), which facilitated the growth of particularly energetic vortices in the first few diameters of an initially laminar jet through controlled excitation. This difference did not continue to high subsonic Mach number jets, presumably because the nozzles had transitional or turbulent boundary layers on their own so no additional effects

were produced by tripping.

Viswanathan & Clark (2004b) report measurements for three nozzles: one with a cubic upstream contour, an ASME nozzle (ASME, 1959) with the contraction forming a quarter of an ellipse followed by a straight section, and a conical nozzle with smooth transitions between sections. Their respective boundary layer thicknesses were estimated to vary by a factor of 3 as deduced from a Reynolds-Averaged-Navier–Stokes solver with a κ – ϵ turbulence model. The sound pressure level (SPL) in the mid-frequency (f) range, near Strouhal number $St_D = \frac{fD}{U_j} \approx 1$, varied by about 3 dB, though it did not seem to have any direct relationship with these nozzle boundary layer thickness estimates, which were predicted to change as a consequence of the nozzle designs but were neither directly measured nor a specific point of investigation. One of our goals is to specifically quantify this aspect of the nozzle exit flow, with minimal other variation. Zaman (2012) provides a pithy discussion of the complex interrelated issues of nozzle contour, turbulence condition, and related factors that might affect noise. We do not reproduce this discussion here, though we were mindful of these issues in crafting our designs. Indeed, a principal goal is to clarify these issues via our single-parameter family of nozzles and detailed measurement of the nearly identical turbulence statistics, when scaled by δ , in our initial shear layers despite their differing thicknesses.

The Tanna *et al.* (1976) data set is one which has been suspected to suffer from rig-noise where sound produced by the flow in the upstream piping contaminates measurements (Viswanathan, 2004). Karon & Ahuja (2013) have since disproved rig-noise contamination as the culprit. Tests were repeated in the same facility used by Tanna *et al.* (1976) with upstream piping unaltered and measurements were made with different run conditions, nozzles of differing sizes, and a muffler installed. The jets were found to follow jet exit velocity to the eighth power scaling and the muffler had no effect on the far-field sound. Spectral differences were determined to be from the choice of nozzle used, confirming the importance of the jet exit condition. Cleaner flow and higher contraction ratios can lead to a laminar exit boundary layer, which produced larger turbulence intensities and higher noise radiation.

The inflow conditions are important but their precise role in sound production has not been established. Being able to account for known conditions in a reliable manner is one of the objectives of this work.

1.5 Simulation-based Prediction

The near-nozzle mechanics of jet noise presents a particular challenge in numerical simulations. The geometric flexibility afforded by such simulations is attractive but remains computationally expensive or even prohibitive for a number of reasons. The fundamental unsteadiness of sound sources and requisite fidelity are at the root of this expense. Lower cost statistical modeling of turbulence as a source of sound has been successful, but does not meet all current fidelity needs. A high-fidelity prediction seems to require that the turbulence be represented in some detail, presumably with large-eddy simulation techniques (Wang *et al.*, 2006). We can anticipate, based on the observations reviewed above, that faithful representation of the near-nozzle turbulent shear layers is required, which will remain a challenge in such simulations. Early jet noise simulations coped with resolution challenges by having either an unrealistically thick turbulent inflow shear layers (Freund *et al.*, 2000) or a thin but laminar inflow shear layers (Freund, 2001). Both approaches significantly reduce resolution requirements, but do not in detail correspond to actual configurations of engineering-scale jets.

Large-eddy simulations, though advancing rapidly (Kim *et al.*, 2014; Nichols *et al.*, 2012; Bogey *et al.*, 2012) only modestly reduce these resolution requirements because the locally largest scales near the nozzle are still small compared to the jet scale. Despite a nominally high Reynolds number, sub-grid-scale dissipation in such simulations, whether via physical models, explicit filtering, or implicit *ad hoc* numerical dissipation, cause the jet to have artificially thick near-nozzle shear layers, with unclear consequences. Unrealistic initial shear-layer turbulence is often pointed to as a cause for disagreement with data (Bodony & Lele,

2005), and simulations have been designed to study this sensitivity. For example, Bogey & Bailly (2010) simulated a Mach $M = 0.9$ laminar-inflow jet with $Re_D = 10^5$ while varying the momentum thickness from $\theta = 0.0015 D$ to $0.0115 D$. Differences in OASPL of 5-8 dB were found depending on the disturbance imposed in the initial shear layer. Motivated in part by the experiments of Zaman (1985*a,b*), Bogey *et al.* (2011) have explicitly included turbulence trips in their simulations and varied initial momentum thicknesses. Here too results are sensitive to the nozzle conditions, with differences from experiments generally attributed to the low momentum thickness Reynolds number Re_θ . Thus, not being able to match inflow conditions, either from lack of available data or such computational challenges, cause uncertainty in the predictions. The present studies are designed, in part, to provide data for quantifying this challenge and guiding modeling efforts to account for it.

1.6 Control

1.6.1 Passive Control

The ultimate objective of jet-noise prediction is, of course, mitigation, which makes the near-nozzle region particularly important because this is where it is most natural to adjust designs to achieve mitigation. We can anticipate that boundary layer details will be particularly important when geometric modifications are of comparable scale to the boundary layer thickness, as they often will be to minimize losses. Control of the unsteady dynamics through manipulation of the initial instability is important for both active and passive control. Chevrons are currently one of the most studied passive devices used for noise reduction, but challenges exist predicting a priori the amount of reduction a particular geometry will give. Experimental parametric studies have been performed (Bridges & Brown, 2004) but for practical optimization, assistance from computation is necessary.

Simulations by Uzun & Hussaini (2009) and Uzun *et al.* (2011) on SMC001 and SMC006 nozzles incorporates the chevron nozzle geometry in the computational grid. The nozzles

used match those of Bridges & Brown (2004). The Reynolds numbers in the simulations are $Re_D = 1 \times 10^5$, compared with $Re_D \approx 1.4 \times 10^6$ in the experimental studies, so discrepancies due to Reynolds number were expected as well as from the simulations having a transitional boundary-layer entering the chevron nozzle. The short domain size in Uzun & Hussaini (2009) limited analysis to higher-frequency sound, above Strouhal number 1.1, as a result of not modeling the collapse of the potential core region where much of the low-frequency sound is produced. (Simulations were performed only up to a distance of $3.75D$ downstream of the nozzle exit.) For sideline measurements, the peak sound was captured well and deviation from experiment is less than 2 dB up to a Strouhal number of 10. Unfortunately, it was not possible to compare the LES nozzle exit conditions with the experiment as the experiment did not make nozzle-boundary layer measurements.

A follow-on study (Uzun *et al.*, 2011) increased the axial domain size to 10 nozzle diameters. Improvements were observed for prediction of lower Strouhal number components of the radiated sound, however only sideline sound was reliably predicted due to loss of information from a coarser grid in the downstream direction. A fully turbulent initial boundary layer was not achieved and it was believed to be due to the inflow generation method. Accurate experimental inflow data would ensure the jets start at the desired condition, which is especially important when looking for even minor reductions in far-field sound. Examples of far-field sound modification from passive devices including chevrons and clamshells are included in chapter 3. It is shown that small modifications to the exhausting flow have a quantifiable effect on the far-field sound

1.6.2 Active Control

Active control strategies would also act in this region of the flow and are expected to be likewise sensitive to the exhaust conditions. Acoustic excitation of shear layers can be generally effective in low-Reynolds number jets (Zaman & Hussain, 1980, 1981; Zaman, 1985*b*) and in high-Reynolds number jets at frequencies around their preferred mode (Jubelin, 1980;

Lu, 1983; Ahuja *et al.*, 1983; Ahuja & Blakney, 1985). To allow manipulation in high-speed and high-Reynolds-number flows, plasma actuators, specifically localized arc filament plasma actuators (LAFPAs), have been studied extensively by the Gas Dynamics and Turbulence Laboratory at The Ohio State University (Samimy *et al.*, 2004; Utkin *et al.*, 2007) for both noise mitigation (Samimy *et al.*, 2007*a*) and flow control (Samimy *et al.*, 2007*b*; Kim *et al.*, 2009) where they have been shown to produce significant mixing enhancement. The plasma actuator in a very basic form can be thought of as a “chevron on demand” and can result in noise reduction without the same levels of thrust loss as a passive solution. This work has also been extended to use in heated jets where Kearney-Fischer *et al.* (2009) found the LAFPAs effectiveness improves as temperature increases. Currently, however, plasma actuators are not a viable option due to their large energy requirements. High amplitude fluidic actuators have likewise been successful for manipulating turbulent shear layers and altering the downstream evolution of jets (Parekh *et al.*, 1996; Freund & Moin, 2000). Whether or not simulations or small-scale experiments can reliably inform full-scale noise control depends in part upon the sensitivity of the mechanism to nozzle boundary layer thickness, which also motivated the present efforts.

1.7 Goal and Organization

Given the importance of the near-nozzle region, we have designed investigations that attempt to isolate complex-geometry flow alterations near the nozzle exit and measure the corresponding far-field sound, informing present engineering designs. Additionally, a fundamental study of the near-nozzle turbulence, in particular the effect of the near-nozzle boundary layer thickness on sound is performed. These allows us to assess the importance of this near-nozzle-exhaust region and quantify how each modification alters the exhaust. With the effect of boundary/near-shear regions established, models can be developed and corrections for near nozzle simulations implemented. Ultimately this will lead to better

predictions of far-field jet noise which in turn will provide opportunity for control.

The design, construction, and validation process of the anechoic facility used throughout this document is detailed in chapter 2. Engineering applications, which include parametric studies on passive control through chevron and clamshell style nozzles are included in chapter 3. Chapter 4 provides the main scientific contribution of this work and details how the near-nozzle exhaust influences the jet development and ultimately the far-field sound, with scalings identified. This is followed by chapter 5 which demonstrates the similar development of the different jets can be anticipated from a linear analysis, supporting the relationships developed in chapter 4. Finally, in chapter 6 concluding remarks are made.

Chapter 2

Experimental Facility and Procedures

Experimental results presented in this dissertation were acquired in the small-scale anechoic jet noise facility which was built for this purpose at the University of Illinois at Urbana-Champaign. This chapter discusses its design, construction, characterization, and validation.

2.1 Facility Design

2.1.1 Anechoic Chamber

The jets are housed in a $2.1\text{ m} \times 2.3\text{ m} \times 2.5\text{ m}$ wedge-tip-to-wedge-tip anechoic chamber for aeroacoustic and velocity field measurements of around 25 mm nominal inner-diameter nozzles. The cloth covered fiberglass wedges were manufactured by Eckel Industries to have a low cutoff frequency of 250 Hz, tested in accordance with the Impedance Tube Method-ASTM-C 384-90. Above this frequency they are reported to absorb 99% of the incident energy. Confirmation of this sufficient to our needs is discussed in section 2.3. Due to the location of the microphones, the actual cutoff is expected to be closer to 400 Hz, which is still below the range of interest in the facility. This was estimated per the ISO 3745 standard that microphone locations must be $1/4$ wavelength (at cut-off) from the wedge tips ISO 3745 (2003). The walls of the chamber were constructed using standard wood-stud framing with a maximum center to center distance of 40 cm. An image of the completed facility is shown in figure 2.1.

The door to the chamber also went through placement and sizing considerations before



Figure 2.1: The anechoic jet noise facility.

the final structure was built. It was positioned along the wall of the chamber facing the lab, as far upstream as possible. The door spans the entire usable height of the inside of the chamber, approximately 2 m high, and 0.91 m wide. The height of the door was chosen to maximize the size of items which could be brought into the chamber while the width was chosen in part to allow the floor grating to be easily inserted and removed from the chamber.

A removable access window is also built into the wall of the facility. It provides optical access from the jet exit to 1.1 m downstream. Running the facility with the window removed allows equipment such as mirrors and cameras to be located on the optical table outside of the chamber, simplifying alignment when possible

To help reduce outside vibration, the chamber is separated from the floor by 2.54 cm thick rubber strips attached along the base supports. The rubber chosen is polyurethane which has good vibration damping properties. Rubber feet (5.08 cm \times 5.08 cm \times 2.54 cm thick) were installed, five along each support. That raised the chamber floor off the lab floor, reducing vibrations but now requiring the chamber floor be able to support any loads within the structure. Extra supports were designed and implemented into the base which allows for greater internal loads. To support these loads, the floor has been constructed using 1.9 cm thick OSD board.

2.1.2 Facility Improvements

Since its completion in early 2010, the anechoic facility has undergone successive modifications to improve the quality of the acoustic data that could be acquired. Example preliminary 1/3-octave measurements taken in the facility are shown in figure 2.2. The multiple spectral peaks are obviously spurious, a clear sign of problems with the original facility design. From this start the facility was improved in a step-by-step process, finally resulting in the current facility, which is able to reproduce accepted jet noise data to within expected small error tolerances. Some of the modifications made are discussed here to illustrate the evolution of the facility to its current capability. After every modification the facility was retested and compared to accepted measurements to assess improvements. The more significant improvements are reviewed here.

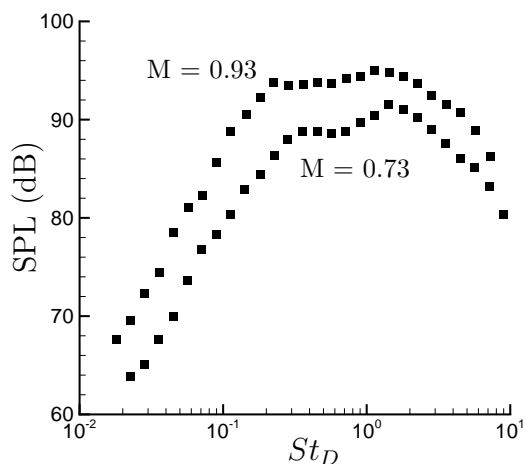


Figure 2.2: Sideline, $\theta = 90^\circ$, 1/3-octave band spectra showing spurious peaks from preliminary tests.

Among the first modifications made was the addition of a flexible polyurethane foam lining to the upstream piping in the two horizontal sections before the first contraction (see figure 2.6). This was done to reduce any noise created in this section as well as attenuate noise from upstream. Care was taken to avoid introduction of a step or other such points of potential flow separation. This involved the manufacture of transition pieces of foam that

ran smoothly from a 17.8 cm inner diameter of the foam lined section back out to a 20.3 cm inner diameter to match the beginning of the contraction, shown in figure 2.3.

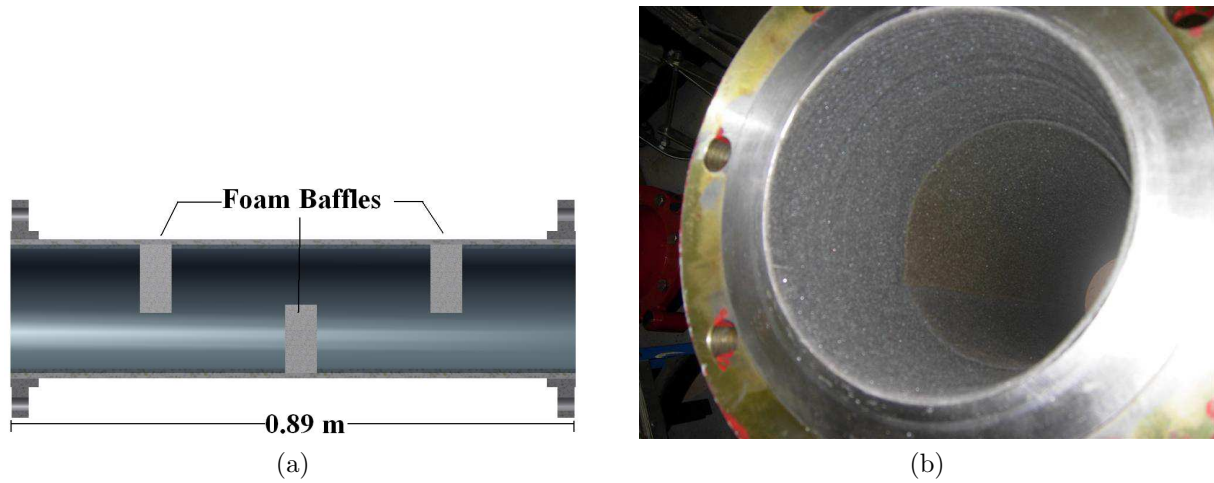
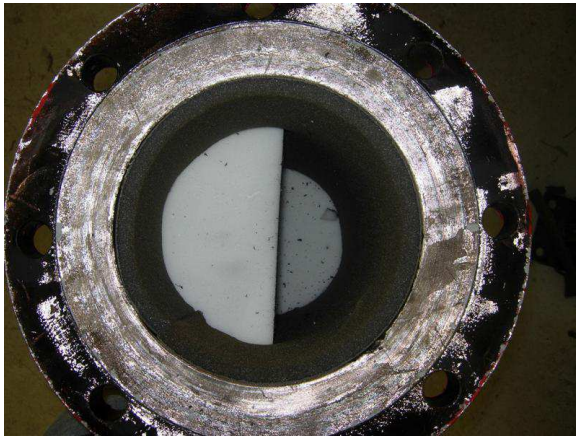


Figure 2.3: Upstream acoustic conditioning: (a) staggered baffles in the upstream muffler section and (b) foam lining and tapered transition piece in the upstream piping.

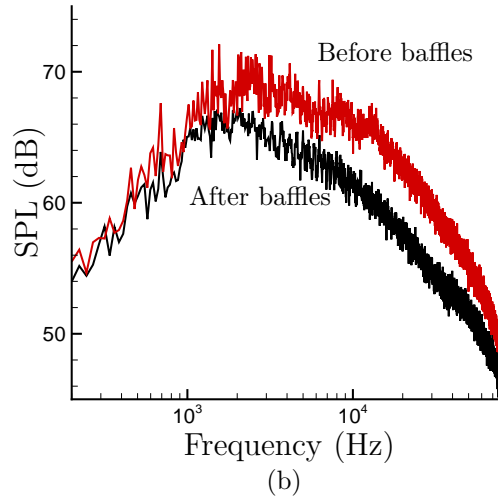
The lining improved results, but the noise levels were still unacceptably high, so three baffles made from Sonex One acoustical foam were inserted into one of the sections of the 20.3 cm piping, shown in figure 2.4. The baffles were fashioned entirely out of foam and inserted to block any direct line of sight from upstream to the jet exit as shown in figure 2.4. These were motivated by reported successful designs (Ahuja, 2003). Their spacing was set to be incompatible with the long wavelength standing modes of the pipes.

A 2.54 cm thick piece of honeycomb (3.18 mm cell size) was placed downstream of the baffles in the 20.3 cm piping section followed by an aluminum screen (1.02 mm cell size). Both components were placed upstream of the 20.3 cm to 10.2 cm contraction and were designed to suppress turbulence. They were positioned after the baffles to reduce any non-uniformity imposed on the flow by the baffles. After this final screen, the flow path is smooth and therefore will not create significant noise. The screen was placed downstream of the honeycomb following the recommendation of Pope & Harper (1966).

At this point in the facility development, there was still evidence of reflections within the chamber. The seemingly largest source was investigated first: the exhaust collector seemed



(a)



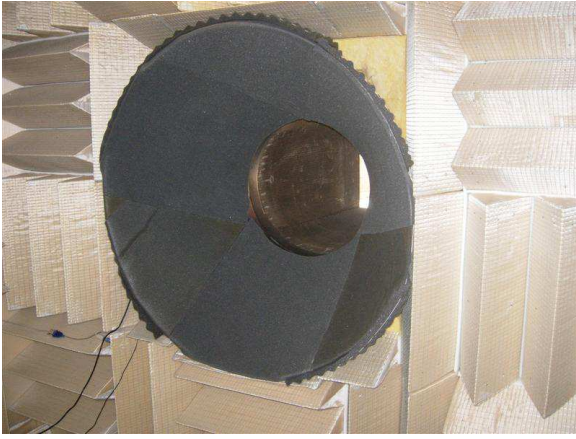
(b)

Figure 2.4: (a) Foam baffles in the upstream piping and (b) the resulting improvements in noise measurements at Mach 0.74.

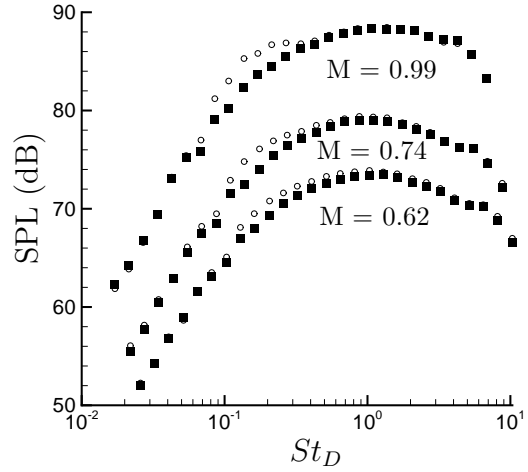
to act as a giant reflector plate downstream of the jet. The effect was so pronounced it was discernible with the human ear while standing inside the chamber. To correct this, the entire collector was coated in the same polyurethane foam material used to line the upstream piping. This removed the low-frequency obviously spurious hump from the spectrum as shown in figure 2.5. This effect at low frequencies was expected given reported experience with poor anechoic chamber designs leading to contamination of jet noise spectra at similarly low frequencies Viswanathan (2006).

2.1.3 Air Supply

Air is supplied to the experimental facility from a series of pressurized tanks (total 140 m³ of air at 890 kPa). These tanks are charged by a 224 kW Ingersoll-Rand SSK HPE300 compressor, which both dries and filters the air. Due to the relatively large amount of air contained in the tanks and the small amount of mass flow required by the jet, 25.4 mm and smaller nozzles can be tested continuously. To minimize spurious acoustic contamination sources, large 20.3 cm piping is used from the compressed air tanks to the control valve that



(a) Foam on downstream collector



(b) Resulting improvement on noise.

Figure 2.5: Exhaust collector improvement: \circ before; \blacksquare after.

regulates the jet flow.

2.1.4 Make-up Air

Special attention was given to replacement air, to make up for that entrained by the jet and exhausted with it out of the lab. We estimate the amount of air needed based upon a reported relationship for turbulent jet entrainment from the experimental measurements of Ricou & Spalding (1961):

$$\frac{m}{m_o} = 0.32 \frac{x}{D} \quad (2.1)$$

where m is the mass flow rate of entrained air, m_o is the mass flow of the jet, x is the distance along the jet axis measured from the nozzle exit, and D is the nozzle diameter. Using this relationship for our 25.4 mm jet at Mach 0.98, it was determined that there will be roughly 4.8 kg/s of air entrained by the jet before it enters the exhaust ducting. To provide this make up air, two open sections have been installed in the upstream wall of the chamber partially inspired by those in the anechoic facility at The Ohio State University (Kerechanin, 2000). These sections are rectangular in cross section, 2.1 m in height and 0.28 m in width. The estimated velocity of air entering through these entrainment sections is 3.5 m/s, which is

about one-hundredth the velocity of the jet. This make-up air is filtered by an aluminum woven-wire screen with 0.1 cm mesh size. The two make-up air sections have a 2.54 cm thick acoustic polyurethane foam absorber lining with egg carton shape to reduce any spurious noise from the lab from entering through these sections. They are also designed with an overhang such that there is no direct line of sight from the lab into the chamber.

The entrance through these make up air sections is covered with a flexible egg-carton foam made from polyurethane. The surface-to-peak thickness is 2.54 cm which for this foam gives a noise reduction coefficient (NRC) of 0.49. This coefficient represents the average sound absorption at 250, 500, 1000, and 2000 Hz. For this layer of foam, the material on average absorbs nearly half the incident sound at these low frequencies. Since lower frequencies are less dissipated by atmospheric absorption, these are the frequencies most likely to suffer from noise reflections. Also, the convoluted shape of the egg-carton works to help reduce sound reflections at all frequencies as it replaces the flat, hard drywall surface with one which will act to diffuse incident sound.

2.1.5 Exhaust

The exhaust starts with a conical 1.2 m diameter bell mouth leading to a 0.6 m \times 0.6 m exhaust duct. It is made of acoustically absorbing perforated metal ducting, and the flow is directed outside the building smoothly using aerodynamic turning vanes to reduce the potential for downstream flow separations to contaminate the measurements in the chamber. The completed facility is shown in figure 2.1, and a cutaway schematic can be seen in figure 2.6.

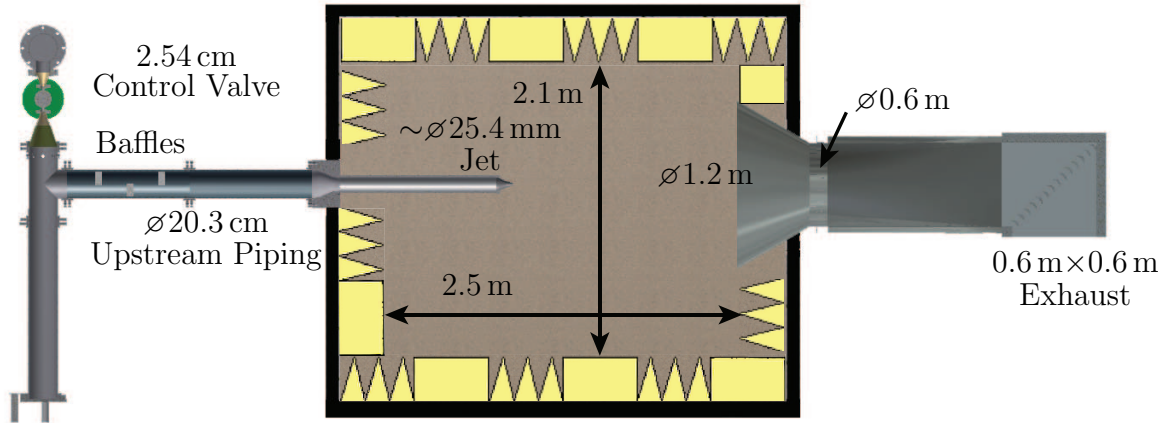


Figure 2.6: Anechoic facility overview.

2.2 Control and Measurement

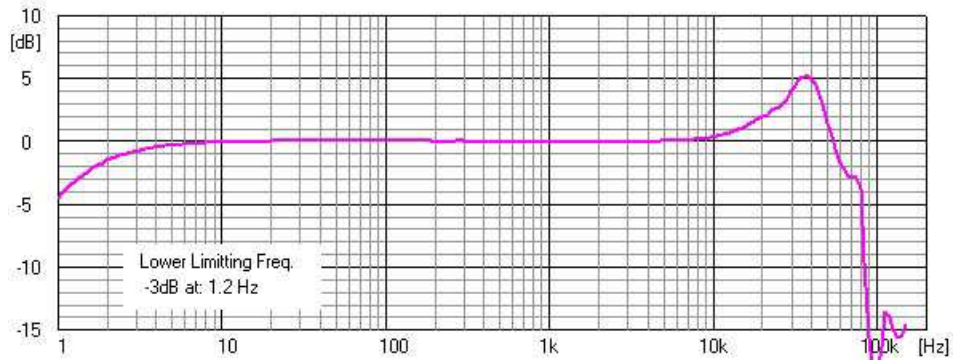
2.2.1 Flow Rate Control

The control valve is a 2.54 cm Fisher 667-ET-DVC6010 Globe Valve Assembly with carbon steel body used in conjunction with a PID control scheme in LabVIEW to keep the flow constant to within ± 0.005 of the target test Mach number despite any slow pressure variations in the supply tank pressure. Variations of less than 0.5% are typically achieved within 10 seconds of setting the condition. The manufacturer specified noise from the valve is less than 83 dB. The stagnation pressure for the jet is acquired using a Setra Model 206 pressure transducer. Both 0-to-172 kPa and 0-to-1720 kPa variants were on hand and used depending on the run condition.

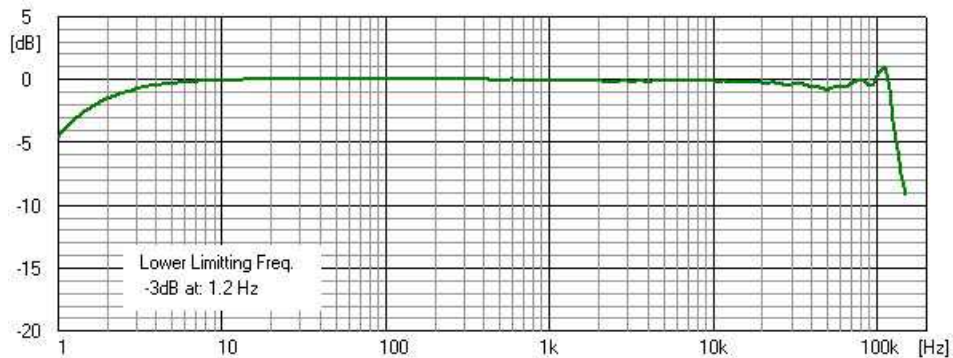
2.2.2 Microphones

The microphones used for all experimental acoustic measurements are Brüel & Kjær type 4939 0.635 cm free-field microphones. These are designed to operate with a flat response over

a frequency range from 4 Hz to 100 kHz and have a dynamic range of 34-to-164 dB. Typical response curves are shown in figure 2.7, which shows measurements with the protective grid both in place and removed. From the figure, it is apparent that the removal of the grid cap improves for high-frequency measurements.



(a) Response with protective grid cap.



(b) Grid cap removed.

Figure 2.7: Typical free-field response of a type 4939 microphone at 0 degrees incident angle. Response data from Brüel & Kjær.

Additionally, it is shown that the microphone supports can have a significant impact on the quality of the data obtained (see figure 2.8). The custom support used here had a small flat section near the diaphragm of the microphone, which caused the obvious standing waves. All microphones now use the Brüel & Kjær supports.

The microphones are connected to a Brüel & Kjær Type 2690 conditioning amplifier. The amplifier performs low- and high-pass filtering and also adjusts the signal level before it is supplied to the data acquisition hardware. The amplifiers interface with the microphones in a way that facilitates individual sensitivity calibration (approximately 4 mV/Pa) and

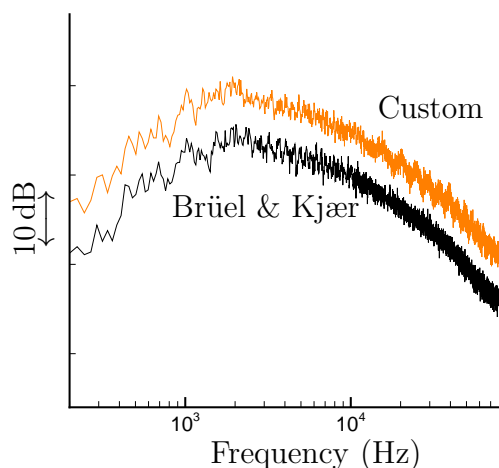
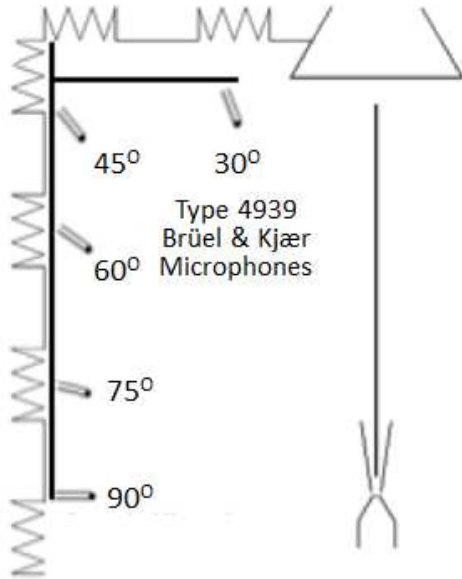


Figure 2.8: Microphone response testing importance of microphone support. The data have been offset for clarity.

provides a consistent, low-noise output. For the Mach 0.9 jets, the output is typically set at 100 mV/Pa for reference. The microphones are mounted on a linear rail which extends toward the rear of the chamber. A typical configuration is shown in figure 2.9.

2.2.3 Other Hardware

A National Instruments data acquisition system was used to record the data from the microphones. BNC cables connect the signal conditioning box to a BNC-2110 connector block, which interfaces with a NI PXI-6133 data acquisition module. This PXI card allows for simultaneous sampling of up to 8 channels at a maximum rate of 2.5 MS/s. While this sampling rate is not required, the simultaneous sampling capability is. For acoustic measurements, it may be necessary to correlate structures at various times, a feature not used in this dissertation but important for facility considerations. The data acquisition system is controlled through custom LabVIEW programs (Virtual Instrument — VI's) with the Sound and Vibration toolkit.



(a) Microphone schematic.



(b) In-chamber microphone positioning.

Figure 2.9: Typical microphone configuration.

2.2.4 Signal Processing

All the spectral data are recorded using LabVIEW along with information about the atmospheric conditions and the microphones used for each channel. The first sampling each day was usually done with no flow and serves as establishing the background noise in the facility. Either a power spectrum or third-octave analysis is performed in LabVIEW, and all subsequent post processing is done using MATLAB. The raw data are checked for saturation, with a warning message displayed if the voltage is within 10 % of the bounds so the operator can investigate further. For the narrowband data, the results of the power spectrum are averaged in bins to reduce signal noise, typically 96.6 Hz in size. Next, background noise is checked and if it is within 3 dB of the recorded test noise an error message is displayed. If not, the background is subtracted to give the sound from the jet flow. Next, the individual microphone calibrations are applied which were provided by the manufacturer. Microphone serial numbers for identification and if the protective grid caps are on or off is obtained from the configuration file. Next, estimated atmospheric attenuation is added back to the signal.

This value is based on the distance away, the temperature, humidity, atmospheric pressure, and noise frequency. The procedure for its calculation is provided in section 2.2.5. Finally, the data are converted to a common distance from the noise source using standard $\sim 1/R^2$ geometric corrections.

2.2.5 Atmospheric Absorption

Atmospheric absorption can be significant, particularly in small-scale facilities. As the jet spectra frequencies scale inversely as nozzle size, smaller nozzles require measurements at higher frequencies. To cope with this, it is most convenient that all data can be compared as usual in their lossless form. Viswanathan (2008) discusses several methods for calculating atmospheric absorption coefficients and for small-scale facilities recommends the method of Shields & Bass (1977), which he deemed superior for high-frequency measurement to the SAE method (SAE ARP866A, 1975), which is used for full-scale engine corrections. At lower frequencies (such as those of importance in full-scale tests), these two methods produce similar results, however at higher frequencies the deviation can be significant. After consulting the ANSI standard (ANSI S1.26-1995, 1995) as well as information from Viswanathan (2008), it was determined that the equations given by the ANSI standard produce results that are effectively indistinguishable from Shields & Bass (1977). We thus employ the ANSI standard. The attenuation coefficient, in dB/m, is:

$$\alpha(f) = 8.686 f^2 \left[1.84 \times 10^{-11} \left(\frac{p_\infty}{p_r} \right)^{-1} \left(\frac{T_\infty}{T_r} \right)^{\frac{1}{2}} + \left(\frac{T_\infty}{T_r} \right)^{-\frac{5}{2}} \left\{ 0.01275 \exp \left(\frac{-2239.1}{T_\infty} \right) \frac{f_{rO}}{f_{rO}^2 + f^2} + 0.1068 \exp \left(\frac{-3352.0}{T} \right) \frac{f_{rN}}{f_{rN}^2 + f^2} \right\} \right] \quad (2.2)$$

The relaxation frequencies for Oxygen and Nitrogen in (2.2) are (ANSI S1.26-1995, 1995;

Symbol	Parameter
α	Attenuation Coefficient (dB/m)
f	Frequency (Hz)
f_{rO}	Relaxation Frequency for Oxygen
f_{rN}	Relaxation Frequency for Nitrogen
h	Absolute Humidity (%)
h_{rel}	Relative Humidity (%)
p_∞	Atmospheric Pressure
p_r	Reference Pressure (1 atm = 101325 Pa)
p_{sat}	Saturated Vapor Pressure
T_∞	Atmospheric Temperature (K)
T_o	Triple-Point Isotherm Temperature for Water (273.16 K)
T_r	Reference Temperature (293.15 K)

Table 2.1: Parameters for the atmospheric absorption equations defined in (2.2).

Bass *et al.*, 1995; Zuckerwar & Meredith, 1985):

$$f_{rO} = \frac{p_\infty}{p_r} \left(24 + 4.04 \times 10^4 h \frac{0.02 + h}{0.391 + h} \right), \quad (2.3)$$

$$f_{rN} = \frac{p_\infty}{p_r} \left(\frac{T_\infty}{T_r} \right)^{\frac{1}{2}} \left[9 + 280h \times \exp \left(-4.170 \left[\left(\frac{T_\infty}{T_r} \right)^{-\frac{1}{3}} - 1 \right] \right) \right], \quad (2.4)$$

$$h = h_{rel} \left(\frac{p_{sat}}{p_r} \right) \left(\frac{p_\infty}{p_r} \right)^{-1}, \quad (2.5)$$

$$\log_{10} \frac{p_{sat}}{p_r} = -6.8346 \left(\frac{T_o}{T_\infty} \right)^{1.261} + 4.6151, \quad (2.6)$$

where the parameters are defined in table 2.1.

2.3 Facility Characterization

The purpose of an anechoic chamber is, of course, to simulate a free-field environment in a laboratory. To establish that the chamber was indeed acceptably anechoic, it was tested

with known sources and without any flow. This is because a jet can have both hydrodynamic and acoustic components of its pressure field, which could compromise the characterization. Ideally, a monopole sound source emitting a broadband noise spectrum would be used. To simulate this an acoustic system with a Radio ST-NG1 white noise generator, an ART 31-band equalizer, an Atlas Sound PA 601 amplifier, and a Selenium D22 Ti Acoustic Driver with a 2.54 cm diaphragm was constructed. This allowed for measurements between 100 Hz and 20 kHz.

To a good approximation, sound did decay as $1/R^2$, where R is the distance from the noise source. These tests were performed with the white noise source positioned at the typical jet exit location. Frequencies up to the 20 kHz limit of the noise source were tested. Example results are shown in figure 2.10. It is clear that the facility is anechoic down the the expected 400 Hz cut-off frequency. Additional plots are located in appendix A.

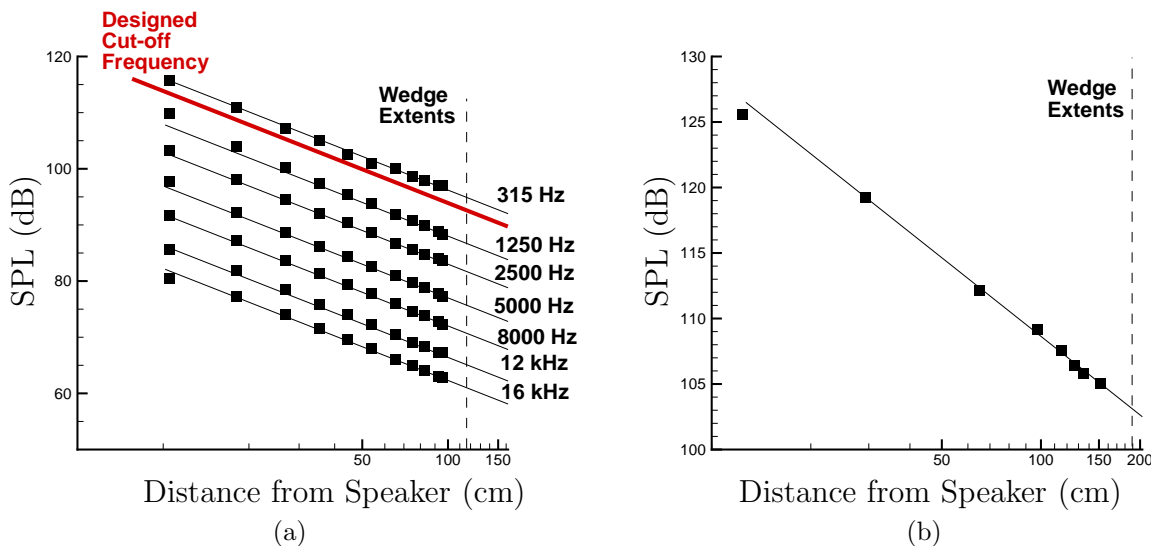


Figure 2.10: Experimental measurements of sound field spherical divergence in chamber ■ and — $1/R^2$: (a) sideline 90° at individual frequencies; (b) downstream 30° OASPL.

Once the facility was deemed to be free of spurious noise, various tests were performed to confirm that accurate jet noise data was indeed being acquired. One of these methods was comparing the overall sound level at different flow conditions with jet velocity U_j^8 . This is the theoretical dependence for quadrupole flow noise (Lighthill, 1952) and has been

measured in carefully designed jet noise facilities (Lush, 1971; Viswanathan, 2004). This scaling is followed closely between Mach numbers of 0.4 and 0.98. Mach number here and throughout this dissertation is defined with relation to the speed of sound in the core of the jet $M = U_j/c_j$. Deviation from the U_j^8 at low Mach number marks the minimum speed at which the facility can operate before rig noise becomes dominant. In our case, this occurs near Mach 0.4 where we see a transition to U_j^4 scaling, which would be consistent with the dipole type sounds of simple flow-structure interactions Curle (1955), presumably from the upstream piping or control valve.

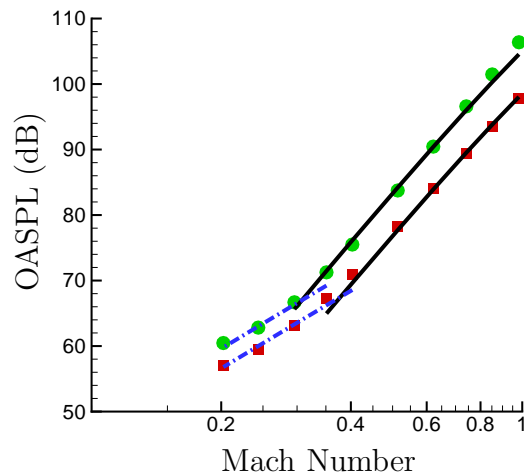


Figure 2.11: Comparison of OASPL with U_j^8 and U_j^4 visual fits at both $\theta = \bullet 30^\circ$ and $\blacksquare 90^\circ$.

2.4 Complex Nozzle Capabilities

A rapid prototyping shop allows for fast manufacture of new nozzle designs. These nozzles are made on a Formiga P 100 Selective Laser Sintering system (SLS) at a current cost of \$0.30 per gram of material. With such technology, complex shapes that would be difficult (and expensive) to manufacture using traditional metal designs, can be made quickly and at roughly the same cost as their baseline counterparts without the complex geometries, all with sub-millimeter resolution (Sippel, 2011). Sample simple designs, which have been made

and tested, are shown in figure 2.12. The chevron nozzle has been designed so the position of the chevrons can be rotated in relation to the fixed microphone array. When scaled appropriately, these nozzles were found to behave consistent with the metal nozzle which was used to characterize this facility. After testing various sized nozzles, it was determined that the 19.0 mm diameter nozzle was the smallest exit area which could produce scalable data, with smaller nozzles showing apparent Reynolds number effects as discussed by Viswanathan (2004).

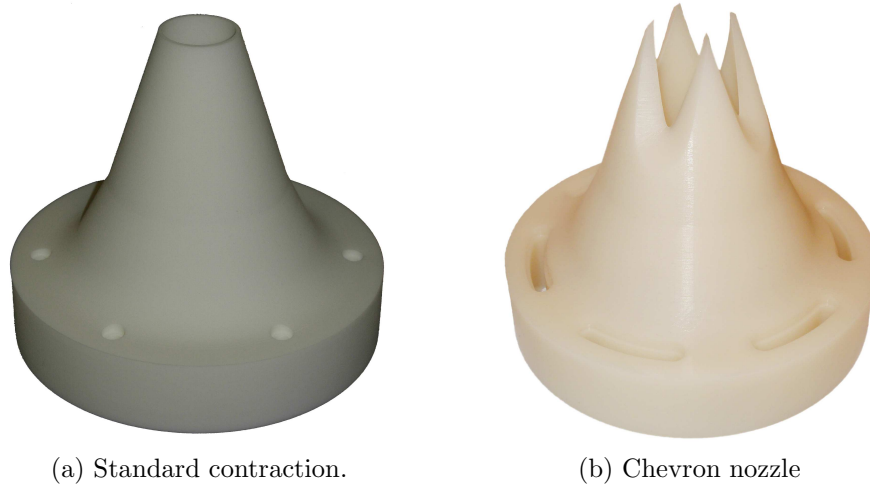


Figure 2.12: Nozzles manufactured with rapid prototyping.

2.5 Facility Validation

2.5.1 Acoustics

In order to validate the facility, measurements were compared with accepted experimental data (Brown & Bridges, 2006; Viswanathan, 2004) in figure 2.13. The data are in excellent agreement, except perhaps for Mach 0.98 measurements taken at $\theta = 30^\circ$, which is off by 2 dB, perhaps due to transonic effects. Also shown is a comparison between a 26.8 mm copper nozzle and a 19.0 mm nozzle made at a cost of about \$10 utilizing the rapid prototyping technology available. The data again are in excellent agreement with nozzles manufactured

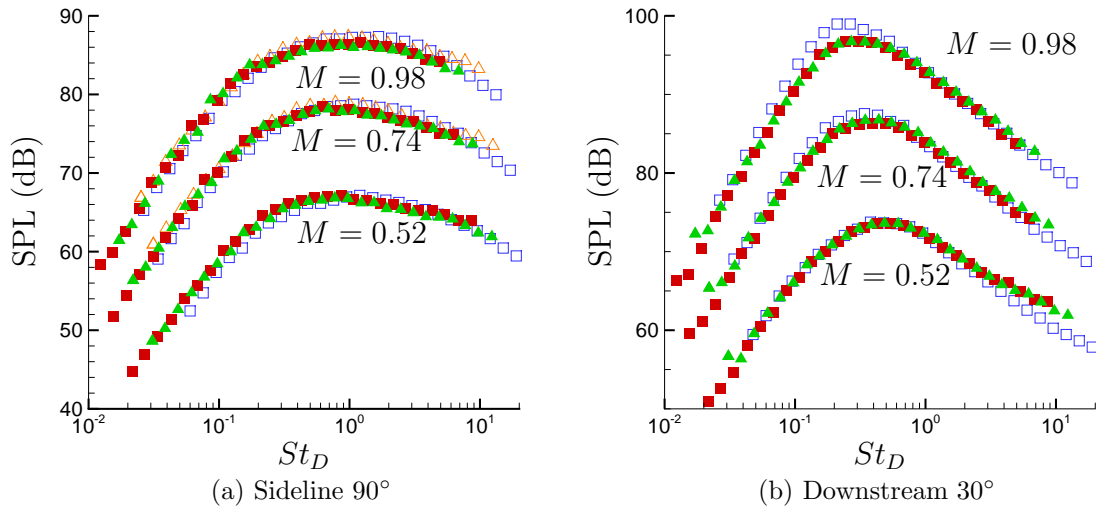


Figure 2.13: Typical 1/3-octave far-field response corrected to lossless conditions at $72D$: \blacksquare $D = 19$ mm rapid prototyped; \blacktriangle $D = 26.9$ mm machined metal; \square Brown & Bridges (2006); and \triangle Viswanathan (2004).

using different techniques able to produce consistent noise spectra when scaled. These data are presented in lossless form with atmospheric absorption effects removed per the method described above in section 2.2.5. The data are also corrected to distances based on nozzle diameter assuming $1/R^2$ spherical divergence. Total acoustic uncertainty has been determined to be less than 0.4 dB with individual contributions detailed in appendix B.

2.5.2 Particle Image Velocimetry

A key aspect to our studies is the measurement of the velocity and turbulence statistics just downstream of the nozzle exits. For this, we used a two-component particle image velocimetry (PIV) system and a PCO camera, see figure 2.14, which provided a ~ 100 pixels/mm maximum resolution. A New Wave Gemini dual-head Nd:YAG laser operating near 80 mJ per pulse at 532 nm creates the light sheet. A working image separation minimum of approximately 300 ns was found. For typical images a 50 mm f/1.4 lens is used with different extension tube sizes depending on the application. To guide the laser, 5.08 cm diameter

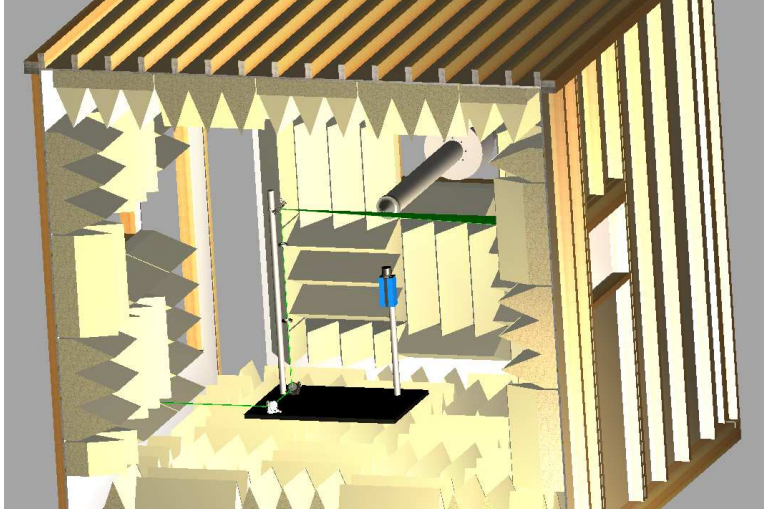


Figure 2.14: In chamber PIV equipment set-up.

high-energy turning mirrors are used. The beam is focused using a 750 mm spherical lens and a -50 mm cylindrical lens creates the sheet. By utilizing a laser power meter, a translation stage, and a knife edge, the full-width-half-maximum thickness of the laser sheet was measured to be 0.19 mm (see figure A.4).

For all PIV experiments, the core flow is seeded with Bis(2-ethylhexyl) sebacate (DEHS) using a Laskin nozzle designed to make $1\ \mu\text{m}$ particles (Humphreys & Bartram, 2001). The entrained air is seeded with a Vicount 1300/180/2.2 kW smoke generator that produces $0.2\ \mu\text{m}$ median diameter particles (Concept Engineering Ltd., 2011).

Most turbulence statistics we report were based upon PIV images extending from $0.04 D$ (~ 1 mm) to approximately $3.5 D$ (~ 90 mm) downstream. Reported results use more than 1000 image pairs processed using the DaVis 8.1 software package from LaVision. Processing began with a 64×64 pixel interrogation zone to generate bulk motion estimates with resulting vector fields applied to 32×32 pixel interrogation windows with 50% overlap. Cross correlations between the image pairs were repeated three times at each interrogation site with the previous result used as an initial guess for the particle motion until velocity field results converged. A 4:1 elliptical interrogation zone with 75% overlap using 32×32 pixels produced indistinguishable results. As a result, all analysis of the data presented was post-processed

with a square 32×32 pixel interrogation zone. Shown in figure 2.15 is a mean velocity field. In figure 2.16 is a comparison of $u'v'$ with Ukeiley (2007). We used a higher resolution, but once the flow is developed and better resolved downstream, the measurements agree reasonably well. All PIV equipment was removed from the chamber when making sound measurements.

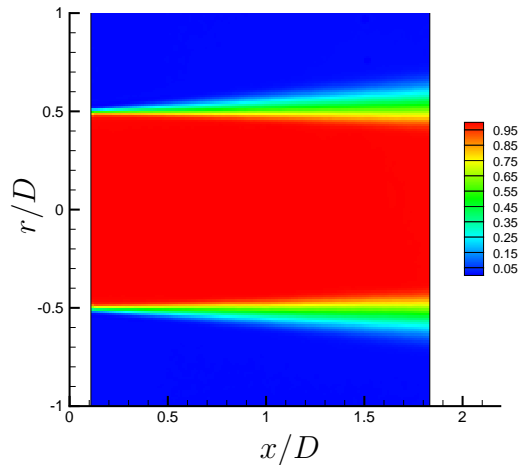


Figure 2.15: Mean velocity field normalized by centerline velocity $\left(\frac{U}{U_j}\right)$ of a Mach 0.98 jet.

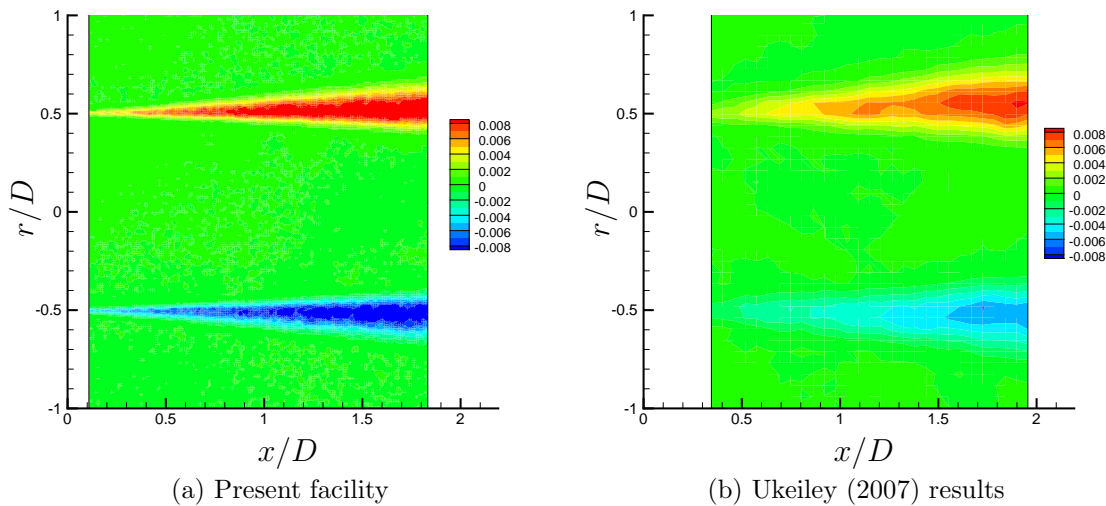


Figure 2.16: Comparison of PIV data by $\frac{u'v'}{U_j^2}$ in a Mach 0.98 flow.

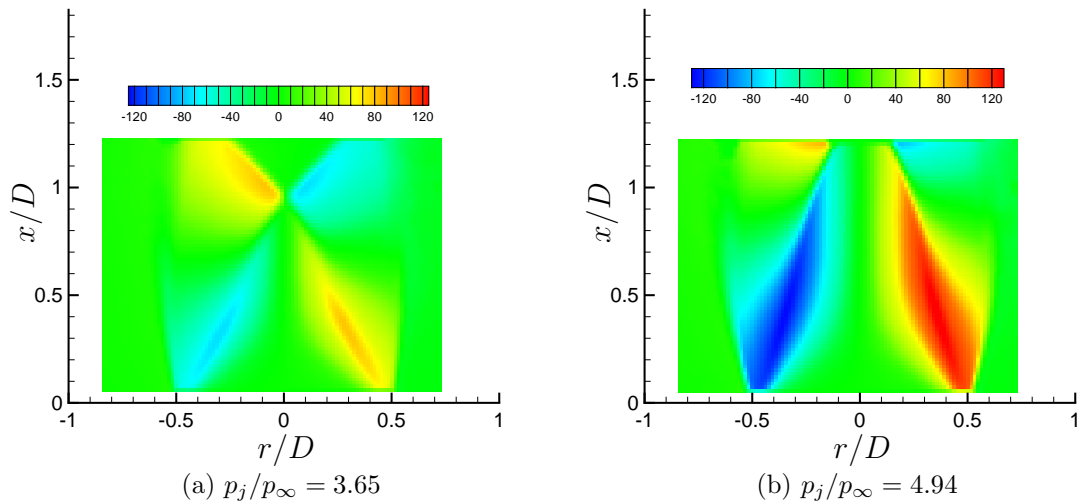


Figure 2.17: Radial velocity (m/s) for the underexpanded jet.

An additional step was taken to demonstrate the facility capabilities for supersonic jets. An underexpanded jet was run at nozzle (p_j) to ambient (p_∞) pressure ratios of 3.65 and 4.94. The resulting near-nozzle radial and streamwise velocity fields are included in figures 2.17 and 2.18, respectively. The location of shocks is readily apparent, demonstrating the ability of the diagnostics to measure in regions of high acceleration and shear, especially important for the accurate near-nozzle results of chapter 4. The acoustic spectra for these two run conditions are included in figure 2.19.

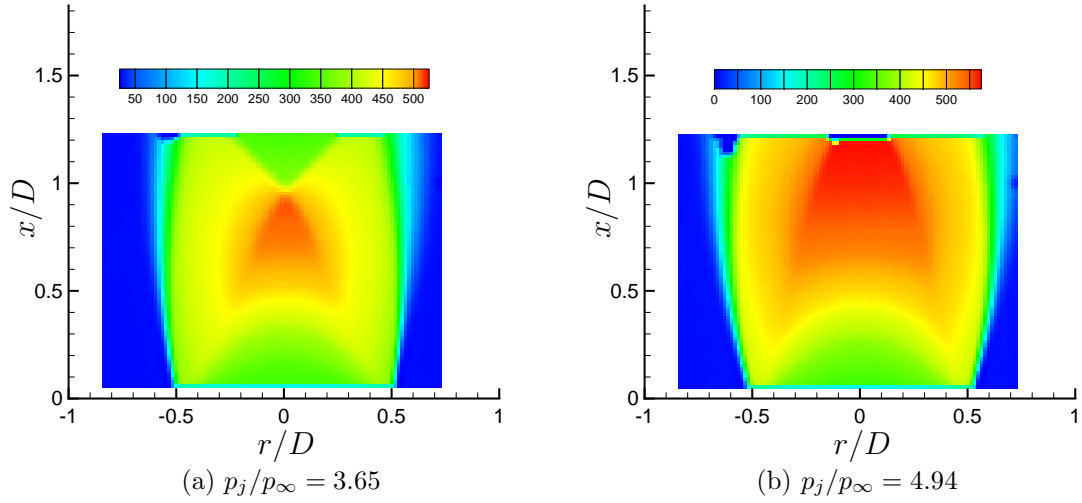


Figure 2.18: Streamwise velocity (m/s) for the underexpanded jet.

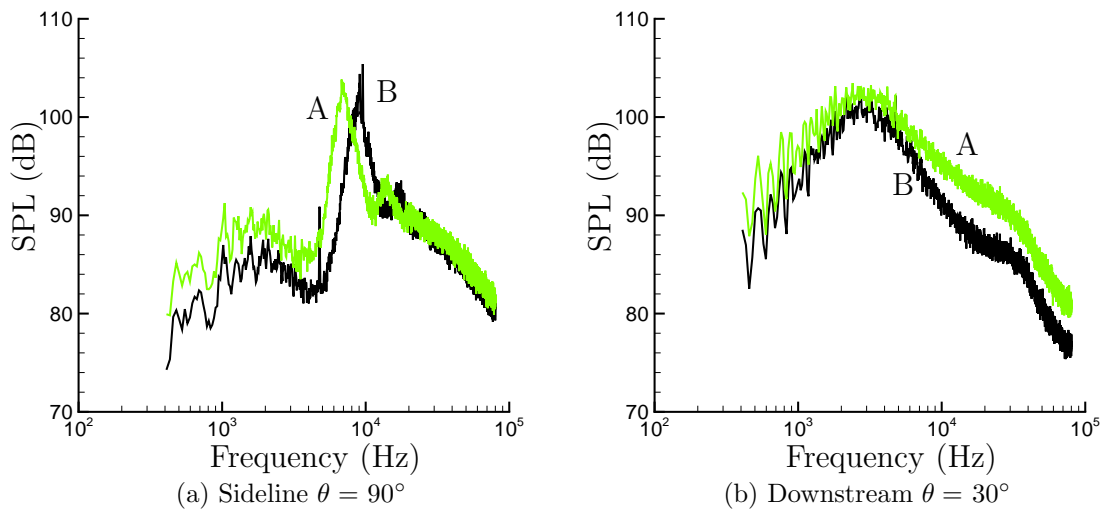


Figure 2.19: Acoustic spectra for the underexpanded jets: (A) $p_j/p_\infty = 3.65$; (B) $p_j/p_\infty = 4.94$.

Chapter 3

Passive Nozzle Control and Noise

The overarching goals of this dissertation, as discussed in chapter 1, entails fundamental aspects of the design and testing of low-noise jet nozzles, which in general might include some active control. Viewed simply, this has two aspects: (1) identifying candidate engineering nozzles for noise reduction and (2) facilitating the efficient testing, whether with experiments or simulations, of proposed designs. Toward this objective, this chapter demonstrates the use of our facility with RPT technology for low-cost testing of families of candidate complex-geometry nozzles. Complementing this chapter, the following chapters 4 and 5 consider a fundamental challenge inherent in all such efforts: the low-Reynolds-number and artificially thick near-nozzle shear layers which are potentially problematic in any such experimental or simulation-based effort.

3.1 Motivation

Aviation jet noise is heavily regulated with additional restrictions anticipated in the future. In the United States, for example, the FAA's FAR 36 Stage 4 noise standards came into effect in January 2006 for vehicles with a maximum take off weight of over 5,670 kgs, demanding a 10 dB EPNL (effective perceived noise level) reduction beyond the previous Stage 3 limits (FAA Title 14 Part 36, 2014). International standards are typically at least as restrictive and must be satisfied by any commercially viable jet. Many current aircraft operate close to FAA and other limits. Predicting the impact of nozzle geometry and placement modifications on noise generation is a significant challenge because jet noise levels are

sensitive to nozzle configurations. There is no experimental or numerical substitute for a full-scale experimental engine test. However, relatively inexpensive, small-scale tests can help avoid full-scale tests to assess the noise impact of design modifications and study noise mechanisms.

Presently, prediction capabilities lack the fidelity to accurately model the noise production from a high-Reynolds-number turbulent jet. Even something as seemingly fundamental as how the thickness of the nozzle initial shear-layer changes noise has not been well studied but is important if the noise production region is to be well understood. An improved understanding of how this near-nozzle-exit region affects the far-field noise will allow for improved noise reduction strategies. For example, the effect of a given chevron geometry and configuration on far-field noise is challenging or impossible to anticipate. Thus, in a design phase, a trial-and-error approach seems to remain an essential aspect when seeking reduction. If the parametric space were better understood, novel noise reduction geometries could be incorporated; this perspective motivates in part the parametric studies herein.

3.2 Chevrons

Chevrons have shown promise as a passive noise reduction strategy. They are thought to alter the mixing layer, which in turn affects the far-field acoustics. The exact mechanisms by which this works is not well understood, however it is believed they work to extract energy from large axisymmetric structures and redistribute the energy into streamwise vortex pairs. An example of chevrons is used on some models of the Boeing 787 “Dreamliner” commercial aircraft, as seen in figure 3.1, which would have been added after extensive and likely costly experimental testing.

A parametric study has been completed by Bridges & Brown (2004). They examined the relationship between chevron geometric parameters, flow characteristics, and far-field noise for both hot and cold jets. A change in length of the chevron was found to change the noise,



Figure 3.1: Boeing 787 “Dreamliner” showing the use of chevrons for noise mitigation in practice. Photo from www.boeing.com.

however the penetration angle is kept constant. They found very little change in the far-field spectra and concluded that “chevron length was not a major impact on either flow or sound when chevron count and penetration were kept constant.”

The present effort looks to quantify the shape of the parametric space for a chevron length change at a constant angle using our relatively low-cost facility. A proper mapping of this space can improve optimization strategies by investigating outstanding questions, improving cost function analysis. A particular goal here was to assess whether or not the flow changes, induced by the chevrons, are continuous with changing geometry (G) or a sudden onset occurs. The difference between the two behaviors is depicted in figure 3.2 where the x-axis could be any number of geometry modifications including chevron length, penetration angle, ect. Understanding this could aid automatic searches of the parameter space, perhaps via adjoint based (Freund, 2011) or other optimization strategies.

3.2.1 Experimental Setup

All nozzles were made from PA 2200 Polyamide White utilizing the Formiga P100 Selective Laser Sintering (SLS) system. Testing was completed for two orientations, first with a chevron tip in the plane of the measurement and second with an inter-chevron valley centered on the plane of measurement. For each orientation, the nozzle was tested twice, once to test

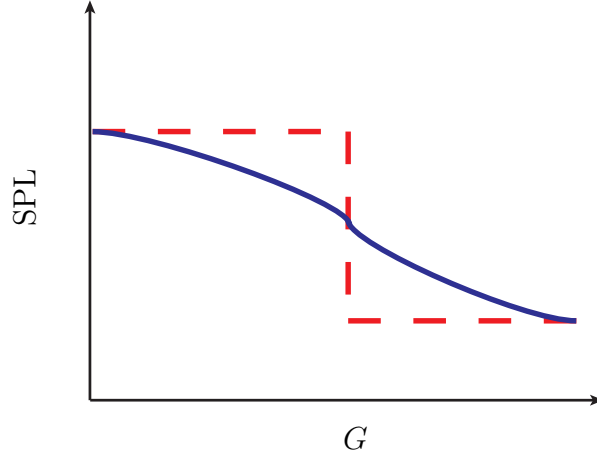


Figure 3.2: Sample far-field sound response to a nozzle geometry (G) alteration: $--$ step response and a $—$ smoother change in sound produced with geometry modification.

the sound radiated to measurement angles θ between 90° and 45° and the second time for the downstream $\theta = 30^\circ$ tests. This is required because of the orientation of the microphones in the array with the downstream microphone located in a different measurement plane due to the spatial limitations of the facility. All acoustics are normalized to $72D$ away with the nozzle diameter taken from the baseline round nozzle design.

The chevron designs were inspired by the nozzles tested by Bridges & Brown (2004) to allow for benchmarking. The baseline nozzle used for his testing included a 5° contraction in the exhaust region and has been scaled and reproduced in figure 3.3. It is an axisymmetric nozzle with an exhaust diameter of 25.4 mm.

The first nozzle set of chevron style nozzles tested kept this 5° taper at the exhaust. This design was shown to have the greatest overall effect on noise from the Bridges & Brown (2004) work with approximately a 5 dB increase at high-frequency for chevrons of length $L = 0.63D$. A profile view of this design is shown in figure 3.4 with the entire array studied in figure 3.5. A comparison is made to the benchmark for both the baseline and $L = 0.63D$ nozzles with excellent agreement as shown in figure 3.6, enhancing confidence in the experimental acoustic results.

In addition to the 5° chevrons, a series of nozzles with a more aggressive 18.2° chevron

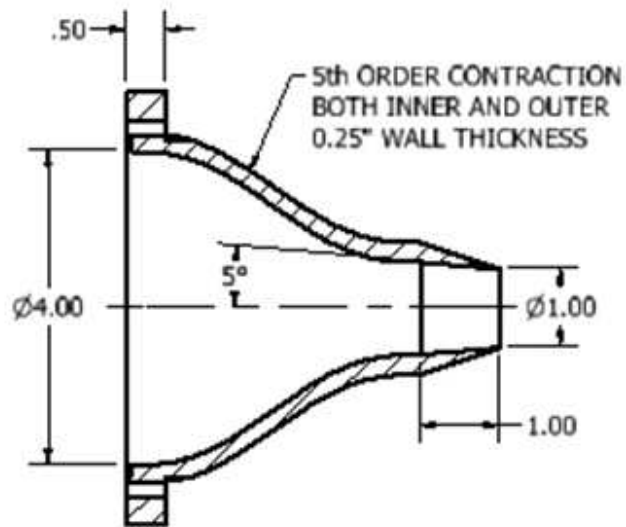


Figure 3.3: Baseline geometry for chevron nozzle studies.

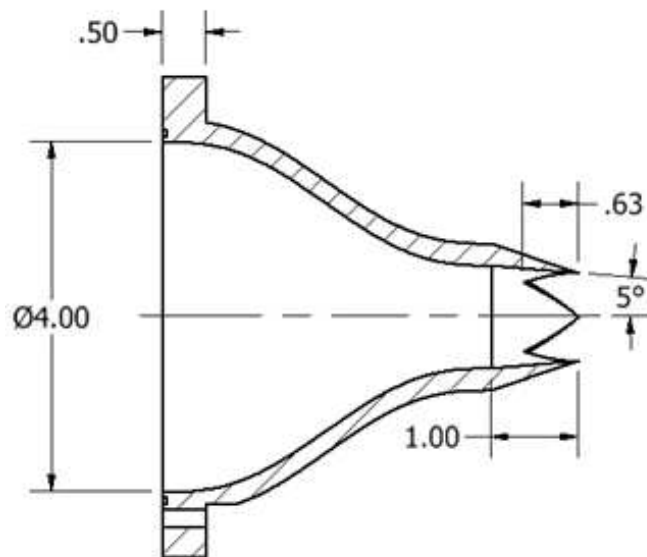


Figure 3.4: Chevron nozzle geometry for 5° testing.

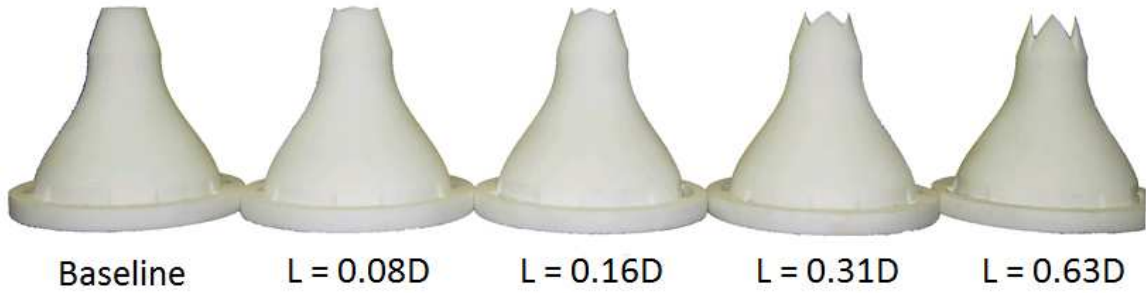


Figure 3.5: Array of nozzles with 5° chevron taper.

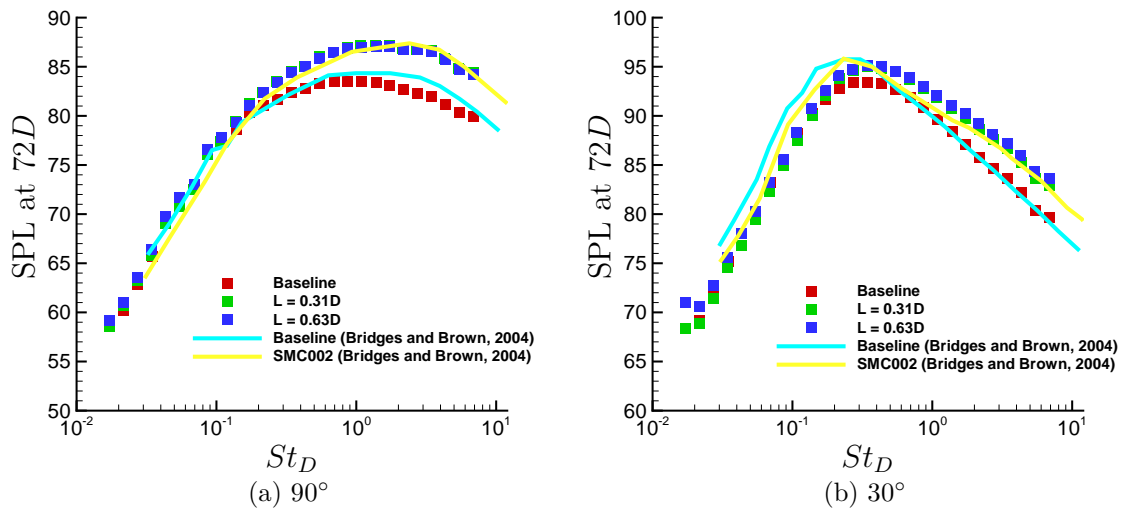


Figure 3.6: Comparison of third-octave acoustic response to Bridges & Brown (2004). The UIUC data are taken at Mach 0.9 while the Bridges & Brown (2004) data were acquired at Mach 0.98 and rescaled to Mach 0.9 using U^8 scaling.

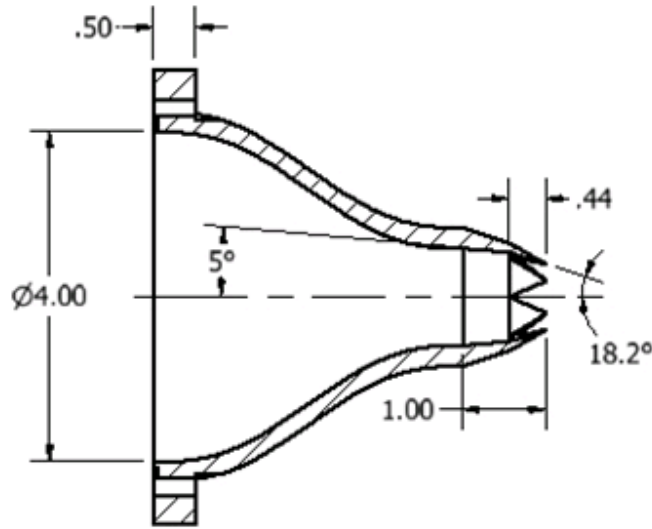


Figure 3.7: Chevron nozzle geometry for 18.2° testing.

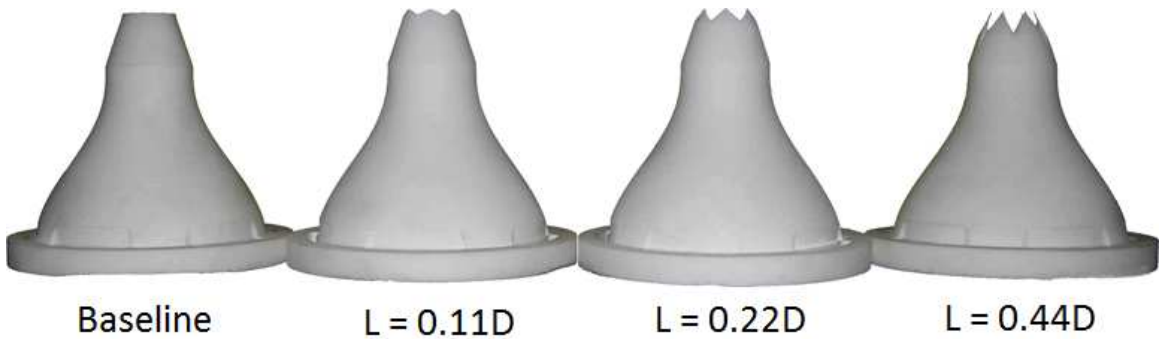


Figure 3.8: Array of nozzles with 18.2° chevron taper.

penetration angle was also tested. This geometry was chosen as it included a sound reduction at lower frequency, with sound reduction being the goal of these nozzle modifications. The nozzle geometry is shown in figure 3.7 with the entire array tested shown in figure 3.8.

3.2.2 Results

The overall sound pressure level (OASPL) for both the 5°-chevron and 18°-chevron nozzles show significant differences in figure 3.9. For the 5°-chevron nozzle, we see an initial overall sound increase as the chevron length increases followed by a leveling off for even larger values. This is observed for both the sideline and downstream measurements and the increase in

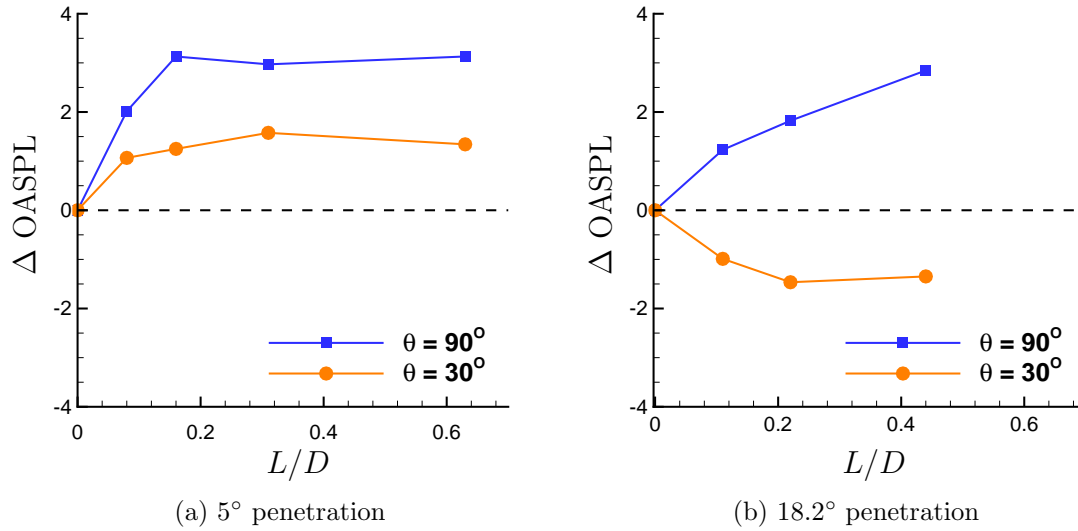


Figure 3.9: Change in overall sound pressure level as a function of the chevron length for both sideline and downstream measurement angles.

chevron length does not necessarily continue the trend noise increase with increasing chevron length. The uncertainty in all of the change in SPL measurements is approximately 0.25 dB. This reduction in uncertainty is due to the overlapping nature of many of the sound sources.

The 18.2°-chevron nozzles behave quite differently. For the sideline measurement angle we see almost a linear increase in sound as the chevron length increases. Initially, there is a corresponding reduction in overall sound levels downstream at $\theta = 30^\circ$, however this reduction reaches its peak for $L \gtrsim 0.2D$. As the sound reduction in one measurement direction has a corresponding sound increase in another for this geometry, trade-offs must be made for design. The reduction in $\theta = 30^\circ$ direction is advantageous as it reduces the most intense sound.

While the OASPL gives an overall picture of the sound field, a more detailed frequency analysis is also performed. Because humans have sensitivity to noise that is strongly frequency dependent, certain frequencies will be weighted more heavily than others. Third-octave spectra are plotted in figure 3.10.

Frequency dependent sound change from the baseline is shown in figure 3.11. At $\theta = 90^\circ$,

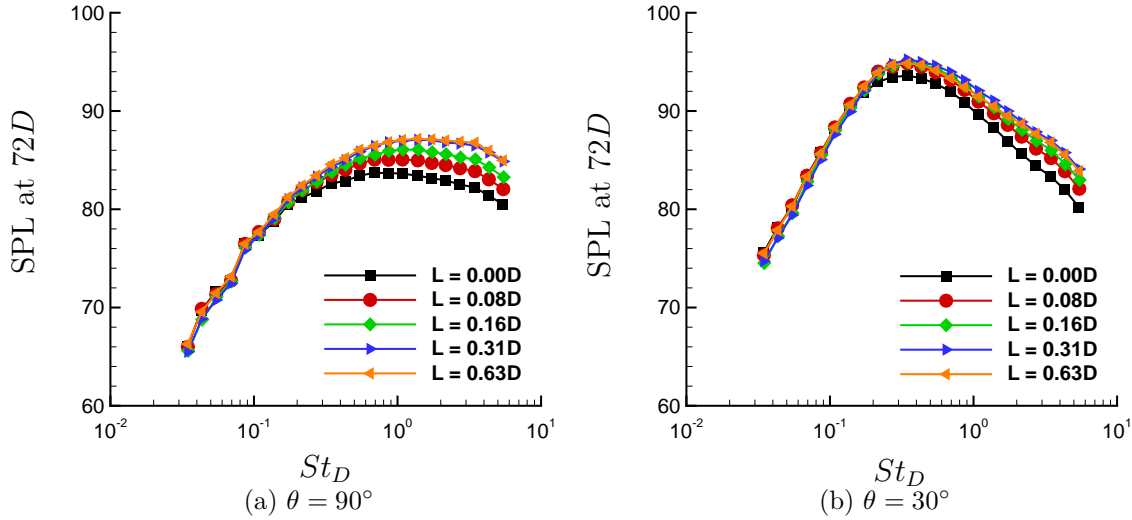


Figure 3.10: Third-octave response for the 5° chevrons at different lengths at both sideline and downstream measurement locations.

the low-frequency response for this nozzle is similar for all length chevrons with little change from the baseline. At higher frequency there is an increase in noise addition as the length increases until there is almost an identical response for the two longest, $L = 0.31D$ and $L = 0.63D$, chevron nozzles. At $\theta = 30^\circ$, we see that there is a reduction in sound levels for the longest chevron when compared with the preceding case while the lower frequencies follow the opposite trend. Referring to figure 3.9, there is a similar overall sound level change, emphasizing the importance of considering the details the frequency response.

Looking more deeply into the difference between these two longest chevron cases, an analysis of the frequency-dependent sound was conducted in relation to the directivity angle and is shown in figure 3.12. While the $L = 0.31D$ nozzle has a similar frequency response for all measurement locations, the $L = 0.63$ results at the $\theta = 30^\circ$ downstream measurement location differs from this trend. These tests were repeated with consistent results found.

The frequency-dependent sound production for the 18.2° chevron nozzles are shown in figure 3.13 for both sideline and downstream measurement locations. There is a reduction in sound at lower frequency and an increase at higher frequencies. This is better visualized

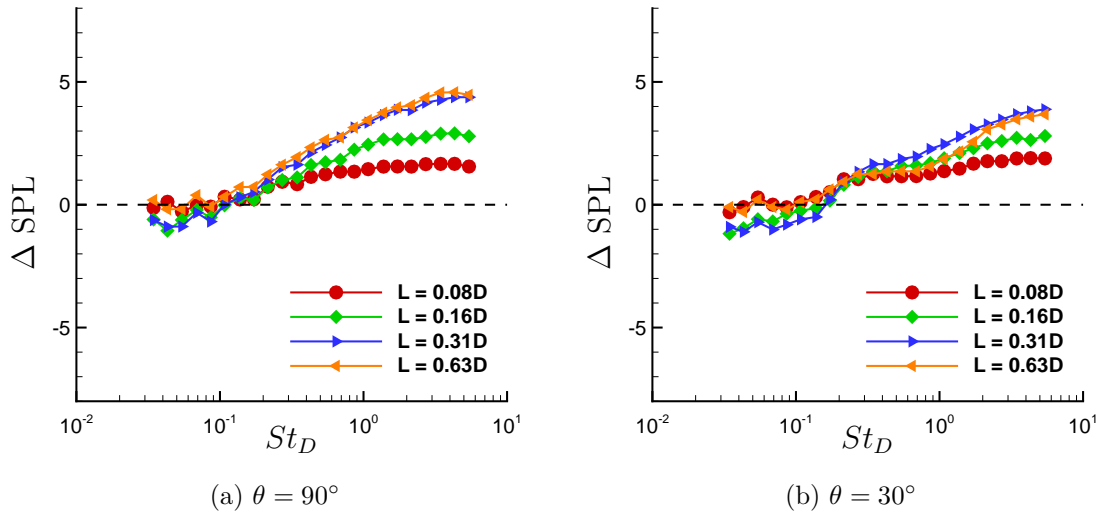


Figure 3.11: Third-octave sound pressure level change from baseline for the 5° chevrons at different lengths at both sideline and downstream measurement locations.

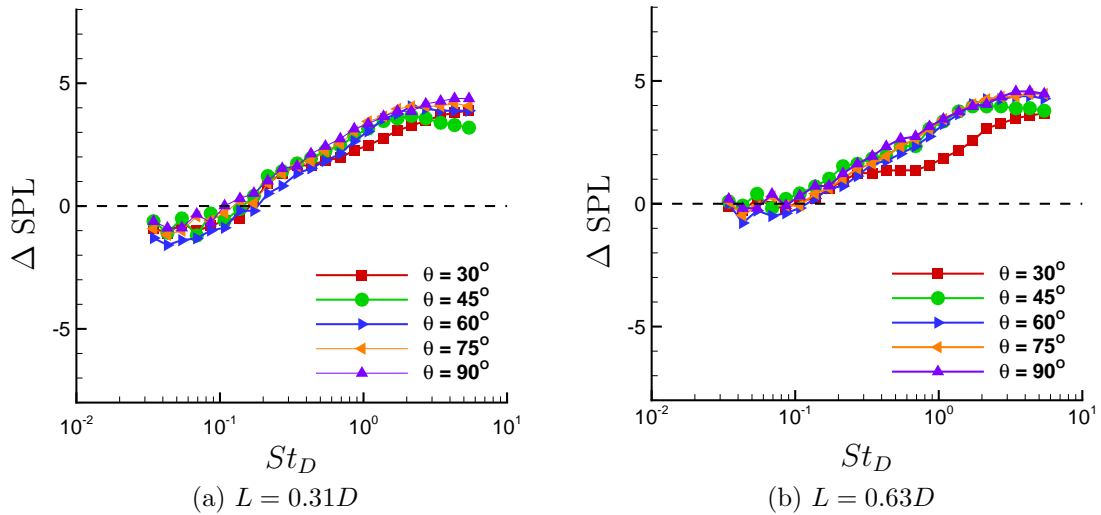


Figure 3.12: Third-octave sound pressure level change from baseline for the 5° chevrons at different measurement locations for the two longest chevrons studied which had similar Δ OASPL.

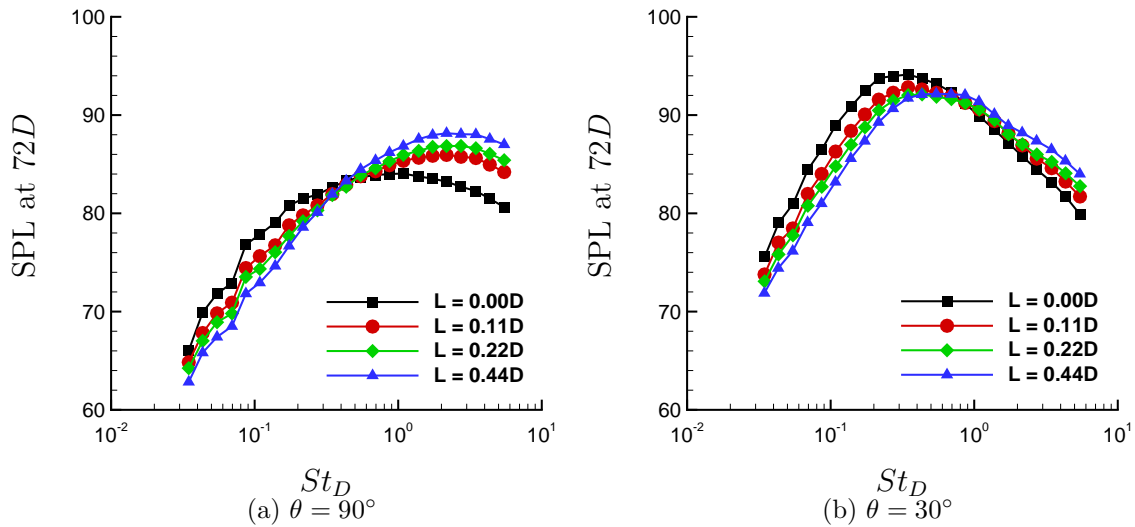


Figure 3.13: Third-octave response for the 18.2° chevrons at different lengths at both sideline and downstream measurement locations.

in figure 3.13 which compares the change in sound from the baseline for the three nozzles tested. The crossover point is consistent between the nozzles and shifts to higher frequencies for the downstream measurements and also reduces the peak levels where the peak levels are increased for the sideline measurements. This is important from a design perspective. It also appears that for a reduction in sound to occur, there needs to be a corresponding addition somewhere else. It can be reasoned that roughly the same amount of energy is exhausting from the nozzle, with the longer chevrons able to better break this turbulence up. This will lead to smaller structures which will inherently emit noise at higher frequencies. Finding a way to push this higher toward out of the range of human hearing will greatly reduce the amount of effective noise from a nozzle but this will take a more in depth understanding of the exact mechanism by which this works which is not available as of this time.

3.3 Small Perturbation Acoustics

The importance of the near-nozzle exhaust conditions has been shown along with the capability to alter the far-field sound using chevrons. While most chevron studies focus on

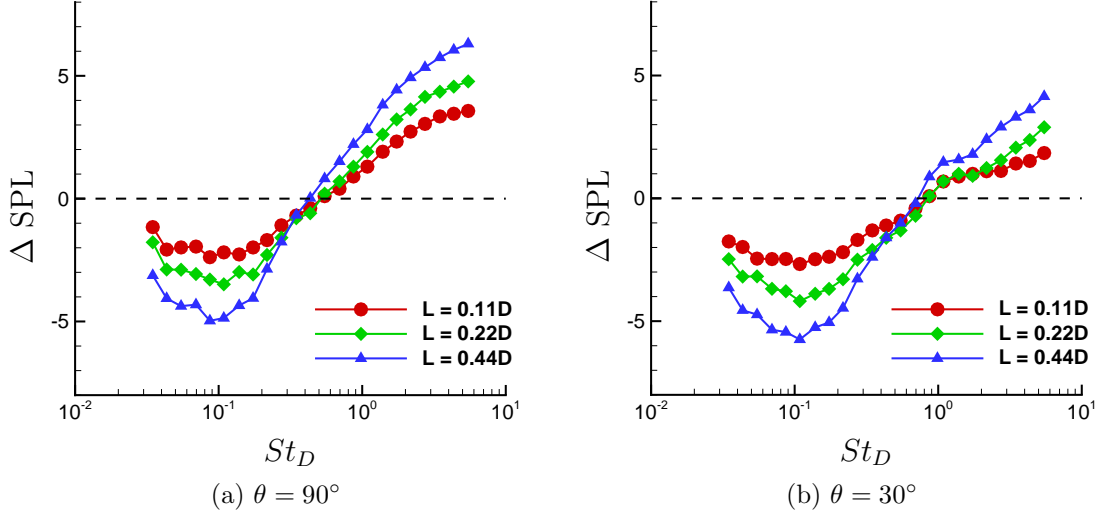


Figure 3.14: Third-octave sound pressure level change from baseline for the 5° chevrons at different lengths at both sideline and downstream measurement locations.

relatively large changes in chevron size, as in the previous sections, a study on the effect of minor perturbations was also designed and completed with the goal of observing quantifiable sub-mm changes to chevron geometry. Understanding the sensitivity that can be measured in experiments and the shape of the optimization space is important for automatic optimization as shown in figure 3.2. A response with no or little gradient would require more detailed *a priori* knowledge for the scheme to know if the optimization was close to a step change.

A nozzle with 6 equally spaced chevrons of length 12.7 mm was designed with mounting brackets on each chevron which allowed for the addition of a Fircelli Technologies PQ12 Miniature Linear Actuator, see figure 3.15. The chevrons had a baseline penetration angle of 5° into the core flow. When mounted, the actuator allowed for sub-millimeter changes to the penetration and provided positional feedback to within ± 0.01 mm. By creating the chevrons out of plastic, the actuators were able to adjust the amount of penetration into the flow. An actuator extension of 2.4 mm was achieved before a slight crack was found at the base of one of the chevrons, which set the limit tested.

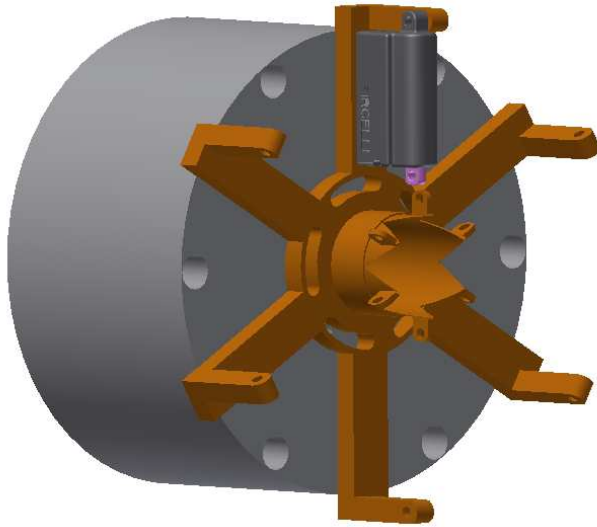


Figure 3.15: CAD depiction of the small perturbation set-up. Machine drawings are provided in appendix C.

Narrowband measurements were acquired for six chevron penetration configurations including the baseline with no actuator movement and are shown in figure 3.16.

The narrowband measurements are then combined into third-octave bins and the baseline configuration subtracted in figure 3.17. This results in an uncertainty reduction to approximately 0.25 dB due to the overlapping nature of some of the uncertainty sources as discussed earlier in this chapter. There is more variation in the noise at lower frequencies, possibly due to reflections from the experimental set-up, however the responses generally look flat, with minimal noise addition from the increased penetration. As the frequency increases to around 10 kHz, there is a shift and the noise from the chevrons shows a continuous increase at high frequencies. In addition, as this penetration increases the amount of noise also increases as shown in figure 3.18. For both of these metrics, a plateau has been reached for the two largest chevron penetrations. The dip in the plot from an actuator extension from 0.4 mm to 0.8 mm may be related to the smoothness of the response to actuation, or a result of measurement uncertainty, further testing would be required for clarity as it is on the order of only 0.1 dB or less.

This study proves the viability of sub-mm precision for optimization, particularly at

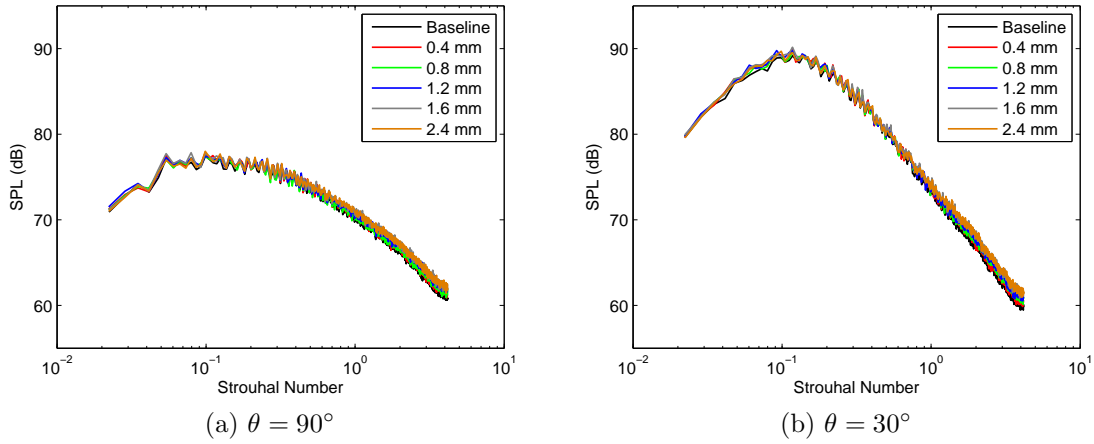


Figure 3.16: Noise measurements for six different chevron penetrations tested.

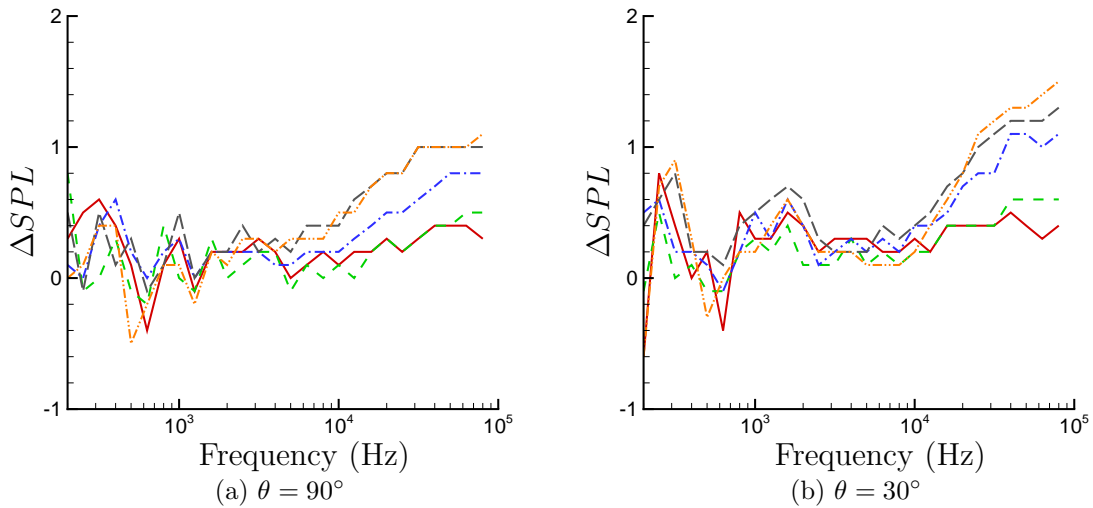


Figure 3.17: Third-octave noise change from the baseline penetration: — 0.4 mm; - - - 0.8 mm; - · - · 1.2 mm; - - - - 1.6 mm; - · - · - · 2.4 mm.

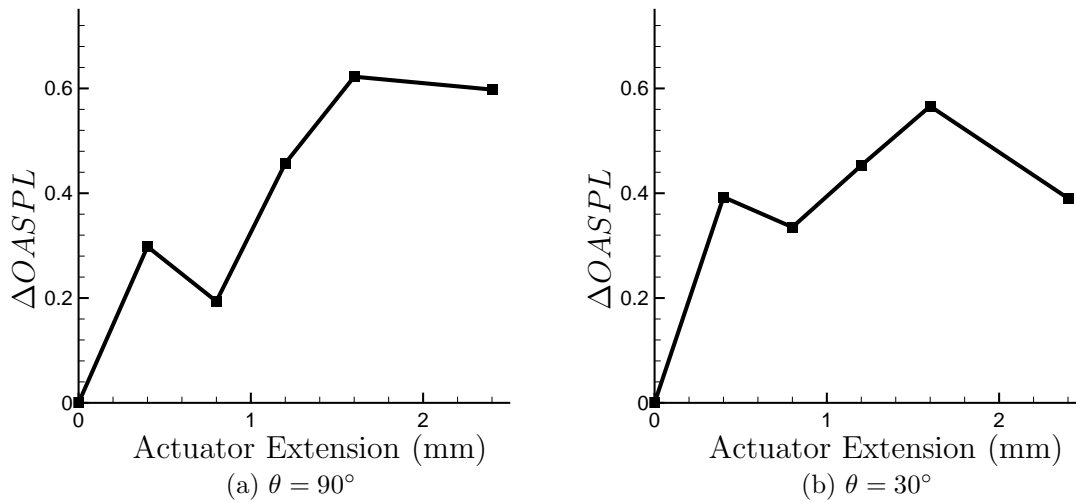


Figure 3.18: Change from baseline in the overall sound pressure level.

high-frequencies which have been shown to be the most computationally difficult to achieve. Additionally, it will allow for the future study of non-symmetric chevron penetration in a less expensive manner than the creation of multiple nozzles.

3.4 Clamshell Nozzles

An analysis of two clamshell-style nozzle geometries, one circular and one elliptical, supplied by Rolls-Royce has been performed. The geometries for the two separate nozzles were supplied as full engineering-scale CAD models and scaled down by a factor of 40. They were designed to attach to the piping system already in place in the chamber using a 5th-order polynomial contraction which put the exit plane of the model (defined in this study as the tip of the clamshell) at a fixed position in the anechoic chamber. The nozzles were manufactured using SLS.

Each nozzle was tested at a Mach number of 0.98. The spectra acquired at sideline ($\theta = 90^\circ$) and downstream ($\theta = 30^\circ$) angles are shown in figure 3.19. Measurements were taken at two nozzle orientations, one with the clamshell tip directed toward the microphone array and

the other perpendicular to this (denoted in the plots as the “valley”). The narrowband data are displayed in 23.4 Hz bins. All spectra are corrected using a local nozzle diameter, defined here as the distance across the nozzle exit along the measurement plane, to a normalized distance of 72 D. The narrowband data clearly shows a number of tones generated by the elliptical nozzle that are not present in the axisymmetric baseline or the circular nozzles, as shown in figure 3.19. The acoustic data are presented as a function of Strouhal to normalize based on the size of the model, however the tones were found to be just under 8kHz and harmonics when measured in frequency space. Also included are normalized plots of streamwise velocity in figure 3.21. These measurements were made using particle image velocimetry (PIV) along a plane perpendicular to the clamshell tips. From these images we can see the thicker shear layer for the elliptical nozzle which can be attributed to the flapping nature of the shear layer discussed below.

Having observed the intense tone for the elliptical geometry, an array of nozzles were designed and manufactured where the exit cross-section transitions from circular to the provided elliptical shape with a ratio of 1.25:1 between the major and minor diameter to attempt to identify if the intense tones were a threshold or continuous in their behavior. The 1.25:1 elliptical nozzle is the same scaled geometry as provided by Rolls-Royce, however the 1:1 circular nozzle has been modified so the nozzle is as similar to the elliptical nozzle as possible except for the exit cross-section.

The first test performed on this new set of nozzles was to find the onset of a significantly separated flow and how the clamshell’s presence alters the exiting flow on the ejector surface using fluorescent surface-flow-visualization. The field of view is identified in figure 3.20.

The oil is a blend of multiple high-viscosity oils typically found in a hardware or automotive store. A fluorescent dye (Tracerline TP-3400) was added which absorbs in the near-UV (activated with a black light) and emits in the visible range, allowing the oil to be visualized using a Mightex camera at a 2 Hz sampling rate.

Utilizing this fluorescent surface-flow-visualization, it was determined that the shear layer

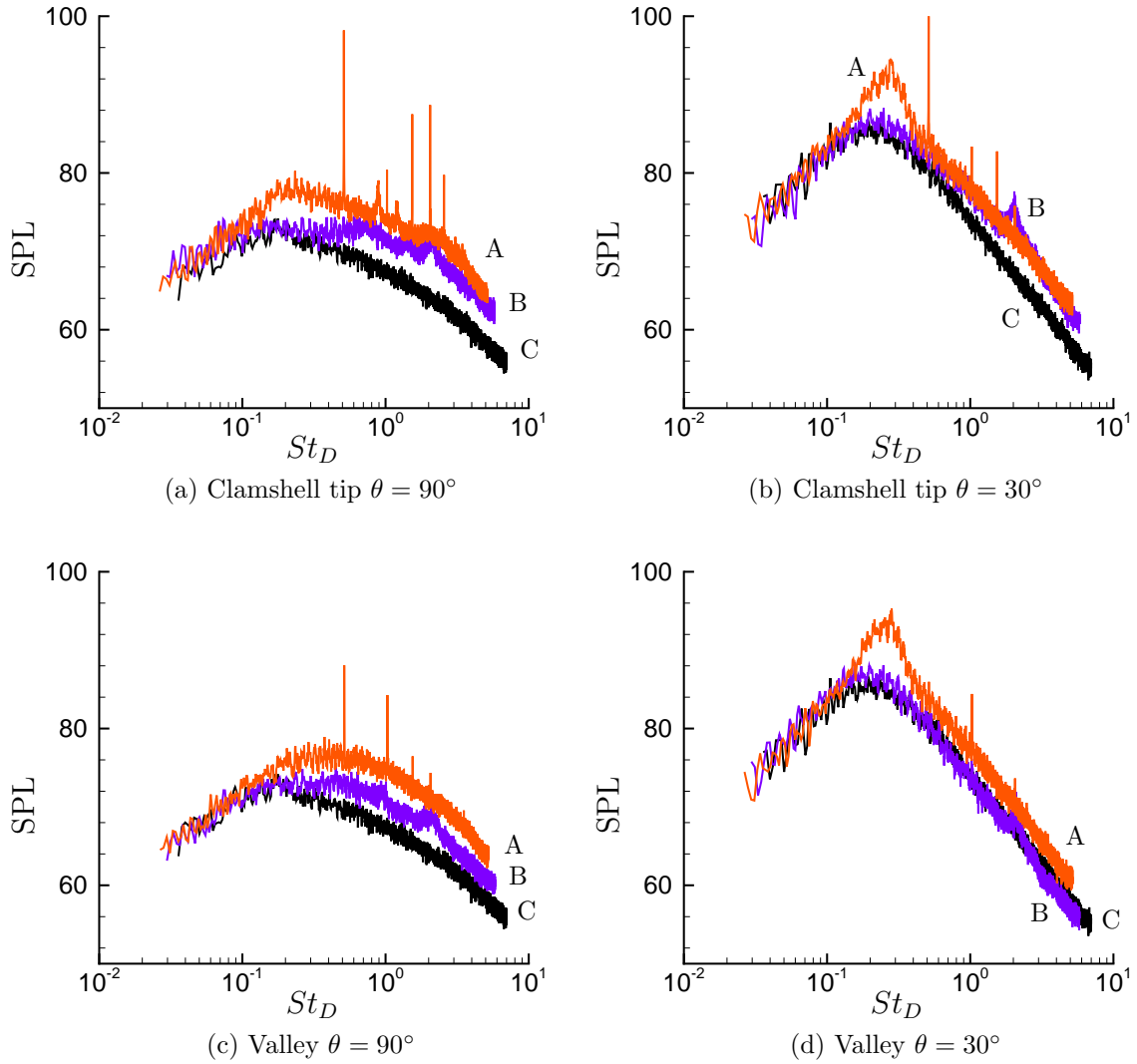


Figure 3.19: Narrowband sound spectra for circular and elliptical clamshell geometries normalized by the hydraulic diameter (D_h) to $72 D_h$: (A) circular exhaust; (B) elliptical exhaust; (C) axisymmetric baseline.

is unable to attach to the clamshell surface in the case of the elliptical nozzle, shown in figure 3.23. In the corresponding video files, it is apparent that in (a) the exiting flow is able to attach to the clamshell surface and a recirculation zone is formed in (b), (c), and (d). As the exit profile becomes more elliptical, the intensity of this recirculation region appears to increase and the formation of two counter-rotating spiral vortices are apparent. This visualization was performed at 2 Hz. High-speed schlieren visualization was also performed

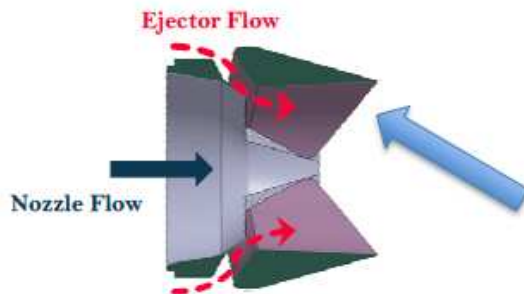


Figure 3.20: Overview of a clamshell style nozzle with surface flow visualization view identified. Image from Thirumurthy *et al.* (2010).

to investigate the short time-scale events which could produce the frequencies of the most intense sound. This high-speed schlieren is able to show shedding from the elliptical nozzle which is not present for the circular nozzle, snapshots in time can be seen in figure 3.24. This was taken with a $20\ \mu\text{s}$ exposure time at 30 kfps to freeze the flow and allow us to capture the high-frequency structures.

By tracking the intensity of light at a particular point in the shear layer as a function of time, the shedding was found to be just under 8 kHz for all nozzles except the circular which produces no shedding, see figure 3.29. This 8 kHz is the same tone that is seen in the narrowband spectra in figure 3.19. It is apparent that the sound associated with this shedding is of more importance in the direction of the clamshell tip as expected. This is the primary plane in which these vortices are created and the acoustic fluctuations should primarily be in this direction. From these tests, controlling this shedding by ensuring the shear layer is able to attach to the clamshell exit should be a first priority when attempting to reduce any noise created by the elliptical nozzle.

3.5 Center Body Nozzle

Data were also collected for a nozzle which included a center body, a competing technology for nozzle control which has been shown to result in acoustic benefits (Knott *et al.*, 1984). The center body support was designed to fit into the existing axisymmetric nozzle while causing

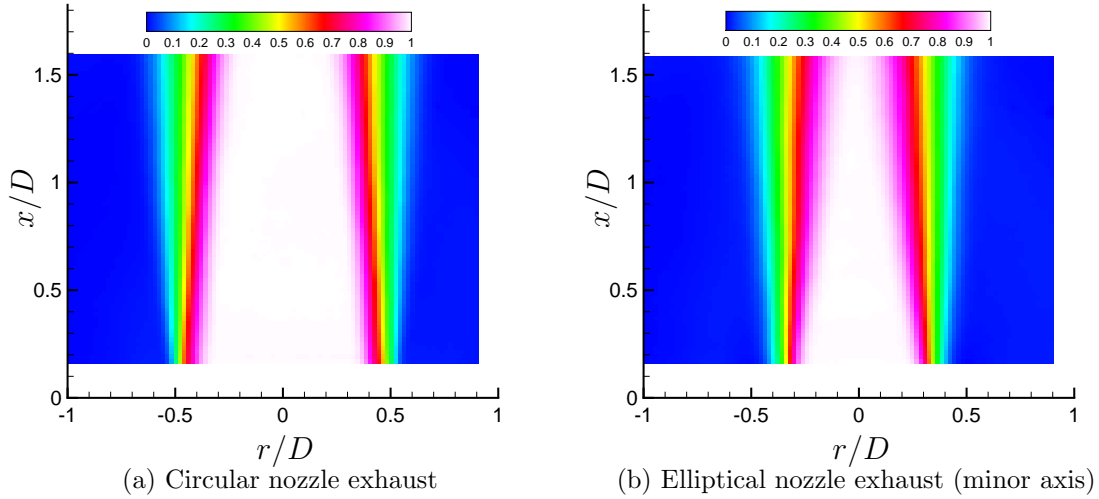


Figure 3.21: Nozzle exit velocity normalized by centerline velocity.

minimal disturbance upstream. The details of the center body is included in the appendix as figure C.45 and the accompanying profile coordinates. The profile is based on Kapilavai *et al.* (2012) who investigated shock–shock and shock–boundary-layer interactions in a shrouded nozzle but did not explore nozzle acoustics.

An image of this style nozzle installed in the facility is shown in figure 3.26 with figure 3.27 showing the orientation of the plug support in the upstream piping. There are two sets of aluminum adjustable cross-braces which hold the center body in place. The center body is made from steel for structural rigidity and tapers to a point in the upstream direction to minimize flow disturbance. The plug is rapid prototyped using SLA technology.

Sound measurements have been acquired for a number of flow conditions and locations as shown in figure 3.28. The importance of finding the correct operating conditions are apparent, with a tone being created at a nozzle pressure ratio of 3.67 which is louder than any of the noise at the faster run conditions.

Compared to an axisymmetric baseline, the noise produced by the plug nozzle is more intense for all frequencies at sideline measurement locations, but only for the peak and high-frequency regions for the downstream measurement location, which is shown in figure 3.29.

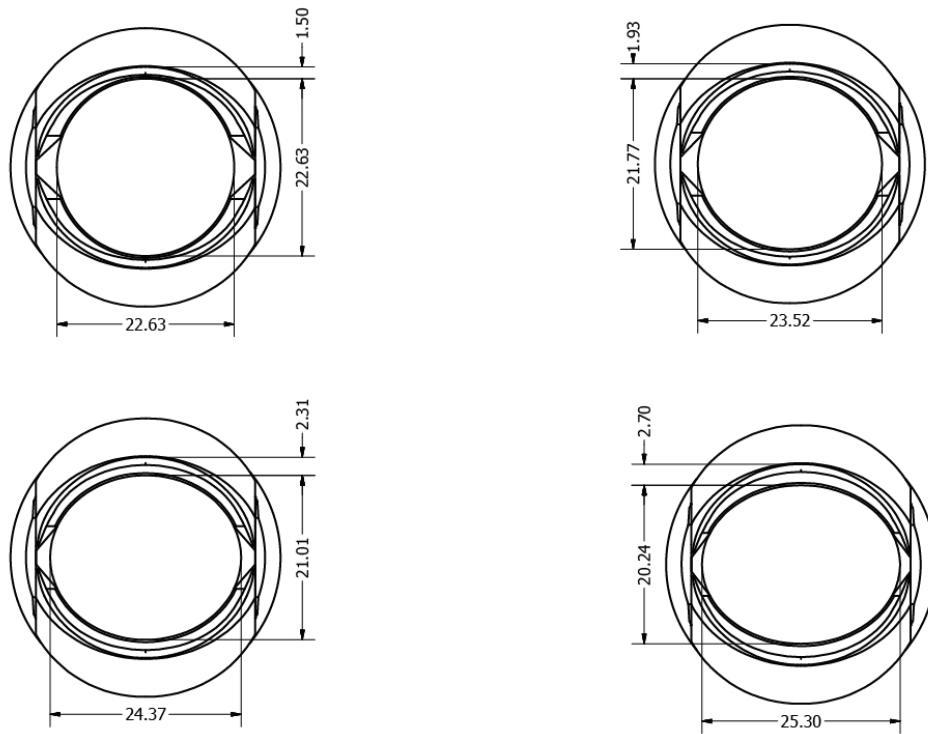


Figure 3.22: Front view of the four nozzles used in the parametric study of a class of clamshell nozzles. The major and minor diameter of the nozzle exits are shown along with the vertical distance between the exit and the nearest point on the clamshell tip. All dimensions are in mm.

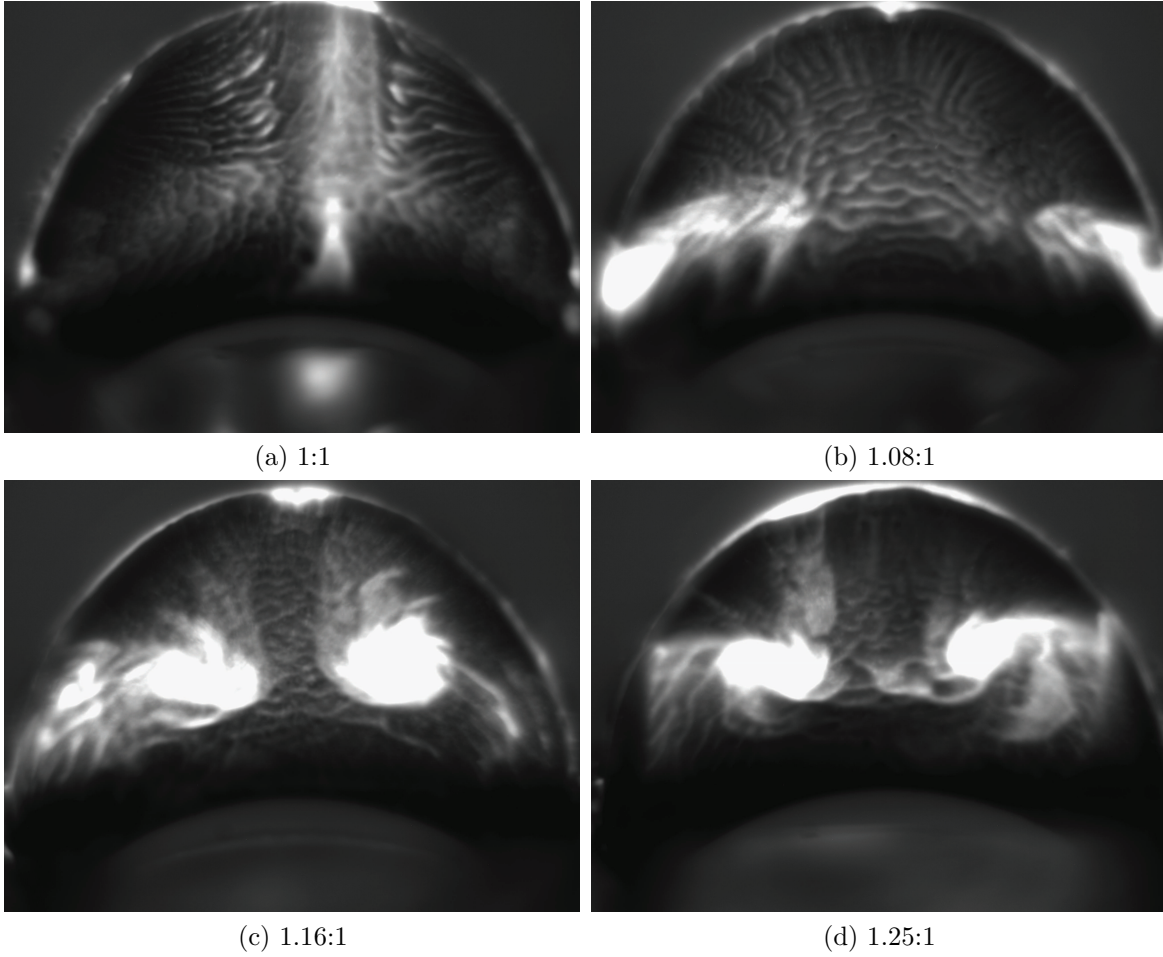


Figure 3.23: Instantaneous surface flow results for a class of clamshell nozzles.

This further demonstrates the complex geometry capability of the facility and provides a preliminary dataset for this geometry.

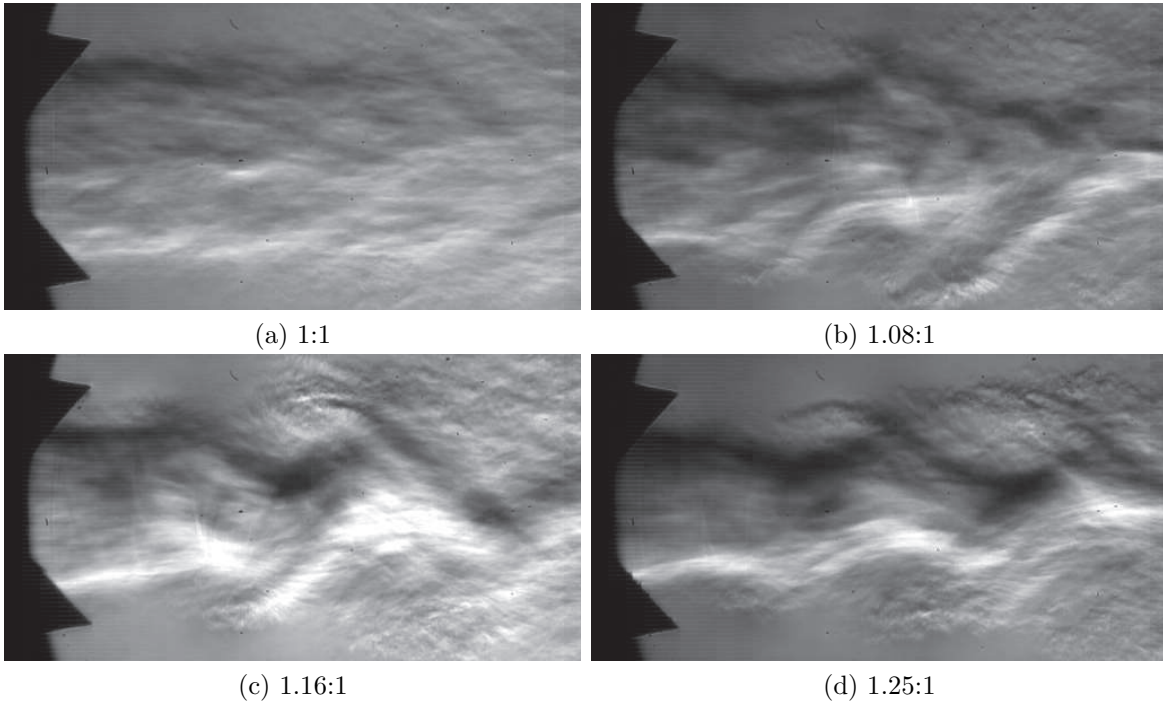


Figure 3.24: High-speed schlieren snapshots with exposure time of $20 \mu\text{s}$.

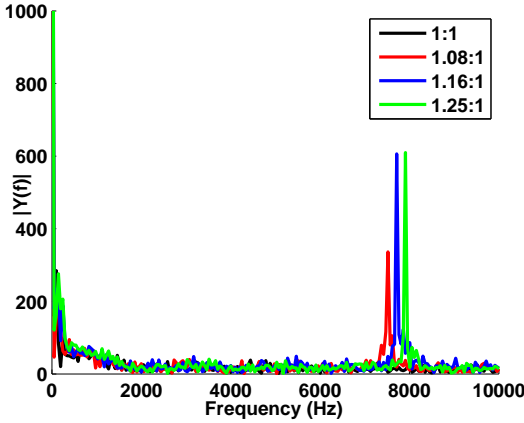


Figure 3.25: Shedding frequency for each nozzle.



Figure 3.26: Center body installed in facility.

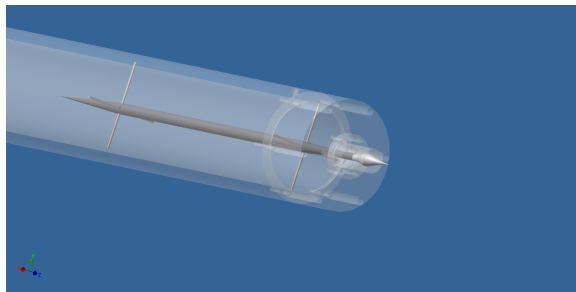


Figure 3.27: View of plug nozzle and supporting hardware.

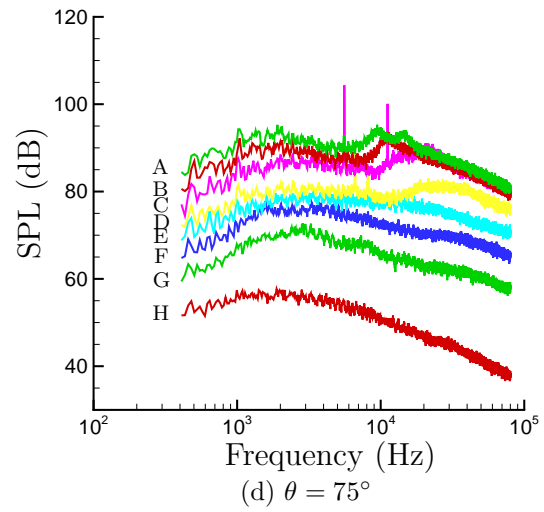
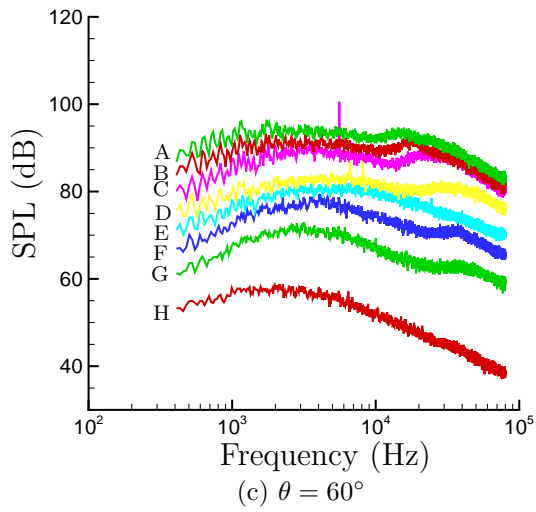
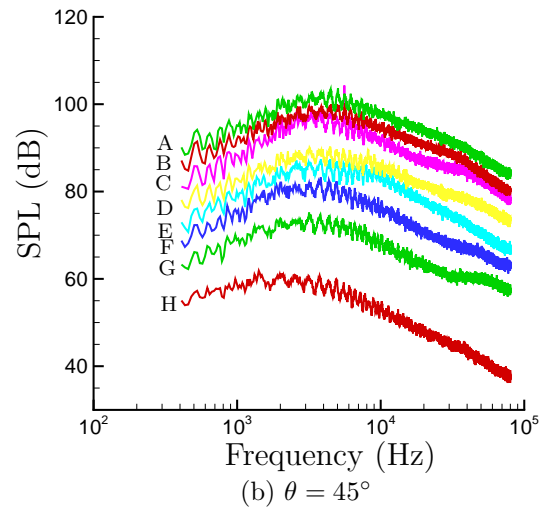
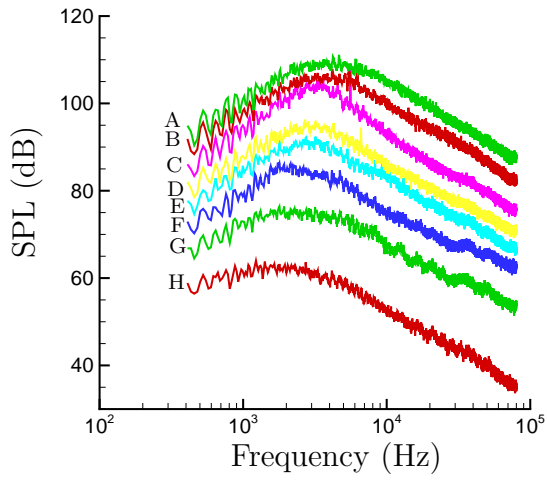


Figure 3.28: Figure continued on next page.

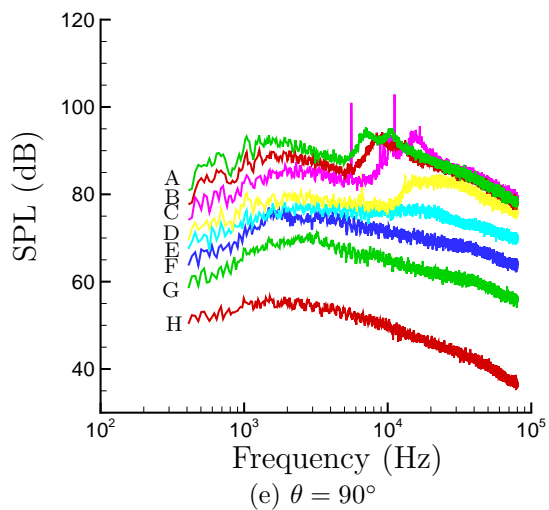


Figure 3.28: Noise from plug nozzle at various exhaust conditions normalized to $72 D_h$: Nozzle pressure ratio = (A) 6.20; (B) 4.94; (C) 3.67; (D) 2.77; (E) 2.14; (F) 1.69; (G) 1.39; (H) 1.19.

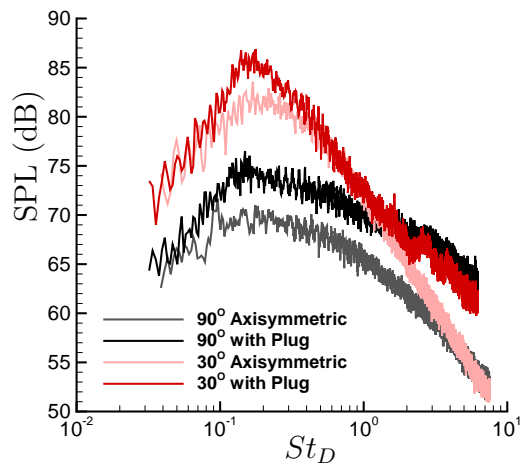


Figure 3.29: Center body nozzle far-field sound at Mach 0.9 compared with an axisymmetric baseline.

Chapter 4

Nozzle Boundary Layer Influence on Far-Field Sound

4.1 Motivation

As discussed in the introduction, the acoustic radiation of jets has been shown to be sensitive to nozzle configuration with no *a priori* prediction capability available for connecting specific configuration changes to specific changes in the far-field sound. A particular reason for this is the sensitivity to the near-nozzle conditions, as illustrated by the nozzles in chapter 3, and as reviewed in chapter 1. Even small nozzle modifications were shown to have a quantifiable effect on the far-field noise. This nozzle-lip/boundary-layer relation is expected to be a key factor in making accurate predictions.

It is also a factor that must be considered when comparing these scale-model tests to both full-scale jet exhaust as well as computational predictions. A full-scale exhaust will have a relatively thinner exhaust boundary layer, altering the range of scales which contribute to the noise when compared with lab-scale models. Large-eddy simulation can be run, however the locally largest scales near the nozzle are small, challenging resolution. Near-nozzle sound-source models, or at the very least more accurate inflow conditions, can improve these computations predictions.

4.2 Nozzles

The nozzles in figure 4.1 were specifically designed to tailor the boundary-layer thickness at the nozzle lip. All three nozzles use the same 5th-order polynomial contraction from the

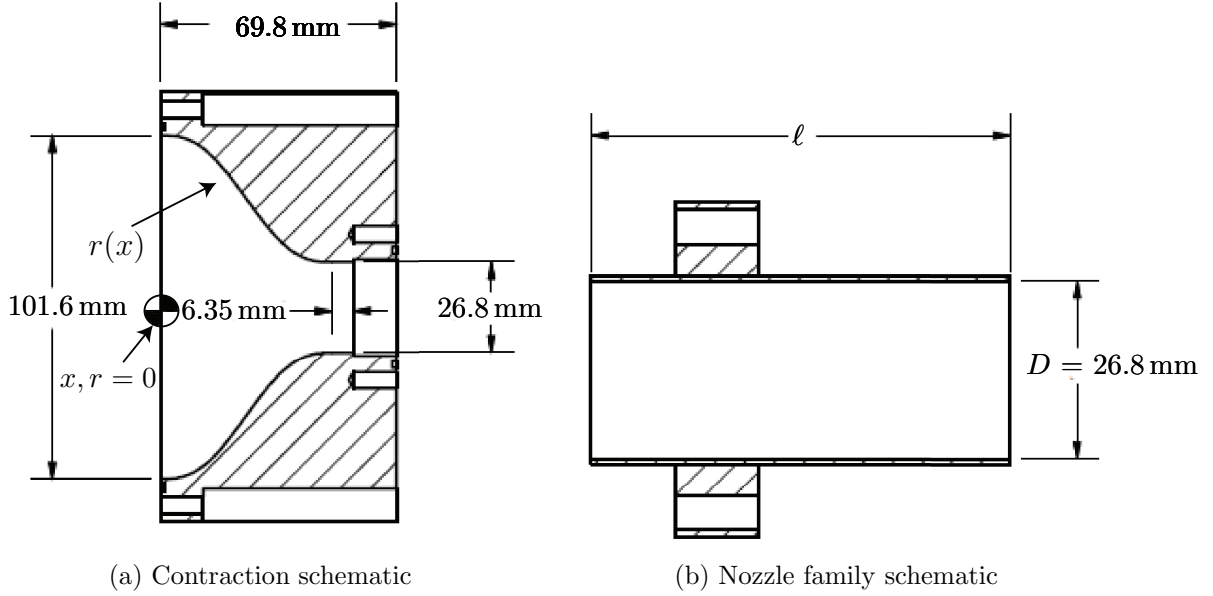


Figure 4.1: (a) Contraction shape: $r(x) = \frac{D}{2} + \left(\frac{D_u}{2} - \frac{D}{2}\right) \left[10 \left(\frac{L-x}{L}\right)^3 - 15 \left(\frac{L-x}{L}\right)^4 + 6 \left(\frac{L-x}{L}\right)^5\right]$, where $D_u = 101.6$ mm is the inlet diameter and $L = 50.8$ mm is the length of the contraction. (b) The $D = 26.8$ mm family of straight-walled nozzles, with the short $\ell = 63.5$ mm nozzle shown. The medium $\ell = 292.1$ mm and long $\ell = 508$ mm nozzles are not shown.

10.2 cm diameter piping down to a straight length of copper tube with inner diameter $D = 26.8$ mm and wall thickness of 0.9 mm. The contraction is designed to have a zero slope and zero curvature at both the beginning and end (Reshotko *et al.*, 1997). The straight-walled nozzles thus differed only in their length, which ranged from 63.5 mm to 508 mm, as tabulated in table 4.1. By using the same contraction, it can be expected that the state of the boundary layer at the beginning of each straight section is the same, so the principal difference will be the length of the boundary layer development, which is quantified in section 4.3.1 with a factor of 3.5 increase in the momentum thickness at exit achieved.

For comparison, two other nozzles, shown in figure 4.2, were also tested. These were manufactured using SLS rapid prototyping. The first has a $D = 19.2$ mm exit and contracts linearly without a straight section. The second has a larger exit diameter of $D = 34.5$ mm, which approximately doubles the mass flow rate. As with the $D = 26.8$ mm straight-walled nozzles it has a 5th-order polynomial contraction followed by a straight section. This is done

Nozzle	Length l -(mm)	Exit Diameter D -(mm)	Contraction L -(mm)
Short	70	26.9	50.8
Medium	298	26.9	50.8
Long	514	26.8	50.8
Large D	63.5	34.5	57.2
Small D		19.2	

Table 4.1: Parameters for nozzles used in exit boundary-layer influence investigation. Refer to figures 4.1 and 4.2 for the contraction schematic.

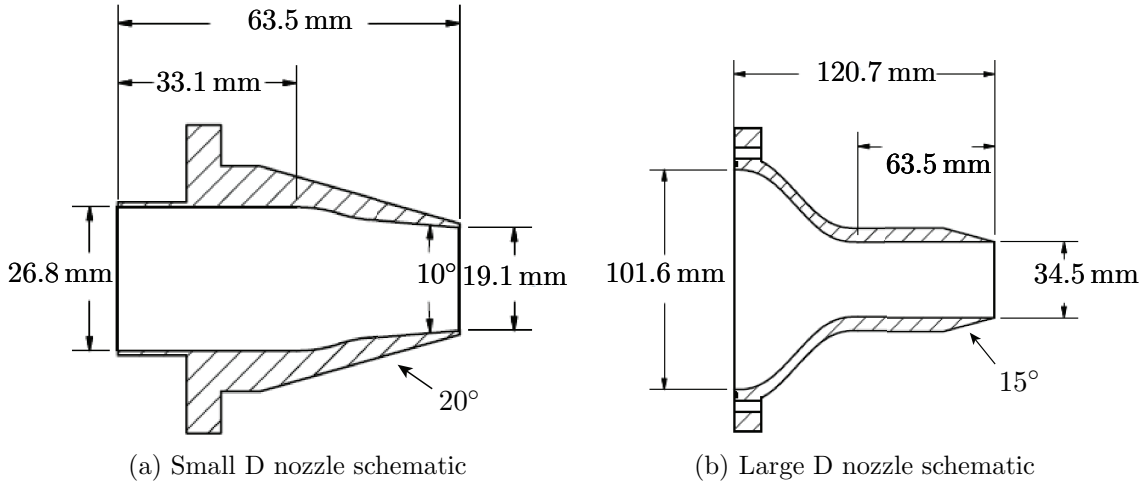


Figure 4.2: (a) Small and (b) large diameter alternate configuration nozzles. Nozzle (a) is inserted into the contraction in figure 4.1a and nozzle (b) has a contraction that follows a similar polynomial reduction.

to confirm relative insensitivity of our results to how the turbulent boundary layer forms in our three primary nozzles, which is considered in detail in section 4.3.

4.3 Results

4.3.1 Nozzle-Exit Boundary-Layer Properties

PIV images were taken within 1-2 mm of the jet exit, which therefore provides very near exit flow-field data. Downstream they extend approximately $3.5 D$ (~ 90 mm). We are

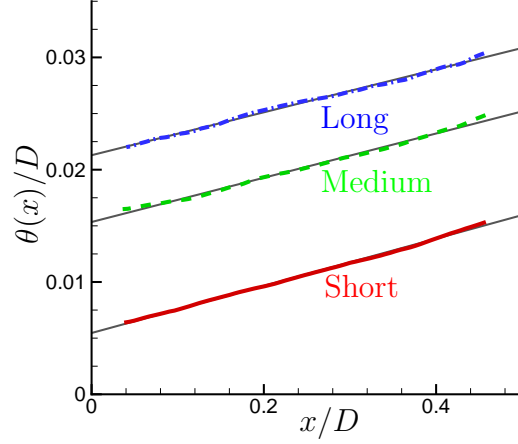


Figure 4.3: Measured momentum thickness for the — short, - - medium, and - · - long nozzles and the linear fits used to extrapolate to nominal nozzle values.

particularly interested in the very-near nozzle shear-layer thickness and its growth. This is quantified with momentum thickness:

$$\theta(x) = \int_{r_{05}}^{r_{95}} \frac{U(x, r)}{U_j} \left(1 - \frac{U(x, r)}{U_j} \right) dr, \quad (4.1)$$

where U is the time averaged streamwise velocity, and $U_j = U(r = 0)$ is its mean on the jet centerline. The integration bounds correspond to the 5 percent points ($0.05U_j$ and $0.95U_j$) in the mean velocity profile. Choosing alternate integration bounds corresponding to $0.02U_j$ and $0.98U_j$ produced indistinguishable results. The downstream spreading of θ is linear, as shown in figure 4.3. A key length scale is its thickness right at the nozzle, which we estimate by linear extrapolation to $x = 0$. These values are tabulated in table 4.2.

Profiles of the streamwise mean flow and turbulence intensity at $x = 0.04D$ are shown in figure 4.4. The shear layer is thicker as expected for the longer nozzles. However it is also clear that the initial shear layer shape reflects their origin as boundary layers within the nozzle, and they do not readily rescale with θ_0 or any single length scale. This gives them a distinct character from what would be expected for a fully developed free shear flow. The streamwise turbulence intensity in figure 4.4b is likewise complex. It seems to show

Nozzle	Initial Thickness $\times 10^3$			$H = \delta_o^*/\theta_o$
	θ_o/D	δ_o^*/D	$S.L._o/D$	
Short	5.46	11.87	40.58	2.18
Medium	15.34	23.45	126.82	1.53
Long	21.29	31.40	169.84	1.47
Large D	8.16	17.59	57.29	2.28
Small D	4.21	12.56	26.84	2.98

Table 4.2: Exhaust values for nozzles used in exit boundary-layer influence investigation. Refer to figure 4.1 for the corresponding schematic.

two distinct regions, one presumably associated with the memory of the boundary layer profile and the other associated with the inflectional instability of the free shear profile. The apparent boundary layer remnant has a relatively shallow rise and reaches a streamwise turbulence intensity of about $0.08 U_j$. This region is markedly sensitive to the boundary layer thickness and is much more pronounced at the same downstream location for the longer nozzles. The second region has a sharply peaked turbulence intensity. Despite the factor of 3.9 variation in momentum thickness, this sharply peaked region is approximately the same for all nozzles. The peak intensity ranges only from $u_{\text{rms}} = 0.12 U_j$ for the long-nozzle case up to $0.14 U_j$ for the short-nozzle case. This two-region structure is similar to measurements reported by Morris & Foss (2003) for an effectively incompressible plane boundary layer leaving a sharp corner and forming a free single-stream planar shear layer with $Re_\theta = 4560$.

4.3.2 Velocity and Turbulence Profiles

Full near-nozzle velocity and streamwise velocity fluctuations are included for all five nozzle in figures 4.5 to 4.14. Similar near nozzle spreading and development can be qualitatively observed along with a visual representation of the relative initial boundary layer thicknesses.

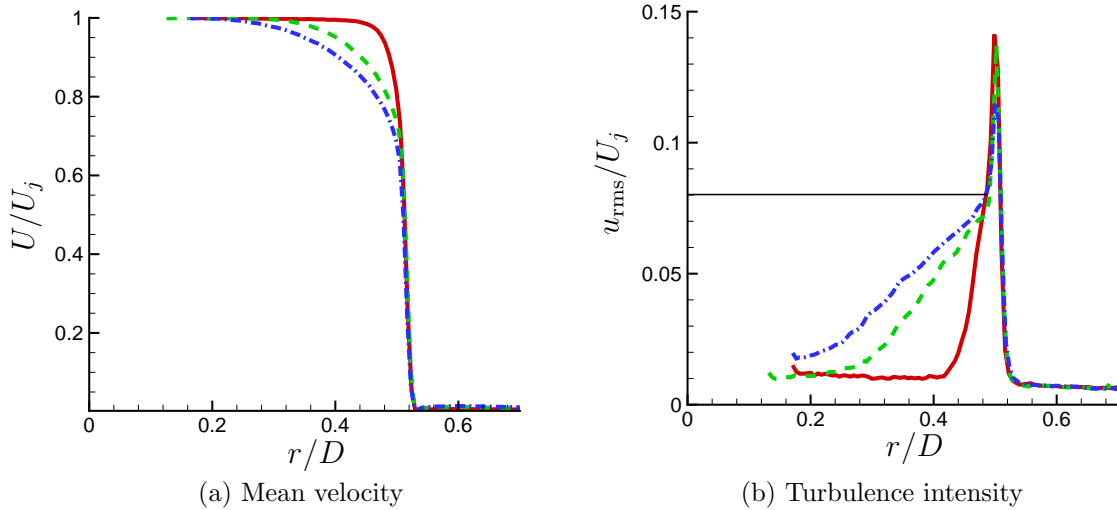


Figure 4.4: Streamwise velocity statistics at $x = 0.04D$: — short; - - - medium; and - · - long nozzles. The horizontal line at $u_{\text{rms}}/U_j = 0.08$ is for reference.

4.3.3 Nozzle-lip Thickness

Seeing these results, sensitivity to the finite thickness of the nozzle lip is a natural concern, since this thickness will potentially affect entrainment, for example, of ambient fluid very close to the separation point. For the basic cases we discuss, the thickness of the nozzle lip at the exit is approximately $0.03D$, indicating the highly turbulent region could be due to the presence of the nozzle lip. (The precise thickness is difficult to ascertain as the inner portion is obscured by the exhausting boundary layer). To demonstrate insensitivity, various lip thicknesses have been tested. This result is in contrast to the dependence found by Zaman (2012), however the thick-lip nozzles in that study approached a jet exhausting from a wall limit, modifying the exhaust conditions far greater than for any of the nozzles used here.

Nozzle-lip thickness was varied by attaching a 12.7 mm long sharpened plastic extension ring to the long nozzle. Changing from the baseline thickness of $0.0332D$ to $0.0172D$ and $0.0093D$, the thinnest of which could not be measured precisely, had no obvious influence on the mean or turbulence statistics at $x = 0.04D$, as seen in figure 4.15.

Also seen in figure 4.15, there are two distinct regions in the shear layer emanating from a

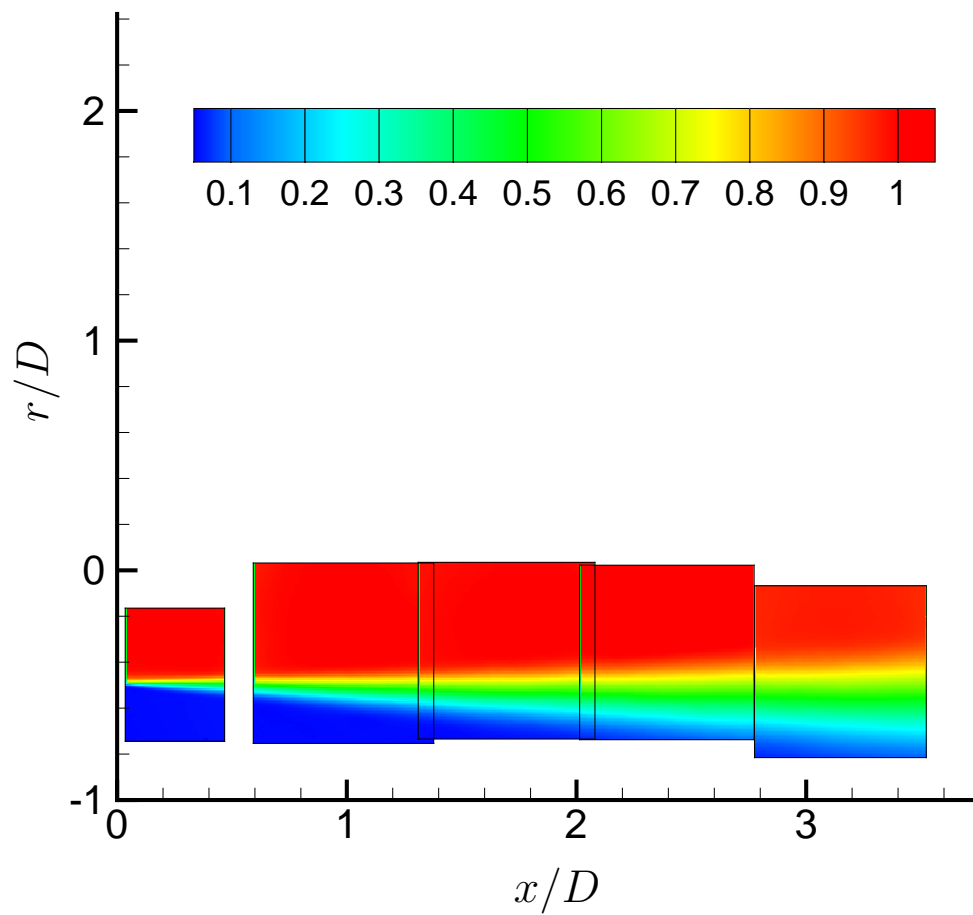


Figure 4.5: Near-nozzle streamwise velocity (U/U_j) for the short nozzle (see table 4.1).

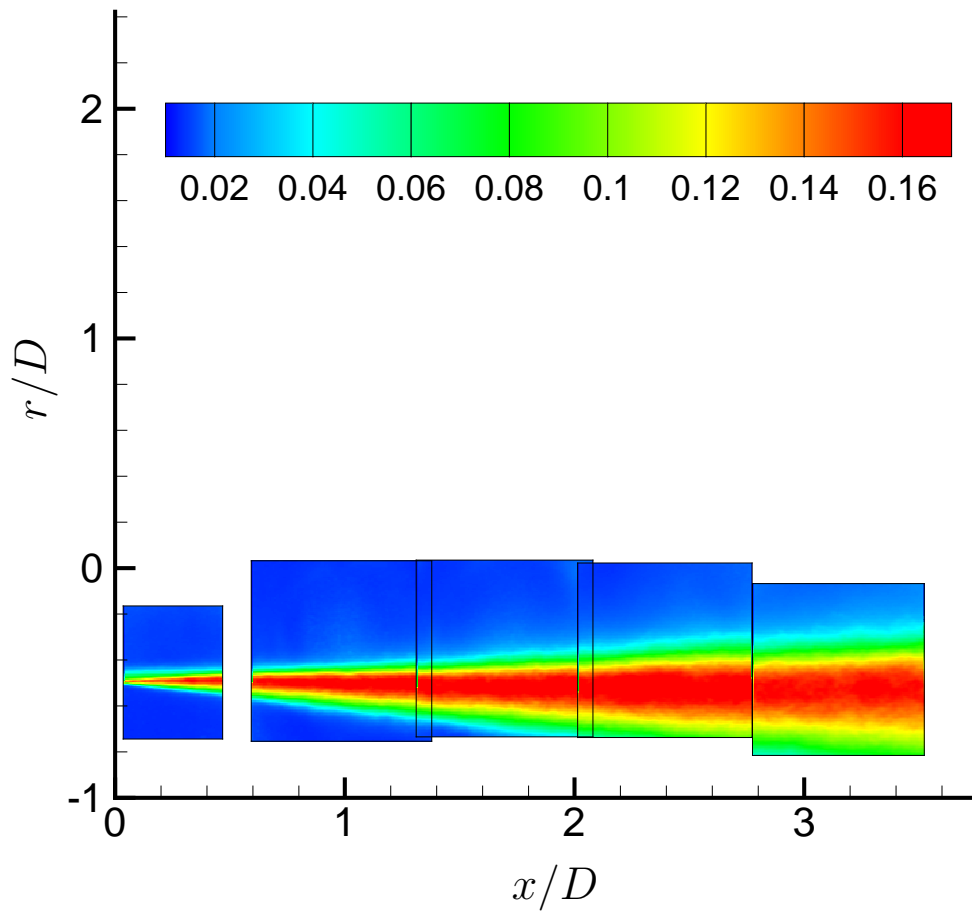


Figure 4.6: Near-nozzle streamwise velocity fluctuation (u_{rms}/U_j) for the short nozzle (see table 4.1).

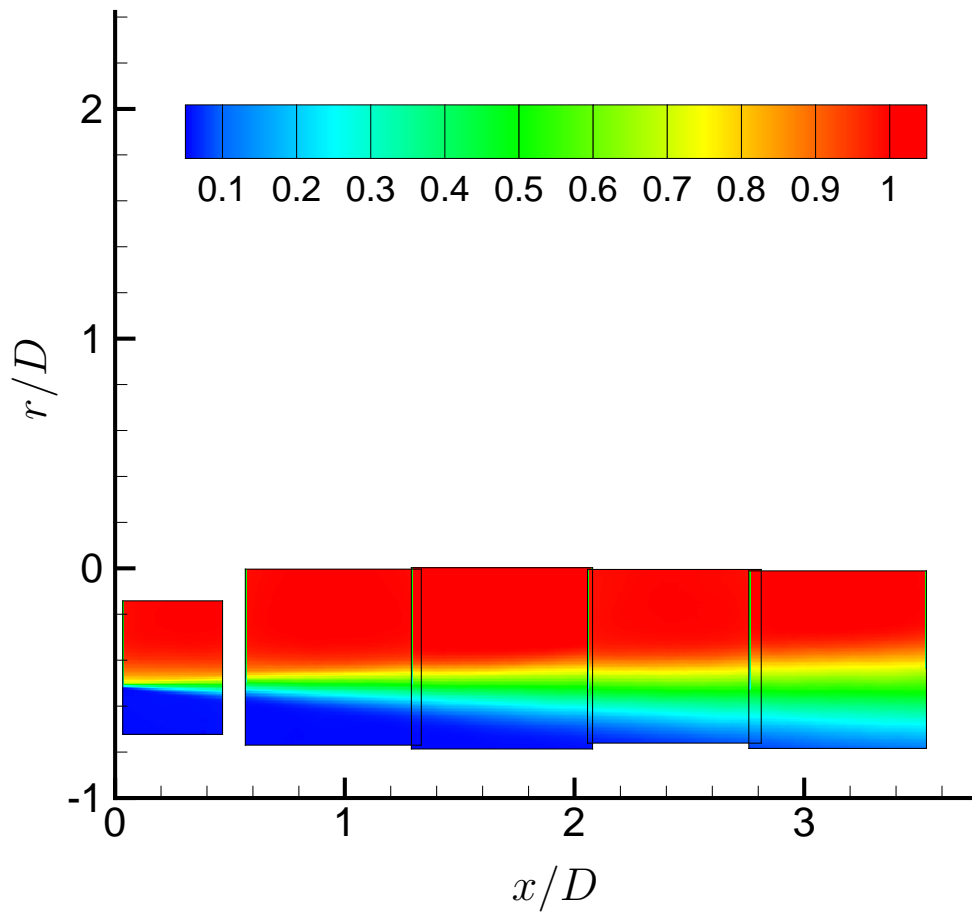


Figure 4.7: Near-nozzle streamwise velocity (U/U_j) for the medium nozzle (see table 4.1).

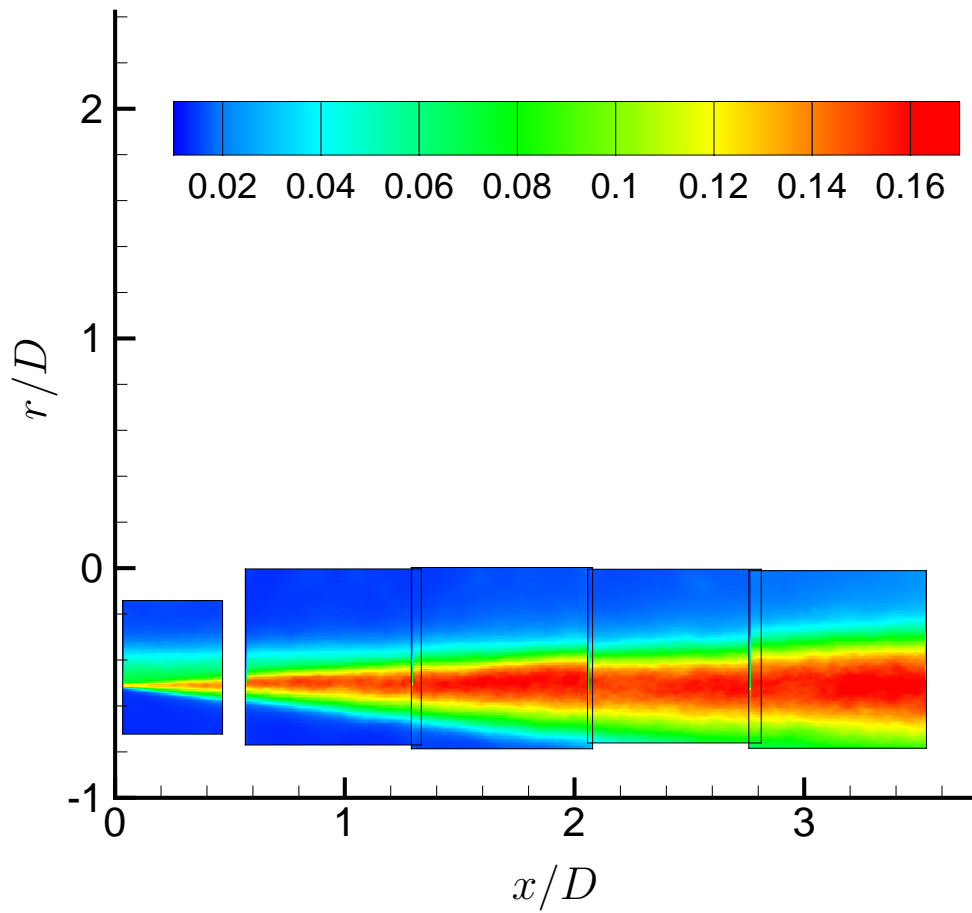


Figure 4.8: Near-nozzle streamwise velocity fluctuation (u_{rms}/U_j) for the medium nozzle (see table 4.1).

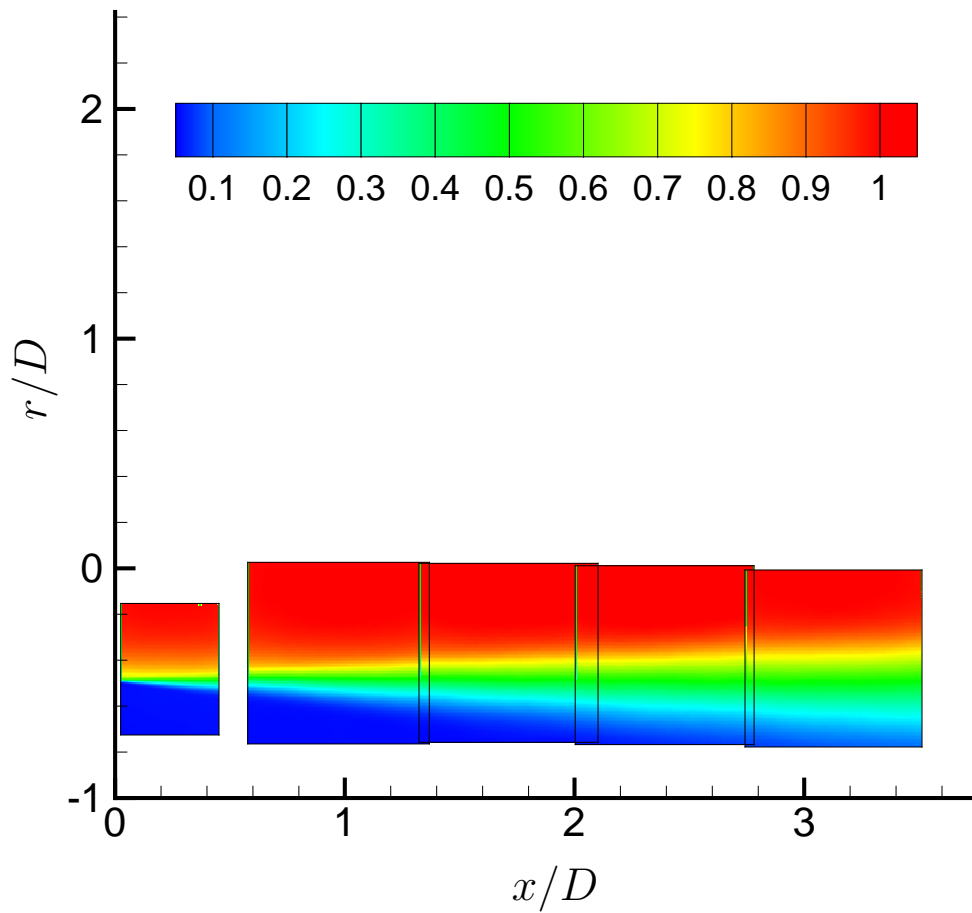


Figure 4.9: Near-nozzle streamwise velocity (U/U_j) for the long nozzle (see table 4.1).

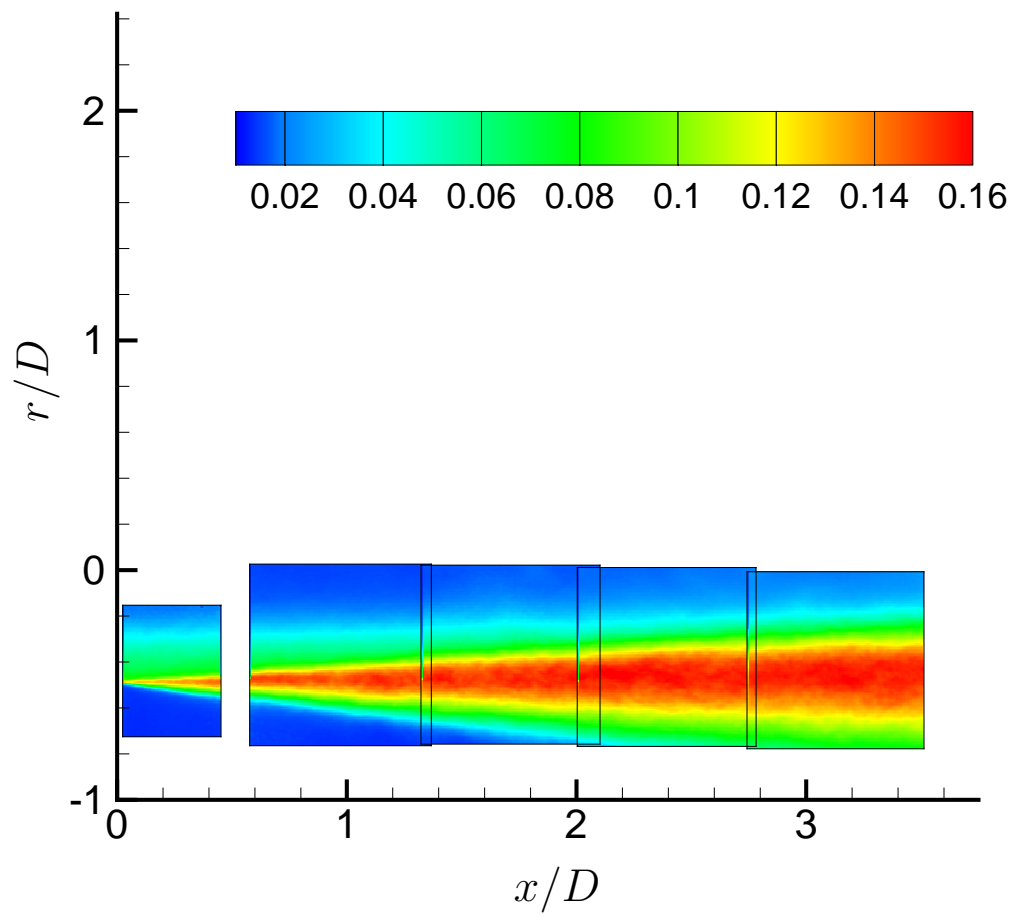


Figure 4.10: Near-nozzle streamwise velocity fluctuation (u_{rms}/U_j) for the long nozzle (see table 4.1).

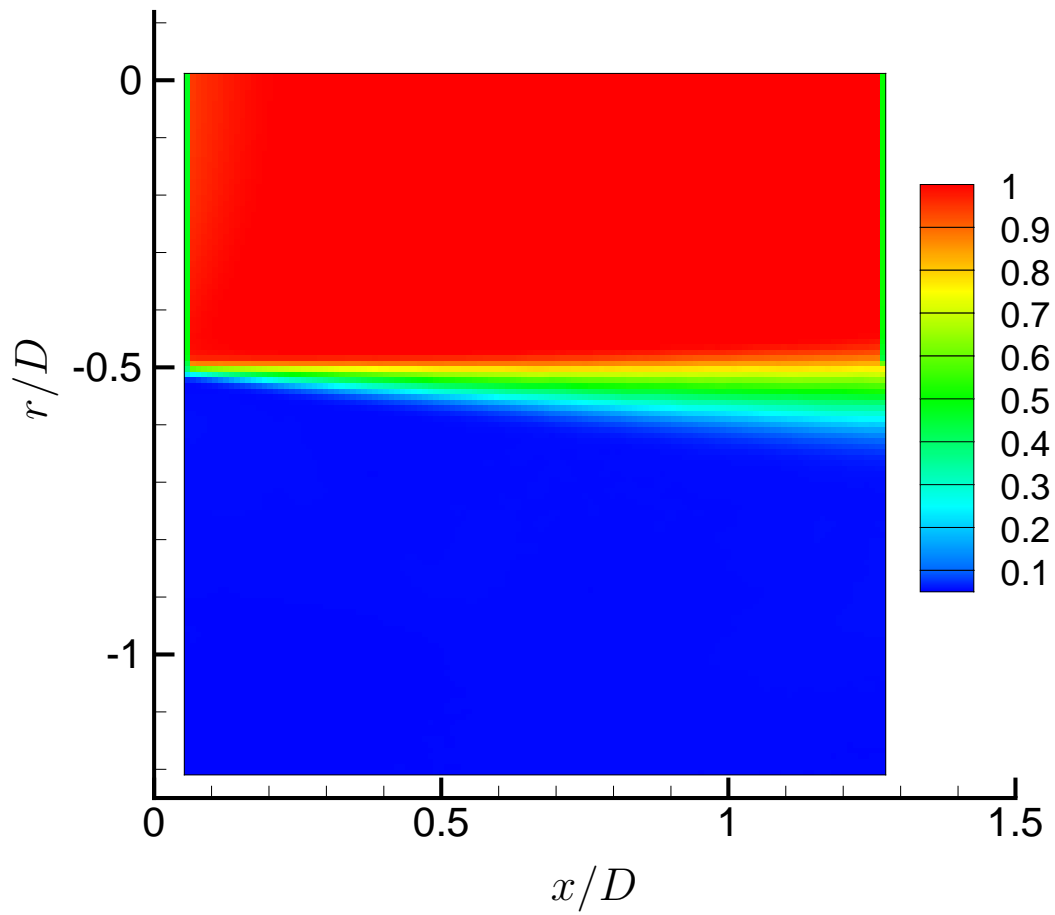


Figure 4.11: Near-nozzle streamwise velocity (U/U_j) for the small nozzle (see table 4.1).

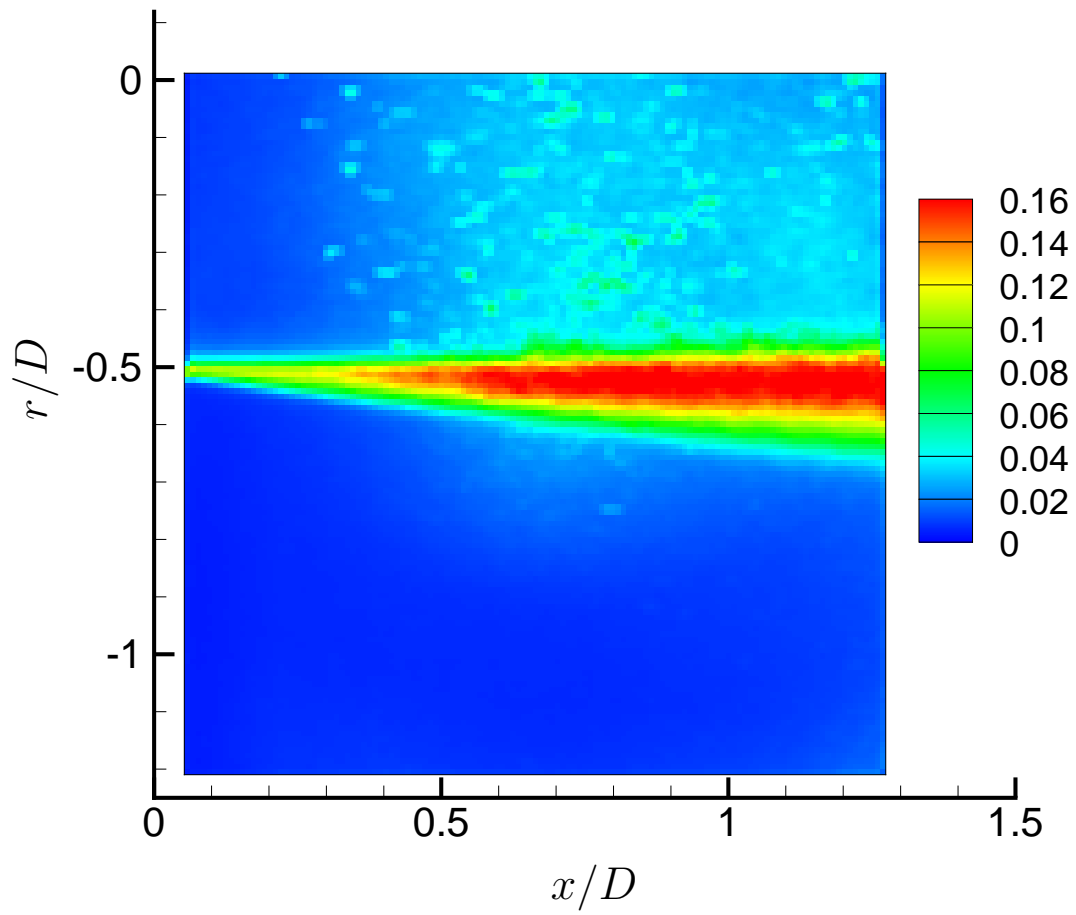


Figure 4.12: Near-nozzle streamwise velocity fluctuation (u_{rms}/U_j) for the small nozzle (see table 4.1).

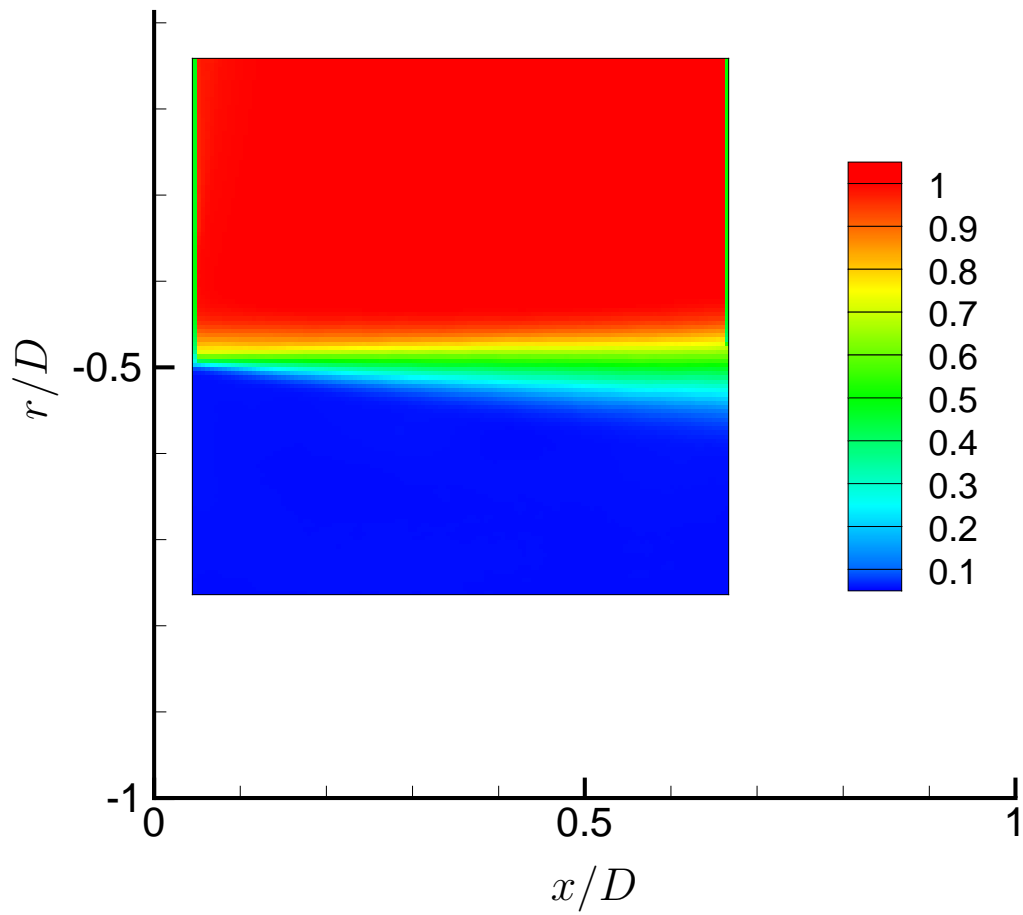


Figure 4.13: Near-nozzle streamwise velocity (U/U_j) for the large nozzle (table 4.1).

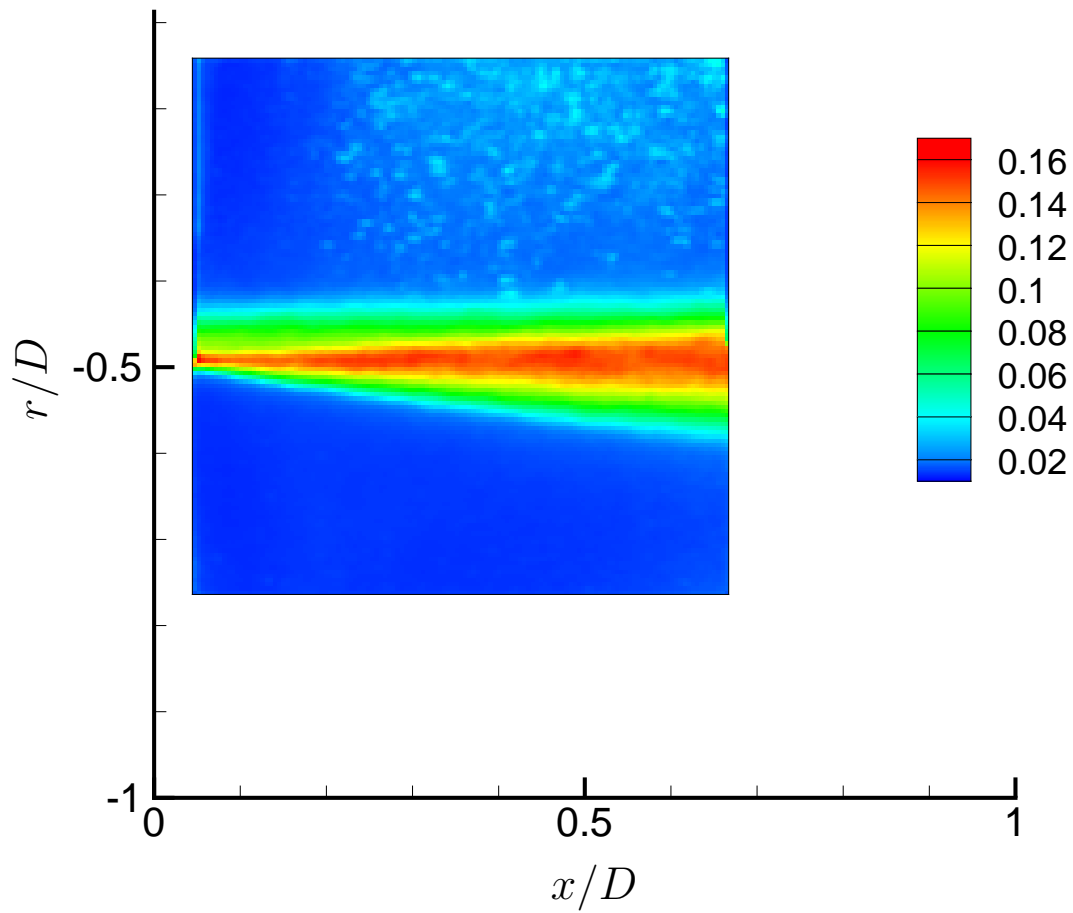


Figure 4.14: Near-nozzle streamwise velocity fluctuation (u_{rms}/U_j) for the large nozzle (see table 4.1).

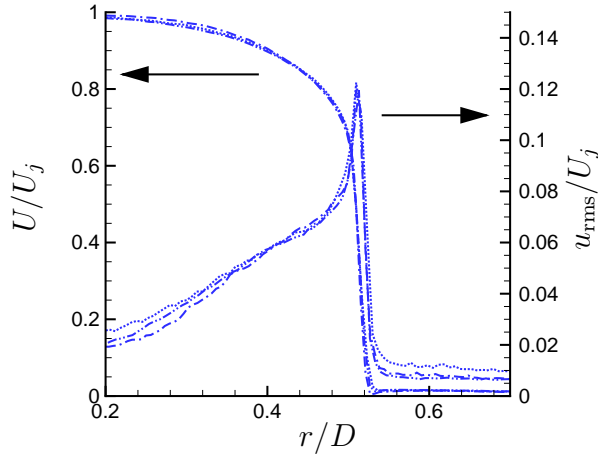


Figure 4.15: Mean flow and streamwise turbulence intensity for different nozzle-lip thicknesses: $d = 0.0332D$; $d = 0.0172D$; and $d \lesssim 0.0093D$.

Nozzle	$\frac{d}{D} \times 10^3$	$\theta_o/D \times 10^3$	FWHM/ $D \times 10^3$
Baseline	33.2	21.2	9.33
Thin	17.2	21.2	9.96
Thinnest	<9.3	20.7	9.11

Table 4.3: Nozzles with various exit-lip thickness, d . In all cases, the long nozzle was used. For the thin and thinnest cases, a 12.7 mm long plastic addition was used to reduce the lip thickness.

jet and both are unchanged based on lip thickness. For the cases plotted, the low-speed side of the shear layer up to the maximum value is extracted and mirrored around the peak. The FWHM is then computed and extrapolated to an exit value to compare the three nozzle exit conditions. This is done with the assumption that there are two distinct regions, and the region caused by the shear of the jet and ambient air is symmetric. Even if these assumptions are not perfectly valid, it still gives an approximation to compare the nozzles. From this we see the value of the FWHM is very close to the same value in all cases with no dependence on nozzle lip thickness. This is quantified in table 4.3.

4.3.4 Far-field Sound

All five nozzles listed in table 4.2 were run at Mach 0.9 and sound field measurements taken. The different near-nozzle behaviors lead to the clear differences in the far-field sound spectra, as seen in figure 4.17. At high frequencies, the long nozzle, with its 3.9 times thicker initial shear layer, generated 3 dB less intensity to downstream angles ($\theta = 30^\circ$). The long nozzle has a thicker boundary layer, which will result in a smaller gradient between the high-speed core of the jet and the low-speed ambient air. To identify the specific characteristics leading to these different mechanisms in nozzles of the same exit diameter, scaling relationships were investigated for these nozzles.

Because the boundary layer is thicker, the longer nozzle has a smaller net mass and momentum flux, more comparable to what might be expected for a thin boundary layer nozzle exiting from a slightly smaller diameter nozzle. We account for this by replacing the nozzle diameter scaling parameter with a hydraulic diameter, a process much the same as correcting for a common thrust. The thicker boundary layer results in a smaller effective diameter of the nozzle. The displacement thickness, δ^* , downstream of the nozzle exit was determined using PIV results. When this scaling is used, collapse of the low-frequency sound occurs. This is shown in figure 4.16 where third-octave data are used to more clearly visualize the low-frequency portion of the spectrum.

The nominally missing thin shear layer region for the thicker boundary layer jets (see figure 4.4) would presumably radiate high-frequency sound because of the smaller turbulent scales it would contain. We can then speculate that portions of the far-field high-frequency spectra might collapse with the initial shear layer thickness. This is supported by the success of $St_\theta = f\theta/U$ at collapsing the high-frequency part of the spectra in figure 4.17d, which also includes the alternate nozzles from figure 4.2.

However, this simple scaling with θ_o is not successful for $\theta = 90^\circ$, even when the spectra are extended following a similar functional form as Tam *et al.* (1996). Figures 4.17a and

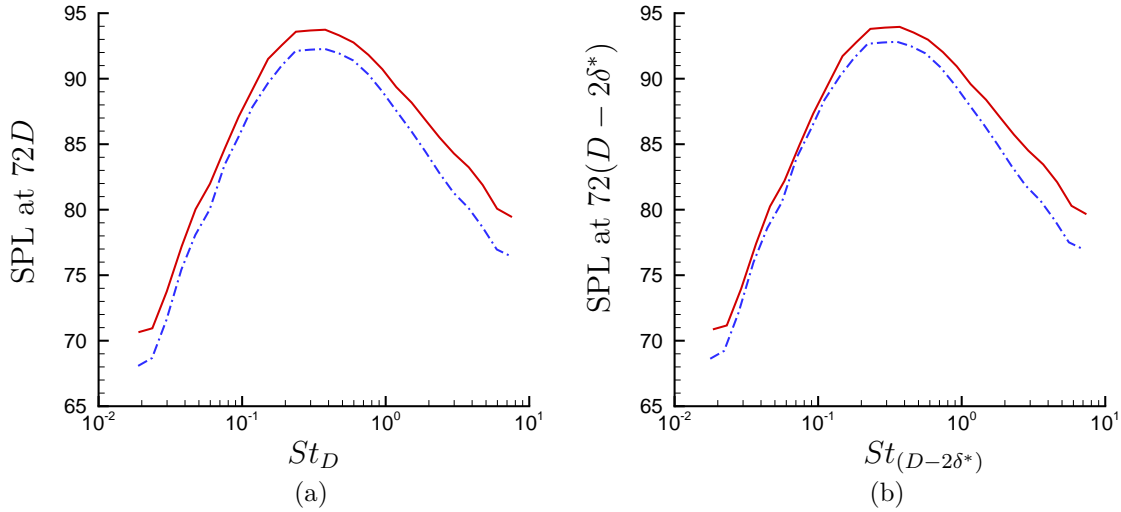


Figure 4.16: Low-frequency scaling improvement using displacement thickness. (a) Baseline third-octave spectra at 30° scaled with nozzle diameter, D . (b) The same data as (a) but now scaled using an equivalent diameter of $D - 2\delta^*$, where δ^* is the experimentally measured displacement thickness. Lines indicate the — short and - - - long nozzles.

4.17b show sideline spectra. These clearly do not collapse so well, which is consistent with the tacit expectation that at 90° the measured sound is made up of contributions from the relatively random turbulence throughout the jet. These ideas are consistent with the role of mean shear in early aeroacoustic theories (Ribner, 1969), wave-like eddy models of noise (Mankbadi & Liu, 1984), and motivate some empirical noise source modeling (Tam & Auriault, 1999). Because this nominally missing portion of shear-layer growth represents a small fraction of the total volume of turbulent flow, we do not expect changes to be so apparent in the sideline sound spectra. The spectra acquired were extended in figure 4.18. The acoustic radiation from the other two nozzles considered, which were not in the same long-medium-short family, similarly collapse when scaled accordingly (figure 4.17d). For this configuration, we subtracted the usual $20 \log(D/D_o)$ to account for the nozzle size, with $D_o = 26.8$ mm, the size of the nozzles in the baseline study.

Measurements at the mid-angles of $\theta = 75^\circ$, 60° , and 45° are shown in figures 4.19, 4.20, and 4.21, respectively. As expected from the above analysis, the measurements further in

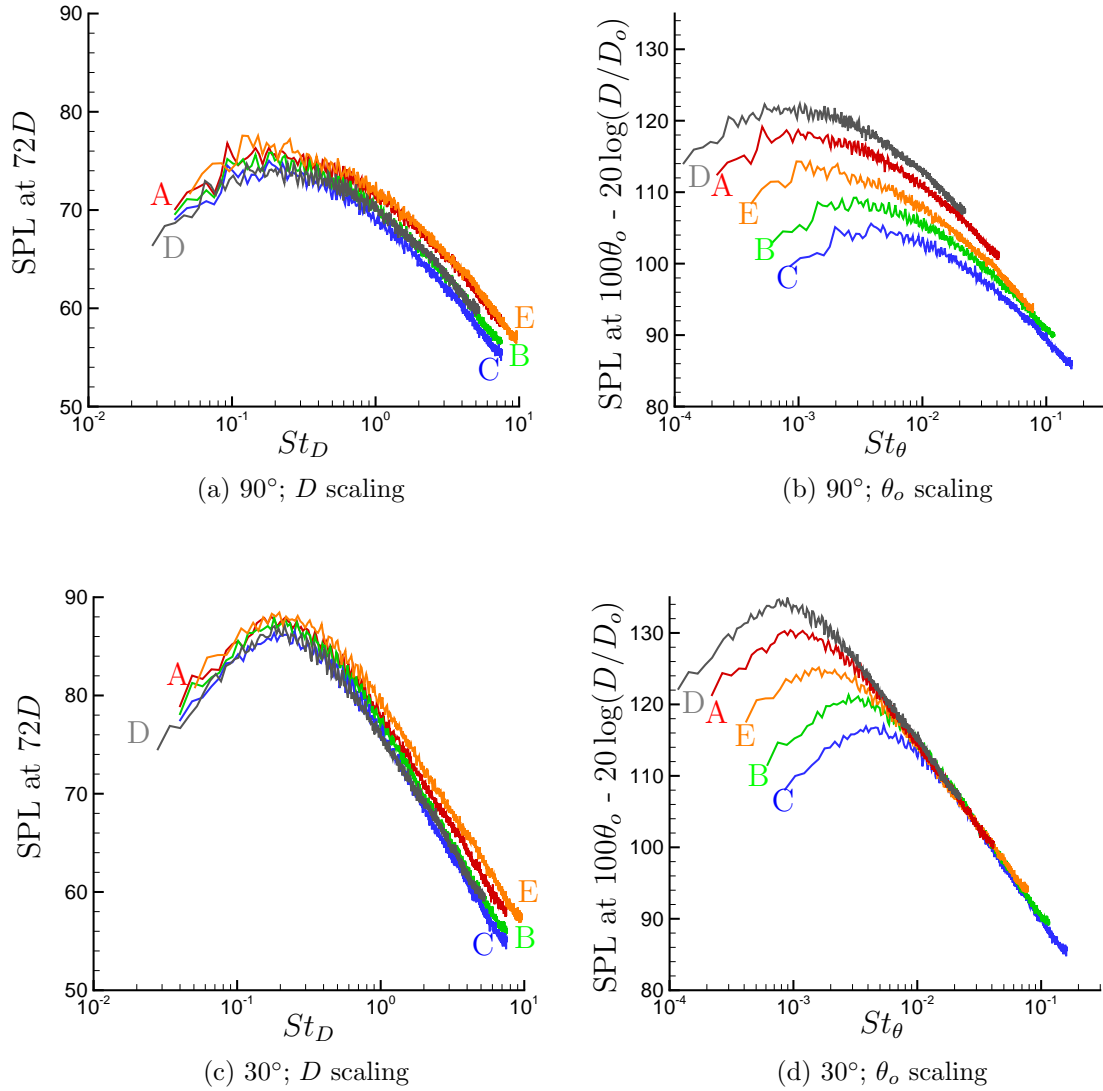


Figure 4.17: Sideline ($\theta = 90^\circ$) and downstream ($\theta = 30^\circ$) noise measurements for the (A) short, (B) medium, (C) long, (D) small D and (E) large D nozzles.

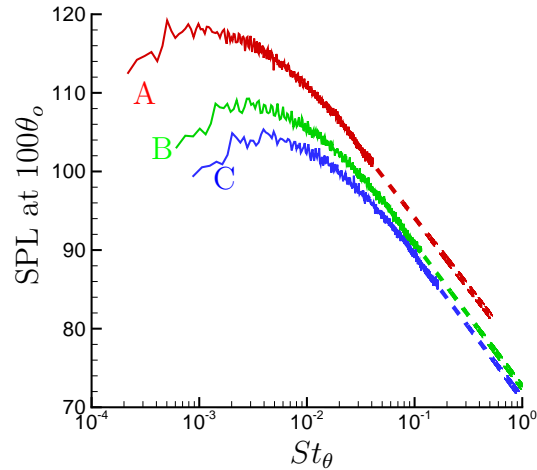


Figure 4.18: Sideline momentum thickness scaling using a least squares fit of the form $SPL = a + b \log f$ for the last half-decade of the experimental spectrum and extending to higher frequency.

the downstream direction appear to better collapse at high-frequency than those at sideline angles.

This scaling relationship at Mach 0.9 has also been investigated for lower speed jets and is shown in figure 4.22. For these, the PIV used only 315 image pairs for each run condition for both the short and long nozzles, which was sufficient to converge the mean flow. A similar collapse was seen at Mach 0.7, however this became less apparent at lower Mach numbers, possibly related to facility limitations which are discussed in chapter 2.

4.3.5 The Turbulent State of the Initial Boundary Layer

As discussed in chapter 1, the initial boundary layer can play an important role in the noise generated by a jet, especially if it is laminar, which is generally thought to facilitate vortex pairing Zaman (1985*a*) that leads to higher sound levels. Unfortunately, it is difficult to differentiate initial turbulence state from nozzle profiles and shape factors alone (table 4.2) so we look to a number of other metrics. Brown & Bridges (2006) identified a particular hump-shaped feature in the far-field spectra from nozzles thought to have a laminar exit flow

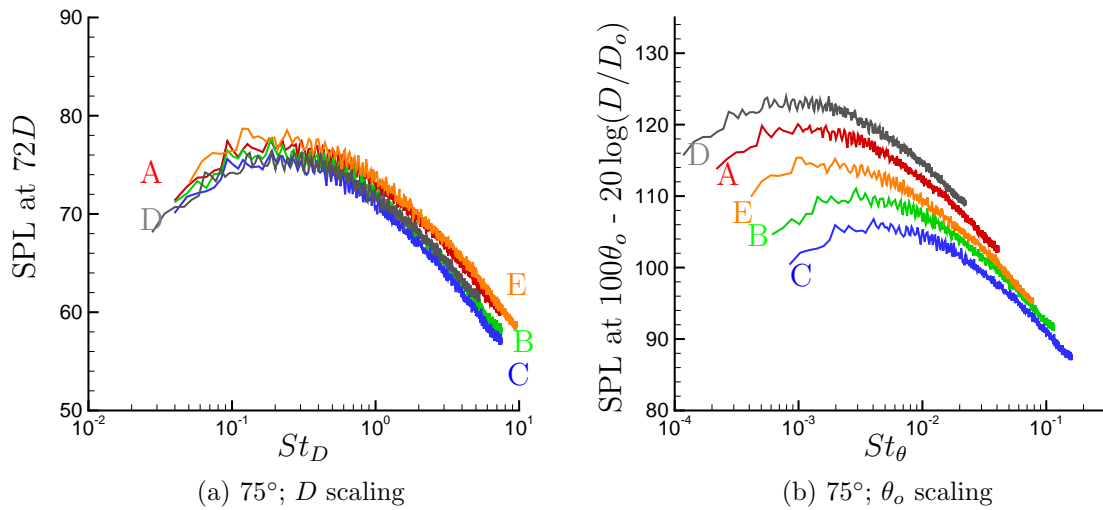


Figure 4.19: $\theta = 75^\circ$ noise measurements for the (A) short, (B) medium, (C) long, (D) small D and (E) large D nozzles.

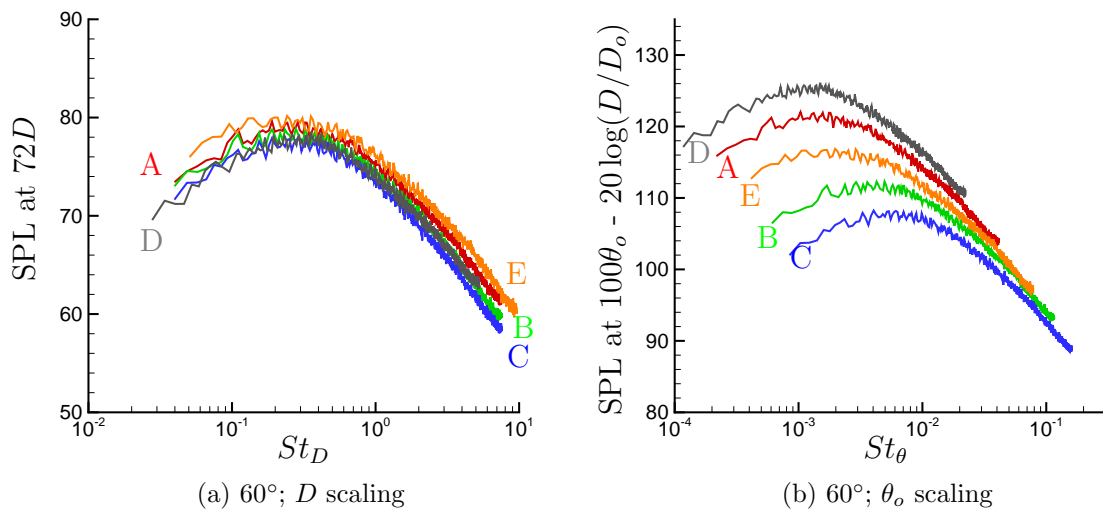


Figure 4.20: $\theta = 60^\circ$ noise measurements for the (A) short, (B) medium, (C) long, (D) small D and (E) large D nozzles.

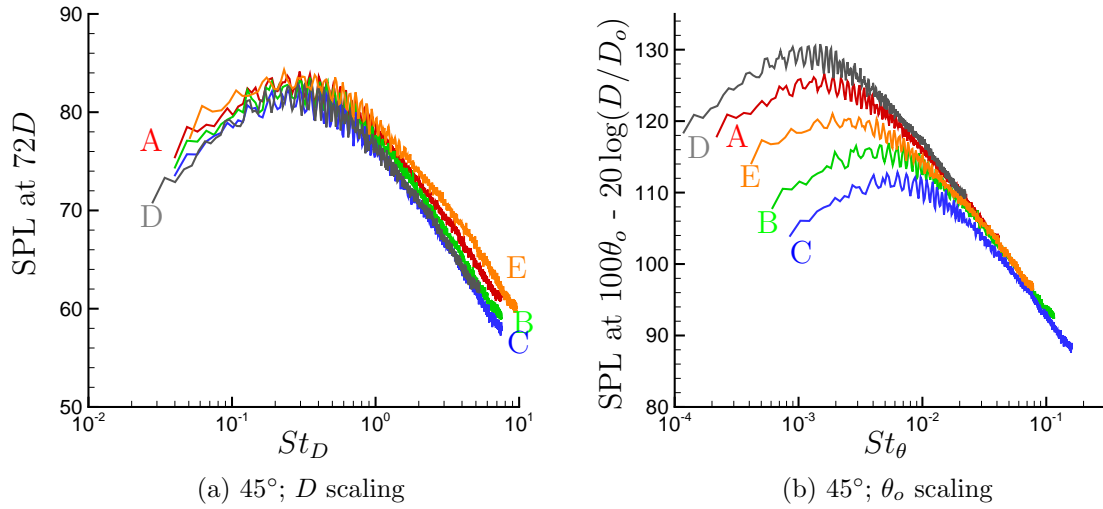


Figure 4.21: $\theta = 45^\circ$ noise measurements for the (A) short, (B) medium, (C) long, (D) small D and (E) large D nozzles.

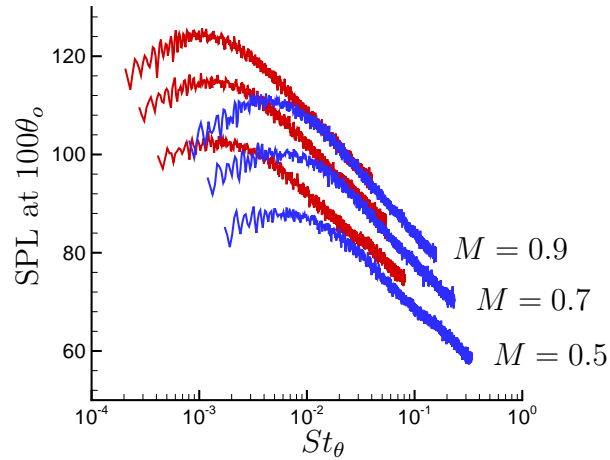


Figure 4.22: Momentum thickness scaling for various Mach numbers.

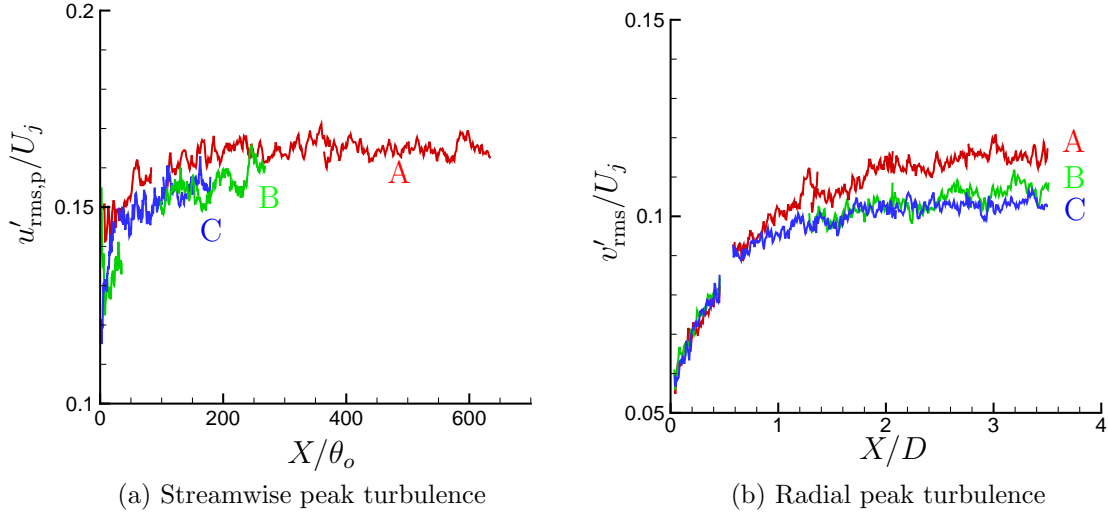


Figure 4.23: Downstream evolution of the peak (a) streamwise and (b) radial turbulence intensity for the (A) short, (B) medium, and (C) long nozzles.

conditions. The spectra we measure, as we shall see in figure 4.17, shows no corresponding feature, supporting a turbulent condition at the nozzle in the present study. Here we also consider several more direct measures that indicate a turbulent nozzle boundary layer, which is an important aspect of this study.

In addition to the linear growth (figure 4.3), the peak streamwise turbulence intensity is nearly uniform (figure 4.23a). It is not exactly uniform downstream, since flow is not expected to be fully developed and in a self-similar state this close to the nozzle, but obvious features consistent with laminar flow (Husain & Hussain, 1979) are not seen. The peak turbulence intensity is consistent with expected turbulence intensities at all points we measure in x ; the peak radial turbulence intensity (figure 4.23b) as expected develops more slowly than the streamwise fluctuation, but is likewise consistent with free-shear-flow turbulence.

If the shear layers are turbulent, they should also be insensitive to the Reynolds number, which is quantified in figure 4.24 and table 4.4. It would have been challenging with our facility to vary Re_D without also changing the Mach number, which varied from 0.2 to 0.9 in acquiring the figure 4.24, but despite the potential for weak Mach-number dependence

Ma	$\theta/D \times 10^3$	
	Short	Long
0.2	5.08	31.33
0.3	6.65	27.83
0.4	6.48	27.15
0.5	6.19	26.32
0.6	6.15	26.02
0.7	5.73	24.88
0.8	5.44	22.52
0.9	5.29	20.78

Table 4.4: The 5-95% momentum thickness calculated for both the short and long nozzle with run conditions ranging from Mach 0.2-0.9.

we see the expected behavior for turbulence for Reynolds numbers ranging over a factor of 6. Though a perfect fit is not expected, it is clear in figure 4.24 that our measurements are far better fitted by the empirical $Re_D^{1/7}$ often seen for turbulence than the $Re_D^{1/2}$ expected for laminar flow (White, 2005). A similar metric was used to support a turbulent nozzle condition by Zaman (2012).

The rapid approach to apparent self-similar behavior we see in figures 4.23 and 4.25 similarly supports a turbulent nozzle flow condition. Shear layers that originate from a separating laminar boundary layer require $1000\theta_o$ to become self similar (Bradshaw, 1966) whereas those from turbulent boundary layers achieve approximate self-similarity in less than $150\theta_o$ (Hussain & Zaman, 1985), with Morris & Foss (2003) finding $x > 100\theta_o$ sufficient for a similarity scaling to collapse the mean streamwise velocity profiles. Figure 4.25 shows that the present turbulence intensity indeed collapses versus $r/\theta(x)$ for $x \gtrsim 100\theta_o$, with essentially the same behavior for both the long and short nozzles (figure 4.28).

4.3.6 Near-nozzle Shear-layer Development

The downstream development of the turbulence in figure 4.26 shows how boundary layer features disappear and it developed towards the expected free-shear-flow behavior.

When the radial coordinate is normalized by D we see the relative persistence of the

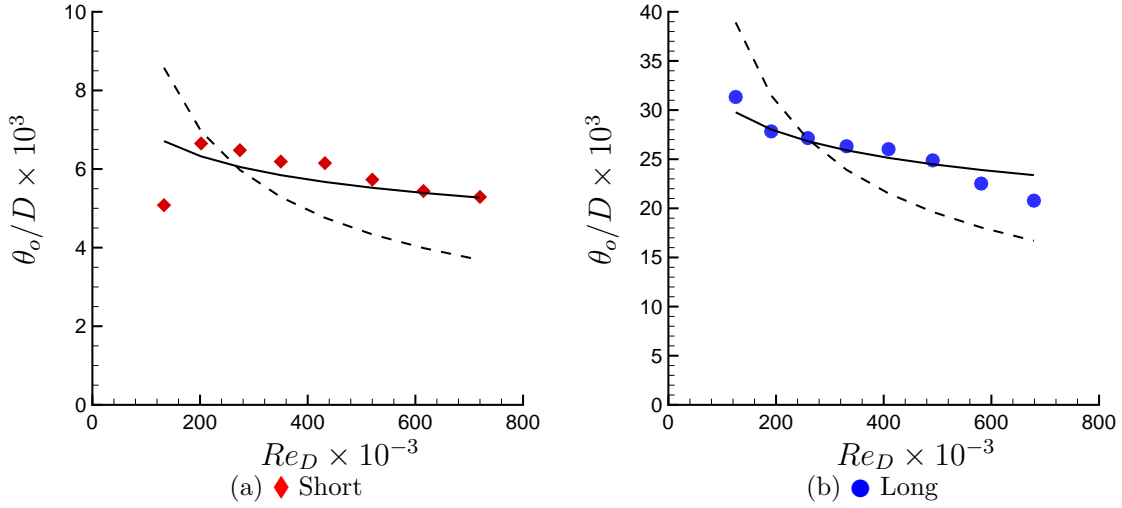


Figure 4.24: Nozzle momentum thickness sensitivity to Re_D with fits — $Re^{1/7}$ and --- $Re^{1/2}$.

turbulence intensity into the core flow, especially for the thick boundary layer of the long nozzle in figure 4.26c. This is presumably a remnant of the boundary layer turbulence from the nozzle. Just before the exit, this boundary layer would be slowly growing. Even if it were to continue at a typical rate for a turbulent boundary layer, it would only grow by a few percent over the downstream distance we consider in figure 4.26. The turbulence intensity is also relatively low in this region though the mean flow is fast, so the turbulence can be expected frozen, leading to its apparent unchanging downstream persistence. This boundary layer remnant appears to be enveloped by the spreading of the peak turbulence, which at about this same x -location shows a similarity collapse when normalized (figure 4.26). The short nozzle shows the same basic behavior, though the boundary layer footprint is, of course, much smaller relative to the diameter.

It is somewhat surprising that despite the obvious difference in the mean flow profile in this region, the peak turbulence seems to develop nearly the same. We investigate this in more detail in chapter 5, where linear instability analysis suggests that the instability modes are indeed insensitive to boundary layer remnant of the nozzle flow.

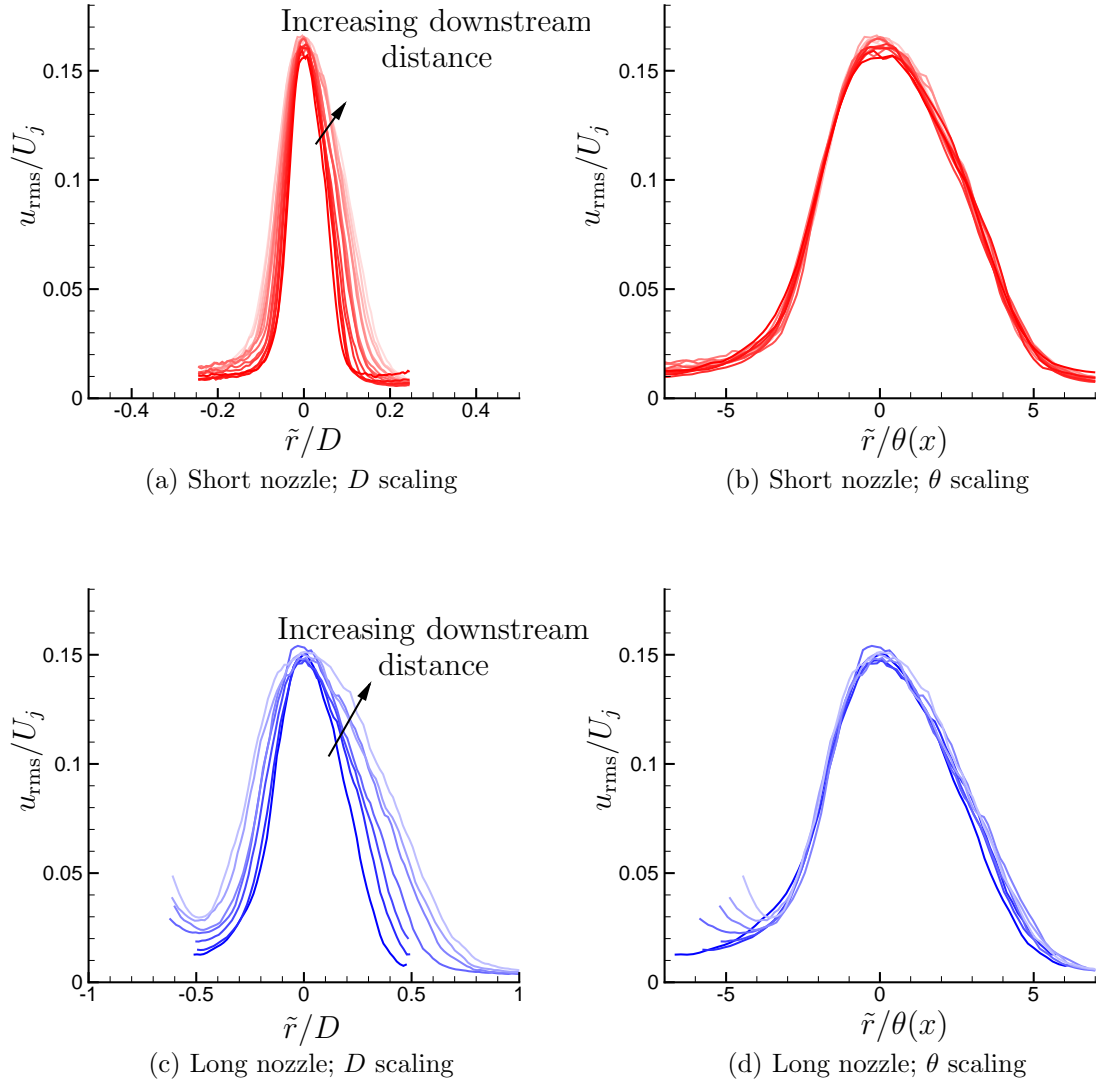


Figure 4.25: Streamwise fluctuations versus $\tilde{r} = r - D/2$ subject to different scaling factors as labeled. The plot lines are lighter in tone for larger x in the downstream direction. (a,b) The short-nozzle data equally spaced from $107\theta_o$ to $240\theta_o$. (c,d) The long-nozzle data equally spaced from $110\theta_o$ to $230\theta_o$.

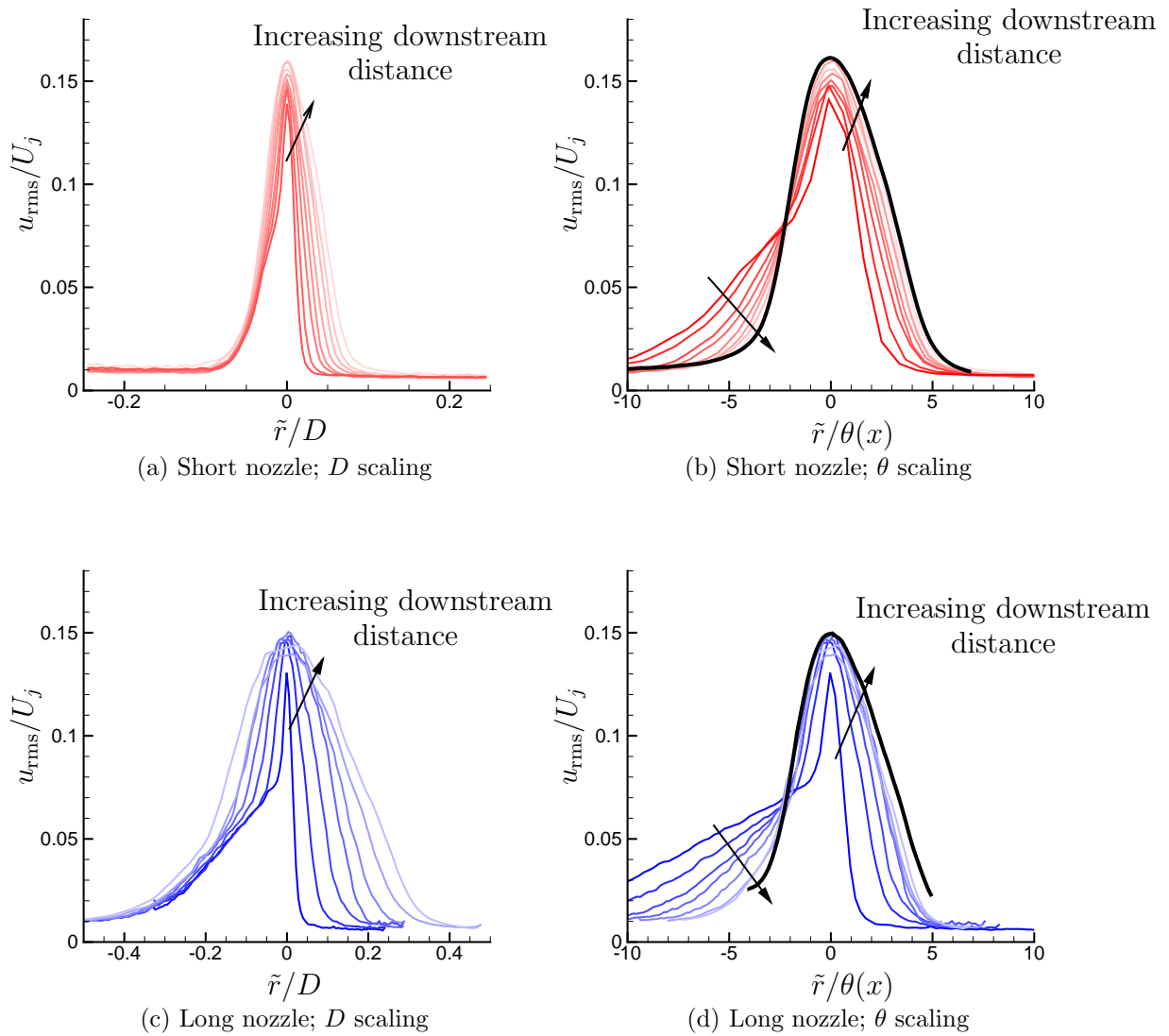


Figure 4.26: Near-nozzle streamwise turbulence intensity from $x = 0\theta_o$ to $100\theta_o$: (a,b) the short nozzle with equally spaced profiles from $x = 9\theta_o$ to $84\theta_o$; and (c,d) the long nozzle with equally spaced profiles from $x = 5\theta_o$ to $95\theta_o$.

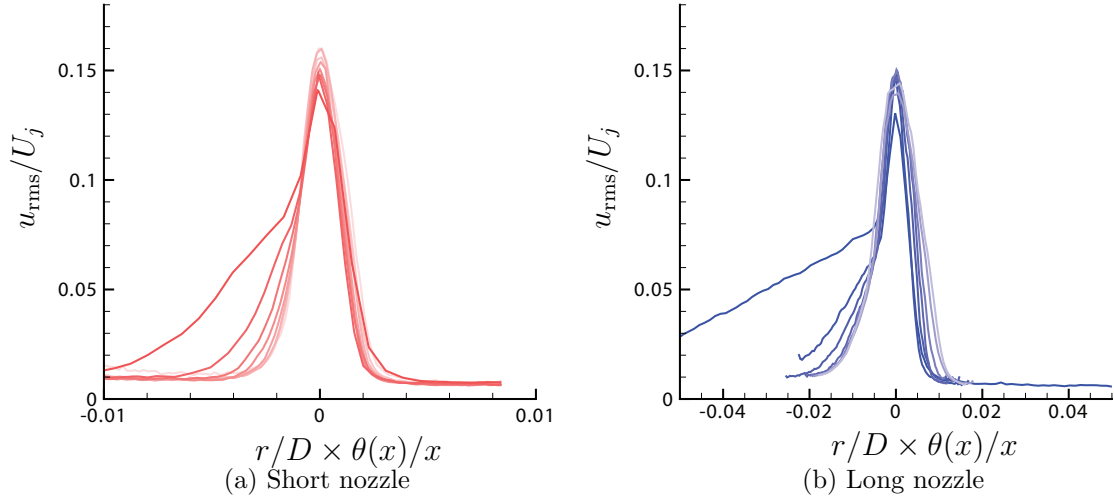


Figure 4.27: The near nozzle streamwise fluctuations normalized by both momentum thickness and downstream distance. Left: Short nozzle data equally spaced from $9\theta_o$ to $84\theta_o$ downstream. Right: Long nozzle data equally spaced from $5\theta_o$ to $95\theta_o$ downstream.

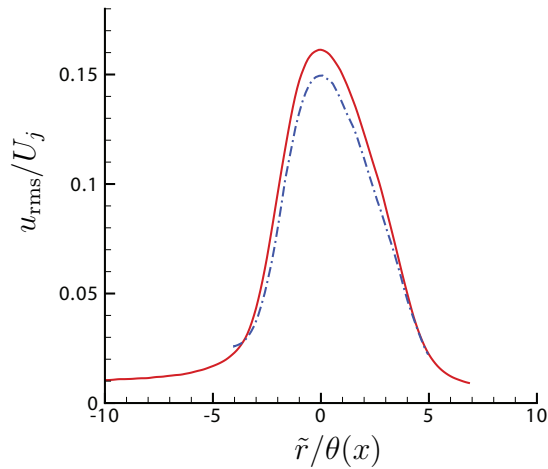


Figure 4.28: Mean downstream (approximately self-similar region) fluctuation profiles for both the — short and - - - long exhaust profiles.

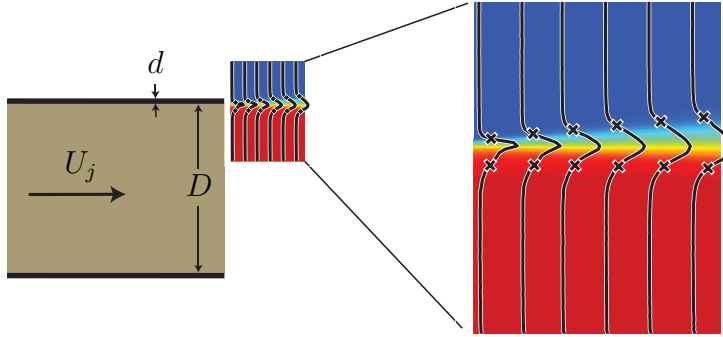


Figure 4.29: Near-nozzle fluctuations plotted with the background contour the jet velocity. Data shown is for the short nozzle. The streamwise fluctuation profiles are from $0.038 D$, $0.113 D$, $0.184 D$, $0.259 D$, $0.335 D$, and $0.411 D$ downstream of the nozzle exit. The \times symbol designates the $U(r)/U_j = 0.05, 0.95$ points.

A comparison between the self-similar profile for the short and long nozzles is shown in figure 4.28. These two profiles are very similar as expected. The only difference is the magnitude of the peak (which sets the behavior near the peak), however this is expected from figure 4.23. Also, the spreading near the nozzle exit is shown in figure 4.29 for reference.

4.3.7 Downstream Evolution

Velocity field statistics were also measured further downstream of the nozzle exit, up to $x = 10D$, which includes the collapse of the potential core. As mentioned previously, this region is important as it is the primary low-frequency noise production region. Using the data shown in figures 4.30 and 4.31, the length of the potential core is less than one nozzle diameter different for the two nozzles, with the distance it takes to reduce to 95% the upstream centerline value, defined similar to Bogey & Bailly (2005), decreasing from $7.90 D$ to $7.13 D$ from the short to the long nozzle (thin to thick initial shear layer). For this plot, all values have been normalized by the expected jet exhaust velocity based on atmospheric conditions at the time of each data set acquisition. These values are consistent with expected collapse lengths, however it is important to note the dependence on the initial shear-layer

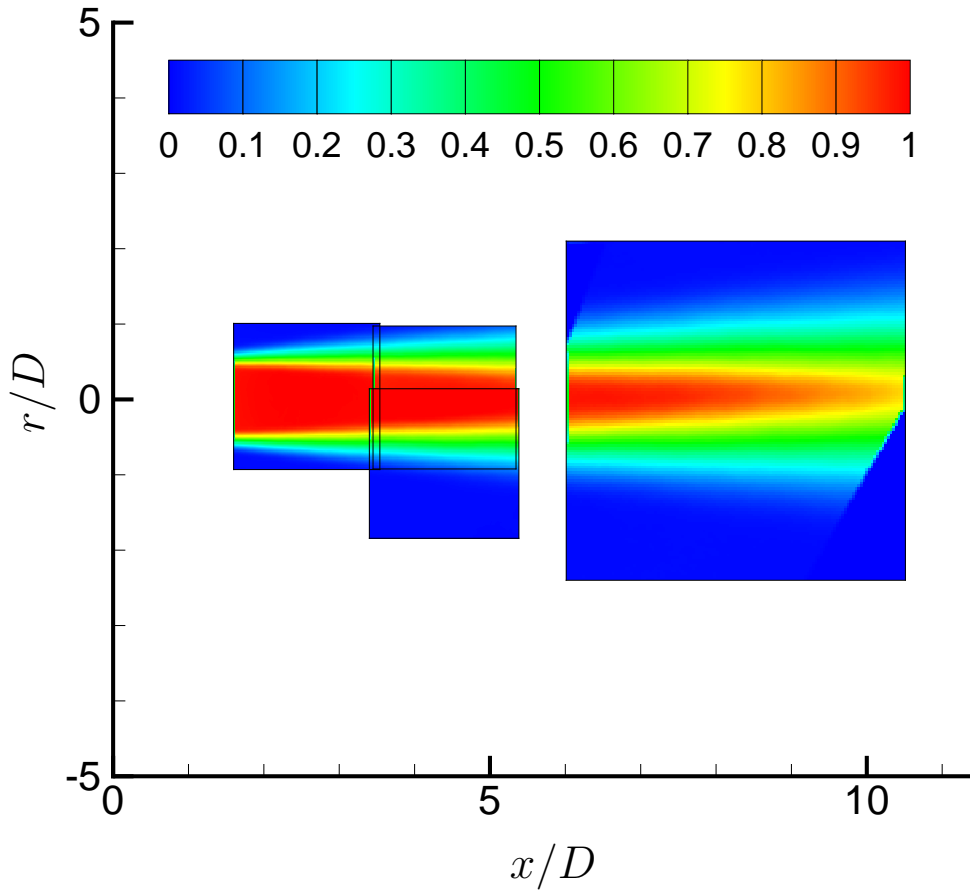


Figure 4.30: Downstream streamwise velocity (U/U_j) for the short nozzle (table 4.1).

thickness.

Additionally, the downstream evolution of the streamwise fluctuation is plotted in figures 4.32 and 4.33. The qualitative similarity of the turbulence development further demonstrates that the different nozzles have little effect on the downstream development of the flows, in this case far downstream of nozzle exhaust into the potential core collapse region.

If we examine the downstream evolution of the shear layer for the short nozzle jet using methods similar to those used in obtaining figure 4.3, we find that it takes until $0.72 D$ for the shear layer momentum thickness to reach the initial value for the long nozzle. This value is close to the difference in distance of $0.77 D$ for potential core collapse and reinforces the

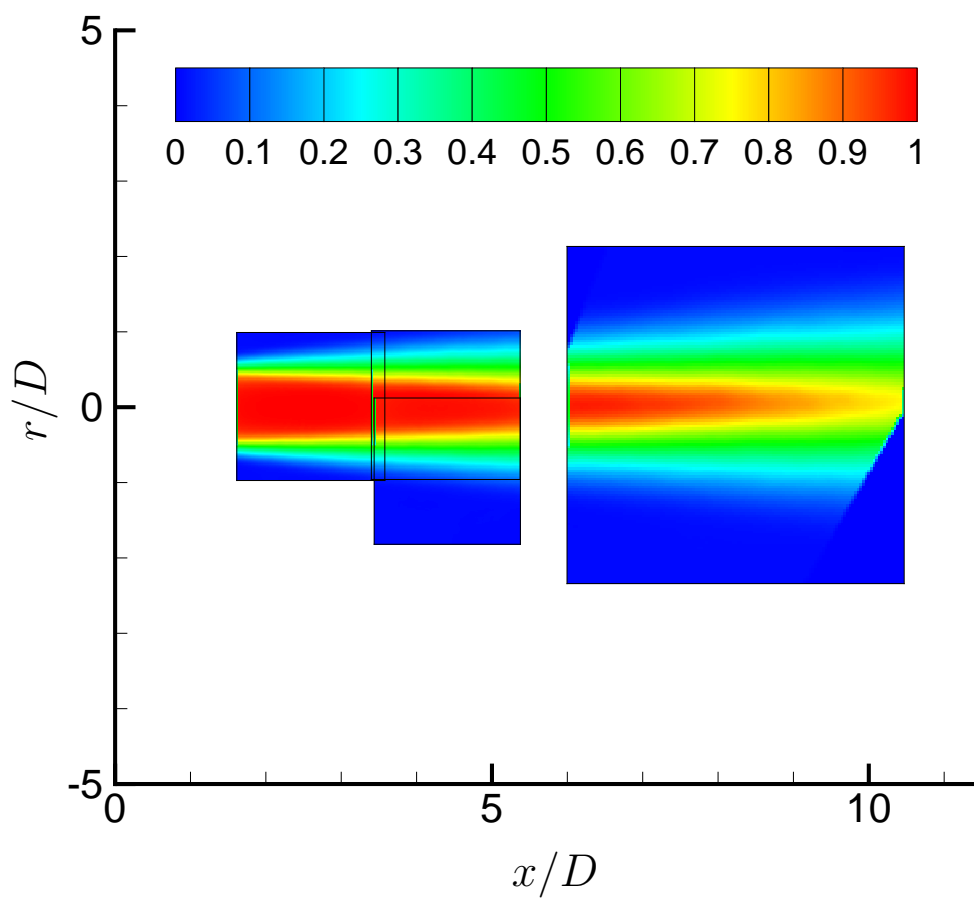


Figure 4.31: Downstream streamwise velocity (U/U_j) for the long nozzle (table 4.1).

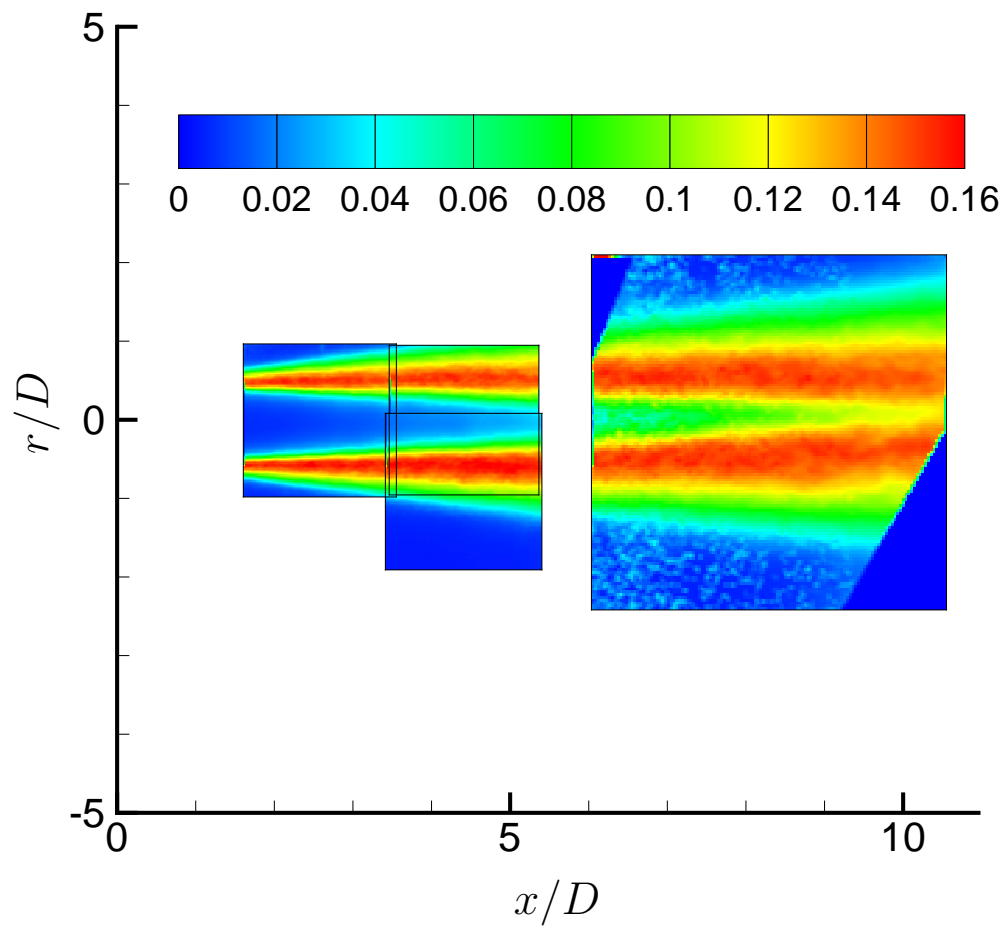


Figure 4.32: Downstream streamwise velocity fluctuation (u_{rms}/U_j) for the short nozzle (table 4.1).

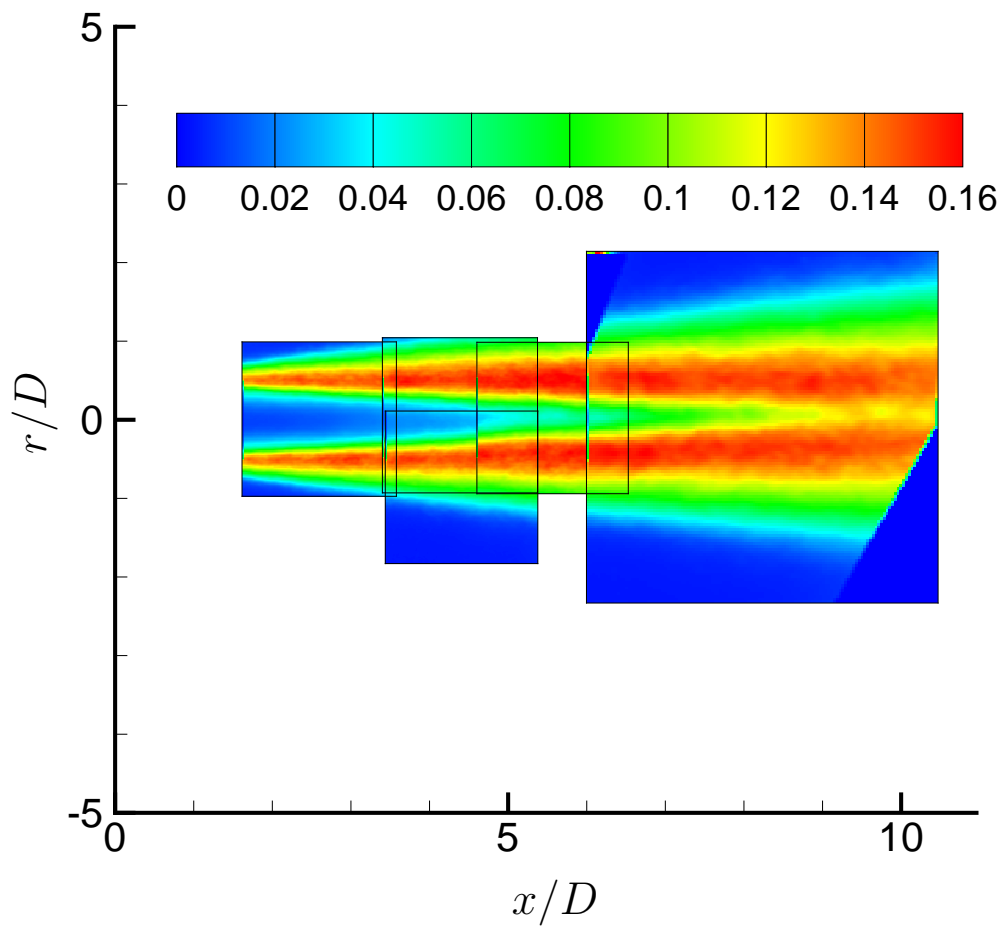


Figure 4.33: Downstream streamwise velocity fluctuation (u_{rms}/U_j) for the long nozzle (table 4.1).

idea of a “missing region” of noise production that short nozzle contains which is not present for the long nozzle as being the source of the excess sound.

4.3.8 Noise Reduction

We note that one effect of a thicker boundary layer is to reduce noise. In a sense, a thick exhaust-boundary layer acts by removing the initial region of shear layer growth up to the point where the shear layer thickness are equivalent. The total acoustic power is reduced with this region now missing, and the potential core closes earlier. There is a smaller noise generation volume, especially that which is associated with shear-layer instabilities and is directed predominantly downstream. Since this is the small δ -scale region near the nozzle exit, it is primarily high-frequency sound sources that are removed by this effect, which is shown in our spectra in figure 4.17.

Many control devices have been implemented in an attempt to reduce noise, with one of the most popular being chevrons. Typically in these efforts, the exhausting shear-layer is altered from the baseline, however the mechanism by which noise reductions arise is not expected to be the same as for the thicker shear-layer here. While a precise understanding is still lacking because it is tied up in the full complexity of jet turbulence, chevrons are believed to affect the flow by disrupting the coherence of large-scale azimuthally correlated vortex-like structures (Alkislak *et al.*, 2005), which have their vorticity redistributed into streamwise-oriented vortex structures. Michalke & Fuchs (1975) suggest that the lowest-order azimuthal modes constitute the most important sound sources, which was supported by the experiments of Juvé *et al.* (1979), who measured their signatures in the acoustic far field. The result is decreased sound near the peak Strouhal number and below ($St_D \lesssim 1$) (Bridges & Brown, 2004). At higher frequencies, however, the streamwise vortex pairs can increase overall turbulence intensity, thereby increasing high-frequency mixing noise. The chevrons can be designed in such a way to minimize the high-frequency penalty or attempt push it to frequencies outside of the audible range, however eliminating it completely remains

challenging (Bridges & Brown, 2004).

Bridges & Brown (2004) also show that deeper chevron penetration through the boundary layer can lead to larger noise reductions at low frequency, however a greater penalty is incurred at high-frequency. It is up to the designer to determine if this trade-off is acceptable. The present results show that without chevrons there are also direct effects of boundary layer thickness, and the interplay of chevrons with its thickness has not been studied in detail, though adjusting this within a design might provide additional tailoring of any other noise-control approach. Losses would be associated with the formation of a thicker turbulent boundary layer, but it is also possible that this could be done with trips somehow activated in an on-demand basis.

Chapter 5

Linear Stability of the Near-nozzle Shear Layers

5.1 Motivation

Despite the different thickness, and turbulence statistics that did not scale well with the local nozzle thickness, there were some remarkable similarities in the downstream development of the turbulence observed in the previous chapter, particularly in figures 4.26 and 4.28. We saw that the apparent remnant of the thicker boundary layer seems to be passive whereas the thickness-insensitive region of the turbulence developed similarly in all cases. This suggests that despite their obvious differences, the initial turbulent shear layers also share some direct similarities, which we investigate by considering the linear stability of the mean profiles of the different cases. While it may seem doubtful that a linear analysis may apply given the fundamentally nonlinear character of the high turbulent intensities, both qualitative and quantitative similarities have been found, which suggest a close link between linear modes and turbulence in free shear flows. Specifically, indications include the mixing layer growth rate (Gropengeisser, 1970; Sandham & Reynolds, 1990; Day *et al.*, 1998), spanwise-oriented rollers (Brown & Roshko, 1974; Hama, 1962; Morris *et al.*, 1990; Roshko, 1993), forced mixing layers (Gaster *et al.*, 1985; Petersen & Samet, 1988), and particular components of supersonic jet noise (Tam & Burton, 1984).

The mixing layer growth rate relation is perhaps the most applicable to the flow-field under study. Simple models based upon these ideas show that the shear layer growth is related closely to the stability characteristics of the mean flow (Viswanathan & Morris, 1992). The maximum instability amplification rate and the growth rate of plane turbulent

mixing layers have been found to decrease in direct proportion with each other as the Mach number increases in a compressible flow (Gropengeisser, 1970; Sandham & Reynolds, 1990; Day *et al.*, 1998). A connection between the two was developed by Morris *et al.* (1990), whose model suggested that for a spatial two-dimensional mixing layer the growth rate is directly proportional to the amplification rate of the most unstable mode. In this perspective, energy is extracted from the mean flow by a linear mechanism, which in turn through nonlinear interactions transfer energy to other turbulence components, which collectively grow the layer (Roshko, 1993).

While much of the above analysis referenced in this regard concentrates on the fully developed, hyperbolic tangent like profiles, there is even evidence of linear mechanisms being able to support some mechanism of wall bounded turbulence (Jiménez, 2013). This would indicate the near-nozzle shear region, which is composed of multiple components in this study, is expected to share characteristics with the corresponding linear system as well.

5.2 Governing Equations

We assume isentropic flow, which simplifies the analysis and is a good approximation for our cold jet, and consider the stability of the mass and momentum equations along with an equation of state for pressure:

$$\frac{\partial \rho}{\partial t} + \frac{\partial}{\partial x_j} (\rho u_j) = 0, \quad (5.1)$$

$$\frac{\partial}{\partial t} (\rho u_i) + \frac{\partial}{\partial x_j} (\rho u_i u_j + p \delta_{ij}) = \rho g_i + \frac{\partial}{\partial x_j} \tau_{ij}, \quad (5.2)$$

$$p = p(\rho, s). \quad (5.3)$$

We also neglect viscous effects, which are known to be minimal in the stability of inflectional free shear flows, and craft the equations in cylindrical coordinates as

$$\frac{\partial \rho}{\partial t} + \frac{\partial}{\partial x} (\rho u) + \frac{1}{r} \frac{\partial}{\partial r} (\rho r v_r) + \frac{1}{r} \frac{\partial}{\partial \theta} (\rho v_\theta) = 0, \quad (5.4)$$

$$\rho \left(\frac{\partial u}{\partial t} + u \frac{\partial u}{\partial x} + v_r \frac{\partial u}{\partial r} + \frac{v_\theta}{r} \frac{\partial u}{\partial \theta} \right) = -\frac{\partial p}{\partial x}, \quad (5.5a)$$

$$\rho \left(\frac{\partial v_r}{\partial t} + u \frac{\partial v_r}{\partial x} + v_r \frac{\partial v_r}{\partial r} + \frac{v_\theta}{r} \frac{\partial v_r}{\partial \theta} - \frac{1}{r} v_\theta^2 \right) = -\frac{\partial p}{\partial r}, \quad (5.5b)$$

$$\rho \left(\frac{\partial v_\theta}{\partial t} + u \frac{\partial v_\theta}{\partial x} + v_r \frac{\partial v_\theta}{\partial r} + \frac{v_\theta}{r} \frac{\partial v_\theta}{\partial \theta} + \frac{v_r v_\theta}{r} \right) = -\frac{1}{r} \frac{\partial p}{\partial \theta}. \quad (5.5c)$$

Small perturbations, indicated with $()'$, are imposed on the base flow, indicated with a $\bar{}$, as

$$\begin{aligned} u &= \bar{u} + u', \\ v_r &= \bar{v}_r + v_r', \\ v_\theta &= \bar{v}_\theta + v_\theta', \\ \rho &= \bar{\rho} + \rho', \\ p &= \bar{p} + p'. \end{aligned} \quad (5.6)$$

The mean is a time average, only dependent upon radial coordinate r , and assumed to be parallel with the streamwise direction so

$$\frac{\partial}{\partial t} \bar{(\quad)} = 0, \quad (5.7)$$

$$\frac{\partial}{\partial x} \bar{(\quad)} = 0, \quad (5.8a)$$

$$\frac{\partial}{\partial \theta} \bar{(\quad)} = 0, \quad (5.8b)$$

$$\bar{v}_r, \bar{v}_\theta = 0. \quad (5.9)$$

Taking (5.6), using (5.7), (5.8), and (5.9) in the non-dimensional forms of (5.4) and (5.5) along with the isentropic condition of (5.3), and linearizing produces

$$\frac{\partial \rho'}{\partial t} + \bar{u} \frac{\partial \rho'}{\partial x} + v_r' \frac{\partial \bar{\rho}}{\partial r} + \bar{\rho} \left(\frac{\partial u'}{\partial x} + \frac{\partial v_r'}{\partial r} + \frac{1}{r} \frac{\partial v_\theta'}{\partial \theta} + \frac{1}{r} v_r' \right) = 0, \quad (5.10)$$

$$\bar{\rho} \left(\frac{\partial u'}{\partial t} + \bar{u} \frac{\partial u'}{\partial x} + v'_r \frac{\partial \bar{u}}{\partial r} \right) = -\frac{\partial p'}{\partial x}, \quad (5.11a)$$

$$\bar{\rho} \left(\frac{\partial v'_r}{\partial t} + \bar{u} \frac{\partial v'_r}{\partial x} \right) = -\frac{\partial p'}{\partial r}, \quad (5.11b)$$

$$\bar{\rho} \left(\frac{\partial v'_\theta}{\partial t} + \bar{u} \frac{\partial v'_\theta}{\partial x} \right) = -\frac{1}{r} \frac{\partial p'}{\partial \theta}, \quad (5.11c)$$

$$\frac{\partial p'}{\partial t} + \bar{u} \frac{\partial p'}{\partial x} = c^2 \left(\frac{\partial \rho'}{\partial t} + \bar{u} \frac{\partial \rho'}{\partial x} + v'_r \frac{\partial \bar{\rho}}{\partial r} \right), \quad (5.12)$$

where (5.12) is a known result for linear acoustics (Pierce, 1989). We define the perturbations in the usual way to have the form

$$\begin{aligned} u'(x, r, \theta, t) &= \tilde{u}(r) e^{i(\alpha x + n\theta - \omega t)}, \\ v'_r(x, r, \theta, t) &= \tilde{v}_r(r) e^{i(\alpha x + n\theta - \omega t)}, \\ v'_\theta(x, r, \theta, t) &= \tilde{v}_\theta(r) e^{i(\alpha x + n\theta - \omega t)}, \\ \rho'(x, r, \theta, t) &= \tilde{\rho}(r) e^{i(\alpha x + n\theta - \omega t)}, \\ p'(x, r, \theta, t) &= \tilde{p}(r) e^{i(\alpha x + n\theta - \omega t)}. \end{aligned} \quad (5.13)$$

where α is the axial eigenvalue, n is the azimuthal wave-number, and ω is the temporal eigenvalue. The coefficients $\tilde{()}$ are the eigenfunctions in the radial coordinate. When inserted into (5.10), (5.11), and (5.12) give

$$\tilde{\rho}(\bar{u}\alpha - \omega) + \tilde{v}_r \frac{\partial \bar{\rho}}{\partial r} + \bar{\rho} \left(\tilde{u}\alpha + \frac{\partial \tilde{u}}{\partial r} + \frac{\tilde{v}_r}{r} + \frac{\tilde{v}_\theta n}{r} \right) = 0, \quad (5.14)$$

$$\tilde{u} = \frac{1}{\bar{\rho}} \left(-\frac{\partial \tilde{\rho}}{\partial r} \frac{\partial \bar{u}}{\partial r} (\bar{u}\alpha - \omega)^{-2} - \frac{\tilde{p}\alpha}{\bar{u}\alpha - \omega} \right), \quad (5.15)$$

$$\tilde{v}_r = \frac{i}{\bar{\rho}} \frac{\partial \tilde{p}}{\partial r} (\bar{u}\alpha - \omega)^{-1}, \quad (5.16)$$

$$\tilde{v}_\theta = -\frac{1}{\bar{\rho}} \frac{n}{r} \frac{\tilde{p}}{(\bar{u}\alpha - \omega)}, \quad (5.17)$$

$$\tilde{\rho} = \frac{\tilde{p}}{c^2} - \frac{1}{\bar{\rho}} \frac{\partial \bar{\rho}}{\partial r} \frac{\partial \tilde{p}}{\partial r} (\bar{u}\alpha - \omega)^{-2}. \quad (5.18)$$

Equation (5.14) can be combined with the other relations to produce a second-order differential equation for the pressure amplitude function \tilde{p} , which is often referred to as the compressible Rayleigh equation:

$$\frac{d^2 \tilde{p}}{dr^2} + \left[\frac{1}{r} - \frac{1}{\bar{\rho}} \frac{d\bar{\rho}}{dr} - \frac{2\alpha}{\bar{u}\alpha - \omega} \frac{d\bar{u}}{dr} \right] \frac{d\tilde{p}}{dr} - \left[\alpha^2 + \frac{n^2}{r^2} - \frac{(\bar{u}\alpha - \omega)^2}{c^2} \right] \tilde{p} = 0. \quad (5.19)$$

Appropriate boundary conditions

$$|\tilde{p}| < \infty \text{ as } r \rightarrow 0.5, \quad (5.20a)$$

$$\tilde{p} \rightarrow 0 \text{ as } r \rightarrow \infty, \quad (5.20b)$$

ensure the solution is bounded at the jet centerline and decays in the far-field. These conditions are implemented via the asymptotic solution in the appropriate limit. The far-field behavior can be specified by developing the asymptotic solutions for large r . Similarly, the $r \rightarrow 0.5$ condition, yields a similar small- r expression. These are (e.g. Mitchell *et al.* (1995))

$$\begin{aligned} \tilde{p} &= k_1 I_n(\lambda_0 r) & \text{as } r \rightarrow 0.5, \\ \tilde{p} &= k_2 K_n(\lambda_\infty r) & \text{as } r \rightarrow \infty, \end{aligned} \quad (5.21)$$

$$\lambda_0 = \sqrt{\alpha^2 - \frac{(\omega - \bar{u}\alpha)^2}{c^2}} \quad \lambda_\infty = \sqrt{\alpha^2 - \frac{\omega^2}{c^2}},$$

where I_n and K_n are the modified Bessel functions of the first and second kind, respectively.

5.3 Numerical Solution

The linear system (5.19) is solved using a shooting method. Here, solutions at the boundaries give starting points for inner and outer solutions. Numerical integration of the Rayleigh equation then allows these to be marched inwards toward a common $r = 0.5$ in the shear layer. For the spatial stability we consider, ω is real valued and specified, and α is iteratively adjusted until the the inner and outer solutions and their derivatives adequately match at $r = 0.5$.

For convenience of computation, we use analytic profiles for the shapes of the input curves to ensure sufficiently smooth profiles and derivatives. For the short nozzle, which had only a small initial boundary layer thickness, we find a hyperbolic tangent profile (5.22) fits the data well when we use the experimental θ_o value, however when this form is fit to the thicker exhaust profile for the long nozzle it does not represent the profile behavior. A plot of this is shown in figure 5.1.

$$\frac{U}{U_j} = 0.5 \left[1 - \tanh \left(\frac{r_o}{4\theta_o} \left[\frac{r}{r_o} - \frac{r_o}{r} \right] \right) \right] \quad (5.22)$$

An analytic function consisting of two hyperbolic tangent profiles was found to more closely match the experimental measurements. It relies on one profile that describes the high gradient region and sets the function to zero in the far field, and another term which models the core of the jet. For a base profile, we use (5.22) with $\theta_{0,1} = 5.46 \times 10^{-3}D$, the experimentally determined momentum thickness for the short nozzle. This is then combined with a shifted hyperbolic tangent profile with a shift, r_s , and thickness, $\theta_{0,2}$ giving the full expression (5.23). The values for the shift and thickness are determined by visually fitting the resulting profile to the experimental results. This profile gives the best compromise between fitting the high-shear region and a smooth transition to the core region which is not

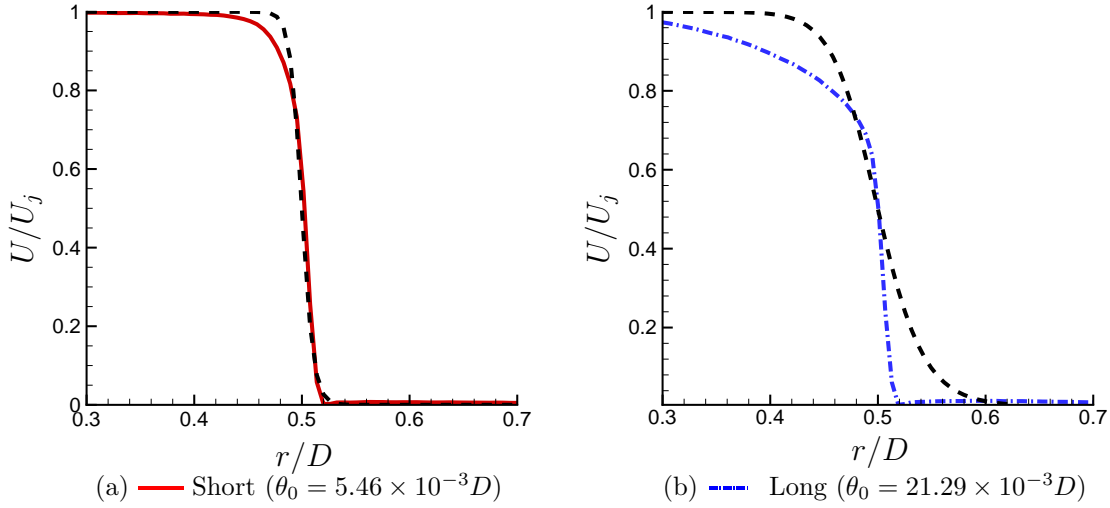


Figure 5.1: Comparison of using the experimentally determined initial momentum thickness as a parameter in (5.22) (---) with the corresponding experimentally determined initial profile.

possible with a single hyperbolic tangent function.

$$\begin{aligned}
 \frac{U}{U_j} &= 0.5 \left[1 - \tanh \left(\frac{r_o}{4\theta_{0,1}} \left[\frac{r}{r_o} - \frac{r_o}{r} \right] \right) \right] \\
 &\quad \times 0.5 \left[1 - \tanh \left(\frac{r_o}{4\theta_{0,2}} \left[\frac{r - r_s}{r_o} - \frac{r_o}{r - r_s} \right] \right) \right] \\
 \text{Base} &\quad \theta_{0,1} = 0.01092r_o \quad r_s = 0 \\
 \text{Short} &\quad \theta_{0,2} = 0.05r_o \quad r_s = 0.06r_o \\
 \text{Long} &\quad \theta_{0,2} = 0.23r_o \quad r_s = 0.16r_o
 \end{aligned} \tag{5.23}$$

The new analytic profiles follow the experimental results much more closely as shown in figure 5.2. Both have a similarly sharp increase in velocity near the outside of the shear layer and the long nozzle has a much more gradual transition to the centerline streamwise velocity.

With the assumption of constant static pressure, a known jet centerline temperature, T_j , and a constant Prandtl number, $Pr = 1$, the density can be found using the Crocco-

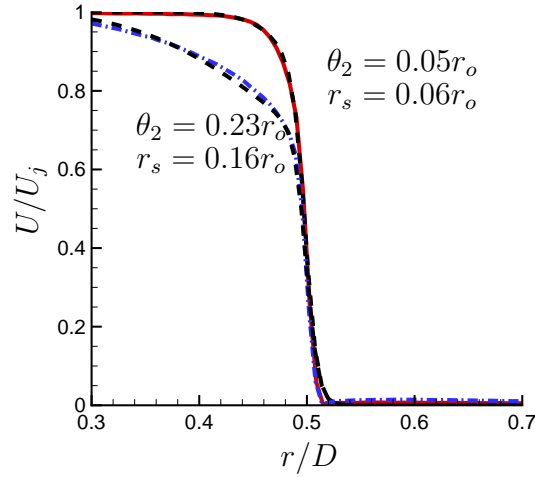


Figure 5.2: Comparison of experimental streamwise velocity data to fits described by (5.23) (----) with the corresponding experimentally determined initial profile for the — short and - - - long nozzles.

Busemann relation (Michalke, 1984):

$$\frac{T}{T_j} = \frac{T_\infty}{T_j} + \left(1 - \frac{T_\infty}{T_j}\right) \frac{U}{U_j} + \frac{1}{2}(\gamma - 1) M^2 \frac{U}{U_j} \left(1 - \frac{U}{U_j}\right). \quad (5.24)$$

For an ideal gas at constant pressure, the equation of state will lead to our density profile:

$$\rho(r) = \rho_\infty \frac{T_\infty}{T(r)}. \quad (5.25)$$

The streamwise velocity, streamwise velocity derivative, density, and density derivative profiles all serve as inputs to the linear stability analysis. The derivative of the streamwise velocity under a parallel flow assumption defines the vorticity which drives the jet instability (Michalke, 1984). This is a particularly important reason that the sharp increase in velocity found in the experimental profiles must be captured well when inflow data are supplied to the stability code.

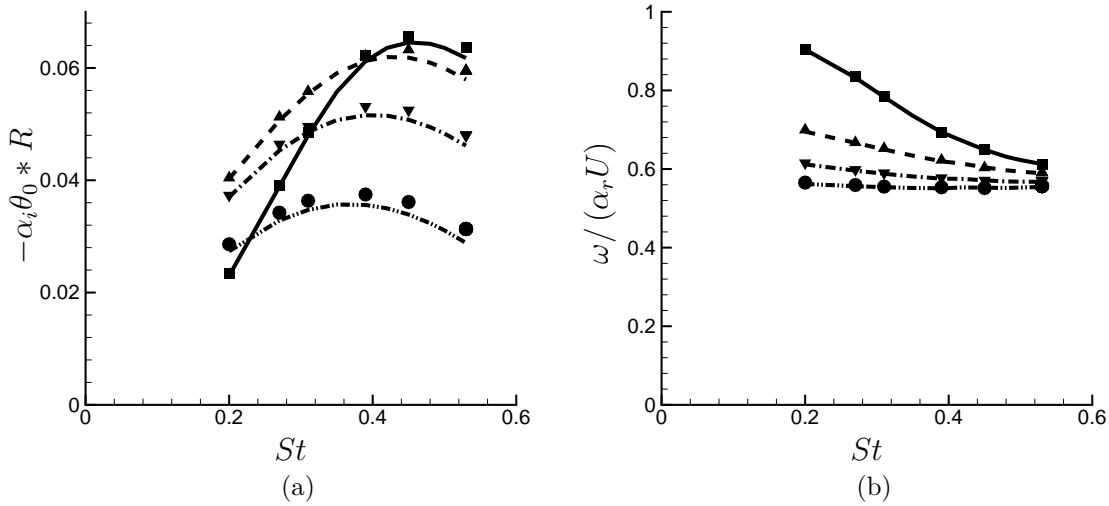


Figure 5.3: Comparison with previous results of Bodony (2004) (symbols) and the current results (lines): mode $m = 0$ \blacksquare (—); $m = 1$ \blacktriangle (- -); $m = 2$ \blacktriangledown (- · - ·); $m = 3$ \bullet (·····).

5.4 Results

Once the numerical solution was validated against a $M = 0.9$ axisymmetric jet with $\theta_0 = 0.089r_o$ from Bodony (2004) (see figure 5.3), the shear layer in (5.23) was reduced to a thickness of $\theta_o = 0.01092r_o$ which served as a baseline. It was found that each of the short and long profiles could be reasonably built up from here.

From the results of this analysis, we are able to plot the instability amplification rates, $-\alpha_i$, along with the phase speed for baseline (only high-shear region), short, and long profiles in figures 5.4 and 5.5. Poor agreement is seen when an attempt to normalize based on the initial momentum thickness as in figure 5.4, which indicates the stability is not governed primarily by the momentum thickness length scale. We do see good agreement in the peak amplification rates of the non-dimensionalized profiles in figure 5.5 considering the large difference in momentum thickness, leading to the conclusion that the instability is primarily driven by the high-shear portion of the profile, which is a common feature shared by all profiles. Additionally, the peak amplification rate reduces in frequency for thicker jets. This may help explain the reduction in high-frequency noise produced by these nozzles.

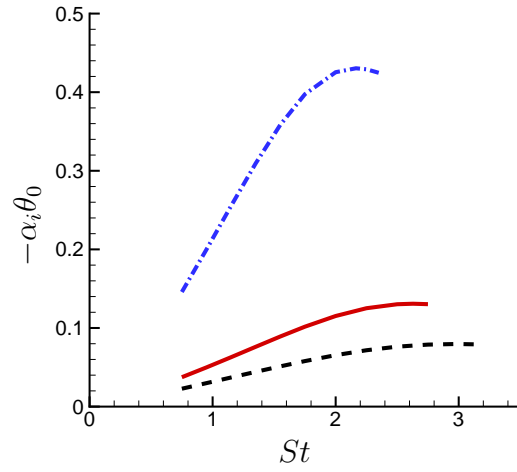


Figure 5.4: Stability analysis with growth rate normalized by the layer thickness: -- tanh baseline; — short; -·-· long.

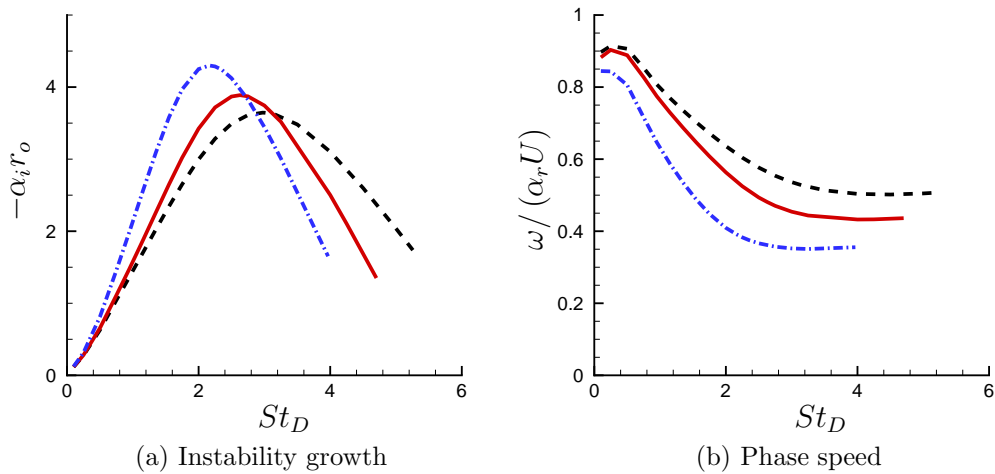


Figure 5.5: Axisymmetric mode $n = 0$ amplification (a) and phase speed (b) for $e^{i\alpha x + i\omega t}$ modes with $\alpha = \alpha_r + i\alpha_i$ linear amplification: --- baseline; — short nozzle; and -·-· long nozzle.

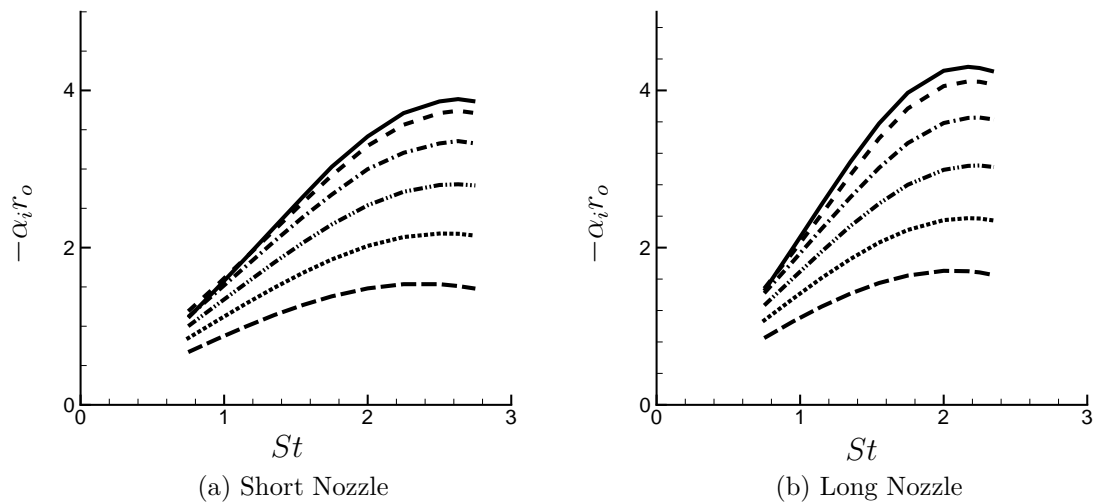


Figure 5.6: Linear instability growth rates as a function of Strouhal number: mode — $n = 0$; - - - $n = 5$; - \cdot - \cdot $n = 10$; $\text{\cdot \cdot \cdot \cdot}$ $n = 15$; $\text{\cdot \cdot \cdot \cdot}$ $n = 20$; and - - - - $n = 25$.

In addition to looking at the mode $n = 0$ response, the analysis was extended to the higher azimuthal order modes. In figure 5.6, modes up to 25 are shown. The growth rate of the first few modes are comparable to mode 0 for both profiles and the higher order modes still have a relatively large peak instability growth rate. This result could be anticipated from the thin shear layers and the high-frequency noise which is measured. It is apparent from this analysis that similar peak instabilities are present for the two profiles which in turn are similar to the baseline high-shear only profile.

The eigenfunction solutions give the radial extent of the first axisymmetric disturbance at the peak amplification frequency and are shown in figures 5.7, 5.8, 5.9, and 5.10. Again, reasonable agreement is found despite the different initial profiles, indicating common stability characteristics.

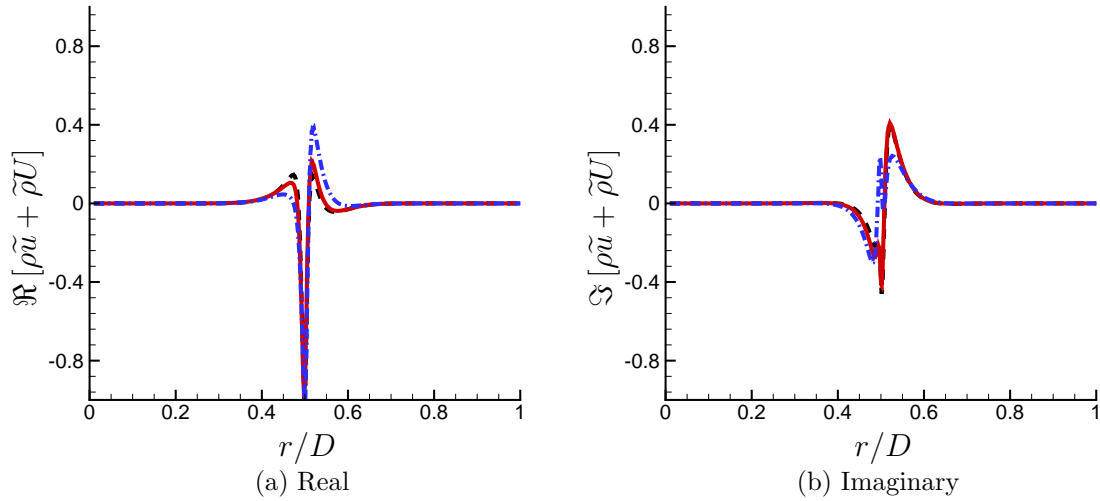


Figure 5.7: Streamwise velocity eigenfunction solution for the $n = 0$ most unstable frequency: --- baseline; — short; -·- long.

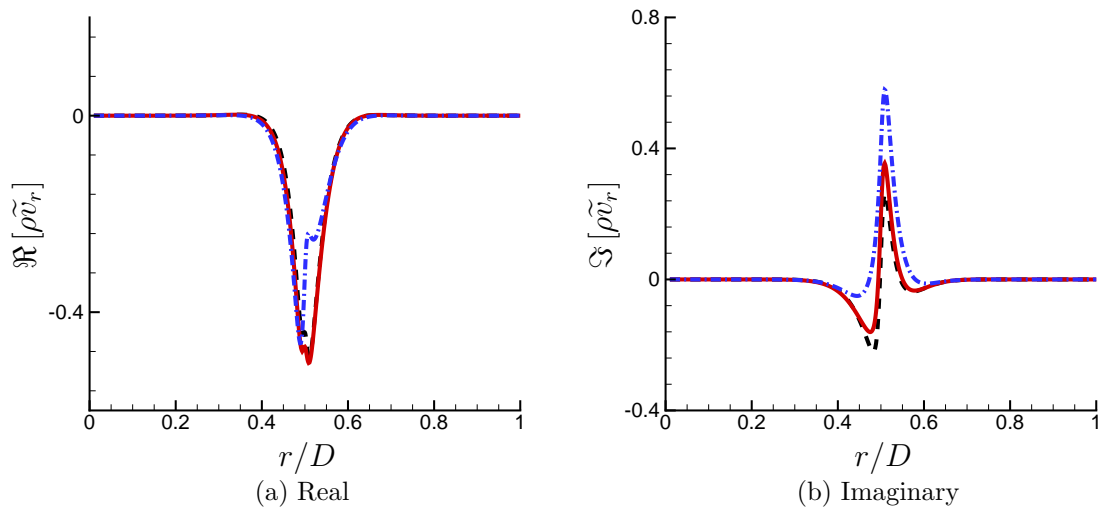


Figure 5.8: Radial velocity eigenfunction solution for the $n = 0$ most unstable frequency: — short; -·- long.

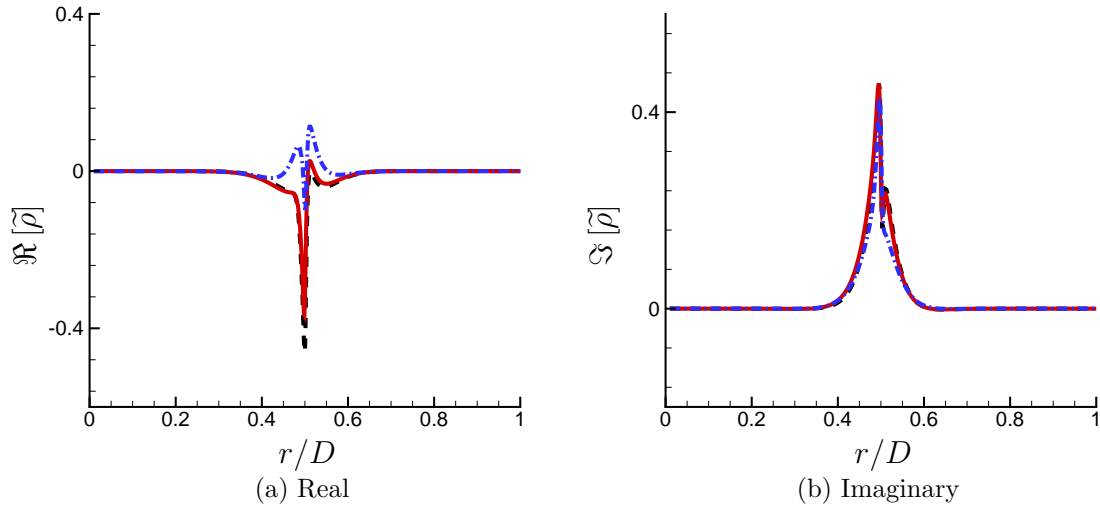


Figure 5.9: Density eigenfunction solution for the $n = 0$ most unstable frequency: --- baseline; — short; - - - long.

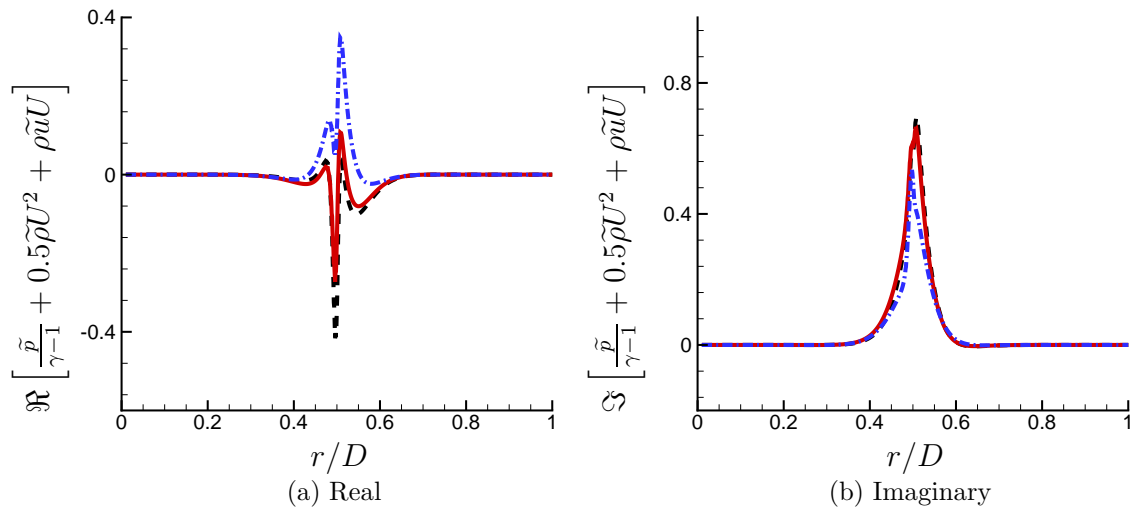


Figure 5.10: Pressure eigenfunction solution for the $n = 0$ most unstable frequency: --- baseline; — short; - - - long.

Chapter 6

Summary and Conclusions

The various aspects of this work are all oriented toward addressing key issues in the pursuit of quieter nozzle designs, either through the use of scale models or by simulations. Either way, there is no reliable way to easily anticipate how a particular nozzle modification will or will not reduce jet noise. Model-scale experiments and simulations offer the best opportunities for assessing utility of designs, but neither provides a perfect representation of a full-scale nozzle of interest. To be low cost, and therefore allow for extensive studies, model-scale experiments require a significantly reduced scale since they have a cost that increases rapidly toward engineering scale. However, the usual scale-similarity that justifies the use of models, is problematic in the nozzle because the boundary layer thickness can have an order-one effect on the far-field sound. The challenge of resolving this same, very thin boundary layer in a simulation likewise makes that challenging.

Our efforts to address these overarching issues centered on a new low-cost aeroacoustic jet noise facility. An anechoic chamber with a $2.1 \text{ m} \times 2.3 \text{ m} \times 2.5 \text{ m}$ working volume has been constructed and demonstrated for noise measurements of small-scale jets. The steps taken to establish the performance of the facility are summarized and data acquisition and processing is described. The facility has been validated by establishing that in the geometric far field the sound pressure level scales with the inverse of distance squared, and that the OASPL follows the expected U_j^8 scaling. We also validate the spectra at $\theta = 90^\circ$ and 30° against existing data and find very good agreement. Complex nozzle geometries can be manufactured using a rapid prototyping process and were shown to produce results that agree with their traditional metal counterparts. The capability to perform PIV measurements has been established and

good agreement with existing data is again obtained.

To demonstrate the geometric flexibility of this approach, a series of experiments were carried out investigating the application of various nozzle exit designs different from an axisymmetric jet which functioned as a passive control strategy. The first considered chevrons of different geometries and lengths. Even with a stable overall sound pressure level, the frequency response was shown to be sensitive to exhaust conditions. Also, the issue of conflicting minima was highlighted where the noise reduction is inconsistent with respect to measurement location. A second study investigated a class of clamshell nozzles and found a high-amplitude tone. The source of this tone was subsequently identified using high-speed schlieren photography and surface oil flow visualization.

While the utility of such experiments for examining complex geometry nozzle modification is clear, their utility depends on either (1) how accurate they are outright for predicting the corresponding large-scale design or (2) whether results could be reliably corrected to provide guidance for larger scales. This comes down to the effects of the artificially thick boundary layer in the nozzles. A similar challenge was discussed in regard to simulations, and the challenge of representing this with a reasonably small number of mesh points.

Motivated by this challenge of the nozzle boundary layer thickness, and the resulting near-nozzle turbulent shear layer thickness, we designed a series of experiments to isolate its effects. This is the first time such a controlled series of experiments was conducted, focusing specifically on the *turbulent* boundary-layer thickness. The turbulence state of the boundary layer, even at significantly lower Reynolds numbers, was established via several metrics, which is important given the widely recognized effects associated with laminar flow at the nozzle. Fluctuation statistics at $x = 0.04 D$ showed out-of-equilibrium turbulence, which is expected this close to the nozzle.

The high-speed part of the shear layer appeared to be a remnant of the nozzle boundary layer, which was particularly pronounced in the thicker boundary layer cases. However, at the outer edge of the jet, the turbulence was approximately boundary layer thickness

insensitive. Its intensity showed a narrow peak, which developed with an apparently self-similar character when scaled with the local momentum thickness despite the persistent retarded velocity associated with the thicker boundary layers toward the core of the jet. This behavior, which was unexpected given the difference in boundary layer thickness, is consistent with the relative insensitivity of the linear instability modes to these particular profiles despite their significantly different thicknesses. The shear at the inflection point is associated with the outer edge of the flow and is nearly the same in all cases, which appears to be most important for the observed instability behavior.

These different flows had an obvious effect on the far-field sound. The high-frequency downstream acoustic radiation scaled with the exit momentum-thickness for all the nozzles considered. This might not be expected since the mean flows were fundamentally different in the thick and thin limits, with differences that are not well characterized by a single thickness length scale. However, as with turbulence statistics, this similarity of downstream radiation might be explained by the relatively similar instability modes they support. The peak spectrum was less effected by the nozzle shear-layer thickness, but also showed a reduced sound in the thicker shear layer cases.

No similar collapse of the acoustic data was found for the measurable portions of the spectrum at $\theta = 90^\circ$. Though it is difficult to prove, this would be consistent with the often-voiced notion that the sideline sound is not associated with predominantly shear-layer supported wave-packet-like structures which are expected to radiate more downstream. The better collapse with D rather than θ_o at all frequencies is more consistent with a source that might correspond to smaller-scale turbulence distributed throughout the jet. Alternatively, the sideline noise could be generated via a different mechanism by the same structures in the flow. While this might be the case, if such a mechanism were responsible for a significant portion of the sideline noise, we would also expect to see some systematic change in the sideline spectra, so we do not find strong support for this perspective.

The implication for numerical simulations of turbulent jet noise is that their often ar-

tificially thick nozzle shear layer might have a significant effect on the predicted far-field sound. However, the apparent collapse of key components of the spectrum, when scaled by the nozzle exit conditions likewise suggest the possibilities of corrections, which might have utility in the application of scale models or simulations to design at engineering scale. Any such correction would also need to recognize that the shear layers in these experiments have a particular form, with an obvious remnant of a nozzle boundary layer and relatively steep portion in the neighborhood of their inflection point. Any thick inflow shear layer in a simulation will not necessarily share this character, the full implications of which cannot be anticipated with our results. A smooth profile, such as a commonly used tanh-profile, would not necessarily be the best choice for modeling a nozzle; it seems that even a thicker shear layer might provide a better alternative, however the steep region of a profile, such as we measure, would not necessarily reduce the resolution challenge, which returns back to the root reason for thick simulation shear layers to start with.

One obvious effect of thicker nozzle boundary layers is to reduce noise, which will have implications for both simulation based predictions of noise suppression, with their often artificially thick shear layers, and engineering implementations. Chevrons, for example, require a particular arrangement and boundary-layer penetration for them to reduce sound, and even then generally only at low frequencies. Generating a thicker nozzle-exit boundary layer, without incurring losses or generating noise, might offer a similarly successful approach to noise control, particularly at high-frequency. This might be best accomplished with retractable passive actuators, which would not then incur significant losses when retracted. Thick boundary-layers might similarly affect active control. In terms of the responsiveness of the near-nozzle jet to actuation, the similar turbulence development and stability might allow scale experiments to examine as least some aspects of control strategies. However, their effect on the far-field sound might be masked by the same shear-layer-thickness sensitivity we report here.

Appendix A

Additional Facility Information

A.1 Additional Facility Characterization

Acoustic measurements were taken in the facility throughout the construction and facility improvement process. Figures A.1 and A.2 show the sound decay from an acoustic source in the facility before reflections were minimized by covering all exposed non-treated surfaces with foam. The deviation from the desired $1/R^2$ decay is apparent.

Once the foam was added to the surfaces, most notably the exhaust collector, the facility behaved in the expected anechoic fashion as indicated by the $1/R^2$ decay in sound level (figure A.3 as the microphone is moved away from the acoustic source).

In addition to characterizing the facility, the laser sheet used for PIV measurements was also characterized. A typical FWHM laser sheet thickness was found to be 0.19 mm (figure A.4) using a laser power meter, a knife edge, and a translation stage.

A.2 Heated Jet

For comparison to engineering jets, it is important to account for the hot gas exhausted as the fluid properties such as the speed of sound and specific heats will change with temperature. It is known that heating alters the acoustic radiation of a jet (Viswanathan, 2004). Considering this was unnecessary for our objectives, but will be for applications.

There are two possible ways to do this, each with advantages and disadvantages. The first is to use heated air and the second is to simulate this using helium. A helium-air

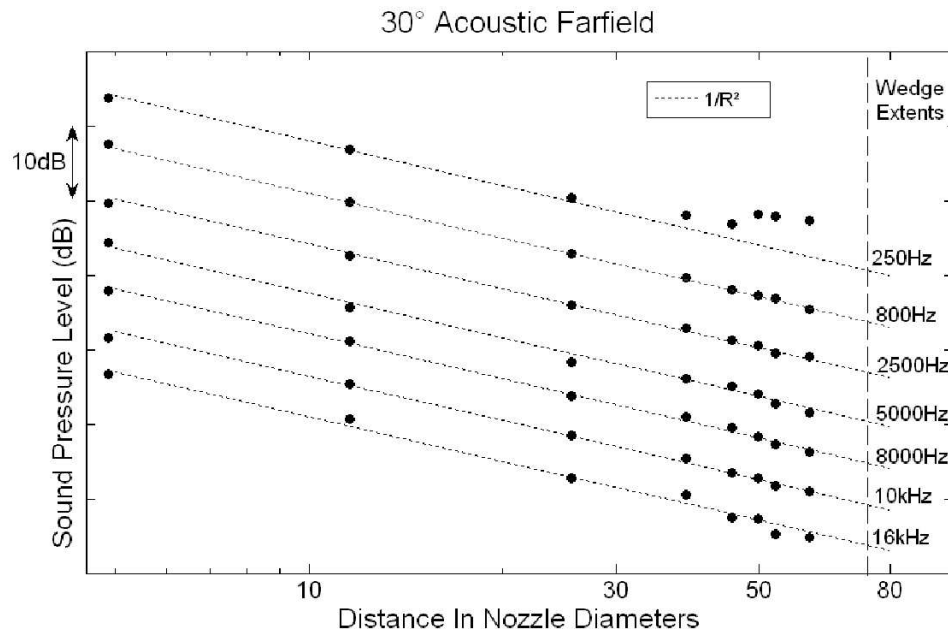


Figure A.1: Far-field measurements at 30° before in chamber reflections were minimized.

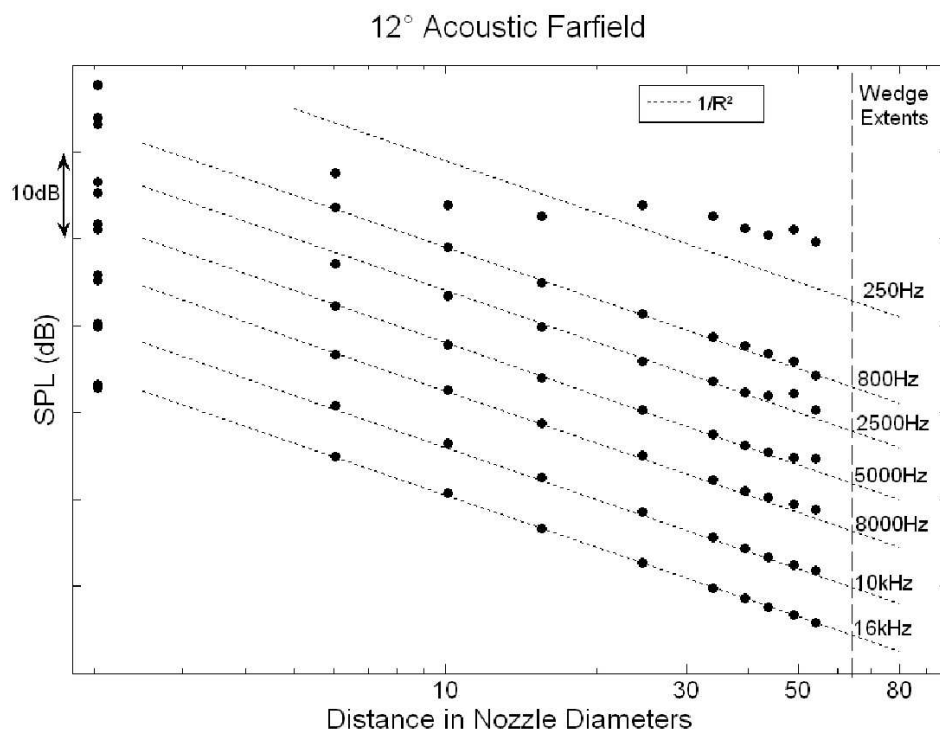


Figure A.2: Far-field measurements at 12° before in chamber reflections were minimized.

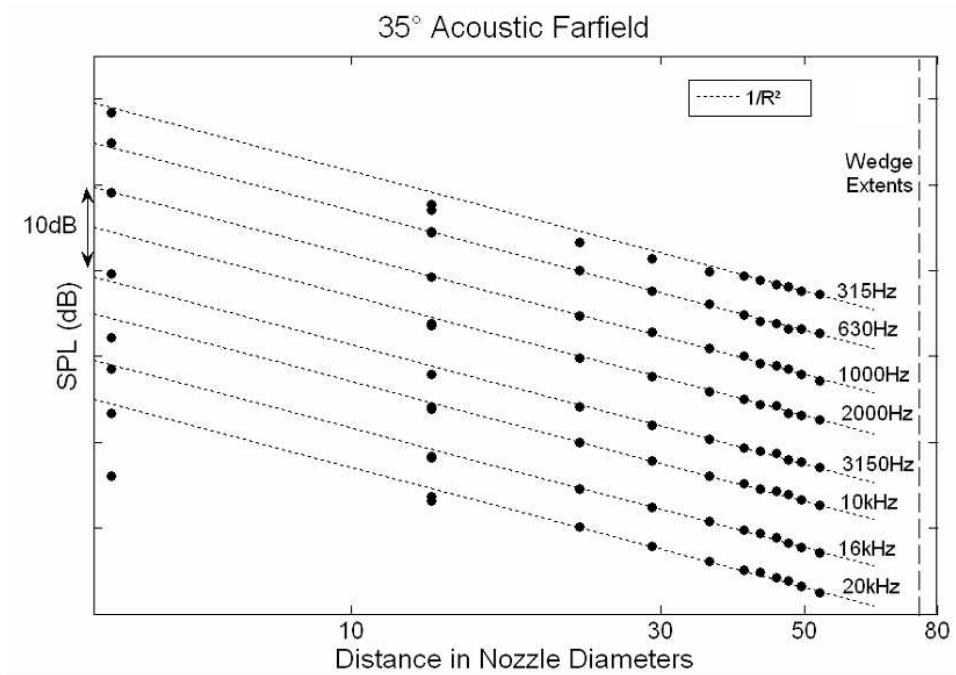


Figure A.3: Far-field measurements at 35° after in chamber reflections were minimized.

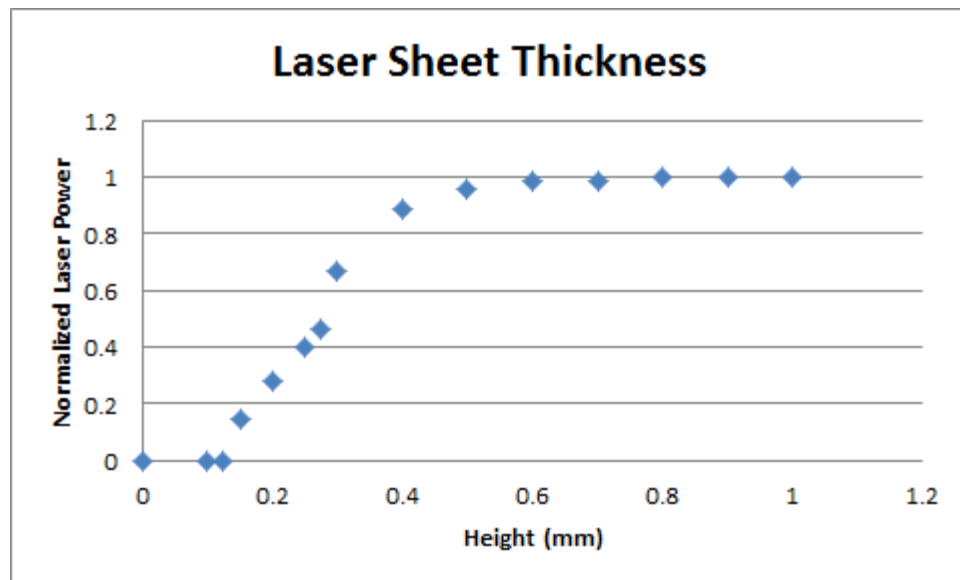


Figure A.4: Laser sheet thickness measurement. The FWHM is 0.19 mm.

mixture allows for either the speed of sound or the ratio of specific heats, γ to be matched to a corresponding hot jet, but not both at the same time.

A.2.1 Helium

A helium-air mixture offers a number of advantages over heating the flow when investigating the noise spectra of a scale-model jet, most notably safety and cost. The heater used is traditionally a combustion or electrical heater. A combustion heater requires working with flammable gasses and the electric heater needs a high-voltage power supply, both of which could be potentially dangerous. Also, combustion heaters have been known to add significant internal noise (Ahuja, 2003), which can render inaccurate jet noise measurements.

The use of helium as a substitute for heating jet flow in aeroacoustic testing has been investigated by a number of researchers including Doty (2002), Doty & McLaughlin (2003), and Papamoschou (2007). Helium has a much lower initial cost and would require only the helium bottles along with the proper valves to inject and mix the helium with the flow. Each bottle of helium would be a standard HP300 cylinder, which would allow for approximately 30 seconds of run time for a 25.4 mm core flow nozzle.

Working at or near ambient temperatures is another benefit of using helium instead of a heated rig. Plastic rapid prototyped nozzles cannot withstand the temperatures required for matching engineering jet flows. Additionally, upstream piping may need a redesign from potential thermal expansion effects.

A.2.2 Validity of Helium Tests

Papamoschou (2007) compared the use of small-scale helium-air mixtures to simulate the acoustics of larger scale heated jets. The study focused on both how realistically helium simulated a hot jet as well as compared density matching versus Mach number matching to determine helium concentration levels. Jet velocity is held constant for both. Both methods

were found to produce data consistent with the heated jet they were simulating with the Mach number matching performing slightly better with a mean deviation of between 1.0 and 1.2 dB as compared to 1.3 to 1.4 dB for the two velocity values tested. Doty & McLaughlin (2003) found that a helium-air mixture agreed to within 2 dB of heated jets and the only noticeable differences appeared to be facility related.

A.2.3 Heater

An in-line heater can be installed during any future modifications to the facility. The heater is a Model 9MRB-05 type CHP circulation heater from Heat Exchange and Transfer Inc. which requires a 460 V 162 amp 3-phase AC input and will provide up to 88 kW of power and a rated 130°C temperature rise. This retrofit would include significant downtime as the upstream piping would require a redesign to ensure the ability to handle the higher temperature.

A.3 Conclusion

Helium is a lower initial cost, easier to work with alternative to heated jet flow that has been proven effective for single-flow axisymmetric jets. The facility has already been designed with the ability to add helium through a series of inlet ports located upstream of the flow conditioning. A heater will provide a significant upgrade in facility capabilities. The best course of action is likely a combination of the two. The heater will allow the flow to be heated while remaining within working temperatures of the facility and the helium can provide for further simulated heat. Rapid prototyping which relies on resins could still be used for moderate temperature rises with helium addition to further change the properties of the flow if necessary to match exhaust conditions.

Appendix B

Measurement Error Analysis

B.1 Acoustics

For all acoustic measurements presented there will be associated uncertainty, however it is low. One source is uncertainty in the atmospheric conditions which will effect the microphone response directly and whose values can be be found from the manufacturer. The microphones give measurements within ± 0.3 dB at a 95% confidence interval. Variation due to temperature is $+0.005$ dB/C, humidity ± 0.1 dB up to 95% relative humidity, and pressure -0.021 dB/kPa.

There is also error associated with atmospheric attenuation related to correctly measuring the distance away from the microphone estimated to be ± 1 cm which is 0.02 dB. The uncertainty from normalizing to a common distance away is 0.05 dB, and the uncertainty associated with measuring the nozzle diameter is <0.01 dB.

Another source of uncertainty relates the exit velocity of the jet. The Setra pressure gauges used have a 0.13% full-scale error with a 0-25 psi measurement range and there is also some deviation in velocity from the PID algorithm which controls the valve to within ± 0.005 of the set point Mach number. Assuming jet noise scaling as U_j^8 the uncertainty is ± 0.25 dB for a Mach 0.9 jet. Finally, facility uncertainty from an RMS deviation from $1/R^2$ decay of noise levels (A.3) will contribute up to 0.18 dB. When all of these sources are included, combined in terms of pressure uncertainty, and then converted back to the more useful decibel scale, the maximum total uncertainty for measurement levels that are typically encountered in the facility is under 0.4 dB. This value is further reduced when comparing

changes in sound levels from the overlapping nature of many of the sources of uncertainty.

B.2 PIV

In order to better assess limitations of the PIV results, an error analysis has been completed and is presented for our high-speed jet at Mach 0.9. Following the procedure of Lazar *et al.* (2010), equipment uncertainty was found to be low, under 2.5 m/s ($\approx 0.9\% U_j$) in the core of the jet, and lower elsewhere. This equipment uncertainty accounts for length calibration uncertainty, image distortion, laser pulse jitter, and the accuracy of the delay generator.

Another potential source of uncertainty is from the particle dynamics, primarily the Stokes drag force which causes the particles to lag the local fluid velocity in regions of fluid acceleration. This lag velocity (B.1) can be calculated knowing properties of the fluid used for seeding and is given by

$$u_f - u_p = \frac{1}{18} \frac{\rho_p d_p^2}{\mu_f} \left(\frac{\partial u_p}{\partial x_p} \frac{\partial x_p}{\partial t} + \frac{\partial u_p}{\partial y_p} \frac{\partial y_p}{\partial t} \right). \quad (\text{B.1})$$

As two different seeding fluids are used, the DEHS in the core of the jet ($\rho = 912 \text{ kg/m}^3$, $d = 1 \mu\text{m}$) and the mineral oil from the smoke generator ($\rho = 800 \text{ kg/m}^3$, $d = 0.2 \mu\text{m}$), the average particle lag in the mixing region will be somewhere in-between the lag from the two individually. To determine the maximum lag possible, only the particle with the largest diameter, the DEHS from the Laskin nozzle is considered. Using the empirically determined mean velocity profile from (5.23), the peak shear near the nozzle exit can be estimated. Using this value in (B.1), and assuming streamwise only flow, produces a peak particle velocity of 1.7 m/s ($\approx 0.6\% U_j$) in the shear layer right at the nozzle exit, and near 0 m/s in the core of the jet. Together with equipment uncertainties, it is clear the PIV measurements presented have minimal velocity uncertainty.

Appendix C

Detailed Facility Specification (CAD Drawings)

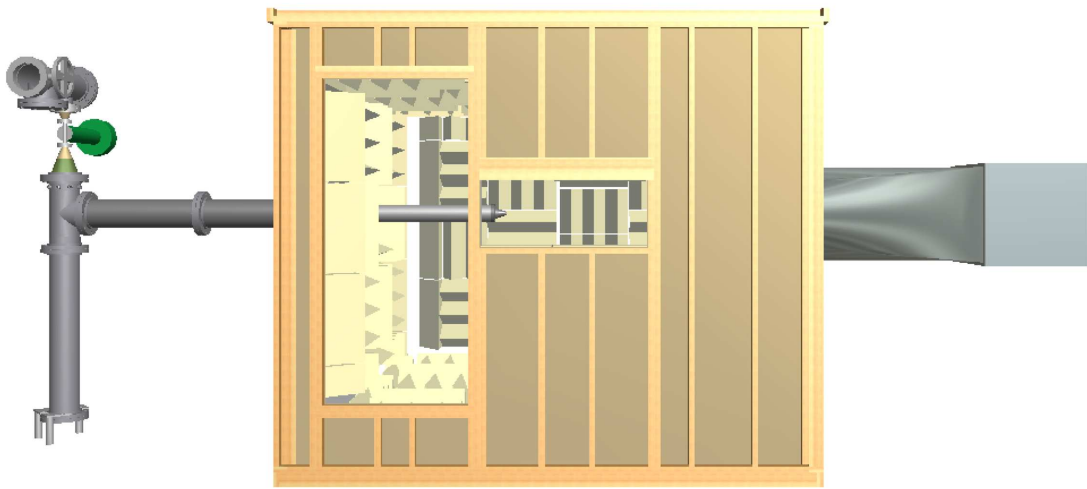


Figure C.1: Aero Lab A overview

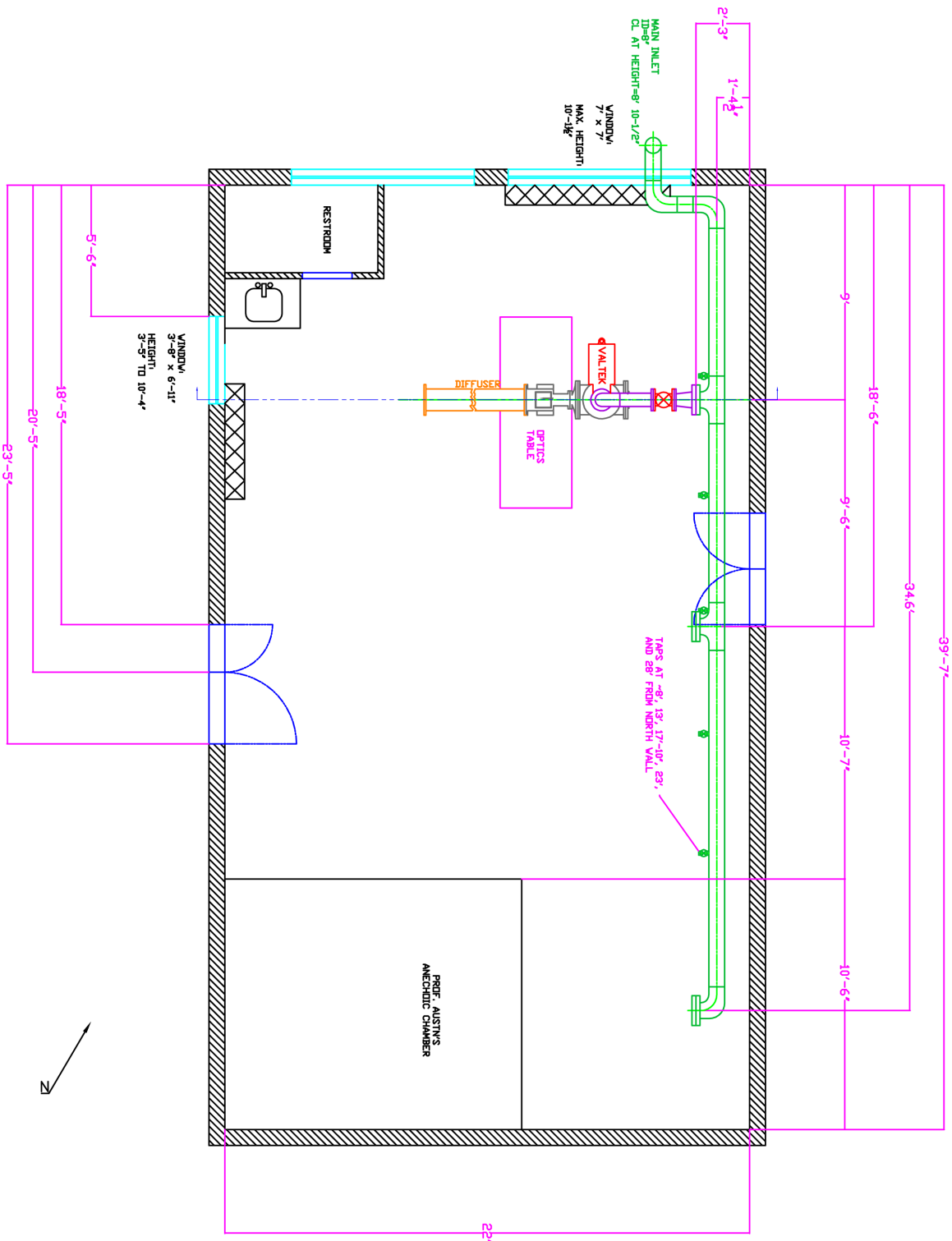


Figure C.2: Aero Lab A general floor plan

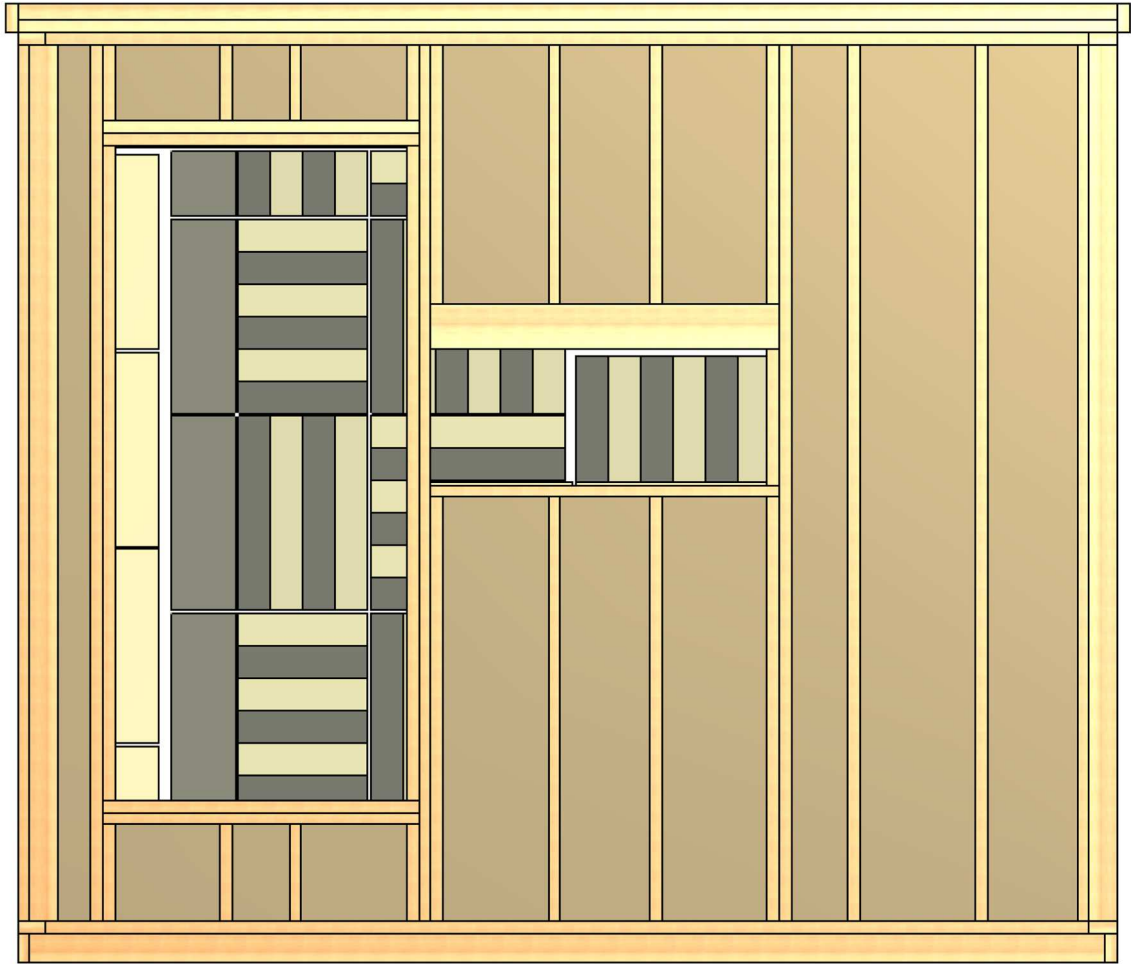


Figure C.3: North wall outside structure. This wall contains the door to the facility as well as the large optical access window.

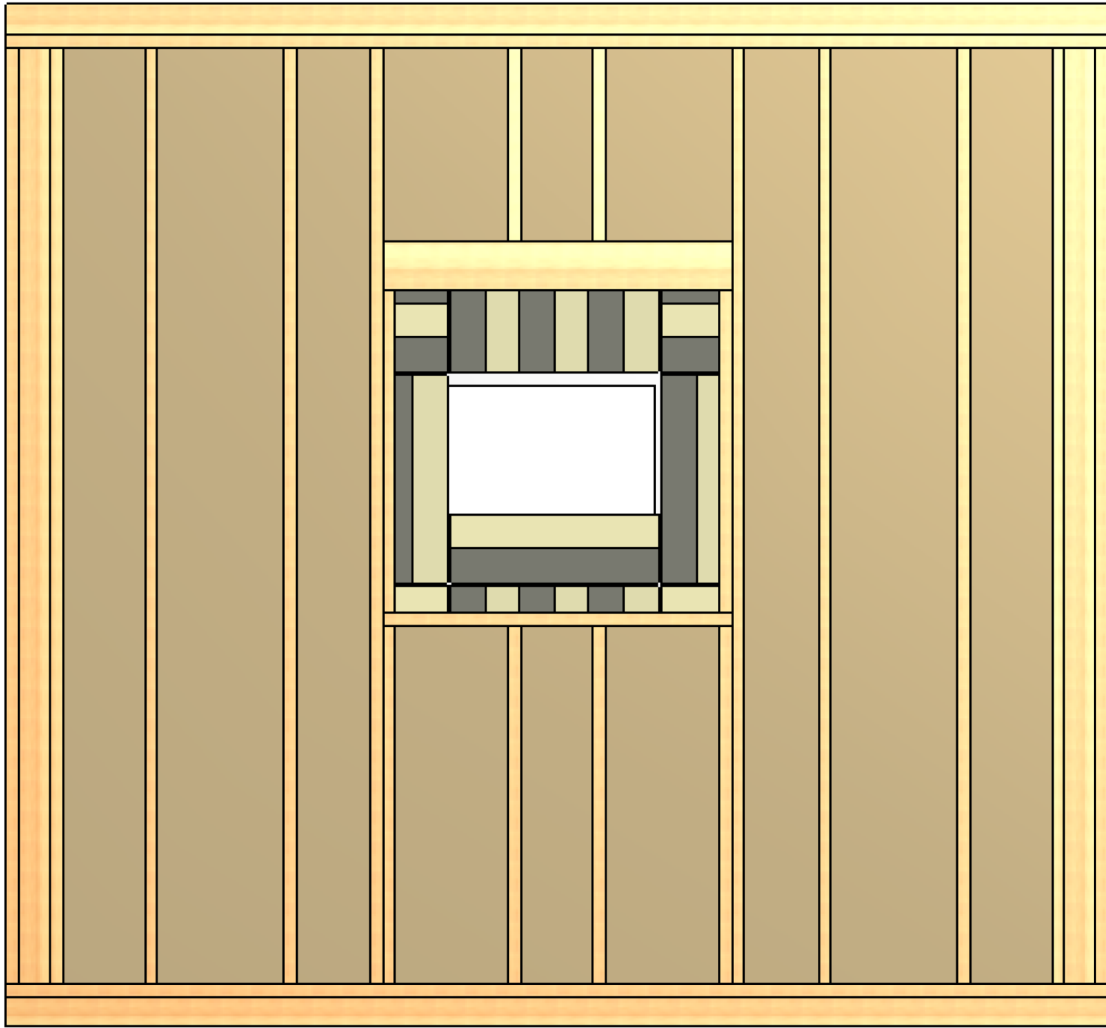


Figure C.4: West wall outside structure. This wall contains the exhaust.

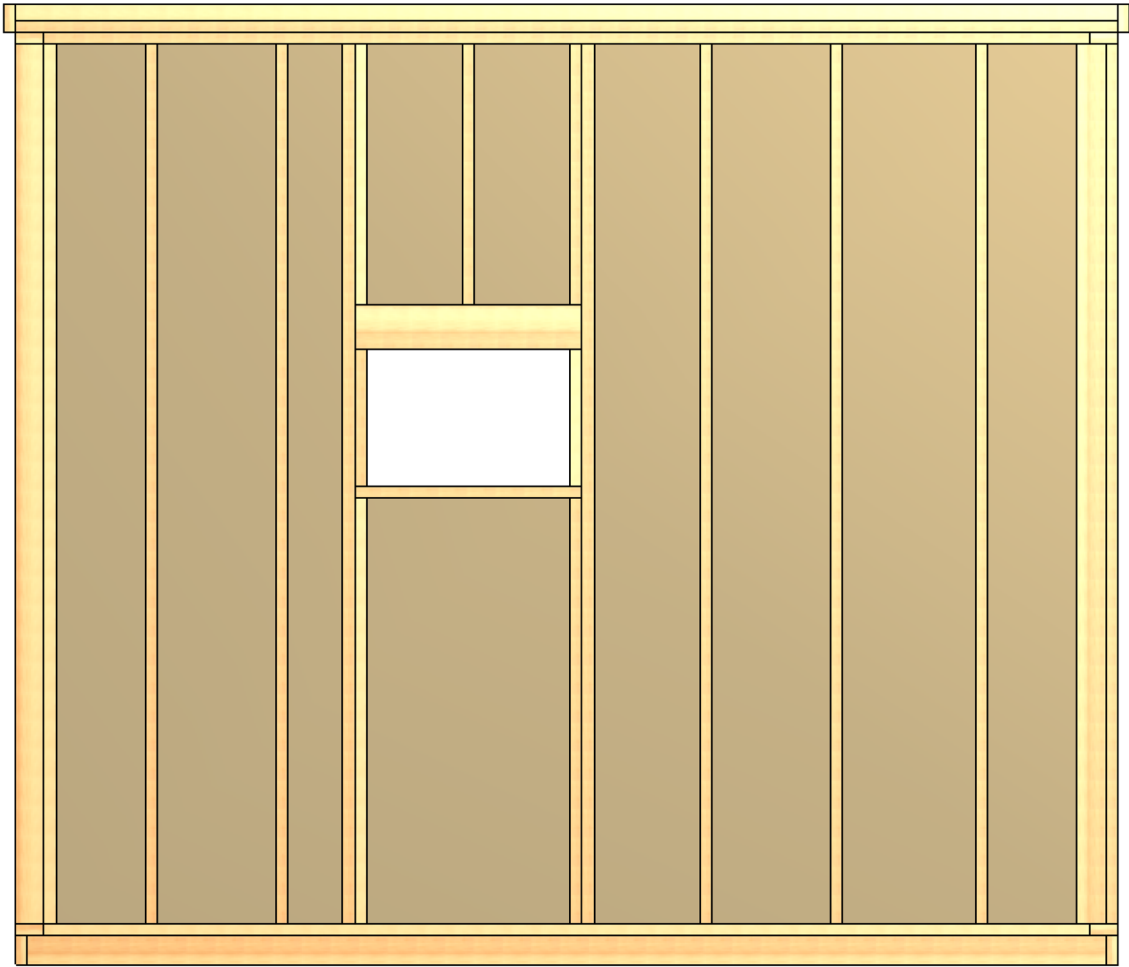


Figure C.5: South wall outside structure.

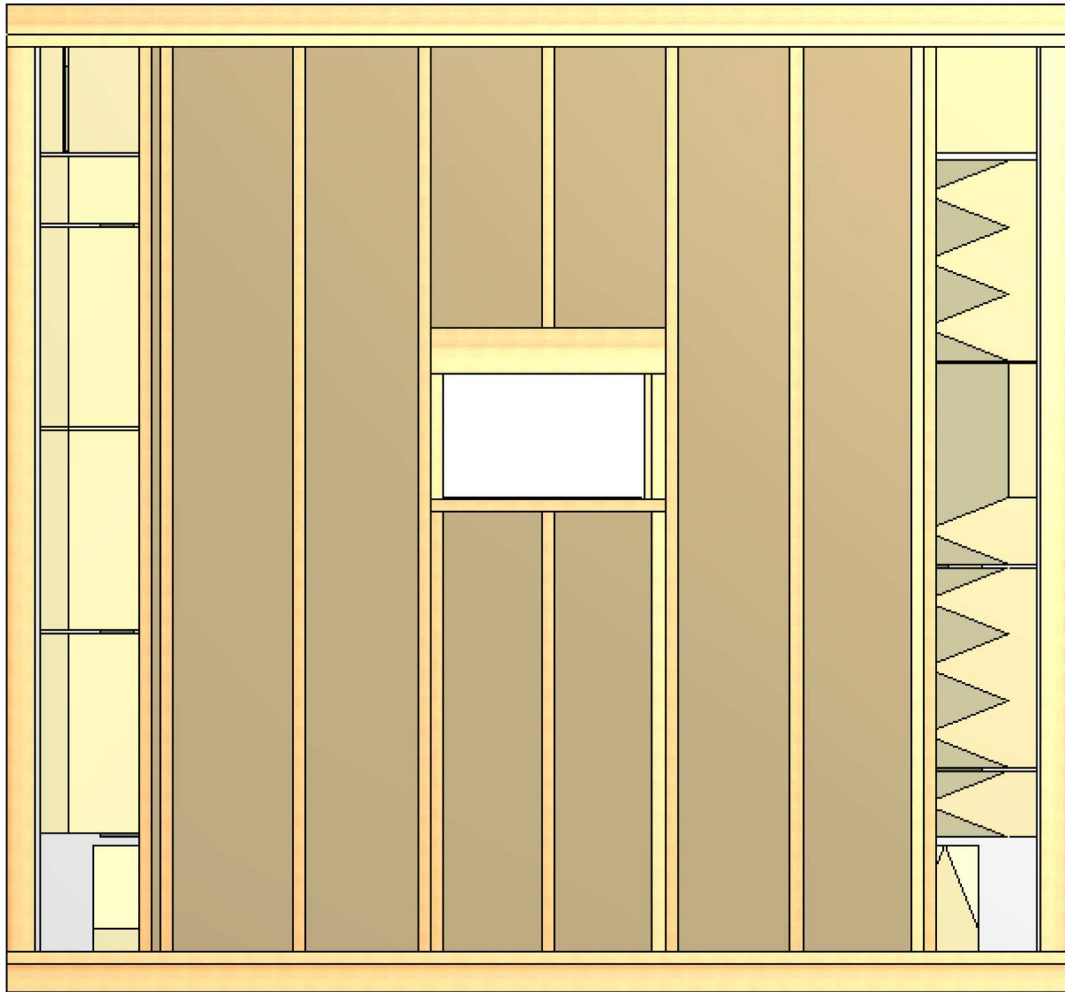


Figure C.6: East wall outside structure. This wall houses the opening for the jet to enter the facility.

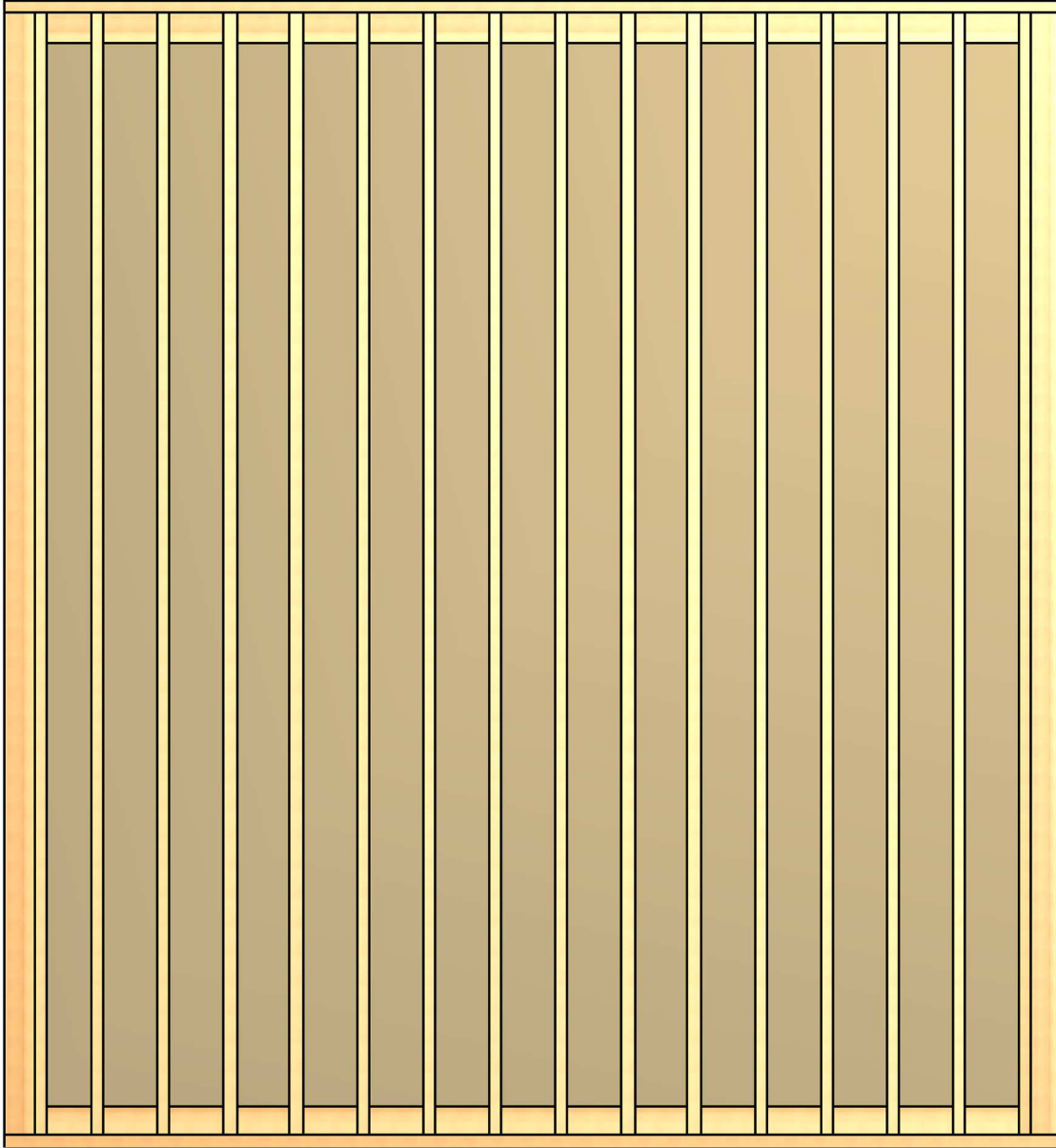


Figure C.7: Roof - outside structure. The 8 in support spacing allows for more load in the facility.

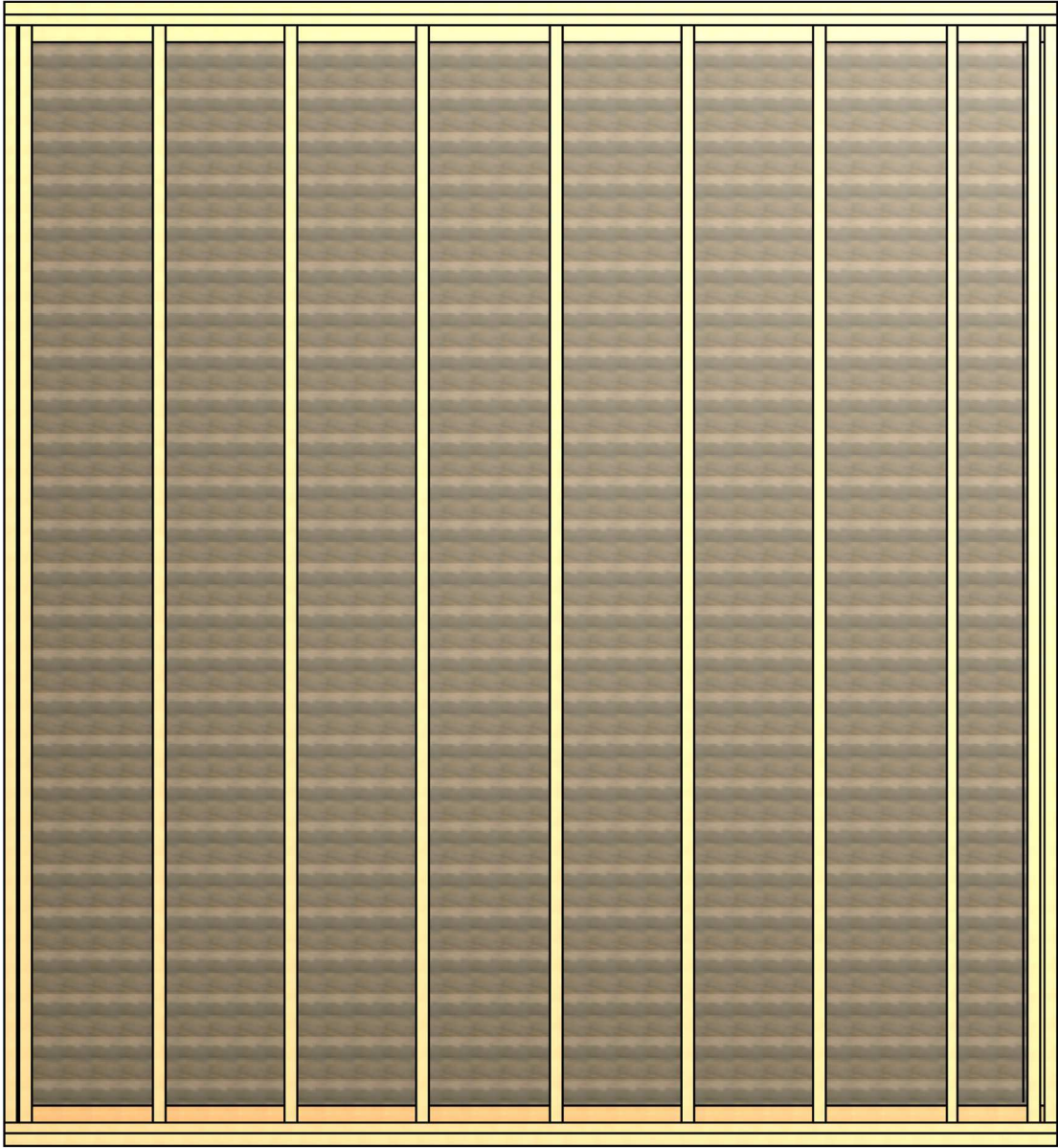


Figure C.8: Floor outside structure.

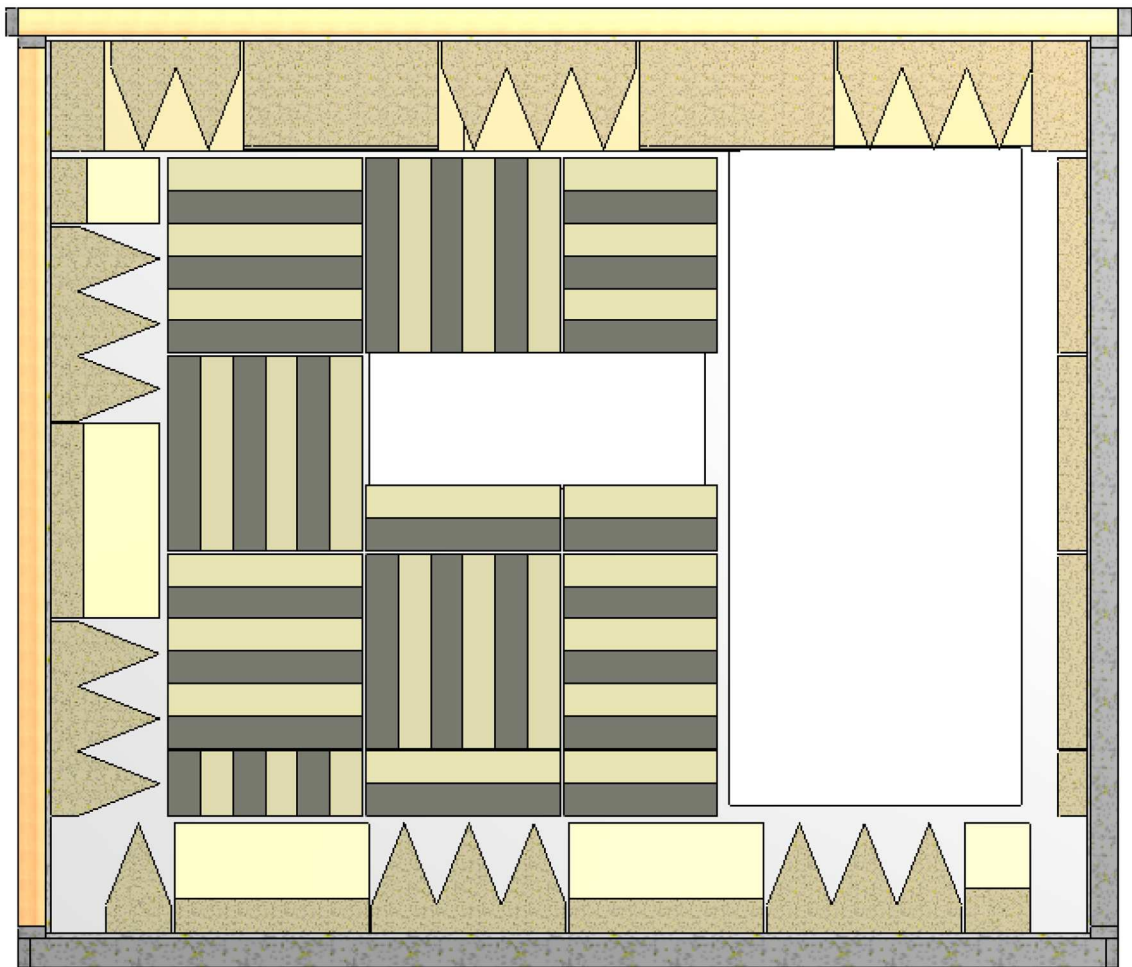


Figure C.9: North wall interior wedge layout.

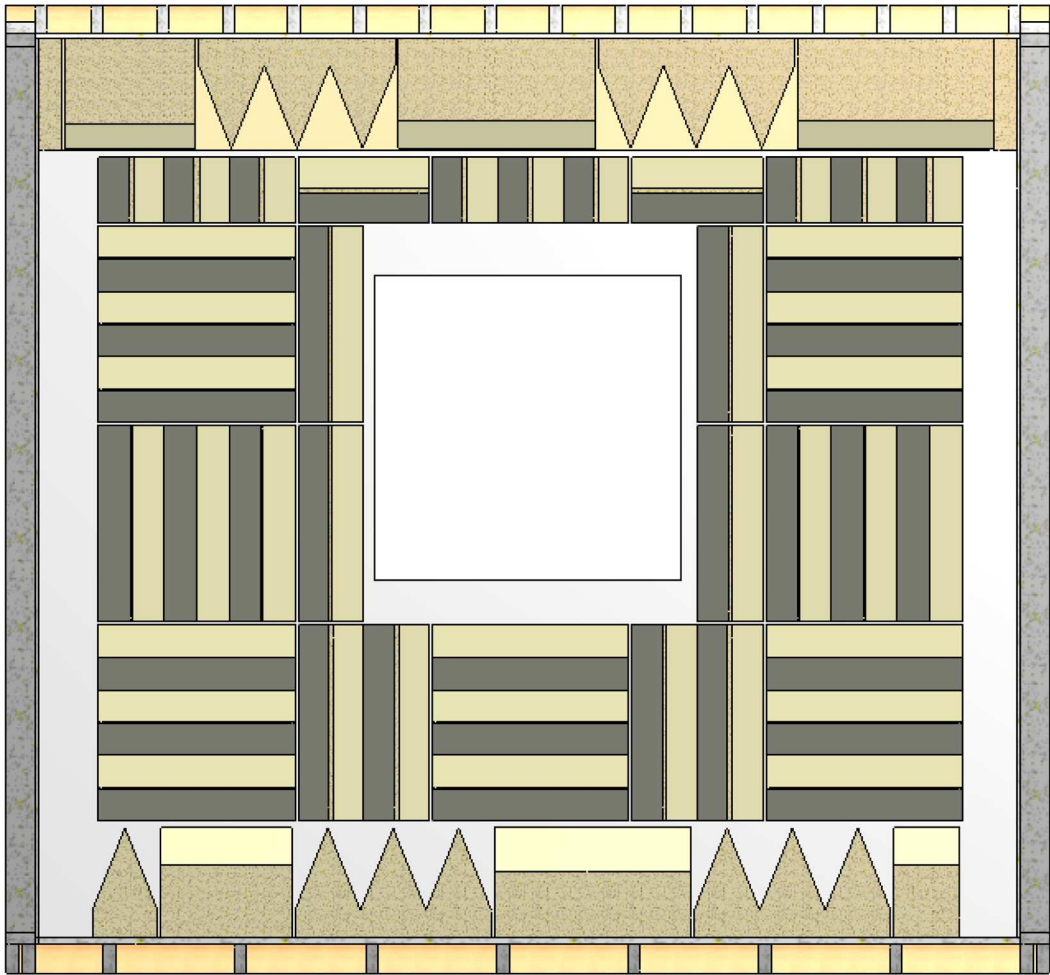


Figure C.10: West wall interior wedge layout.

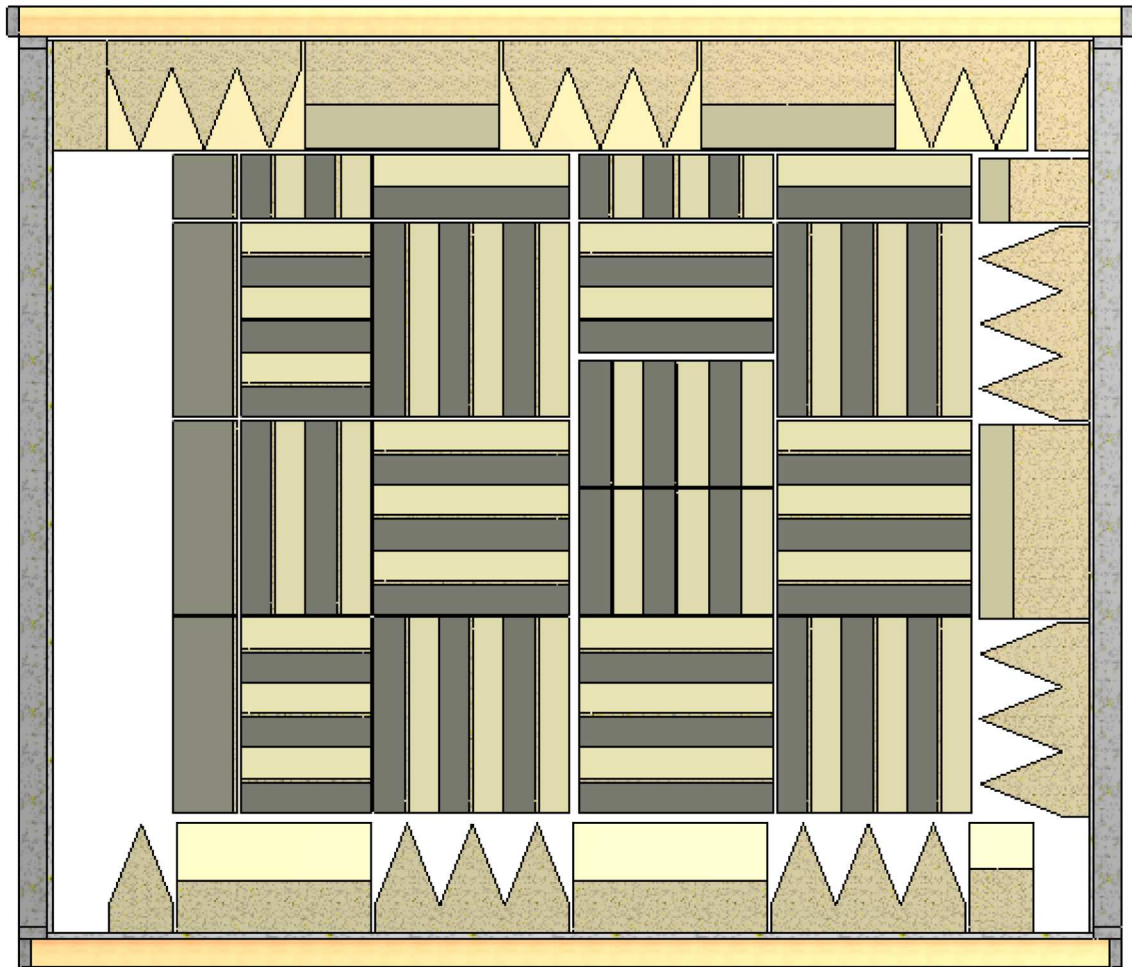


Figure C.11: South wall interior wedge layout.

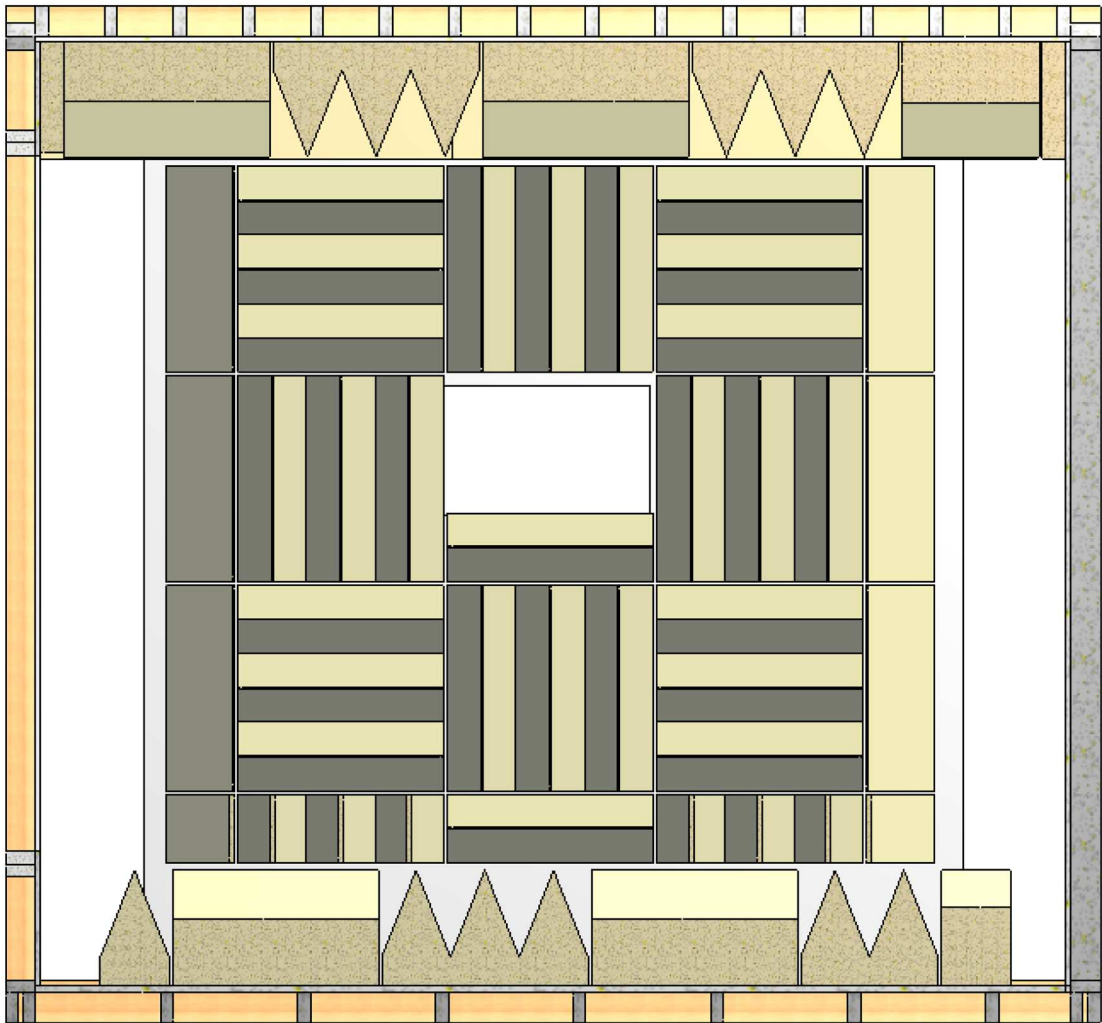


Figure C.12: East wall interior wedge layout.

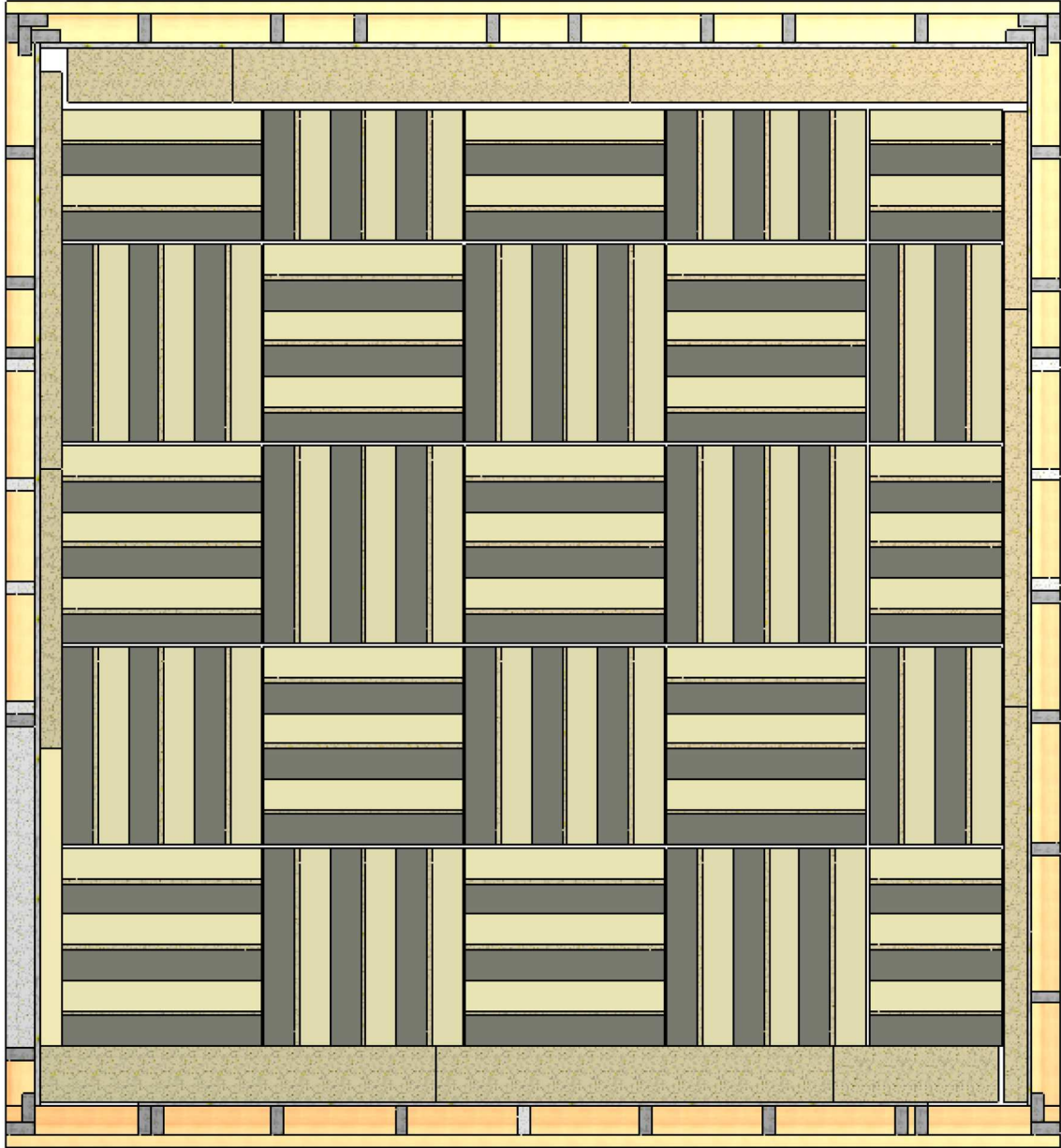


Figure C.13: Roof interior wedge layout.

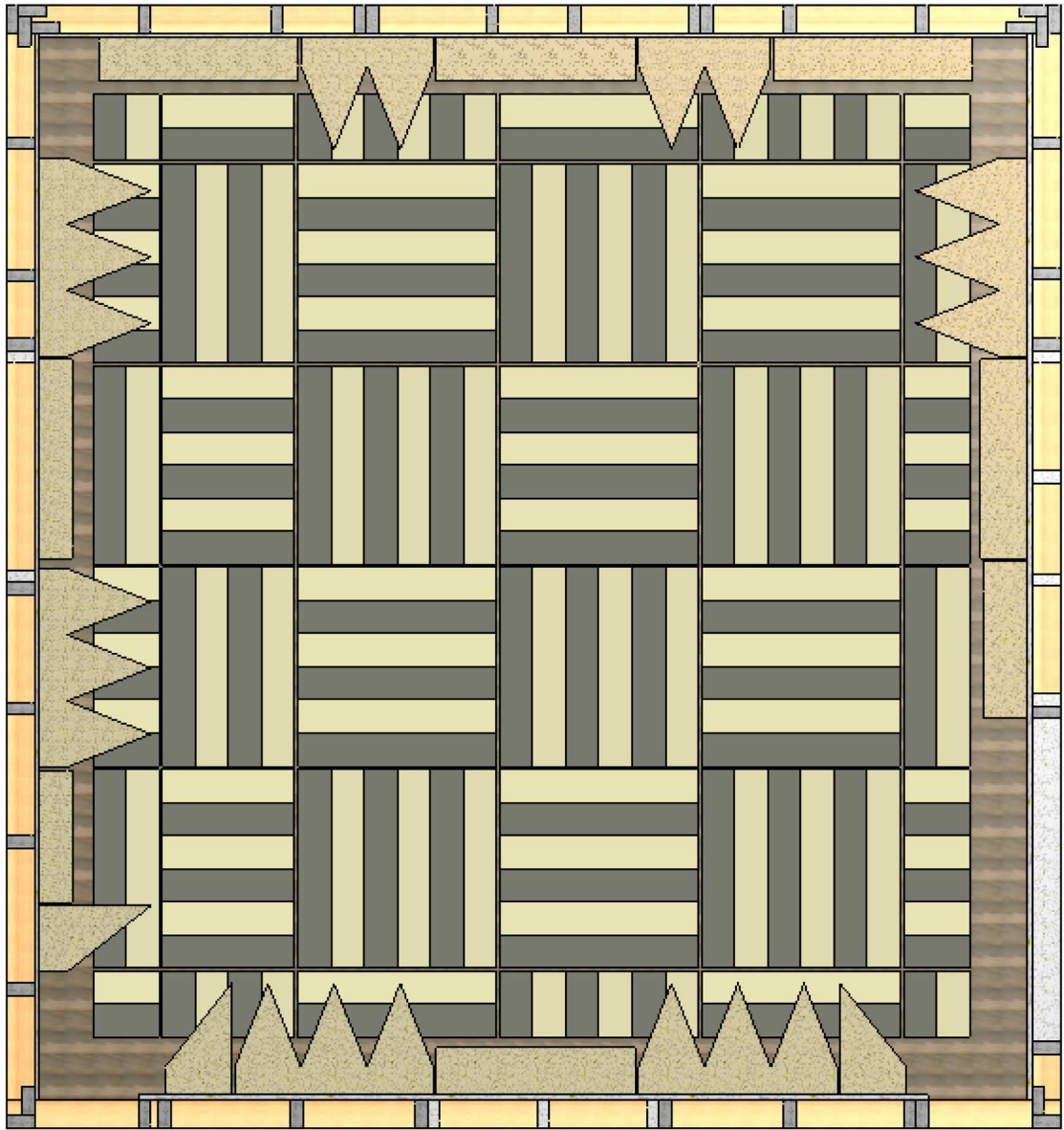


Figure C.14: Floor interior wedge layout.

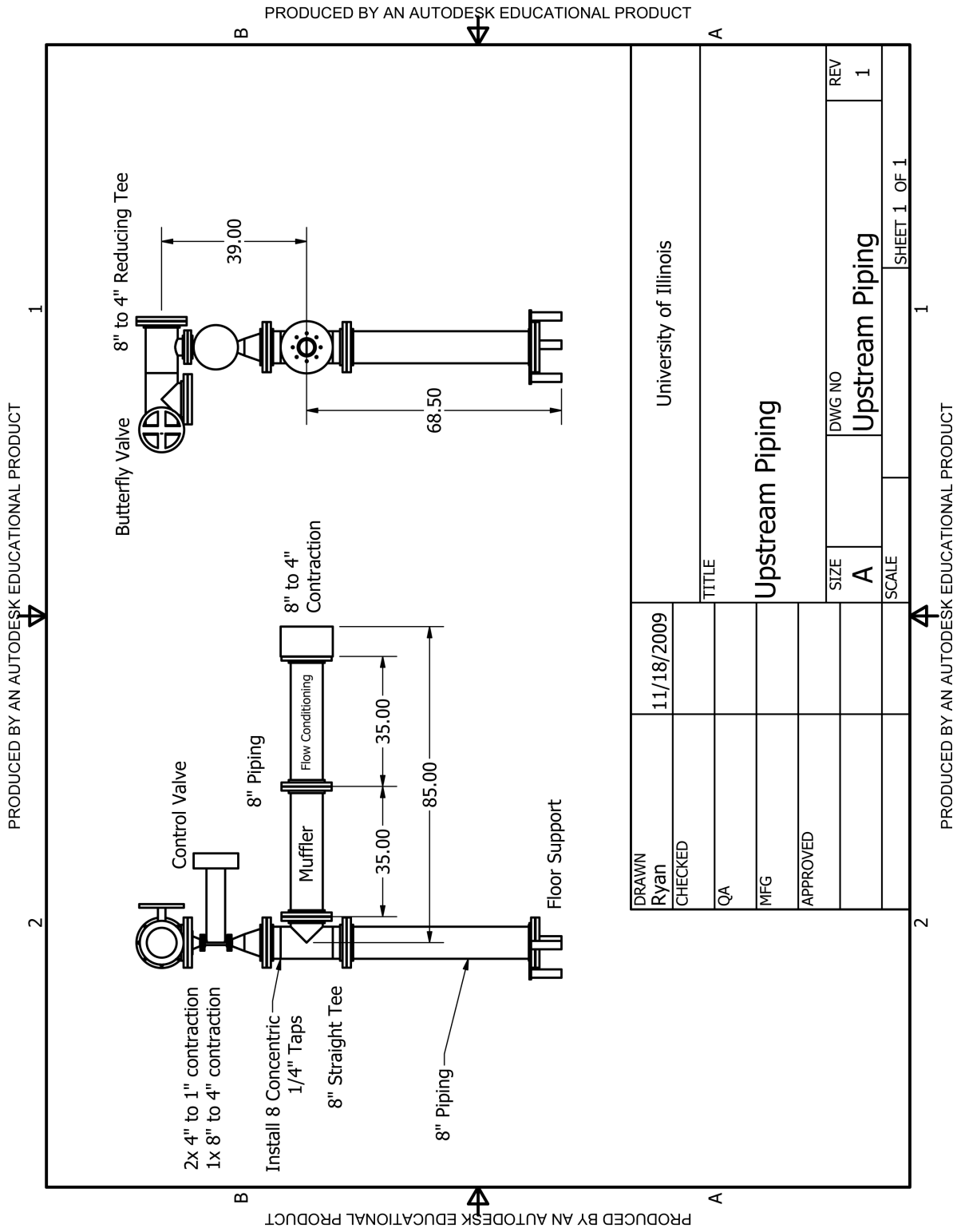


Figure C.15: Overview of the piping before entering the chamber

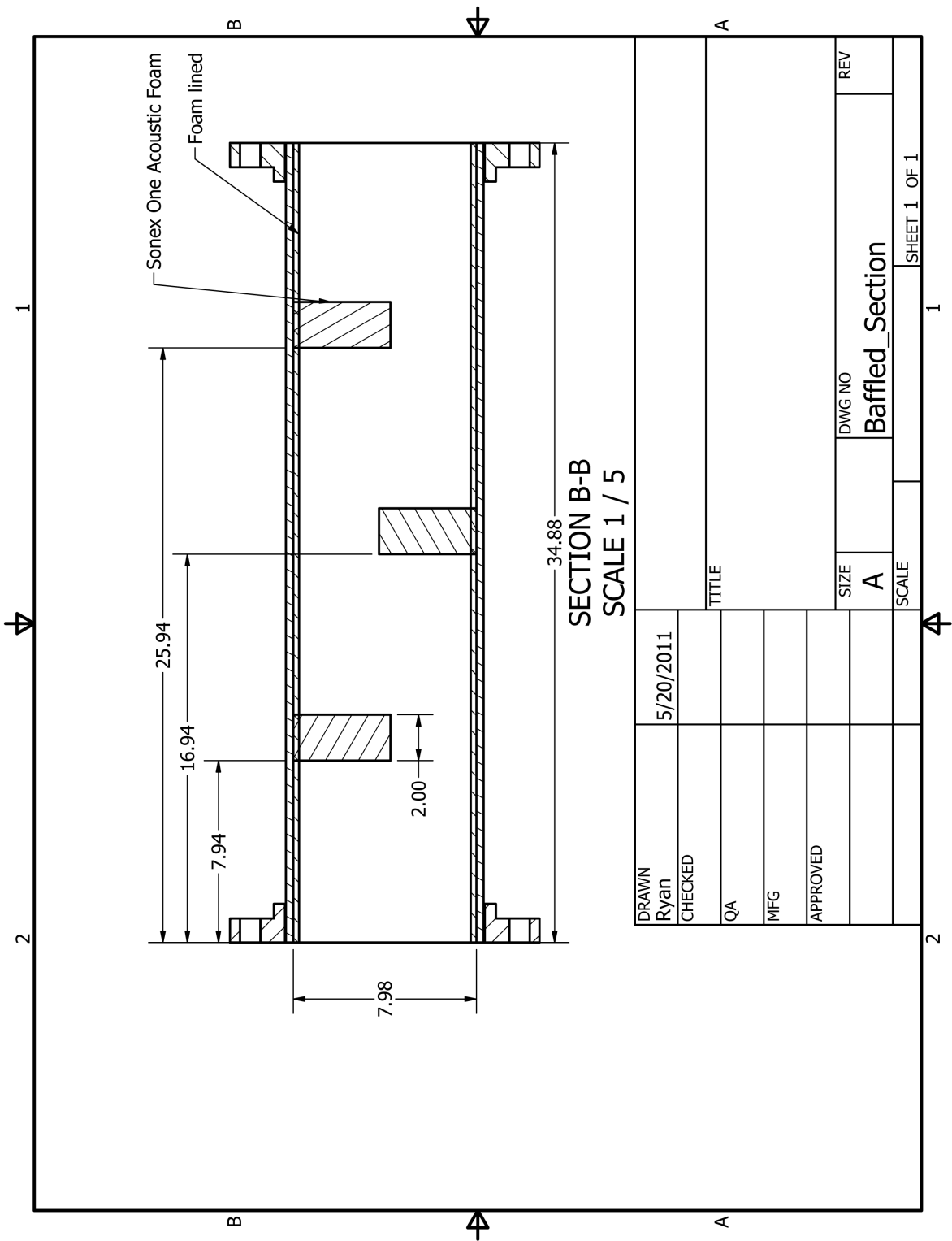


Figure C.16: Baffled section of the upstream piping

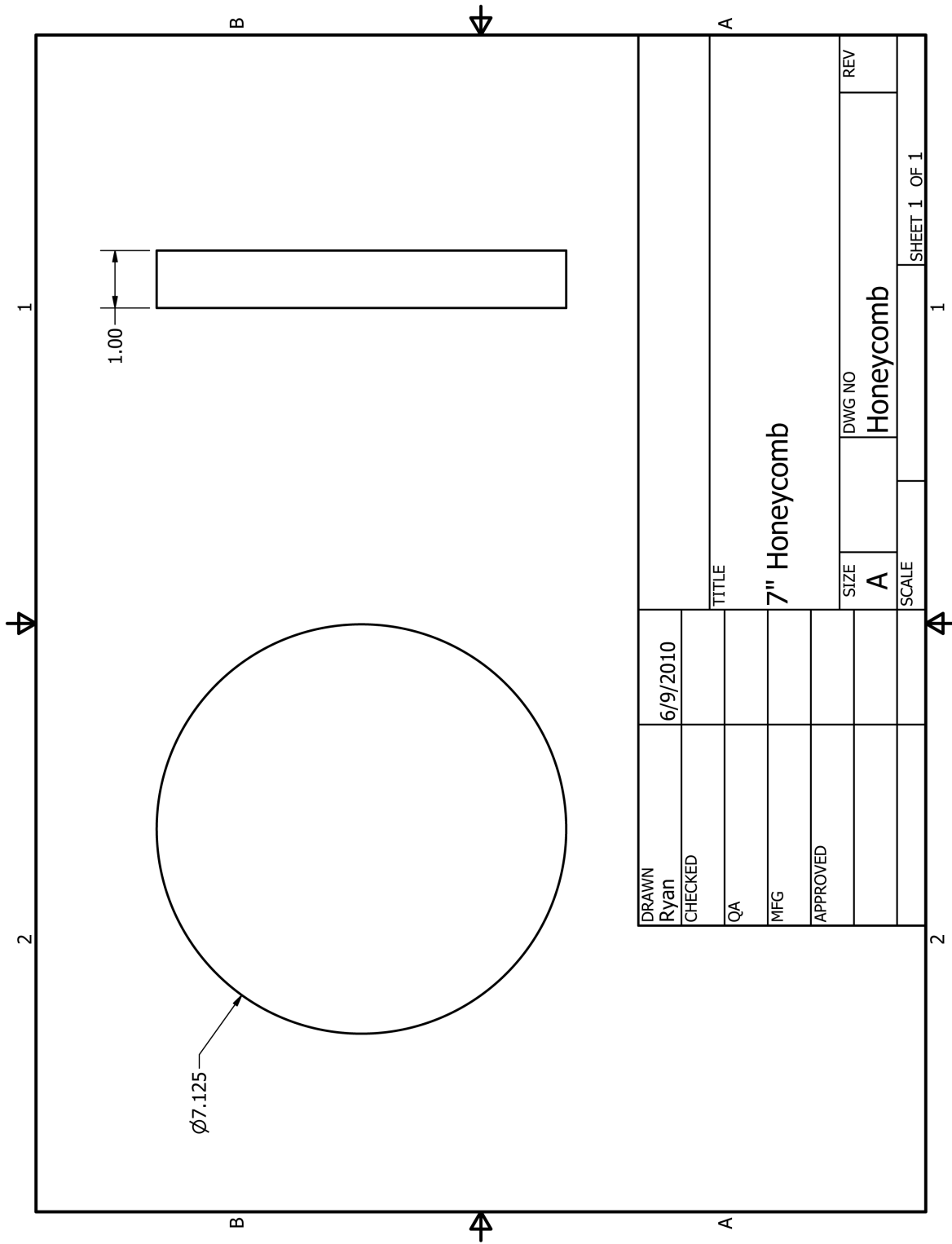


Figure C.17: Honeycomb dimensions

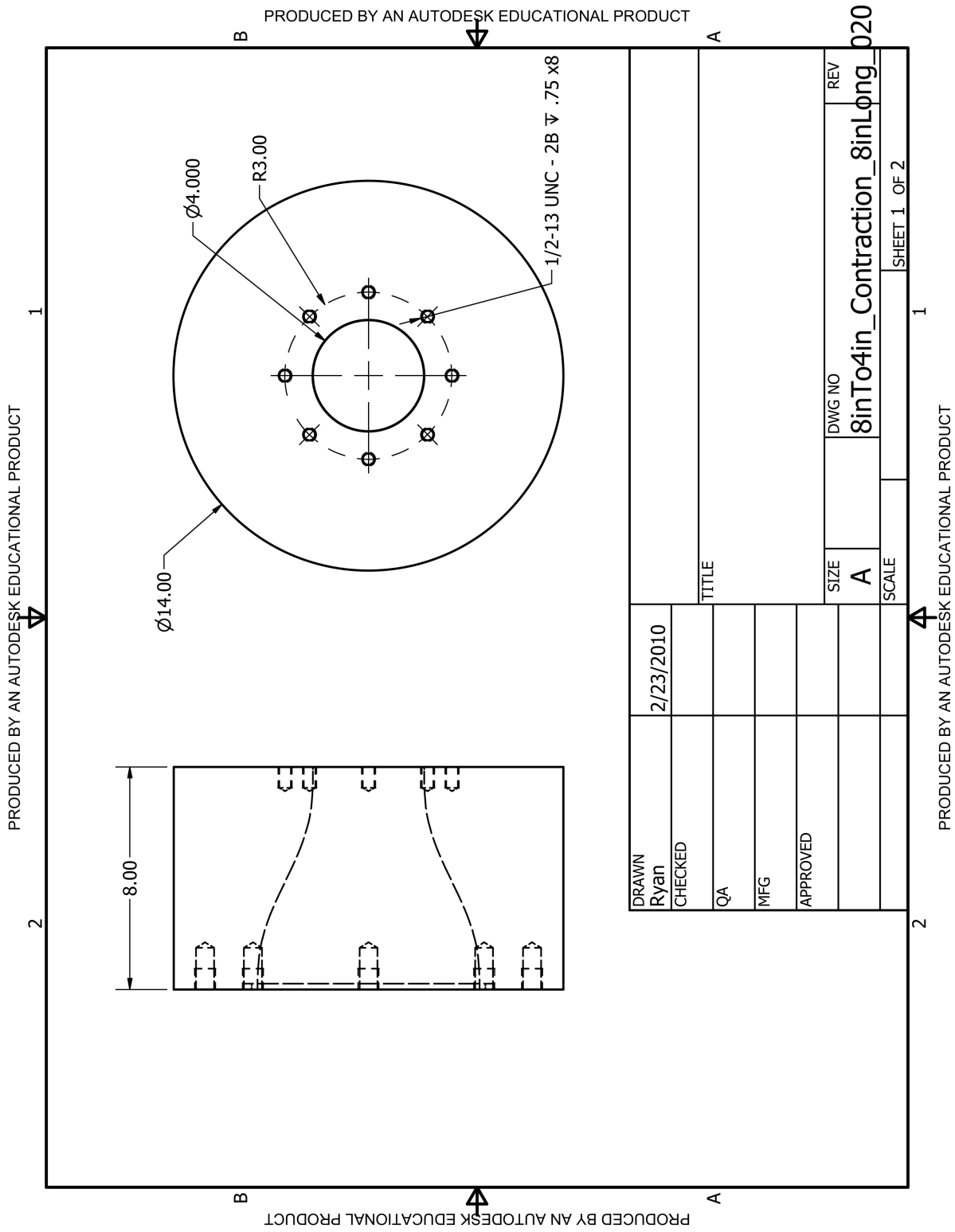


Figure C.18: 8 inch to 4 inch aluminum contraction

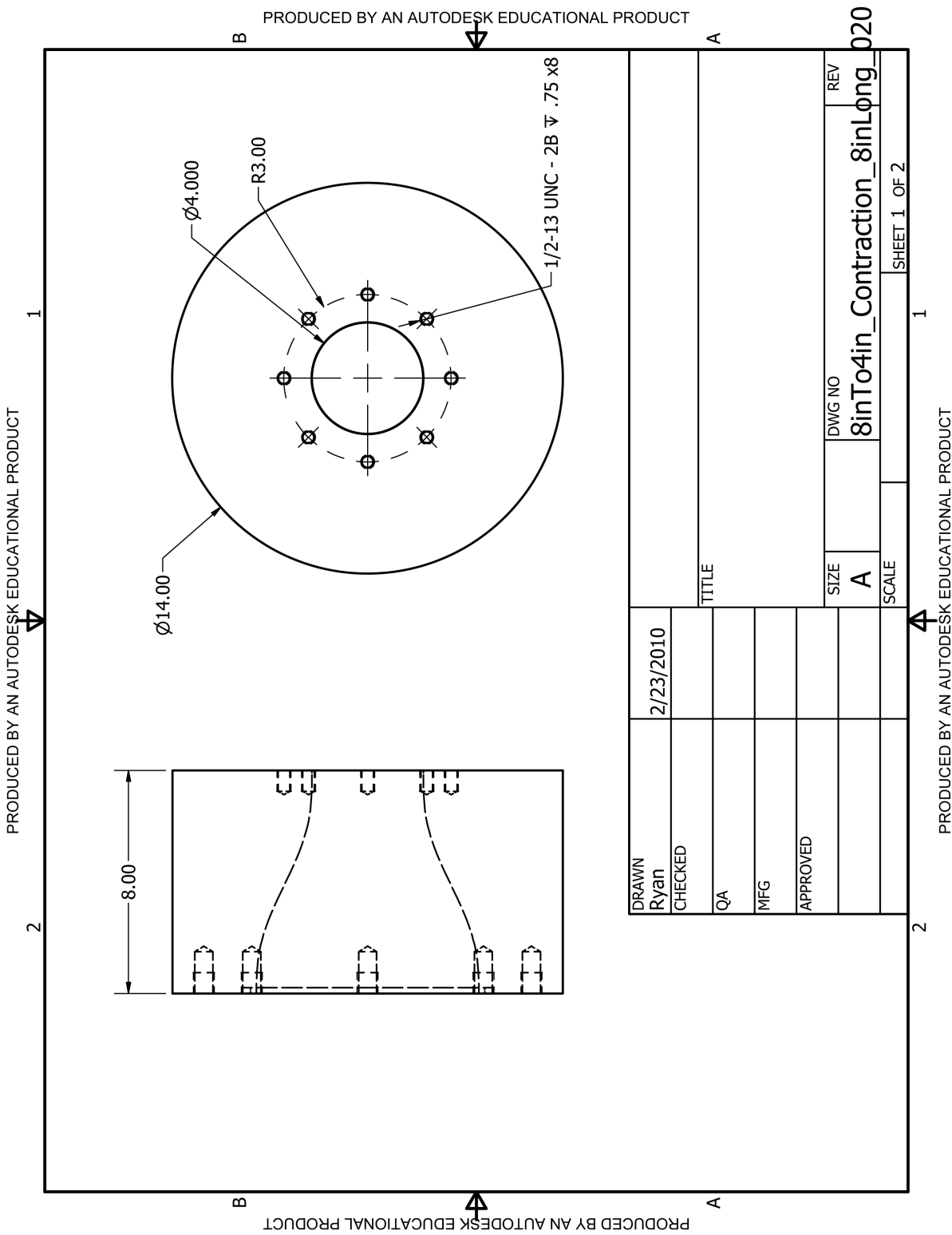


Figure C.19: 8 inch to 4 inch aluminum contraction

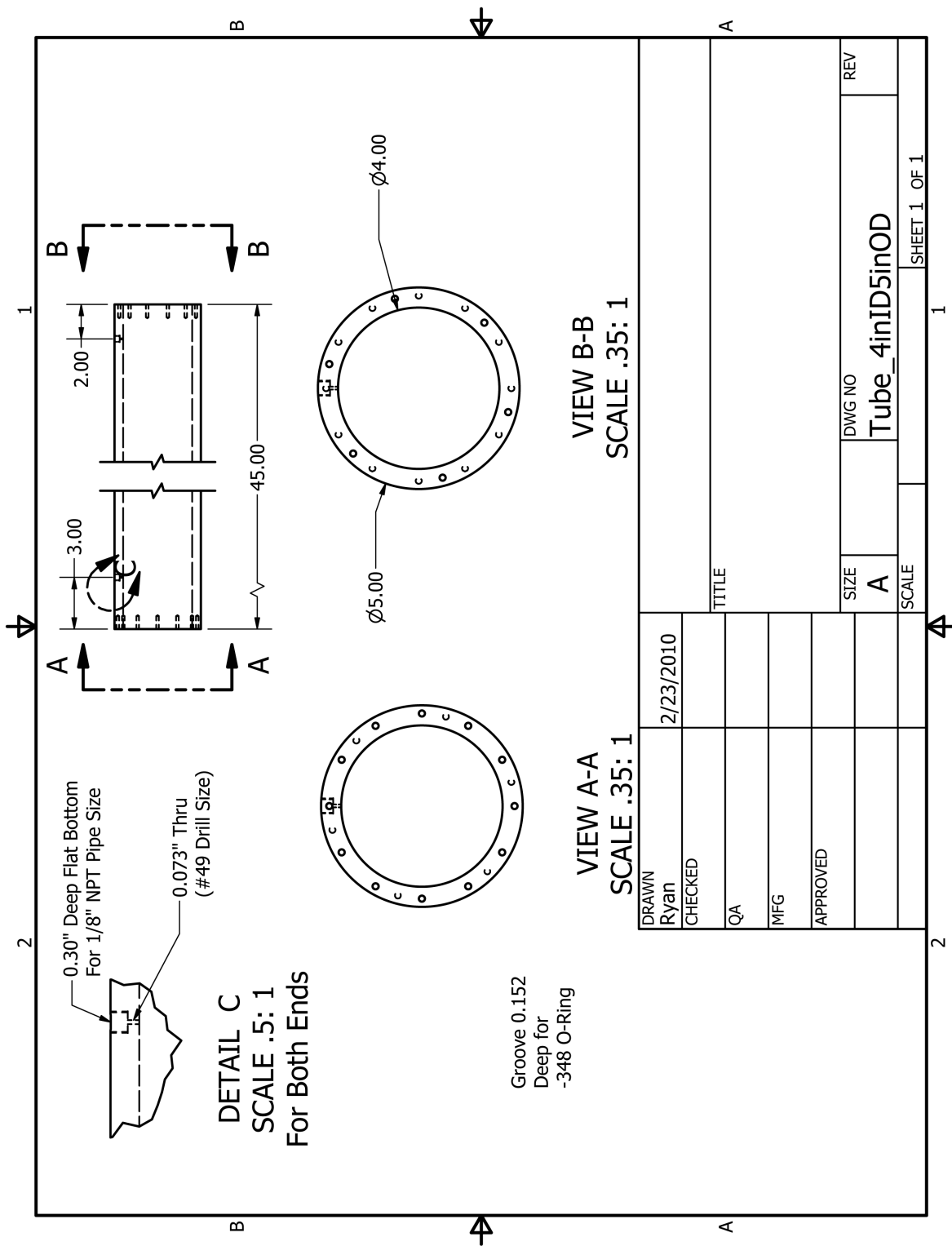


Figure C.20: In chamber piping for the short copper nozzle

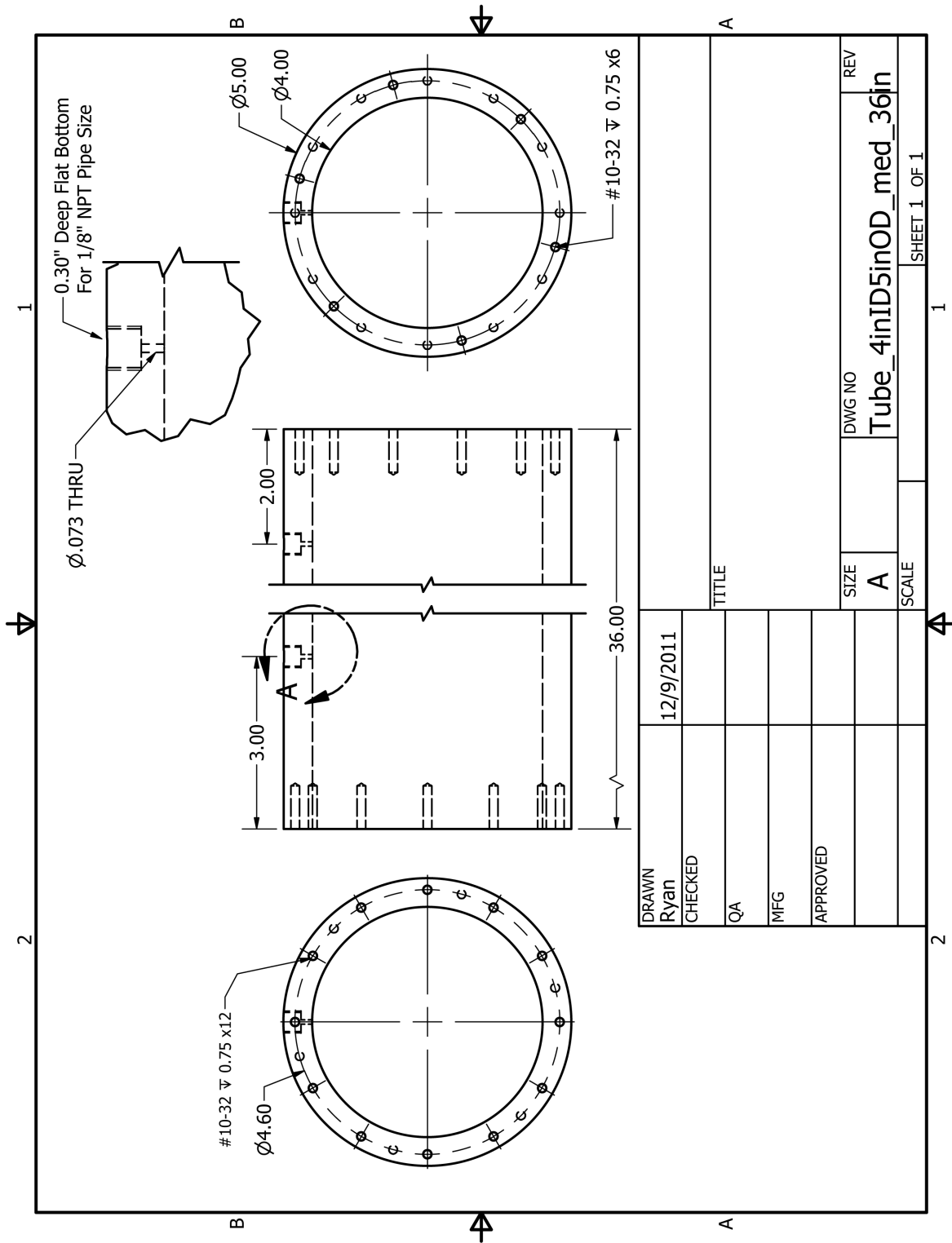


Figure C.21: In chamber piping for the medium copper nozzle

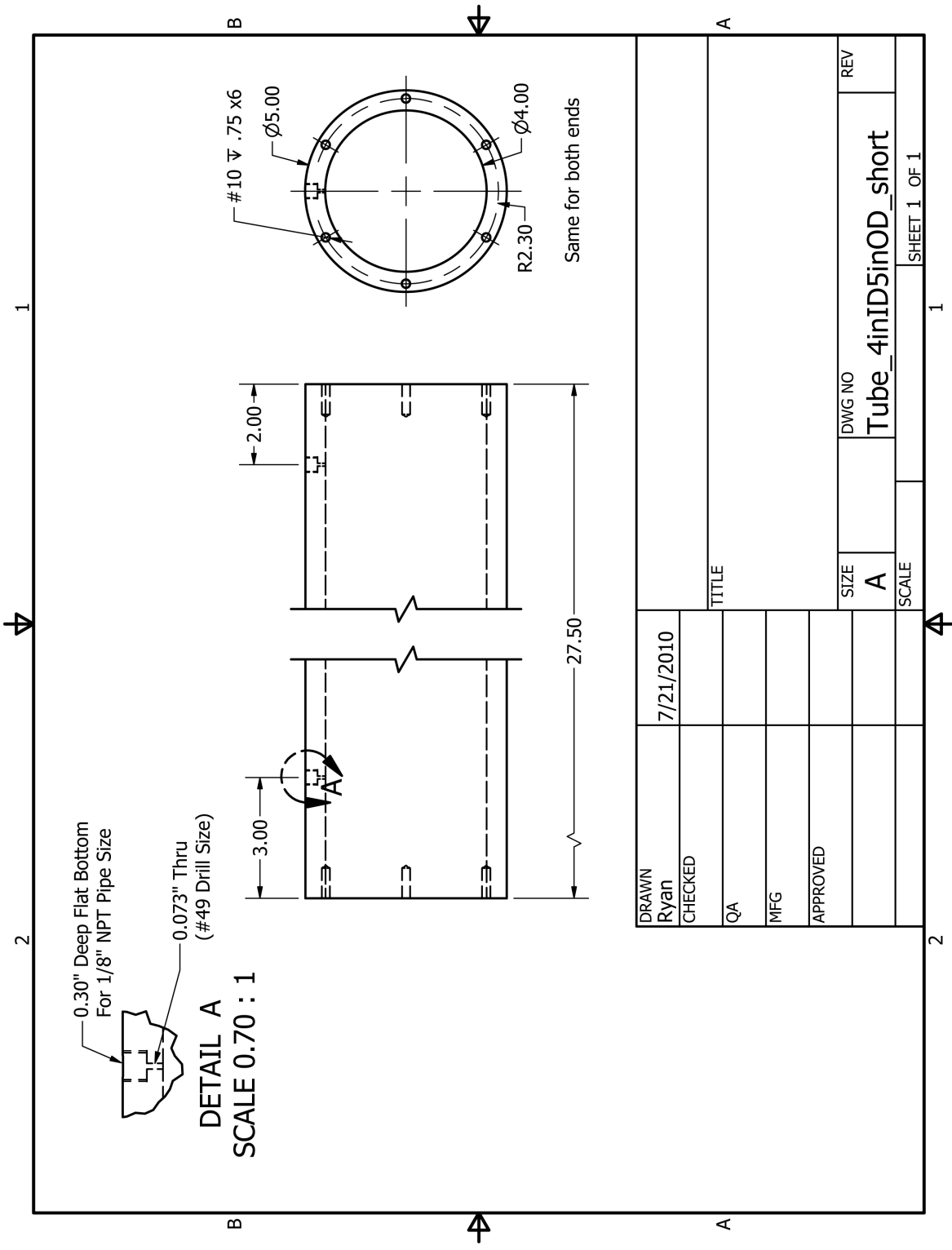


Figure C.22: In chamber piping for the long copper nozzle

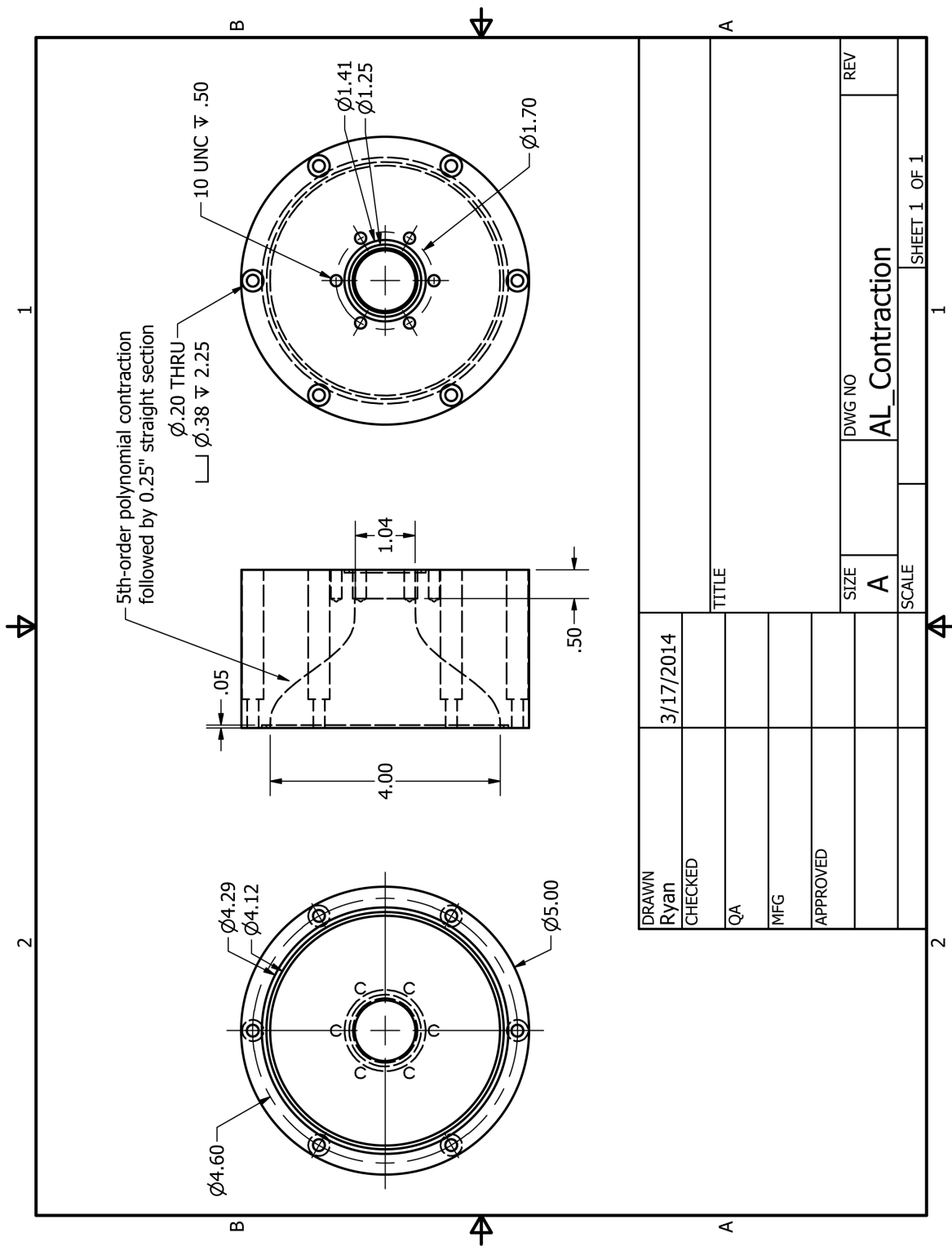


Figure C.23: Contraction from 4 inches to 1 inch used for many nozzles in the facility

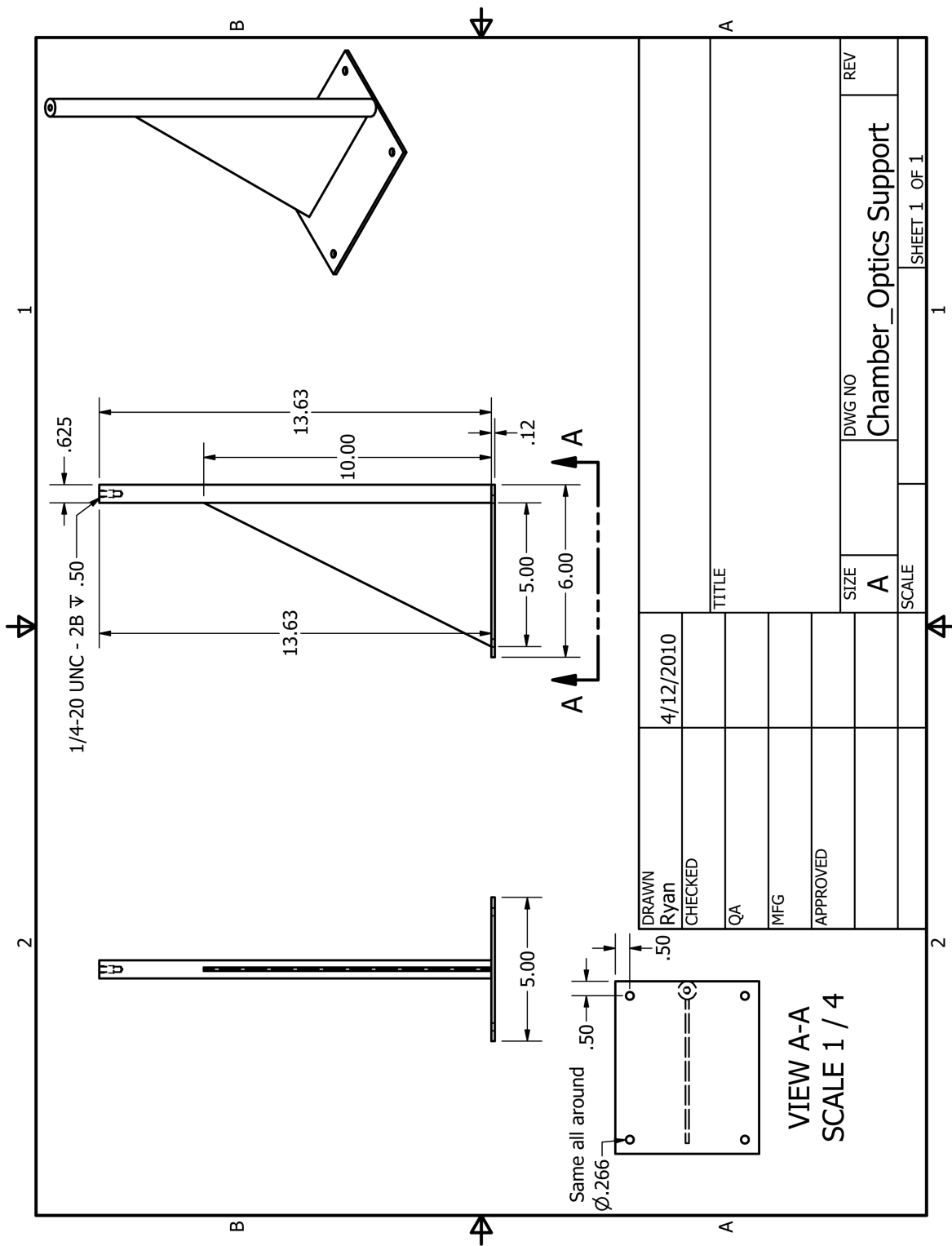


Figure C.24: Support to fit between floor wedges

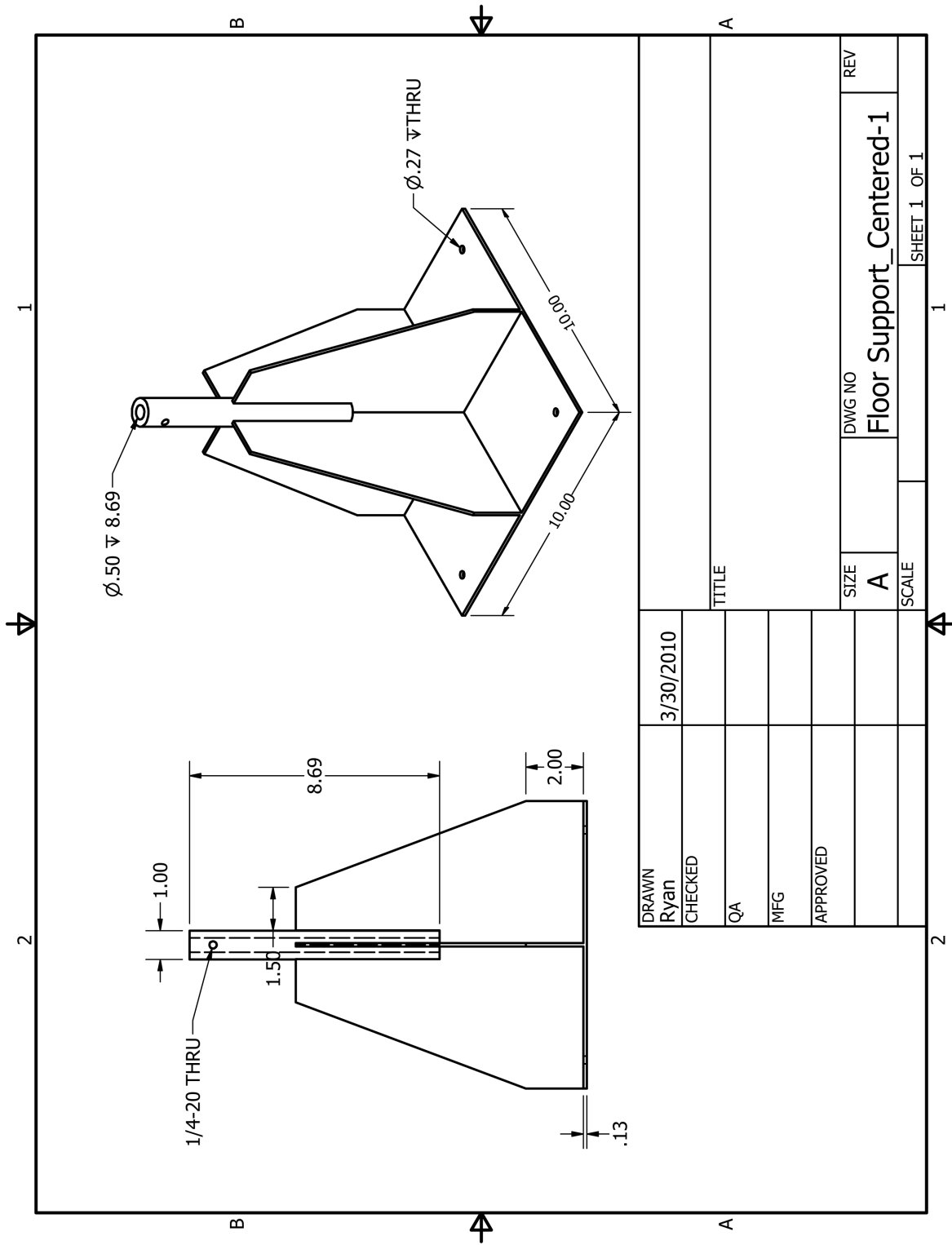


Figure C.25: Support to fit between floor wedges

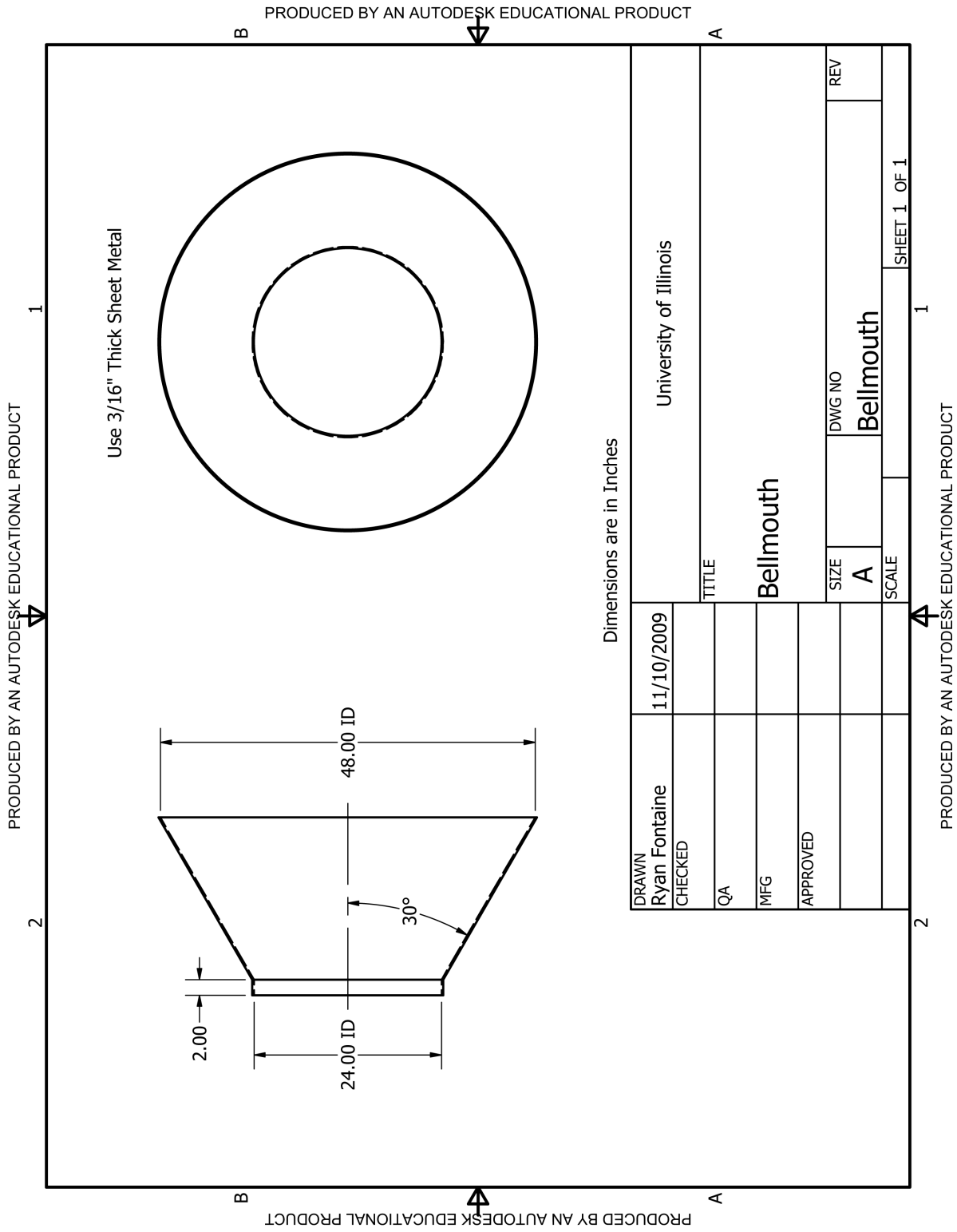


Figure C.26: Exhaust collector

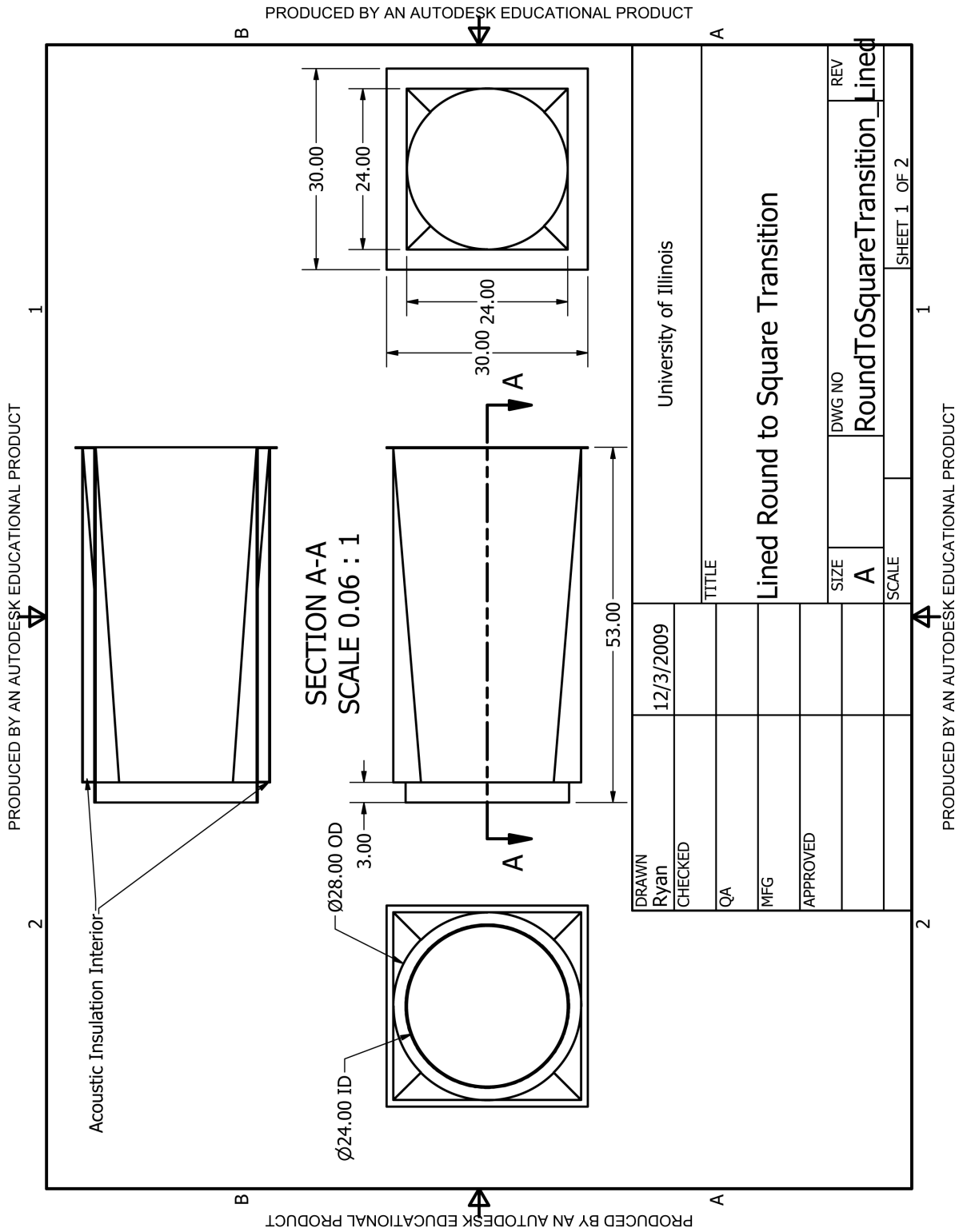


Figure C.27: Smooth, acoustically treated exhaust transition from round to square cross section

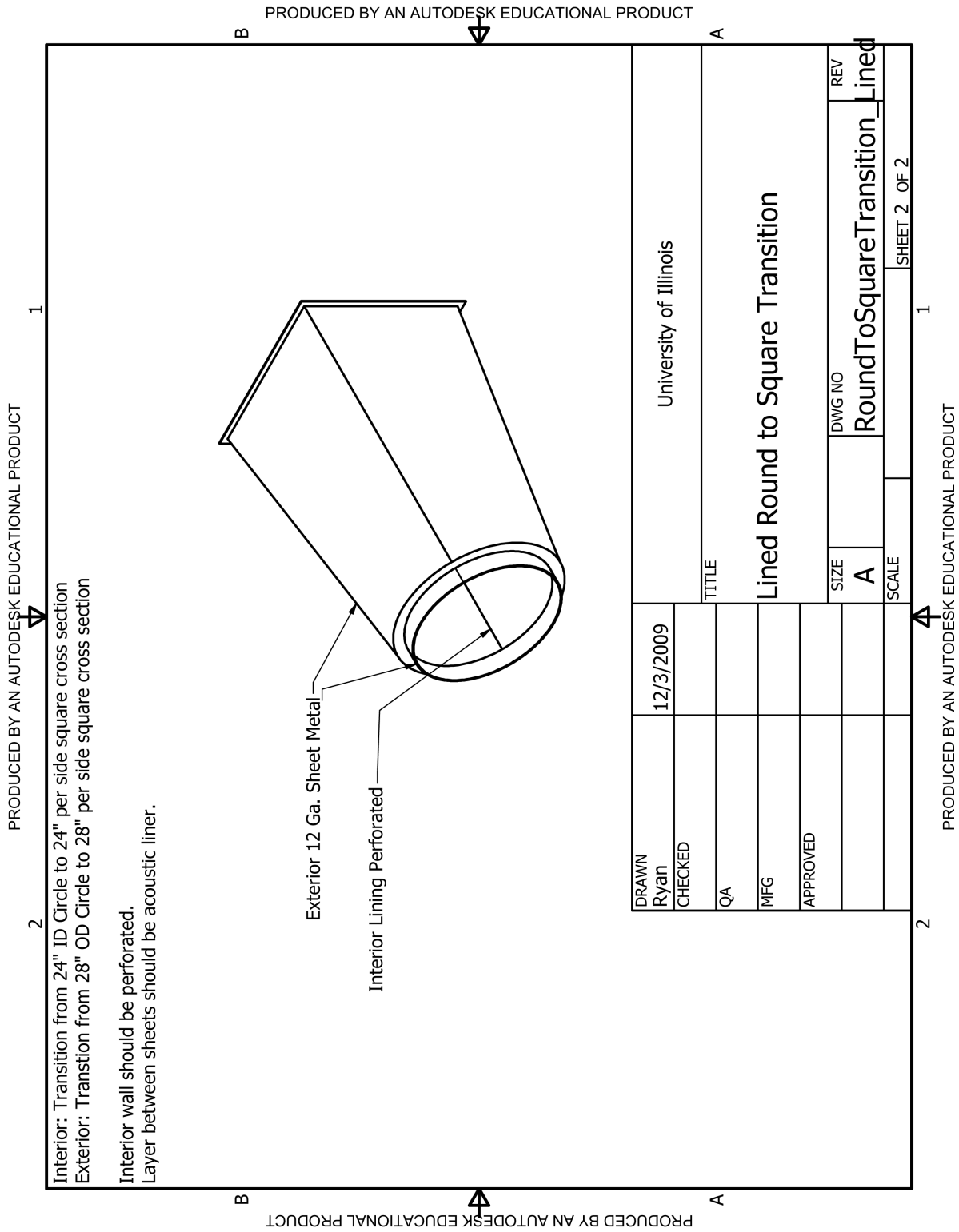


Figure C.28: Smooth, acoustically treated exhaust transition from round to square cross section

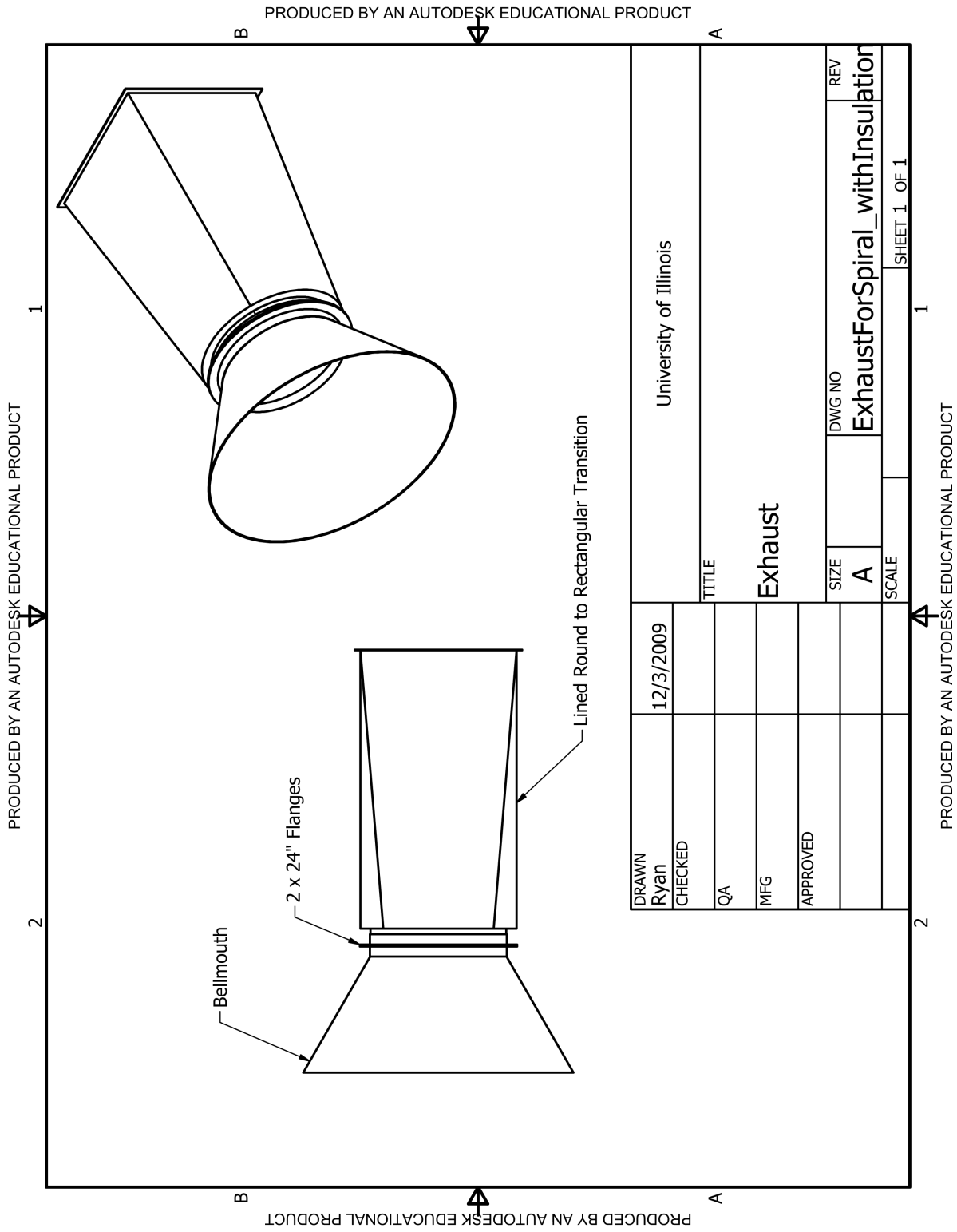
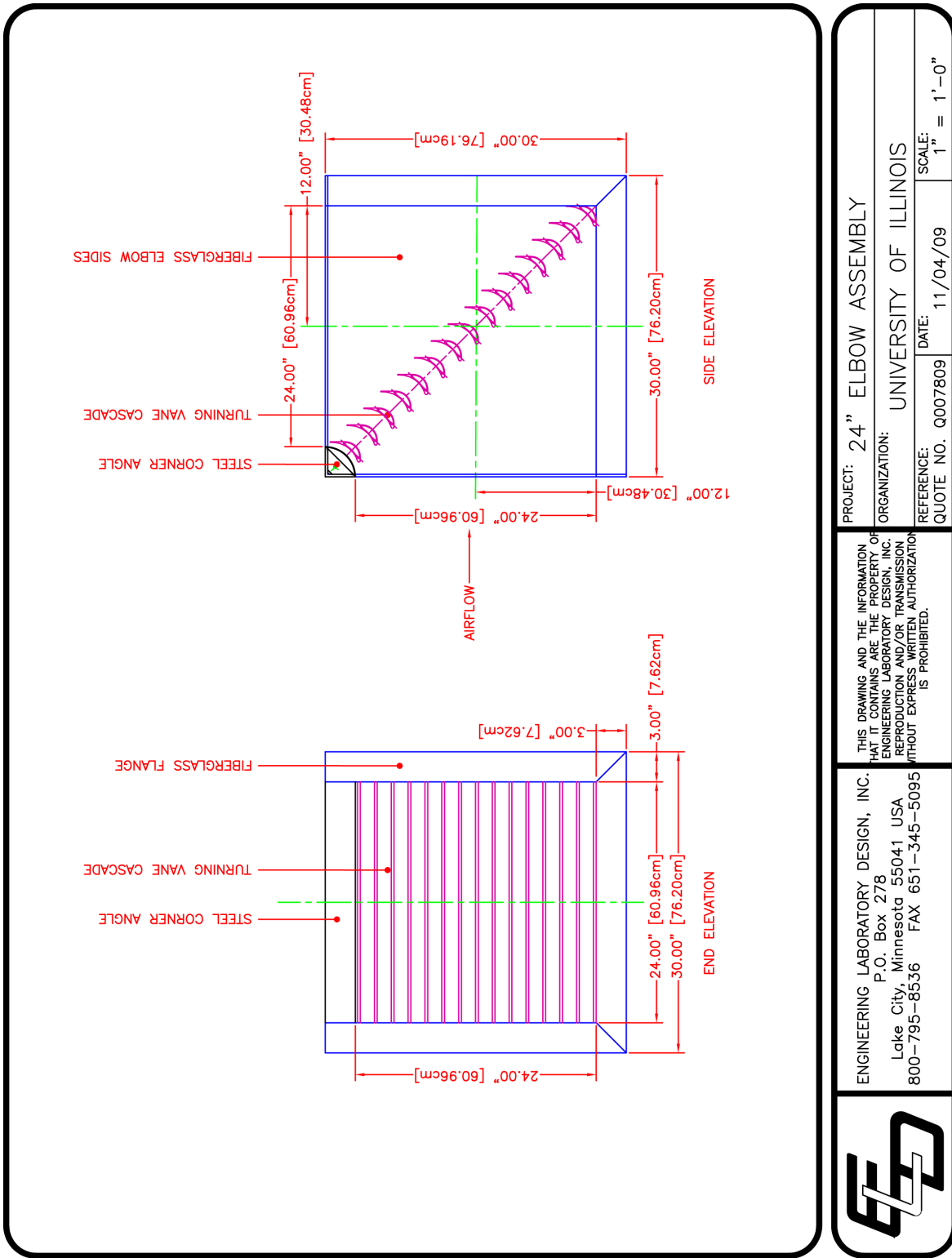


Figure C.29: Exhaust from facility constructed by Spiral Manufacturing




	PROJECT: 24" ELBOW ASSEMBLY ORGANIZATION: UNIVERSITY OF ILLINOIS REFERENCE: QUOTE NO. Q007809 DATE: 11/04/09 SCALE: 1" = 1'-0"
	THIS DRAWING AND THE INFORMATION CONTAINED HEREIN ARE THE PROPERTY OF ENGINEERING LABORATORY DESIGN, INC. REPRODUCTION AND/OR TRANSMISSION WITHOUT EXPRESS WRITTEN AUTHORIZATION IS PROHIBITED.
ENGINEERING LABORATORY DESIGN, INC. P.O. Box 278 Lake City, Minnesota 55041 USA 800-795-8536 FAX 651-345-5095	

Figure C.30: Exhaust vanes designed by ELD

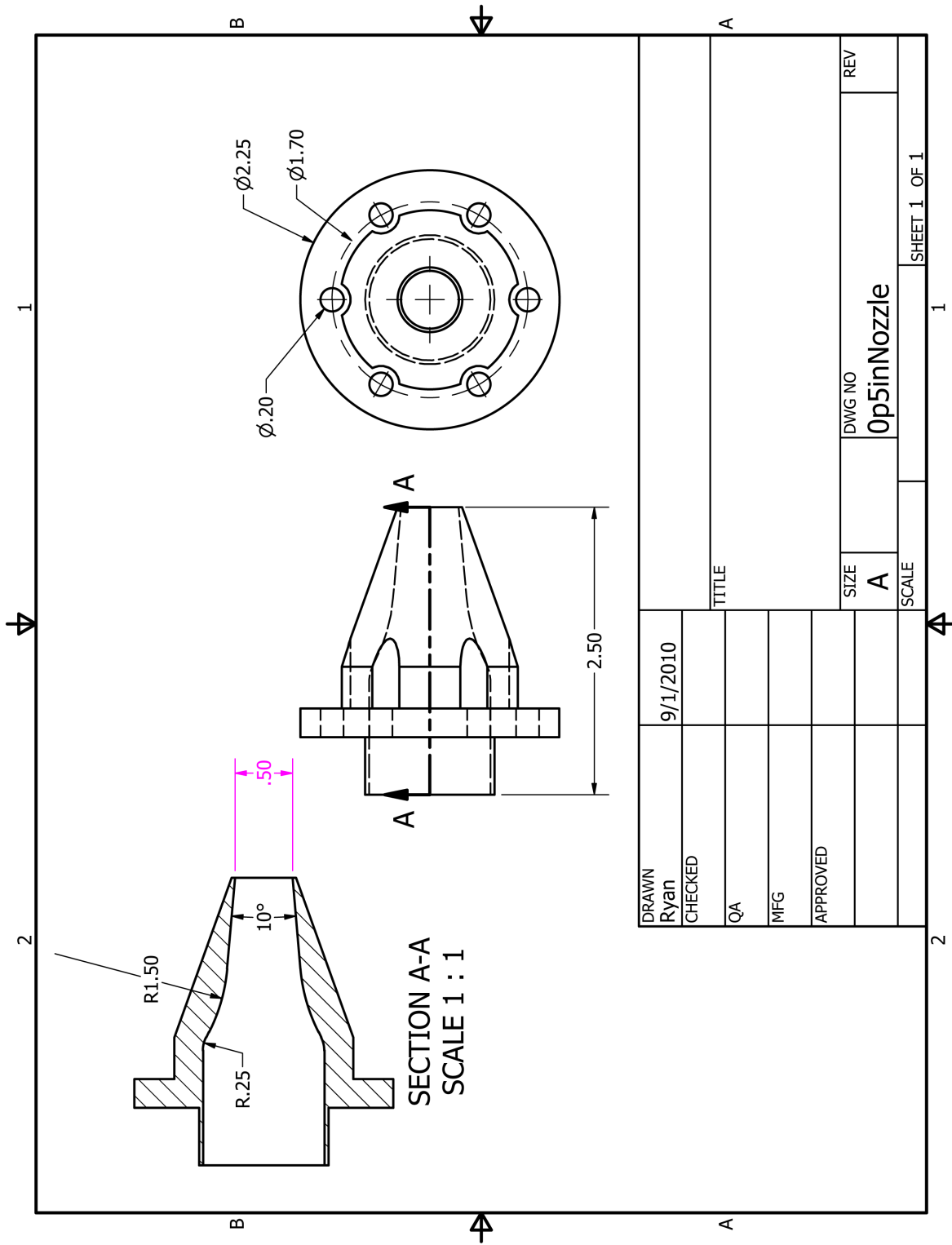


Figure C.31: Subsonic nozzle with a 0.5 inch diameter exhaust

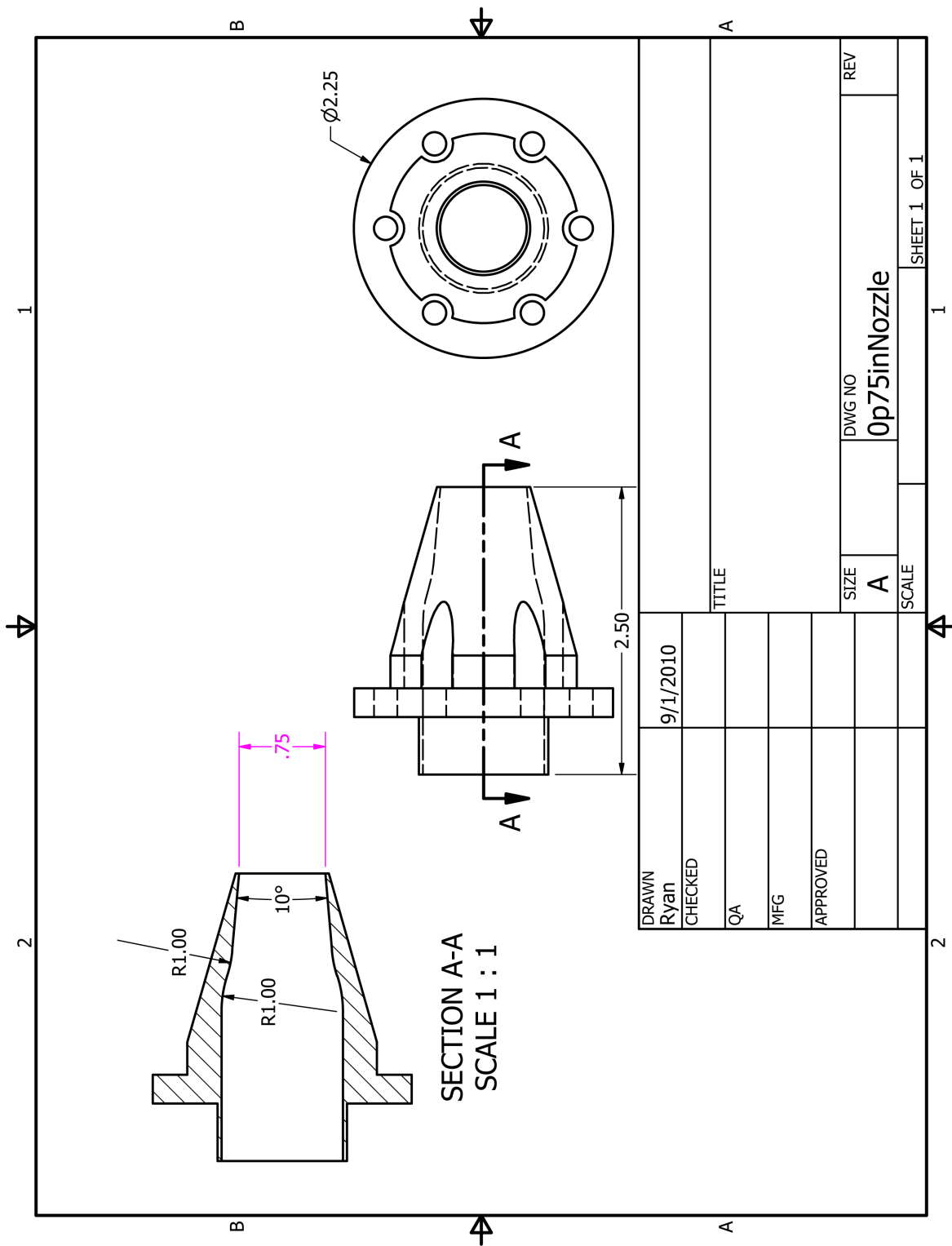


Figure C.32: Subsonic nozzle with a 0.75 inch diameter exhaust

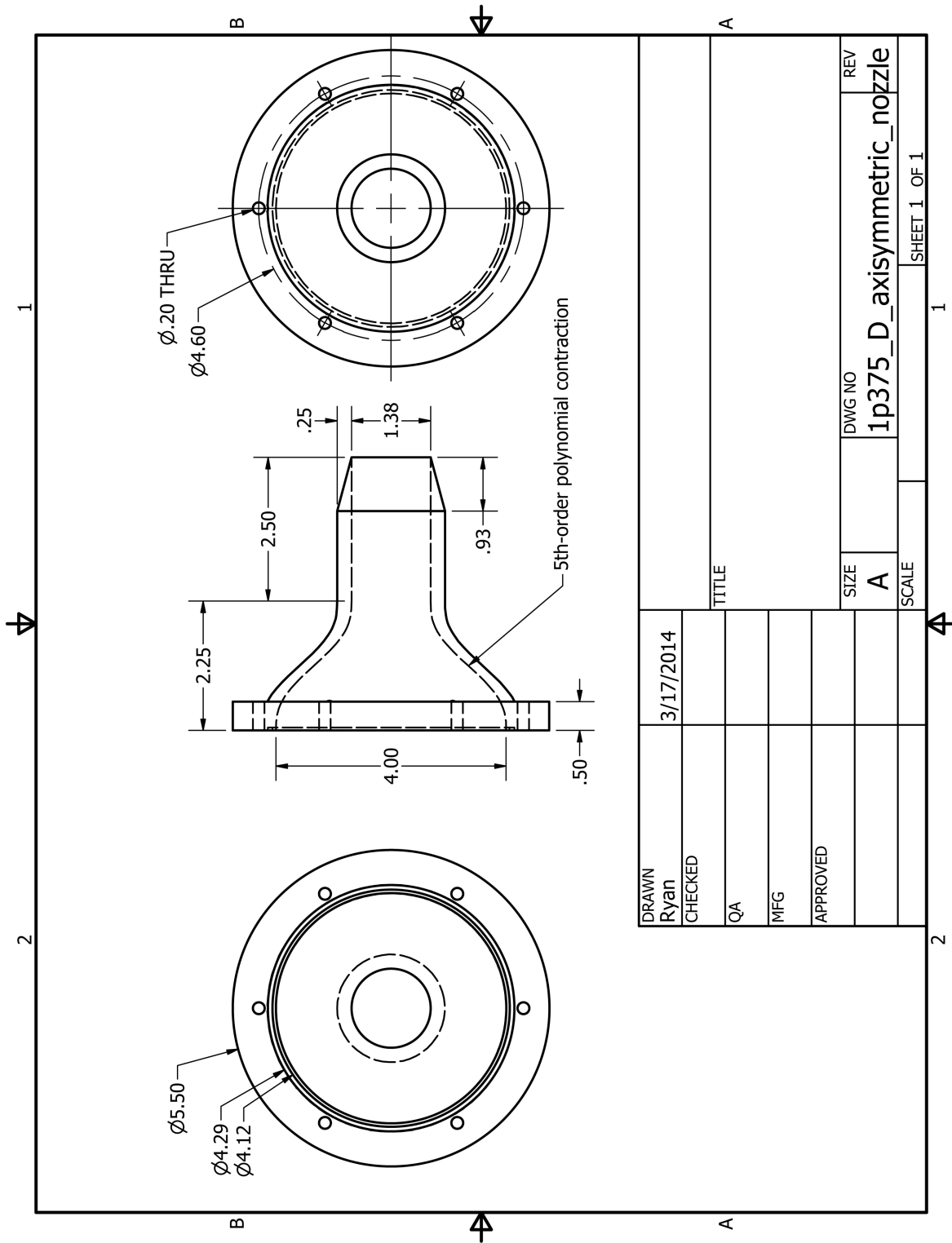


Figure C.33: Subsonic nozzle with a 1.375 inch diameter exhaust

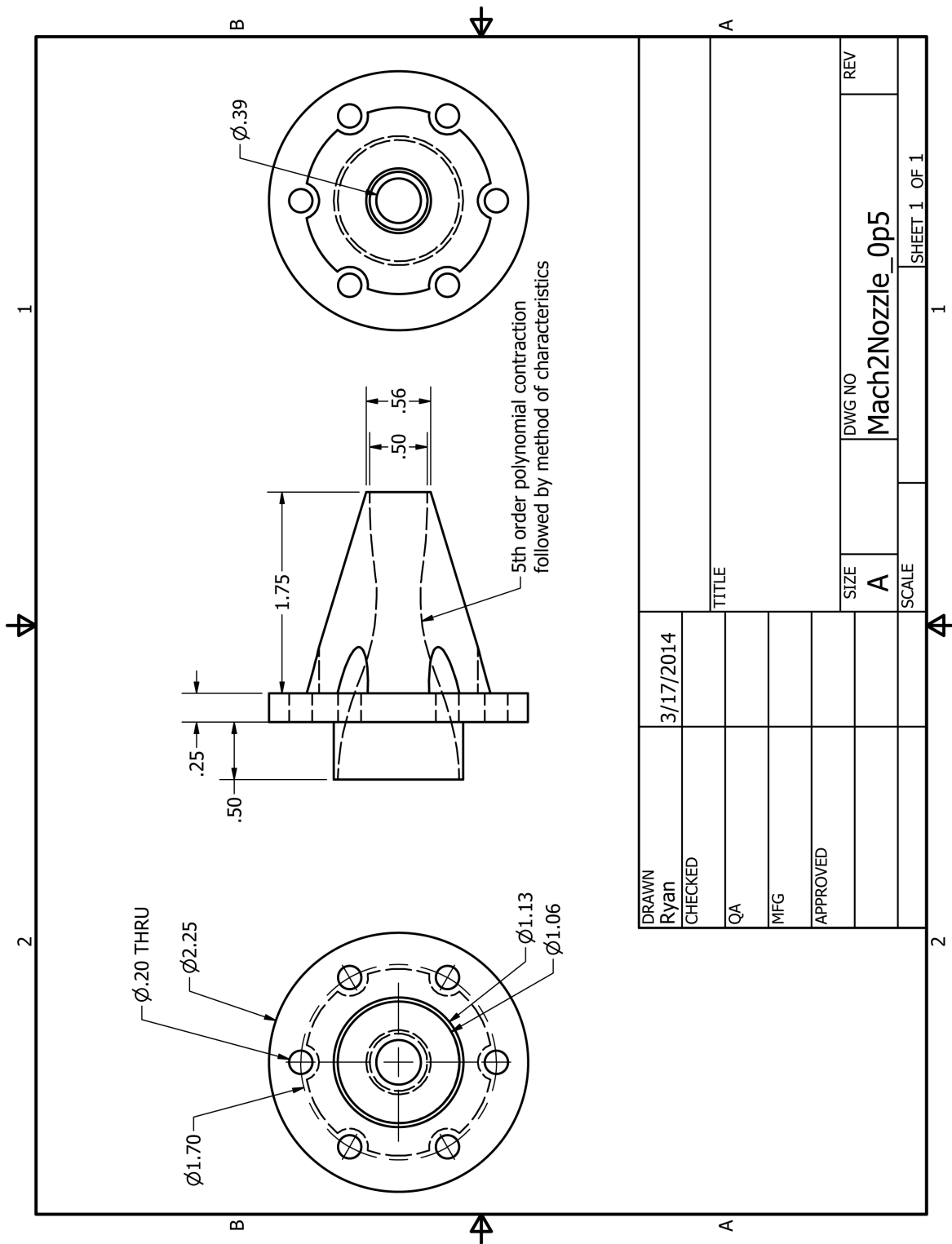


Figure C.34: Nozzle designed for perfect expansion at Mach 2 using the method of characteristics

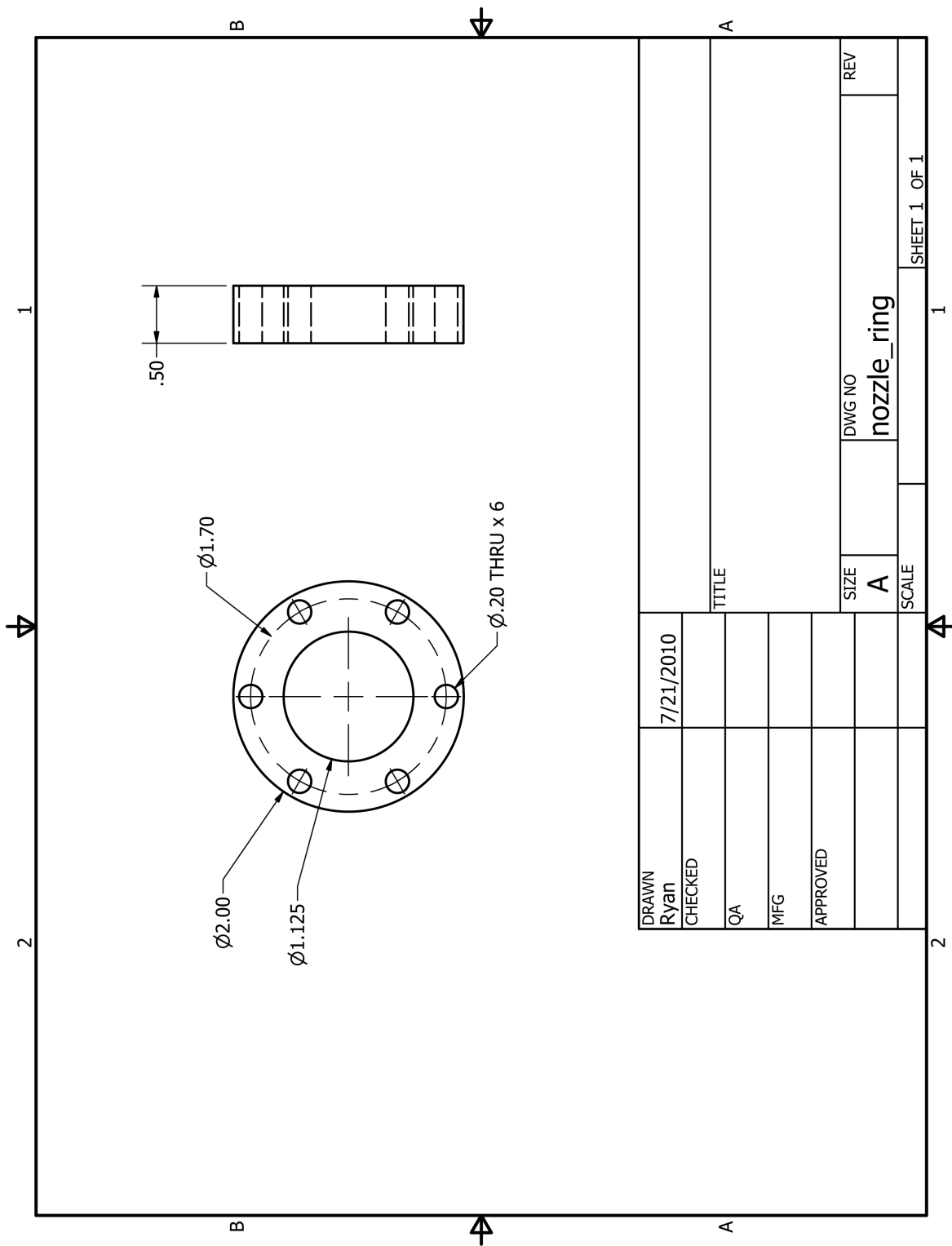


Figure C.35: Attachment ring which is soldered to the copper tubing to form nozzles

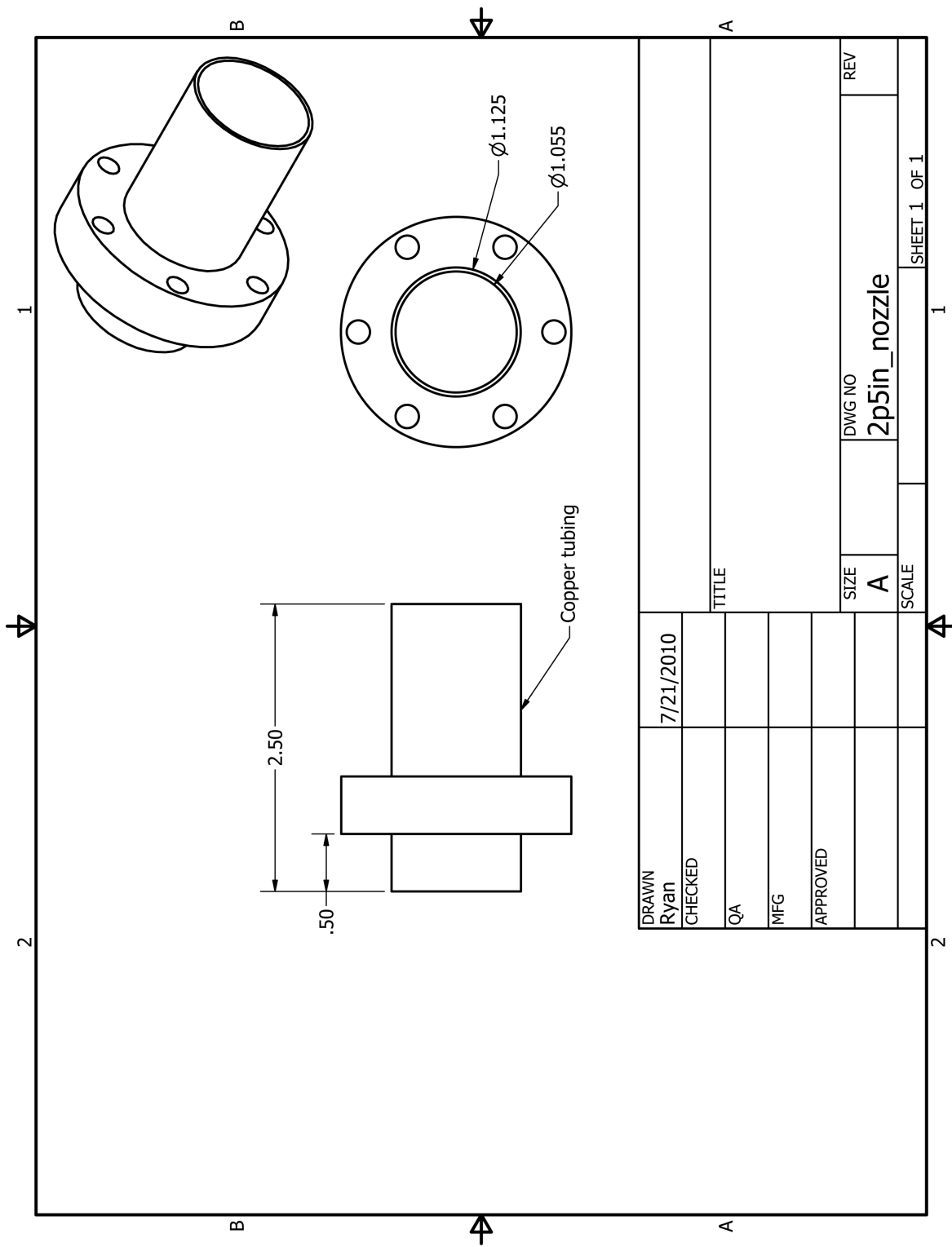


Figure C.36: Short copper nozzle

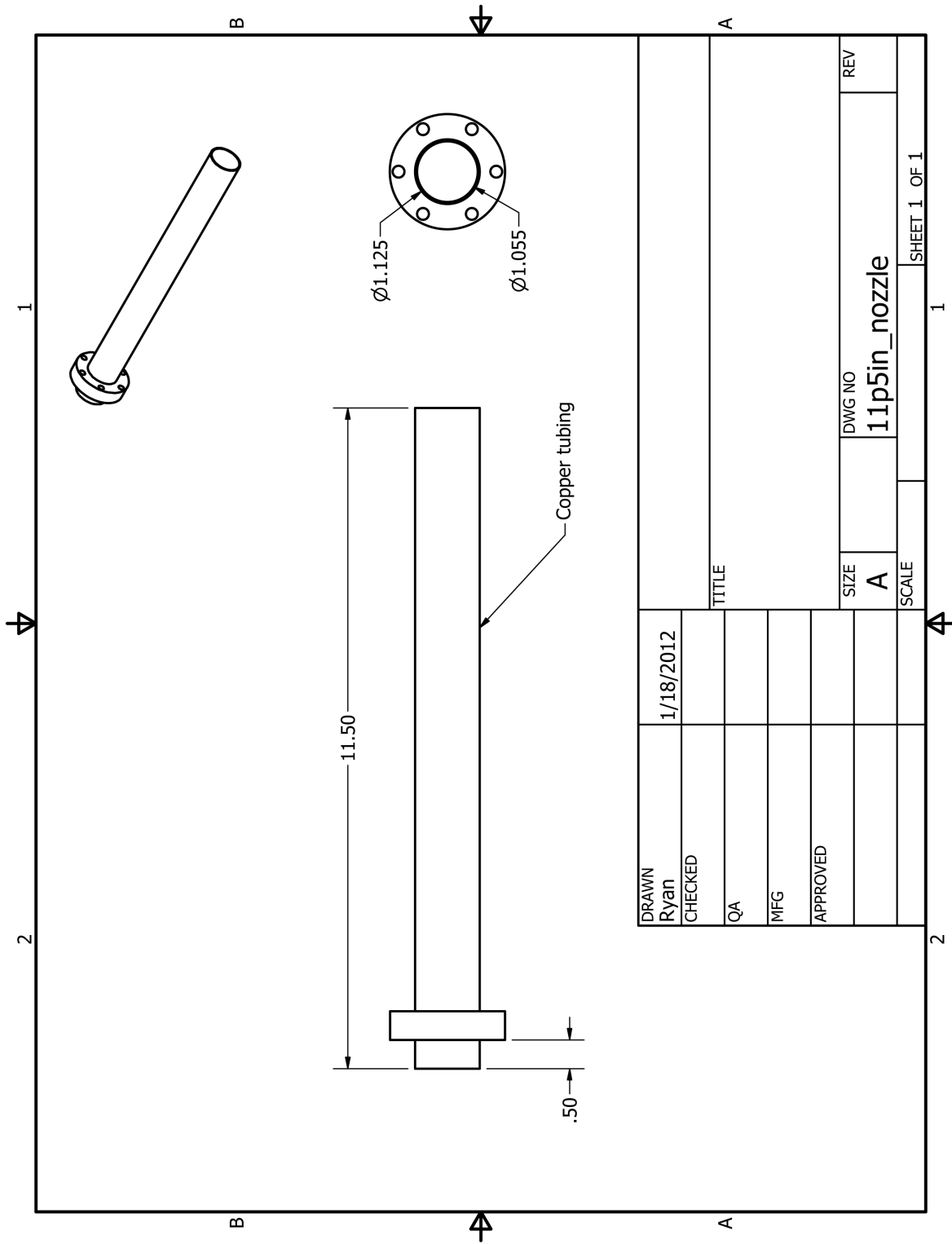


Figure C.37: Medium copper nozzle

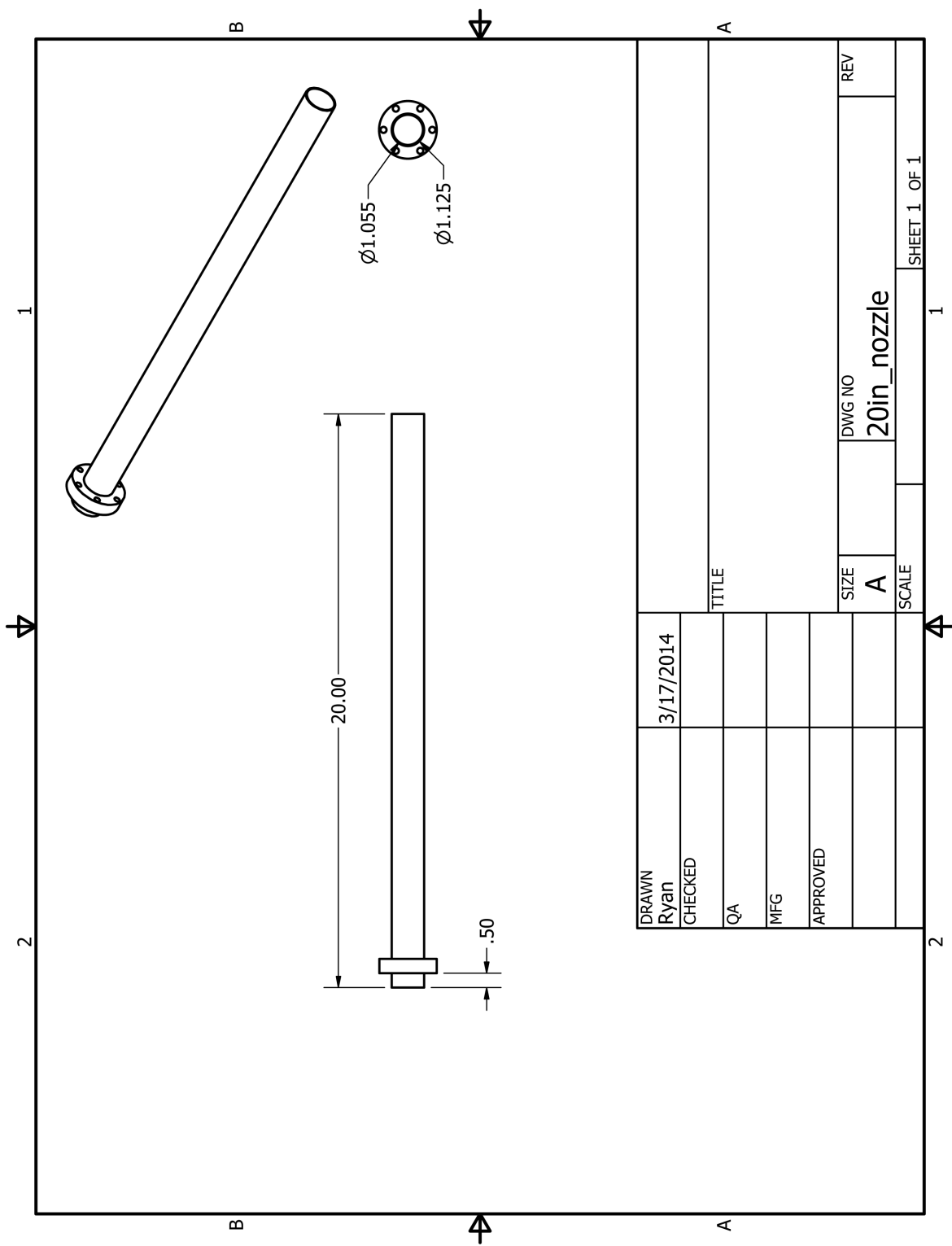


Figure C.38: Long copper nozzle

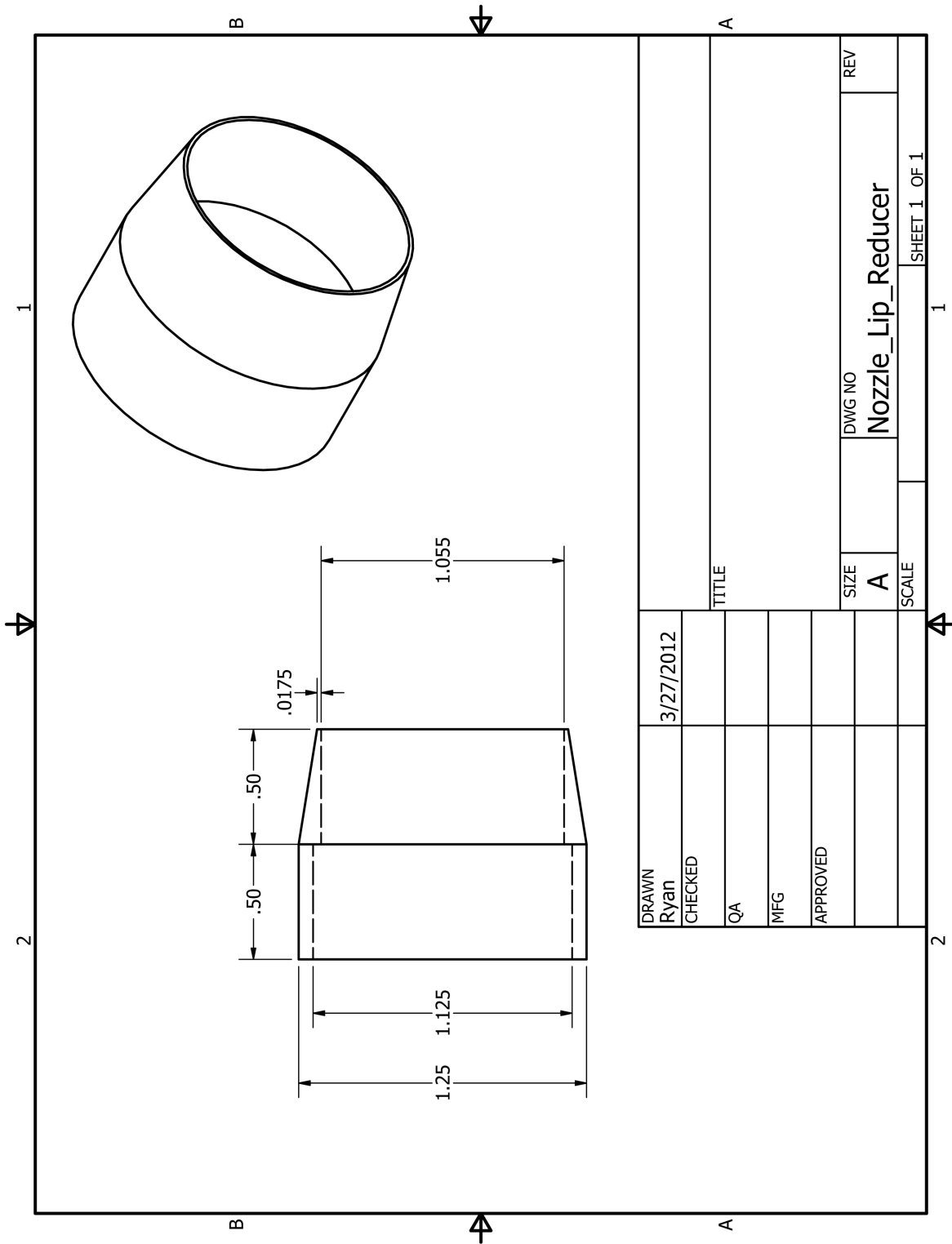


Figure C.39: For testing the effect of the nozzle lip thickness

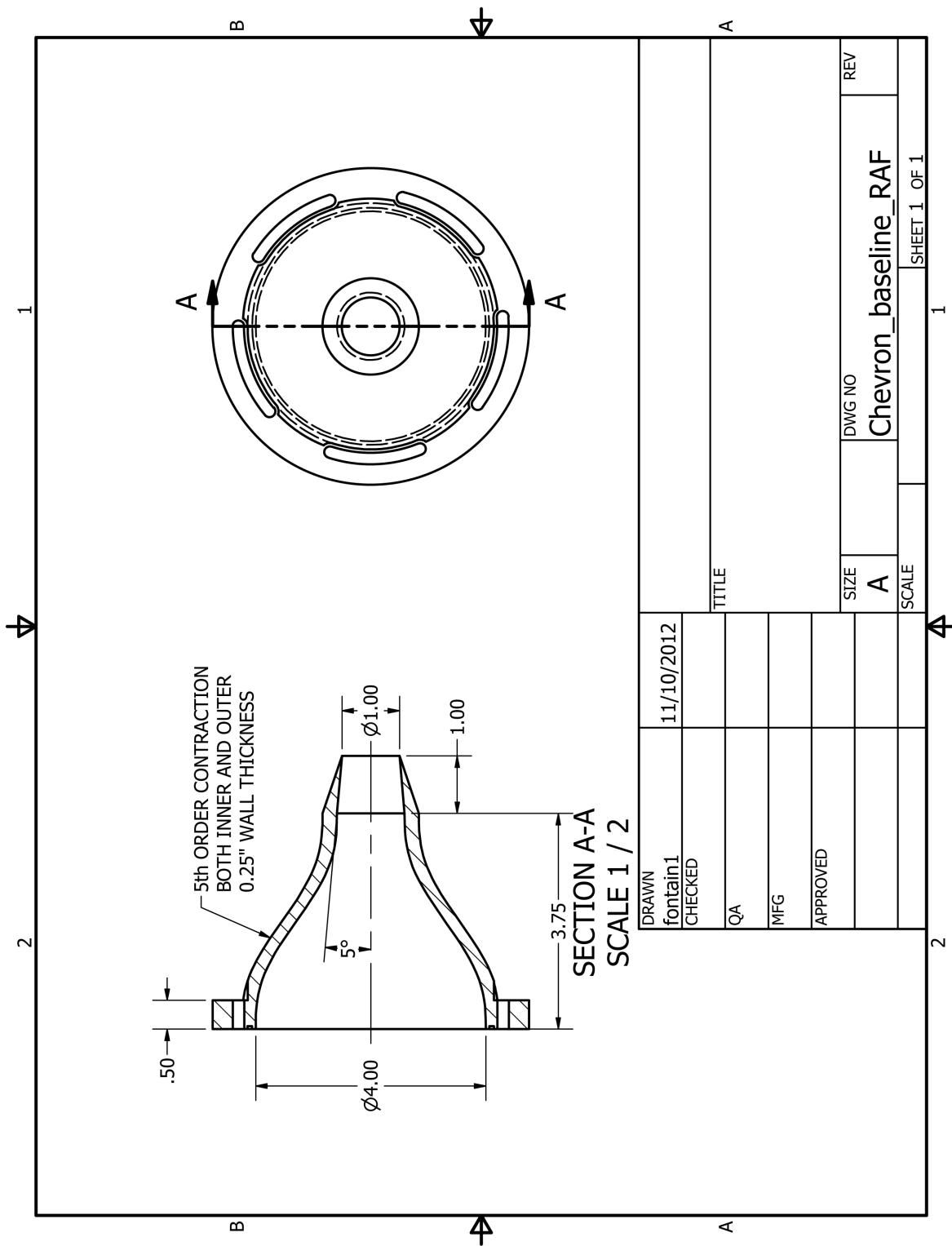


Figure C.40: Baseline axisymmetric nozzle which had all chevrons “cut” into it

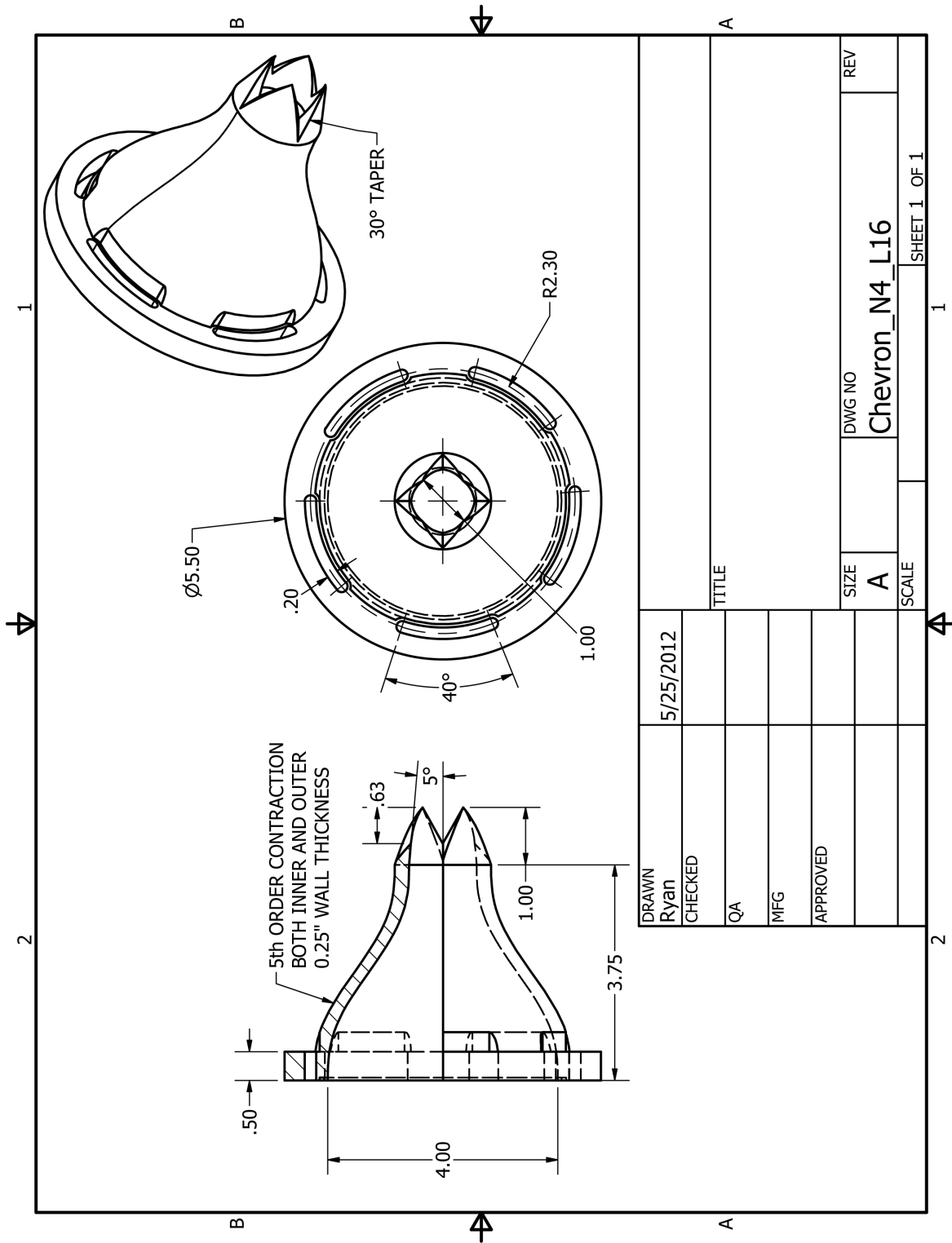


Figure C.41: Sample 5° penetration four chevron nozzle

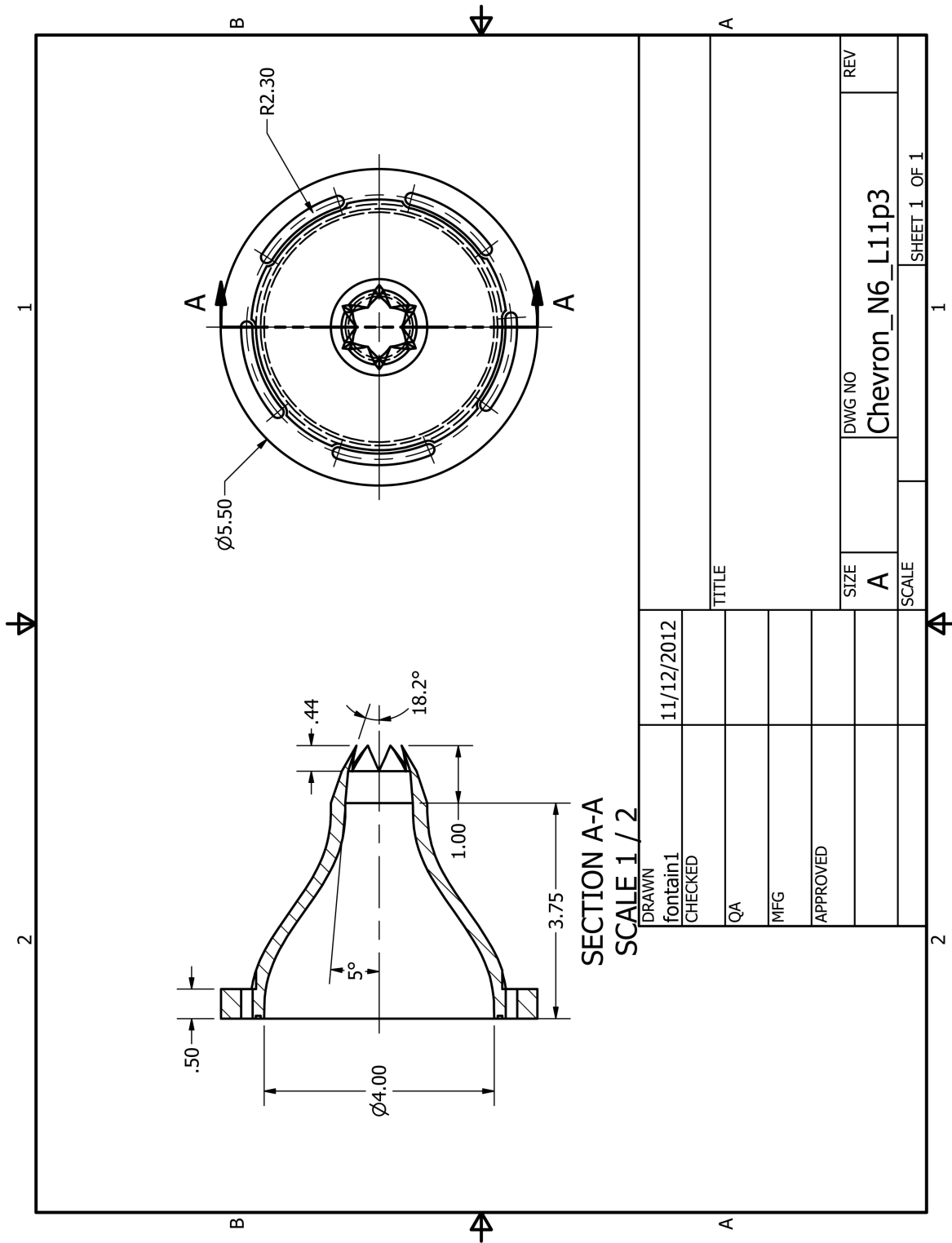


Figure C.42: Sample 18.2° penetration six chevron nozzle

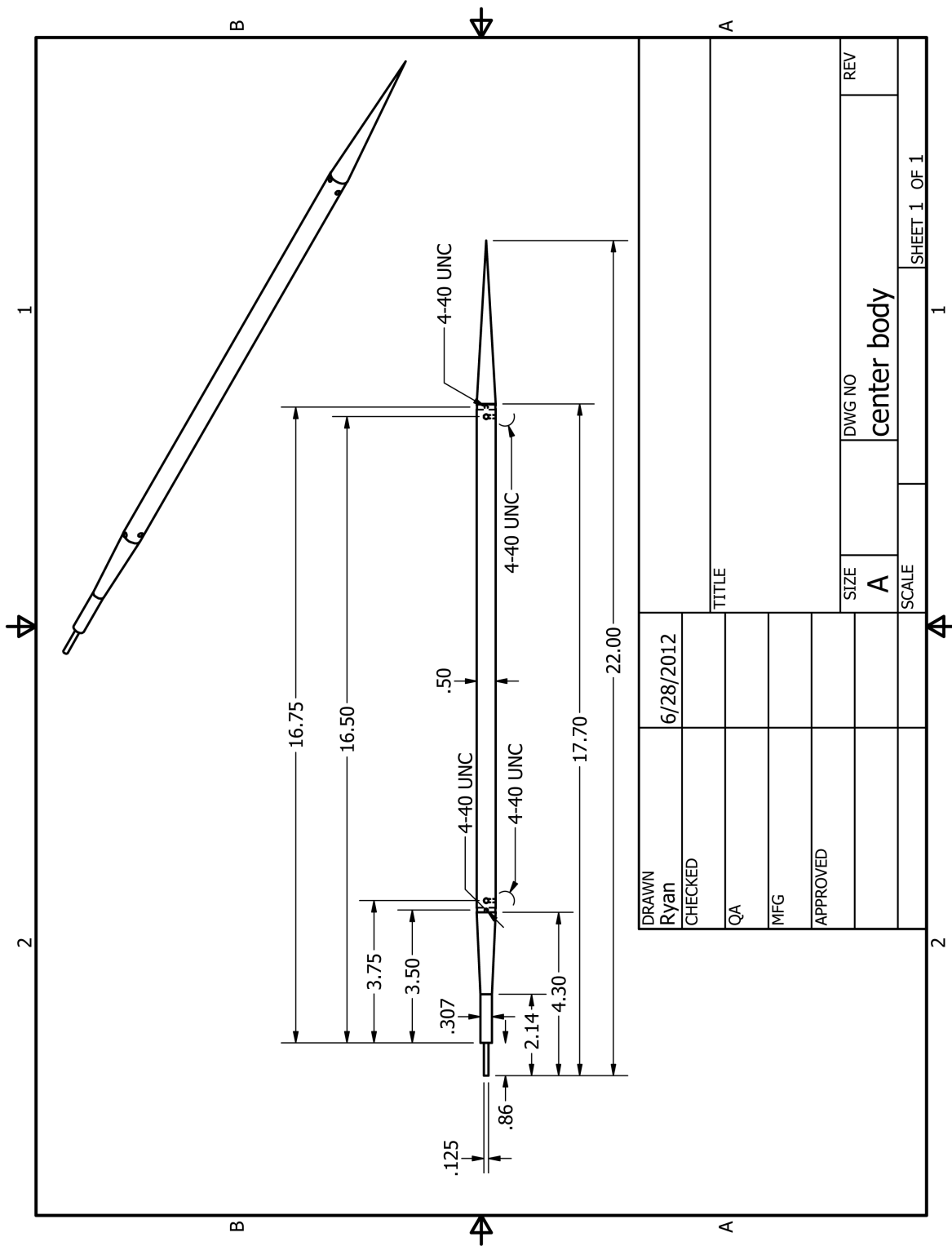


Figure C.43: Aerodynamic center body used to hold the plug at the nozzle exit

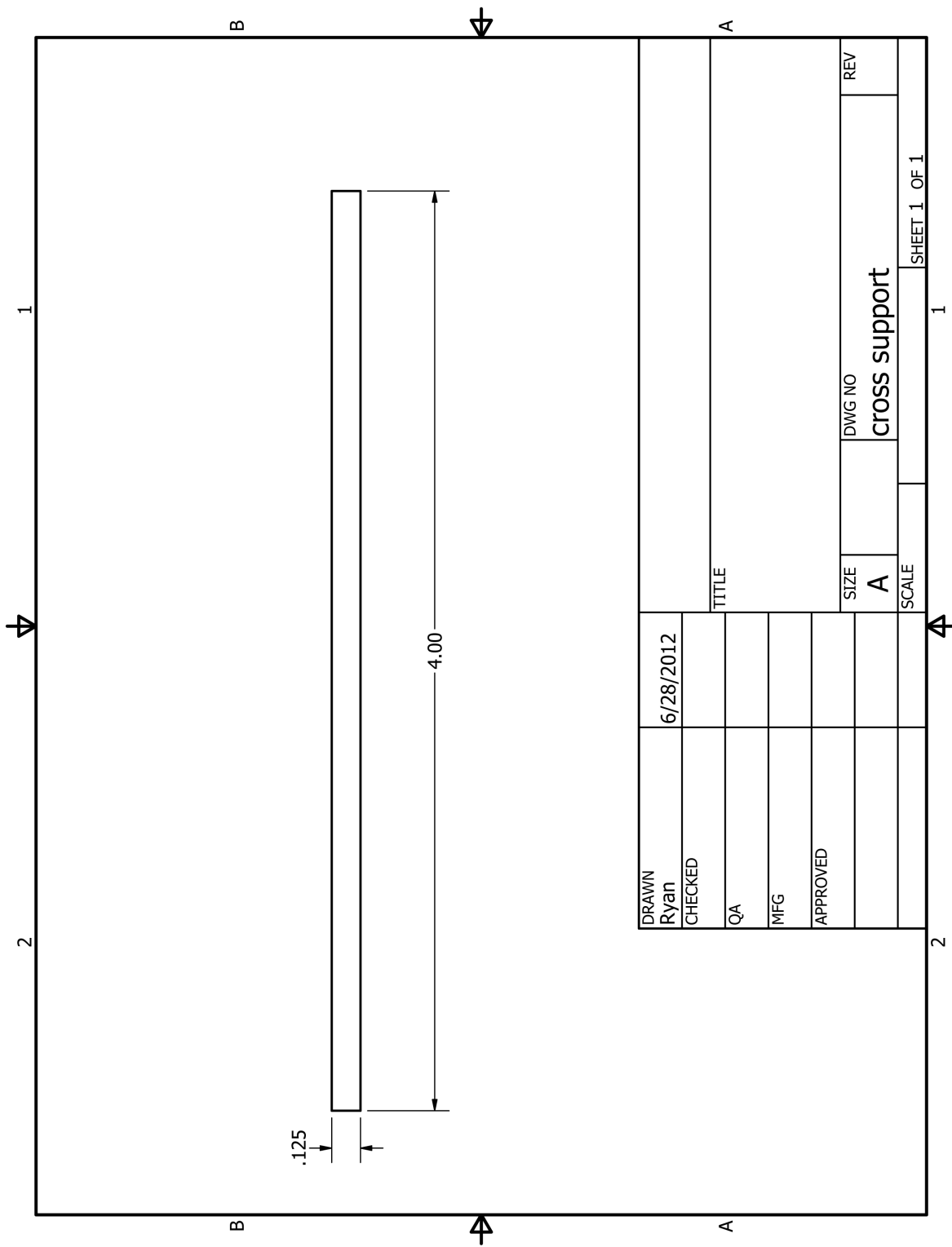
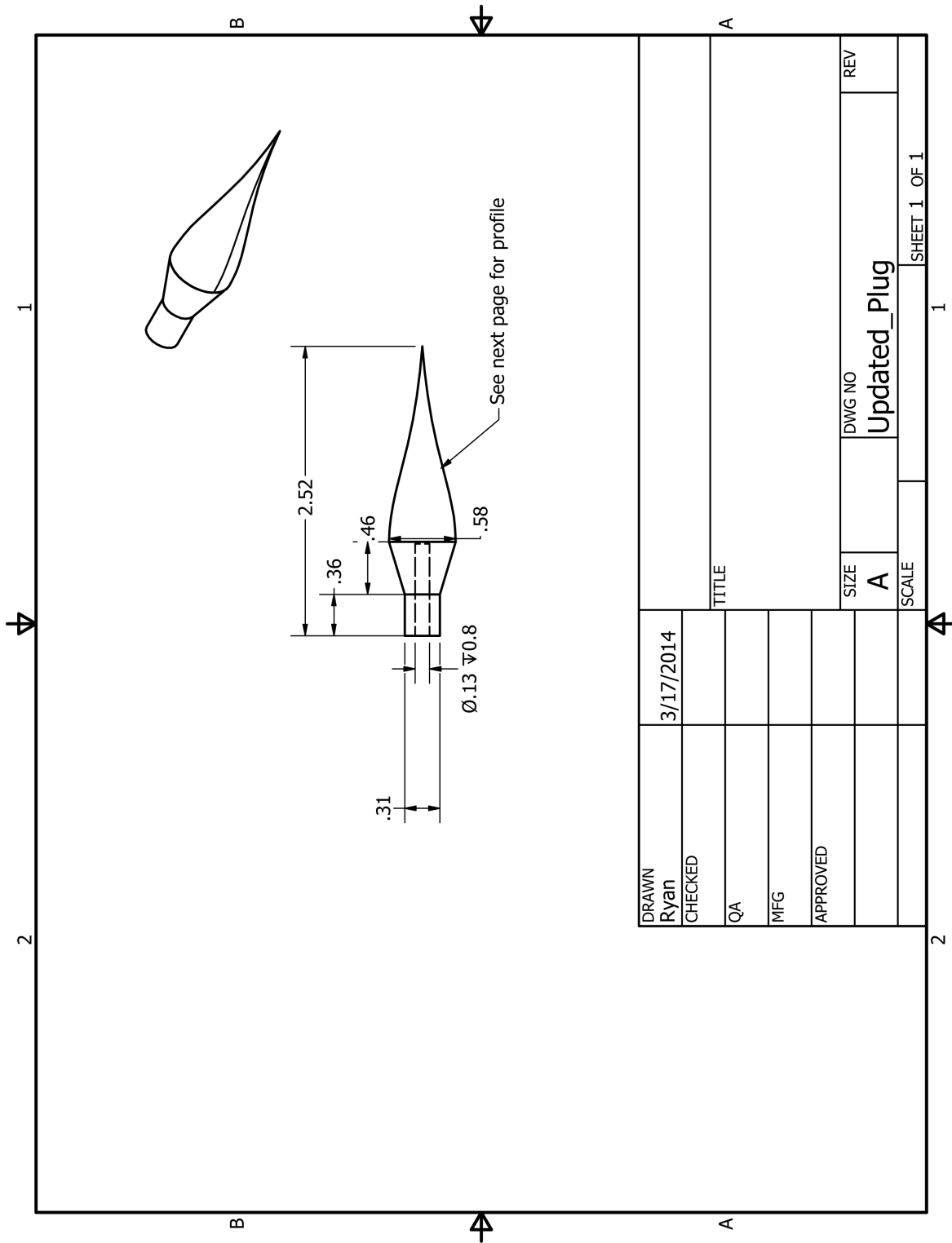


Figure C.44: Cross support to hold the center body in place



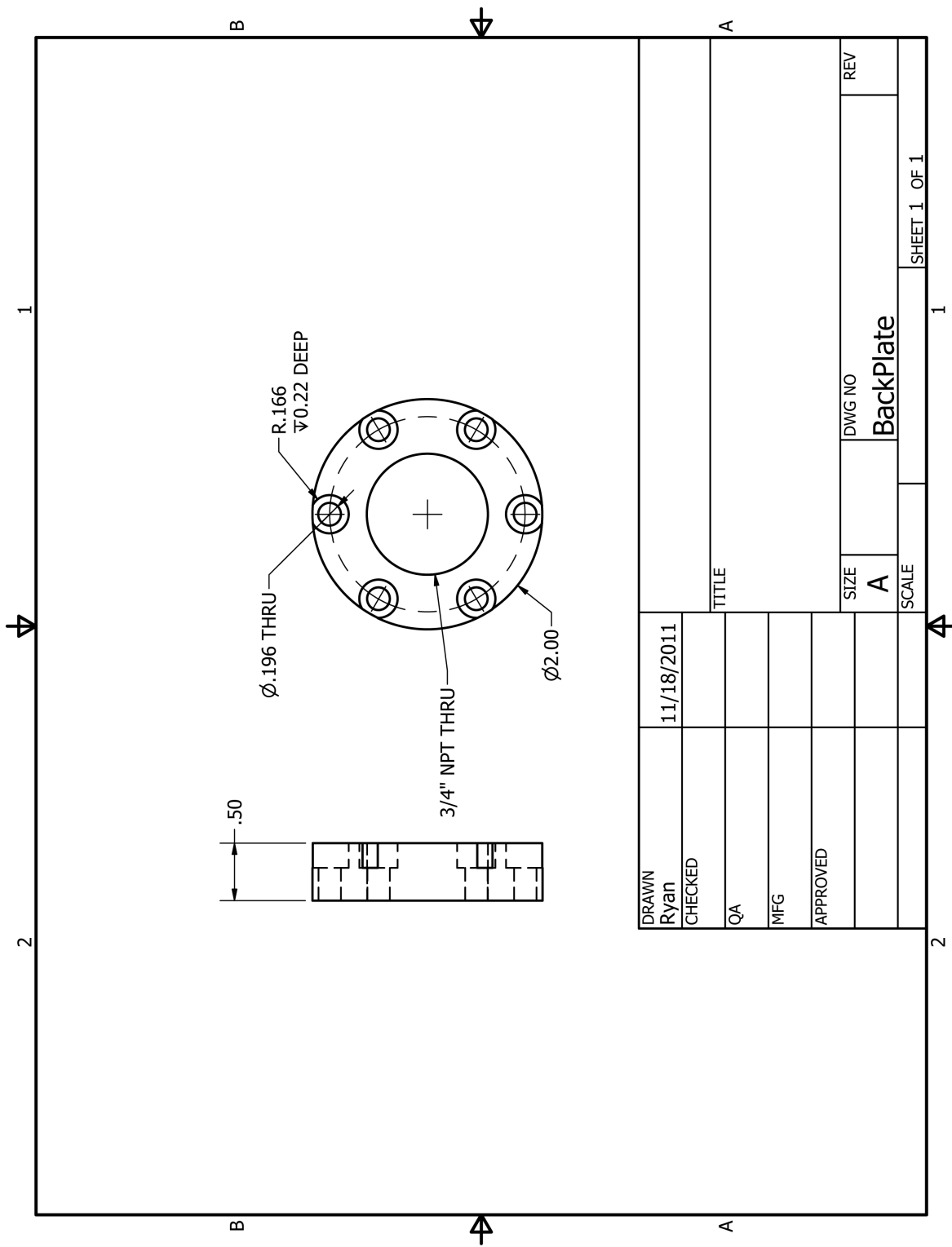
DRAWN	3/17/2014	TITLE		REV
Ryan				
CHECKED				
QA				
MFG				
APPROVED				
		SIZE	DWG NO	
		A	Updated_Plug	
		SCALE		
				SHEET 1 OF 1

Figure C.45: Plug geometry

X	Y
0	0.153522
0.36102	0.153522
0.819295	0.29105
0.828669	0.291027
0.838617	0.290979
0.846472	0.290923
0.857493	0.29082
0.869167	0.290648
0.881519	0.290268
0.891244	0.289843
0.90485	0.289119
0.92292	0.287927
0.938262	0.286768
0.95442	0.2854
0.971412	0.283762
0.989256	0.281773
1.007968	0.279418
1.027568	0.276694
1.04807	0.273584
1.069484	0.270057
1.097548	0.265057
1.121045	0.260582
1.145468	0.255653
1.170819	0.250283
1.197092	0.244484
1.22428	0.238264
1.252368	0.231638
1.281339	0.224628
1.311171	0.217259
1.341837	0.209561
1.373305	0.201571
1.405539	0.193329
1.438497	0.18488
1.472131	0.176272

X	Y
1.506391	0.167561
1.541211	0.15877
1.576543	0.150014
1.612356	0.141494
1.648538	0.133102
1.68499	0.124797
1.721622	0.11657
1.758339	0.108411
1.804213	0.098292
1.840883	0.090742
1.87745	0.083784
1.913736	0.076982
1.949672	0.070411
1.985188	0.064143
2.020217	0.058241
2.054695	0.052752
2.088547	0.047651
2.121707	0.042897
2.154114	0.038457
2.185713	0.034288
2.216458	0.030359
2.24631	0.026644
2.275241	0.023146
2.303229	0.01988
2.330258	0.016857
2.356319	0.014086
2.381403	0.011566
2.405509	0.009293
2.42864	0.007264
2.450802	0.005462
2.472001	0.00384
2.492251	0.002356
2.511565	0.000979
2.520878	0.000322

Figure C.46: Plug geometry coordinates in inches



DATE	11/18/2011	TITLE	
DRAWN	Ryan	SIZE	A
CHECKED		DWG NO	BackPlate
QA		SCALE	
MFG		REV	
APPROVED		SHEET 1 OF 1	

Figure C.47: Mach 3 jet back plate

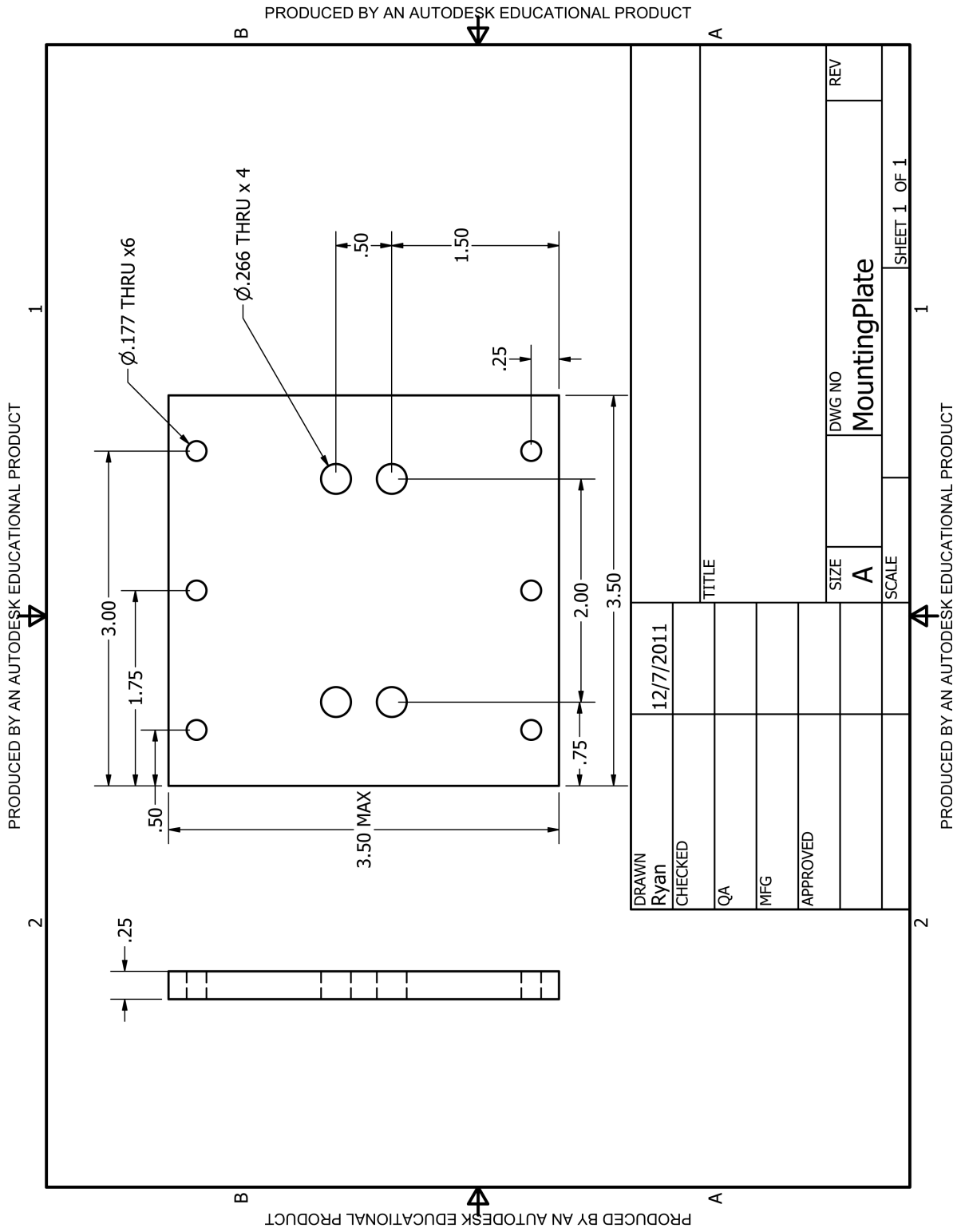


Figure C.48: Mach 3 jet mounting plate

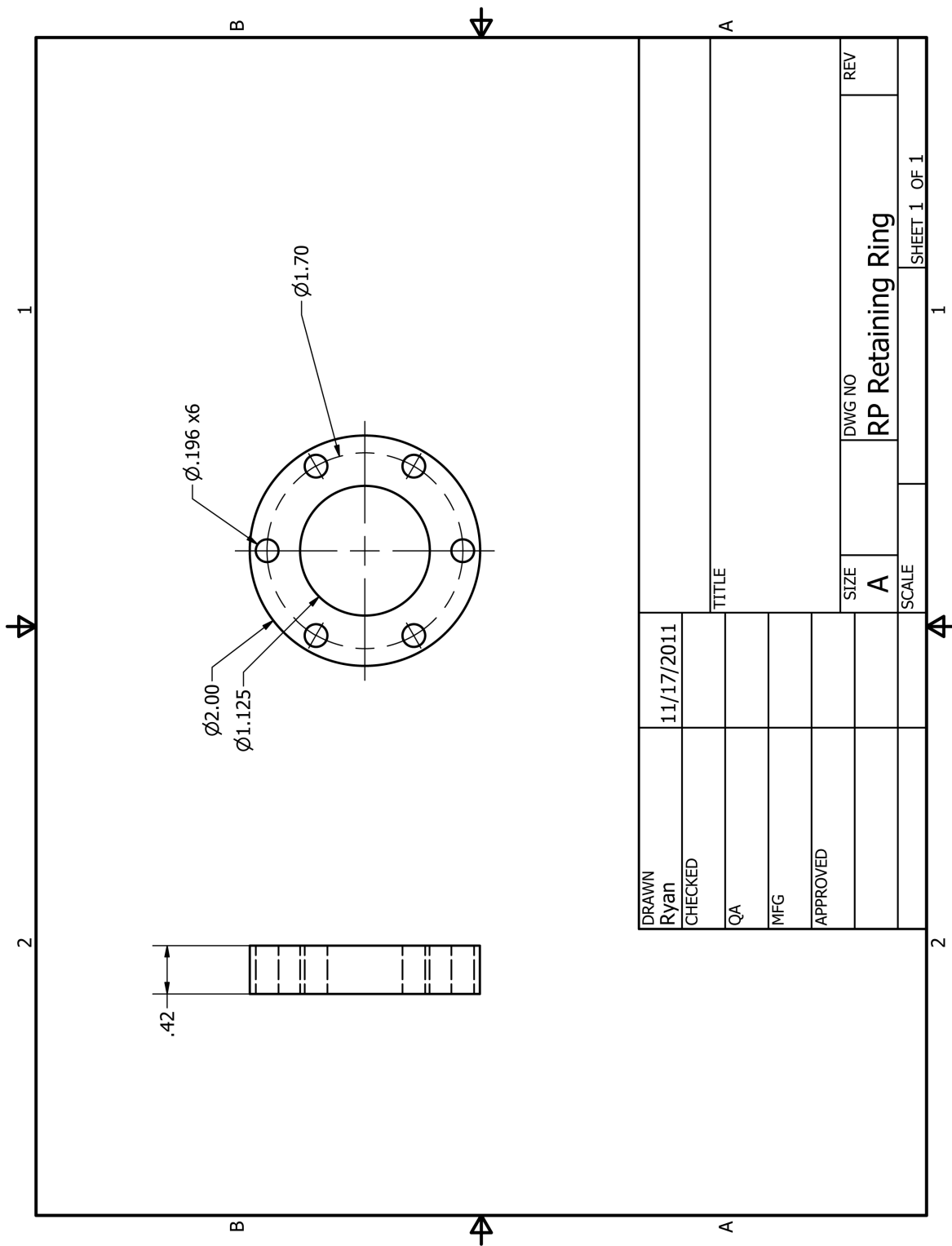


Figure C.49: Metal retaining ring to reinforce nozzle mounting

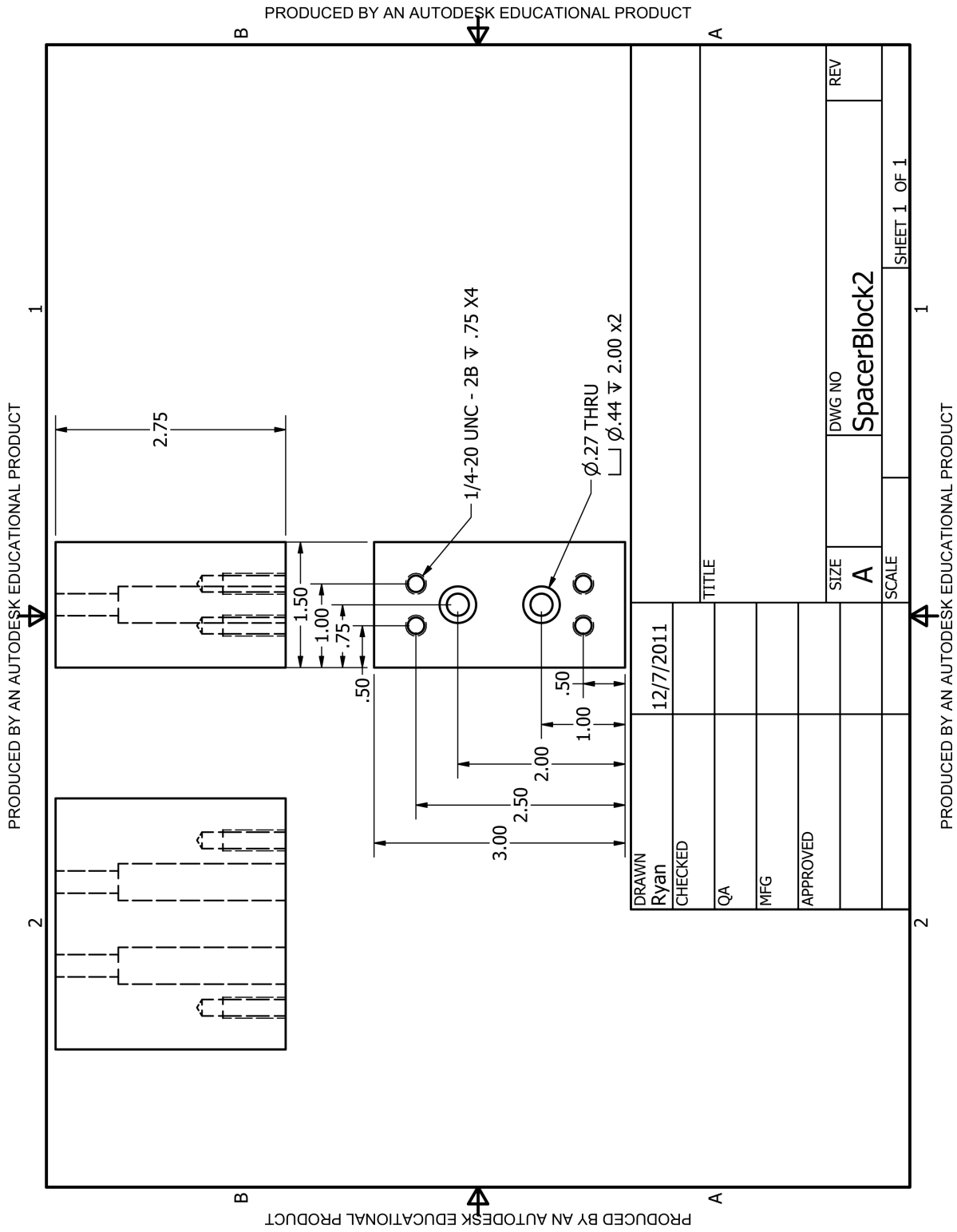


Figure C.50: Spacer to put jet at the center of the tunnel

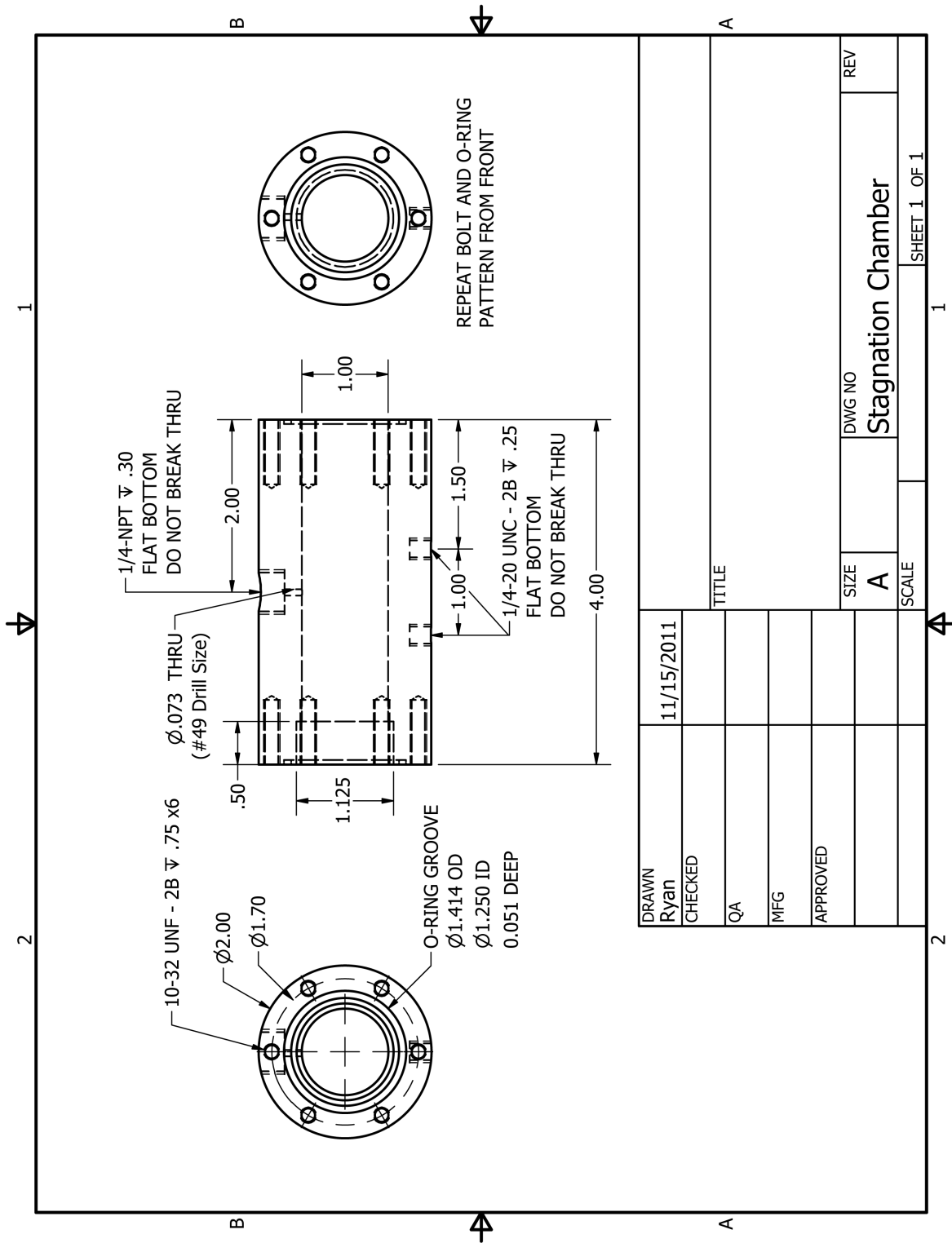


Figure C.51: Stagnation chamber

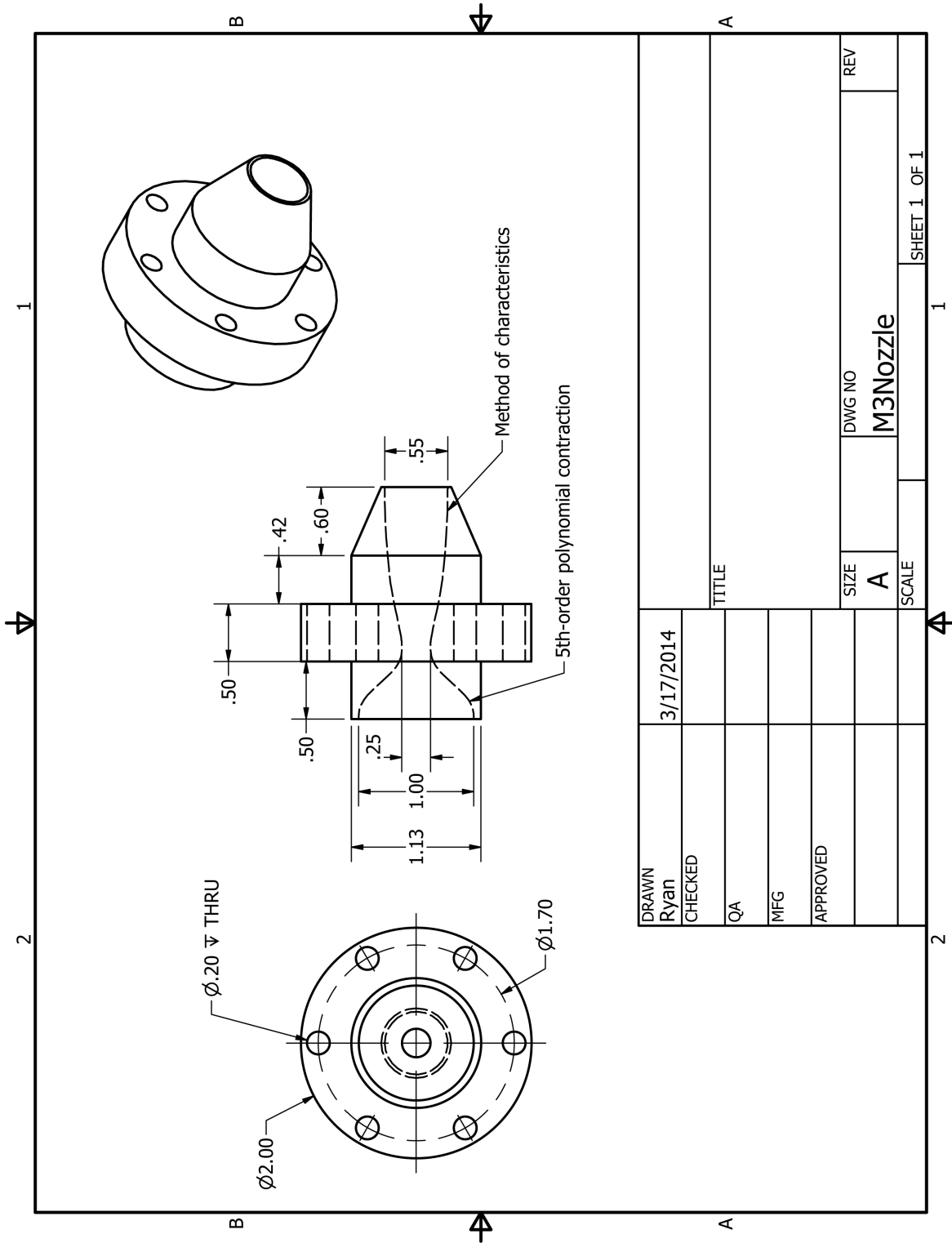


Figure C.52: Mach 3 nozzle designed using the method of characteristics

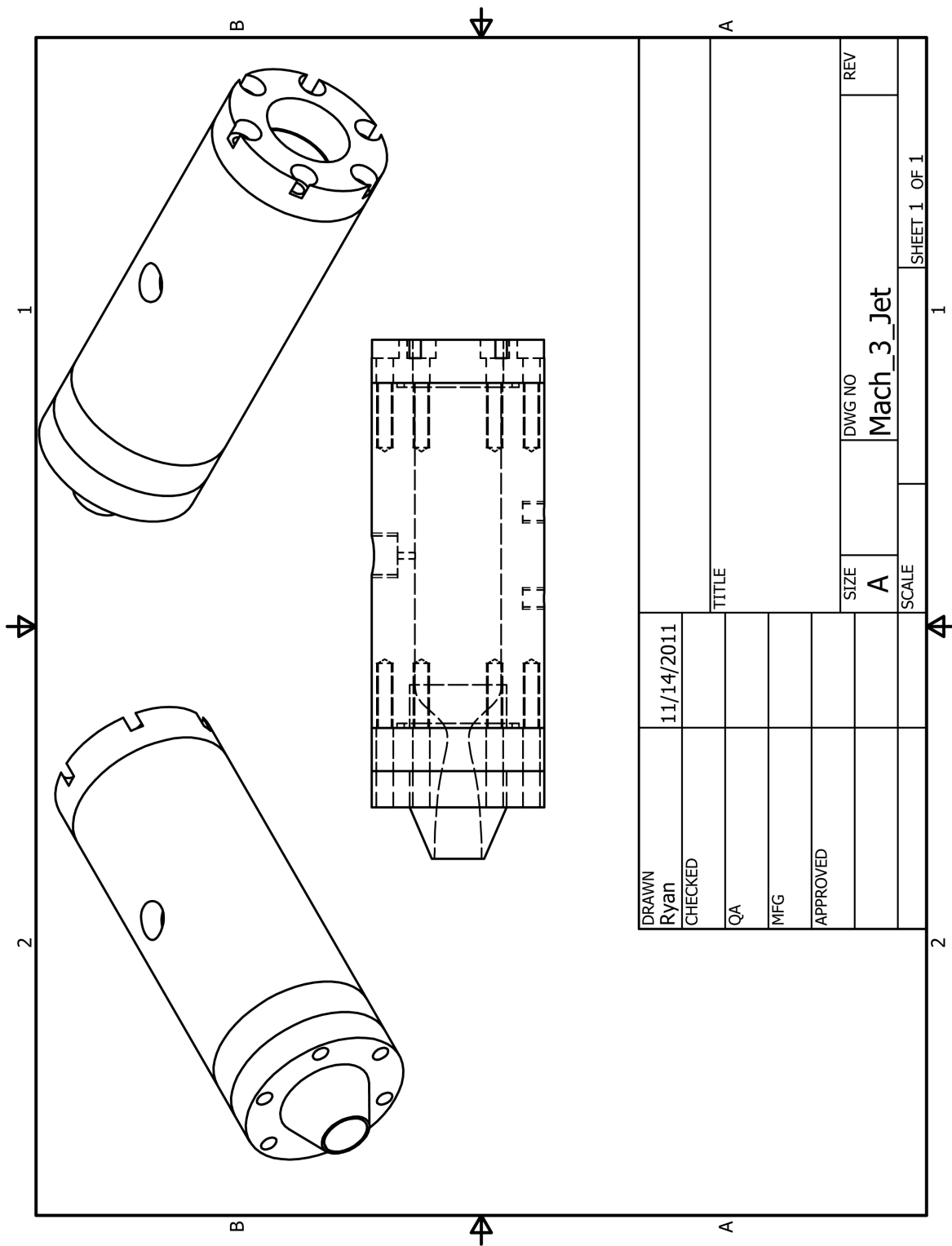
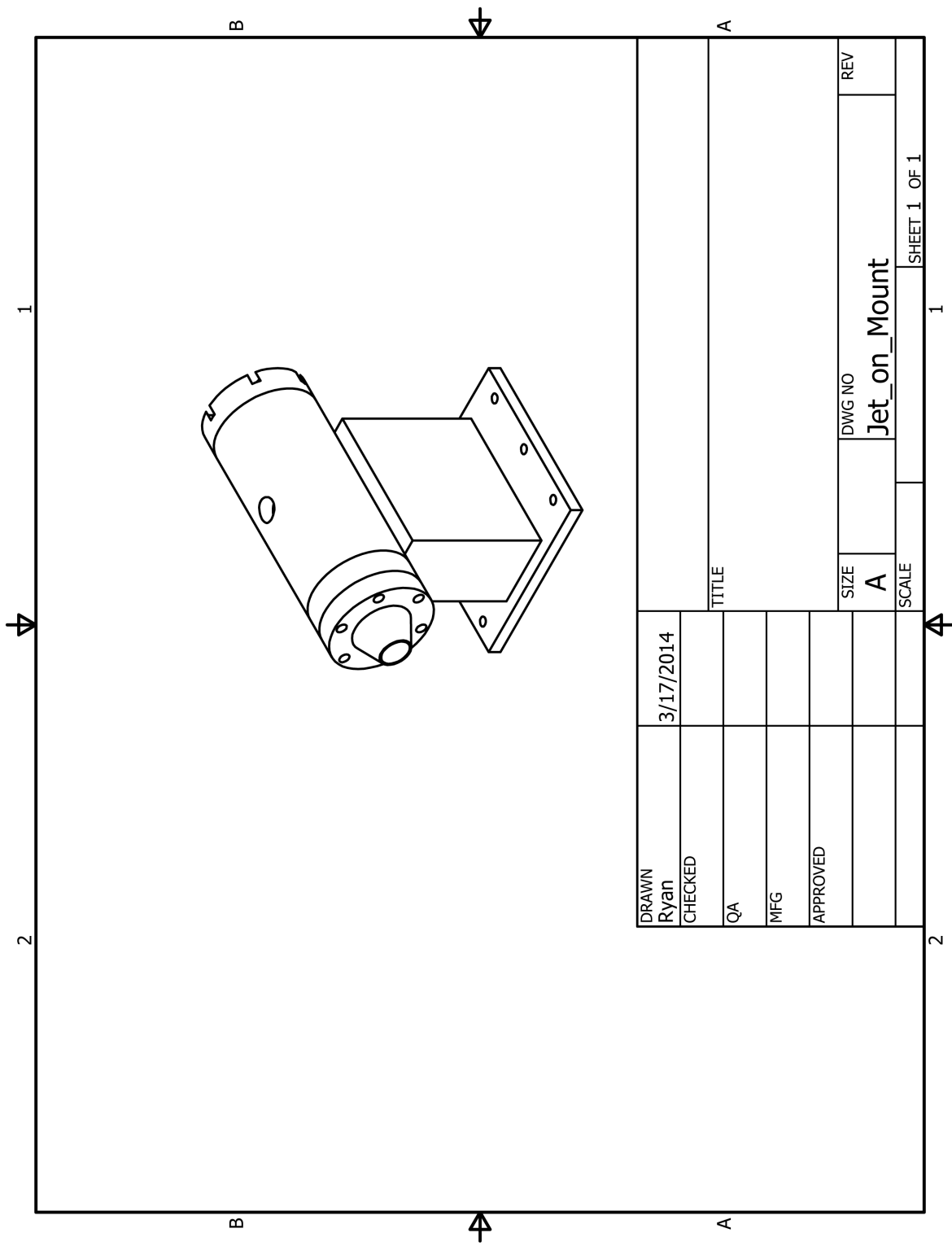


Figure C.53: Overview of the Mach 3 jet



DRAWN	3/17/2014									SHEET 1 OF 1	
Ryan											
CHECKED											
QA											
MFG											
APPROVED											
			TITLE		SIZE		DWG NO		REV		
					A		Jet_on_Mount				
					SCALE						

Figure C.54: Full support structure overview of the Mach 3 jet

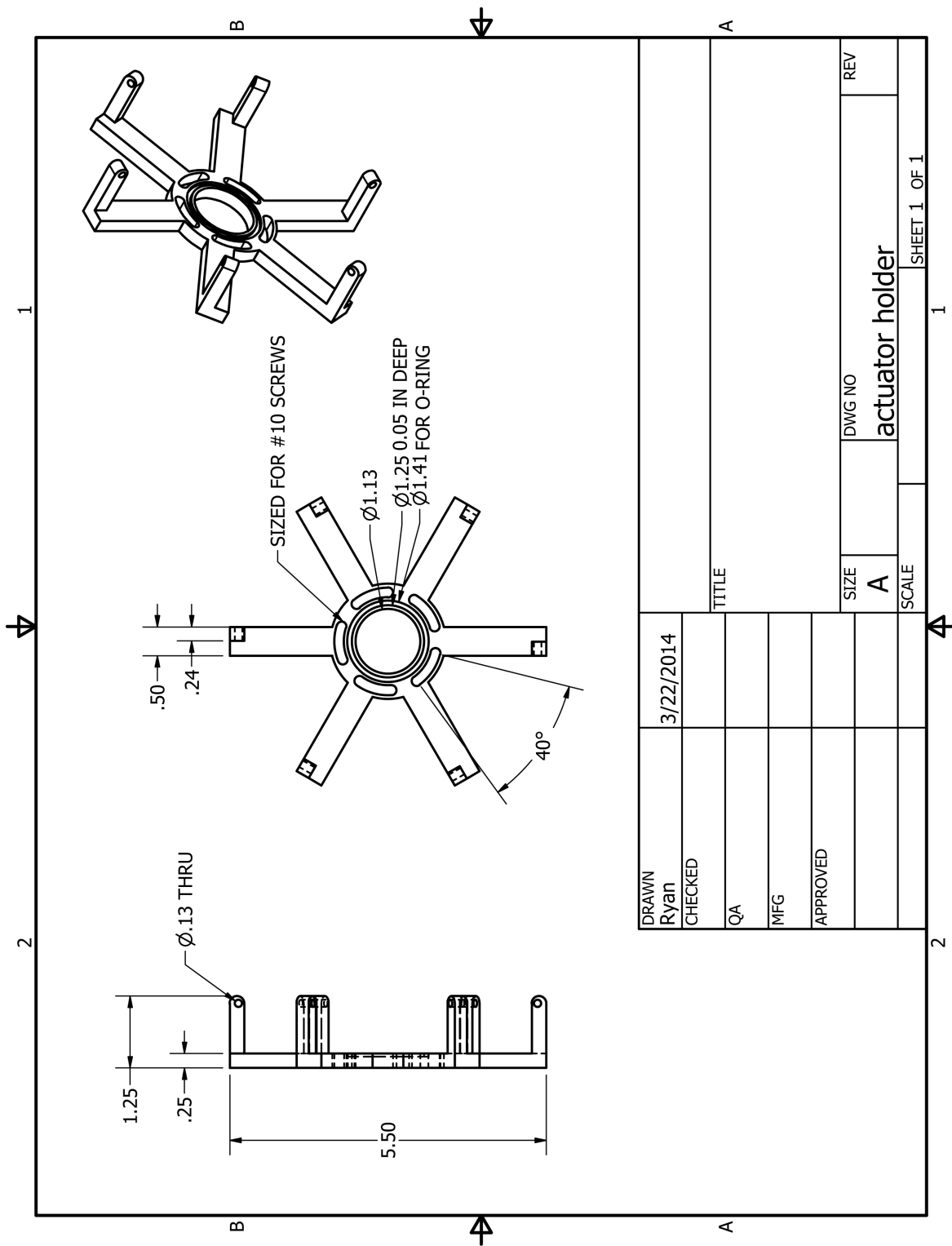


Figure C.55: Mounting bracket for linear actuators for chevron perturbation study

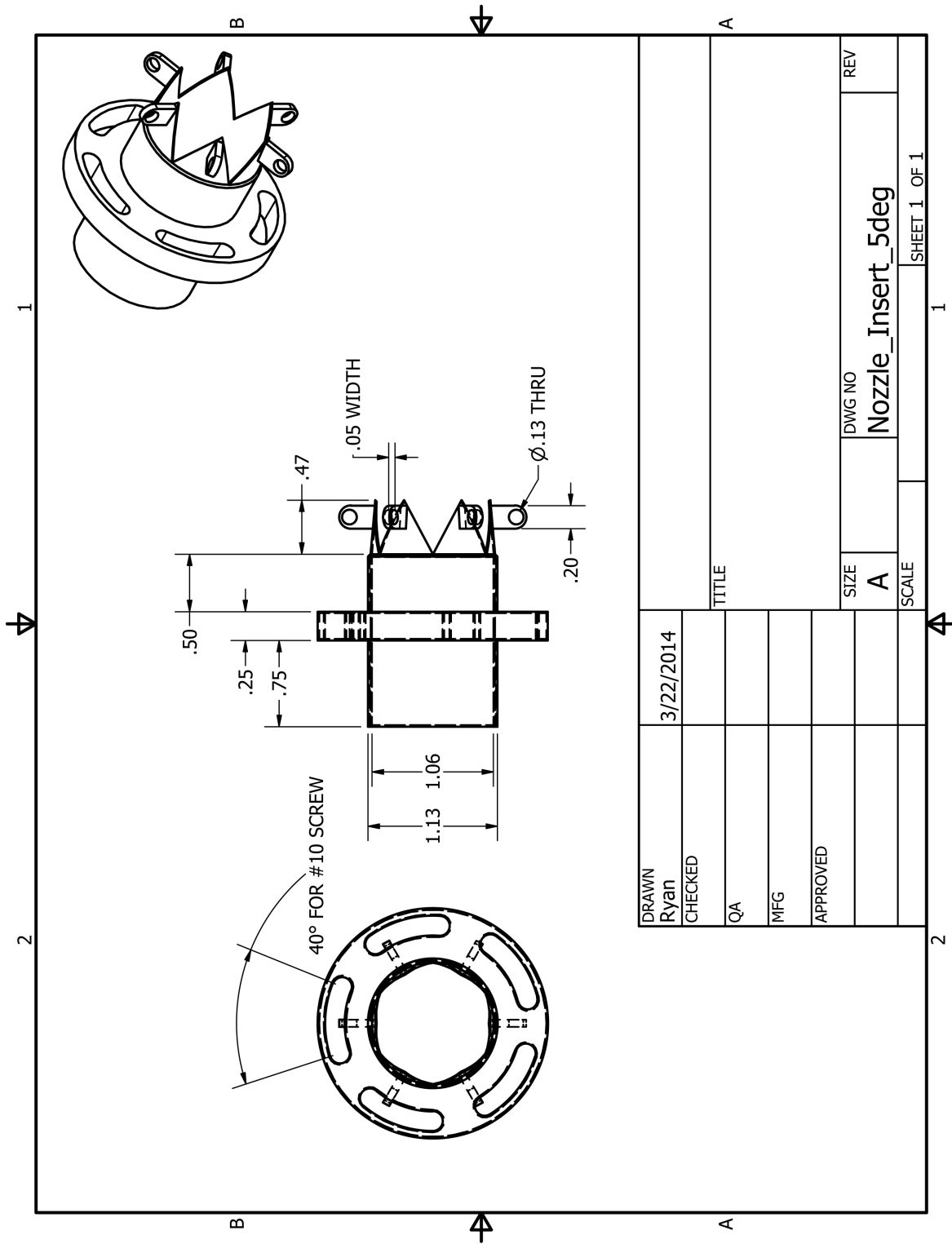


Figure C.56: Nozzle used for the small perturbation experiments with a 5° baseline penetration angle

Appendix D

List of Tests Conducted in the Facility

Nozzle	v_j/c_amb	Date	Run	Background	Primary Objective	Notes
Short Copper	0.9	2012/02/01	3	1	BL Test	
Med. Copper	0.9	2012/02/01	7	1	BL Test	
Long Copper	0.9	2012/02/01	6	1	BL Test	
Old Chevron	0.9	2011/04/21	1	7	Chevron Test	Old Long Chevron 90-45 tip
Old Chevron	0.9	2011/04/21	11	7	Chevron Test	Old Long Chevron 30 tip
8mm Chevron	0.9	2012/06/22	3	1	Chevron Activation Test	Tip 90-45
8mm Chevron	0.9	2012/06/22	4	1	Chevron Activation Test	Tip 30
8mm Chevron	0.9	2012/06/22	5	1	Chevron Activation Test	Valley 90-45
8mm Chevron	0.9	2012/06/22	6	1	Chevron Activation Test	Valley 30
16mm Chevron	0.9	2012/06/22	7	1	Chevron Activation Test	Tip 90-45
16mm Chevron	0.9	2012/06/22	8	1	Chevron Activation Test	Tip 30
16mm Chevron	0.9	2012/06/22	9	1	Chevron Activation Test	Valley 90-45
16mm Chevron	0.9	2012/06/22	10	1	Chevron Activation Test	Valley 30
Chevron Baseline	0.9	2012/06/22	2	1	Chevron Activation Test	
16mm Chevron	0.98	2012/07/13	2	1	Compare with Bridges SMC002	Tip 90-45
16mm Chevron	0.98	2012/07/13	3	1	Compare with Bridges SMC002	Tip 30
4mm Chevron	0.9	2012/07/13	4	1	Chevron Activation Test	Tip 90-45
4mm Chevron	0.9	2012/07/13	5	1	Chevron Activation Test	Tip 30
4mm Chevron	0.9	2012/07/13	6	1	Chevron Activation Test	Valley 90-45
4mm Chevron	0.9	2012/07/13	7	1	Chevron Activation Test	Valley 30
Plug Nozzle	0.5	2012/07/13	8	16	Gulfstream Plug Test	Effective Diam = 0.879"
Plug Nozzle	0.7	2012/07/13	9	1	Gulfstream Plug Test	Effective Diam = 0.879"
Plug Nozzle	0.9	2012/07/13	10	1	Gulfstream Plug Test	Effective Diam = 0.879"
Plug Nozzle	1.1	2012/07/13	11	17	Gulfstream Plug Test	Effective Diam = 0.879"
Plug Nozzle	1.3	2012/07/13	12	17	Gulfstream Plug Test	Effective Diam = 0.879"
Plug Nozzle	1.5	2012/07/13	13	18	Gulfstream Plug Test	Effective Diam = 0.879"
Plug Nozzle	1.7	2012/07/13	14	18	Gulfstream Plug Test	Effective Diam = 0.879"
Plug Nozzle	1.85	2012/07/13	15	19	Gulfstream Plug Test	Effective Diam = 0.879"
1.36" diam Nozzle	0.9	2012/07/11	3	1	BL Test	rapid prototyped large exit
Med. Copper	1.5	2012/06/18	2	1	ONR Underexpanded Jet	
Med. Copper	1.7	2012/06/18	3	1	ONR Underexpanded Jet	
Med. Copper	0.9	2012/06/18	4	1	ONR Underexpanded Jet	to compare with
Plug Nozzle Old	0.9	2012/07/11	2	1	Gulfstream Plug Test for Pres.	Old, updated 7/13

0.75" Nozzle	0.98	2010/09/21	2	1	Various Nozzle Sizes	
0.75" Nozzle	0.74	2010/09/21	3	1	Various Nozzle Sizes	
0.75" Nozzle	0.52	2010/09/21	4	1	Various Nozzle Sizes	
0.5" Nozzle	0.98	2010/09/22	1	1; 9/21	Various Nozzle Sizes	
0.5" Nozzle	0.74	2010/09/22	2	1; 9/21	Various Nozzle Sizes	
0.5" Nozzle	0.52	2010/09/22	3	1; 9/21	Various Nozzle Sizes	
2mm Chevron	0.9	2012/08/11	2	1	Chevron Activation Test	Tip 90-45
2mm Chevron	0.9	2012/08/11	3	1	Chevron Activation Test	Tip 30
2mm Chevron	0.9	2012/08/11	4	1	Chevron Activation Test	Valley 90-45
2mm Chevron	0.9	2012/08/11	5	1	Chevron Activation Test	Valley 30
0.75" Nozzle	0.9	2012/08/11	6	1	Various Nozzle Sizes	
Chevron Baseline	0.9	2012/08/14	2	1	Chevron Activation Test 2	
2mm Chevron	0.9	2012/08/14	3	1	Chevron Activation Test 2	Tip 90-45
2mm Chevron	0.9	2012/08/14	4	1	Chevron Activation Test 2	Tip 30
4mm Chevron	0.9	2012/08/14	5	1	Chevron Activation Test 2	Tip 90-45
4mm Chevron	0.9	2012/08/14	6	1	Chevron Activation Test 2	Tip 30
8mm Chevron	0.9	2012/08/14	7	1	Chevron Activation Test 2	Tip 90-45
8mm Chevron	0.9	2012/08/14	8	1	Chevron Activation Test 2	Tip 30
16mm Chevron	0.9	2012/08/14	9	1	Chevron Activation Test 2	Tip 90-45
16mm Chevron	0.9	2012/08/14	10	1	Chevron Activation Test 2	Tip 30
Circular Clamshell	0.98	2011/09/07	1	0	RR Clamshell Test	Circular Tip 90-45
Circular Clamshell	0.98	2011/09/07	2	0	RR Clamshell Test	Circular Tip 30
Circular Clamshell	0.98	2011/09/07	3	0	RR Clamshell Test	Circular Valley 90-45
Circular Clamshell	0.98	2011/09/07	4	0	RR Clamshell Test	Circular Valley 30
Elliptical Clamshell	0.98	2011/09/07	5	0	RR Clamshell Test	Elliptical Tip 90-45
Elliptical Clamshell	0.98	2011/09/07	6	0	RR Clamshell Test	Elliptical Tip 30
Elliptical Clamshell	0.98	2011/09/07	7	0	RR Clamshell Test	Elliptical Valley 90-45
Elliptical Clamshell	0.98	2011/09/07	8	0	RR Clamshell Test	Elliptical Valley 30
Elliptical Clamshell	0.98	2011/09/13	1	9	RR Clamshell Test	Elliptical Tip 90
Elliptical Clamshell	0.85	2011/09/14	2	9	RR Clamshell Test	Elliptical Tip 90
Elliptical Clamshell	0.74	2011/09/15	3	9	RR Clamshell Test	Elliptical Tip 90
Elliptical Clamshell	0.64	2011/09/16	4	8	RR Clamshell Test	Elliptical Tip 90
Elliptical Clamshell	0.52	2011/09/17	5	7	RR Clamshell Test	Elliptical Tip 90
Elliptical Clamshell	0.41	2011/09/18	6	7	RR Clamshell Test	Elliptical Tip 90

Short Copper	0.98	2012/01/30	1	3	Compare with Literature	
Boulders	0.98	2011/05/05	13	19	Trip BL	
Short Copper	0.1-0.9	2013/03/02	13-21	1-3	Momentum Thickness Scaling	POSSIBLE BAD CHANNEL FOR SOME
Long Copper	0.1-0.9	2013/03/02	4-12	1-3	Momentum Thickness Scaling	POSSIBLE BAD CHANNEL FOR SOME
0.495" Aluminum	0.9	2013/03/06	1		Heat Transfer Measurements	NO ACOUSTICS No flow
0.495" Aluminum	0.9	2013/03/06	2		Heat Transfer Measurements	After 1 minute
0.495" Aluminum	0.9	2013/03/06	3		Heat Transfer Measurements	3 minutes after 2
0.495" Aluminum	0.9	2013/03/06	4		Heat Transfer Measurements	change limits to +/-0.1V
0.495" Aluminum	0.9	2013/03/06	5		Heat Transfer Measurements	change to 1 MHz sampling
Md = 1.6 ONR Propc	Prat = 2.0	2013/04/19	3	6	Data for ONR Proposal	
Md = 1.6 ONR Propc	Prat = 3.5	2013/04/19	4	5	Data for ONR Proposal	
Actuated Chevron	0.9	2013/05/26	11-23	0	Actuated Nozzle Test	Small perturbation Changes

References

- AHUJA, K. K. 2003 Designing clean jet noise facilities and making accurate jet noise measurements. 41st Aerospace Sciences Meeting and Exhibit.
- AHUJA, K. K. & BLAKNEY, D. F. 1985 Tone excited jets, part IV: Acoustic measurements. *Journal of Sound and Vibration* **102** (1), 93–117.
- AHUJA, K. K., WHIPKEY, R. R. & JONES, G. S. 1983 Control of turbulent boundary layer flows by sound. AIAA 8th Aeroacoustics Conference.
- ALKISLAR, M. B., KROTHAPALLI, A. & LOURENCO, L. M. 2005 The effect of stream-wise vorticity on the aeroacoustics of a Mach 0.9 axisymmetric jet. 11th AIAA/CEAS Aeroacoustics Conference.
- ANSI S1.26-1995 1995 *Method for Calculation of the Absorption of Sound by the Atmosphere*, ANSI s1.26-1995 edn. American National Standards Institute.
- ASME 1959 *Fluid Meters, Their Theory and Application*, 5th edn. American Society of Mechanical Engineers.
- BASS, H. E., SUTHERLAND, L. C., ZUCKERWAR, A. J., BLACKSTOCK, D. T. & HESTER, D. M. 1995 Atmospheric absorption of sound: further developments. *J. Acoust. Soc. Am.* **97** (1).
- BODONY, D. J. 2004 Aeroacoustic prediction of turbulent free shear flows. PhD thesis, Stanford University.
- BODONY, D. J. & LELE, S. K. 2005 On using large-eddy simulation for the prediction of noise from cold and heated turbulent jets. *Physics of Fluids* **17** (8), 085103.
- BODONY, D. J. & LELE, S. K. 2008 Current status of jet noise predictions using large-eddy simulation. *AIAA Journal* **46** (2), 364–380.
- BOGEY, C. & BAILLY, C. 2005 Effects of inflow conditions and forcing on subsonic jet flows and noise. *AIAA Journal* **43** (5), 1000–1007.
- BOGEY, C. & BAILLY, C. 2010 Influence of the nozzle-exit boundary-layer conditions on the flow and acoustic fields of initially laminar jets. *Journal of Fluid Mechanics* **663**, 507–538.

- BOGEY, C. & MARSDEN, O. 2013 Identification of the effects of the nozzle-exit boundary-layer thickness and its corresponding Reynolds number in initially highly disturbed subsonic jets. *Physics of Fluids* **25** (5), 055106.
- BOGEY, C., MARSDEN, O. & BAILLY, C. 2011 Large-eddy simulation of the flow and acoustic fields of a Reynolds number 10^5 subsonic jet with tripped exit boundary layers. *Physics of Fluids* **23** (3), 035104.
- BOGEY, C., MARSDEN, O. & BAILLY, C. 2012 Effects of moderate Reynolds numbers on subsonic round jets with highly disturbed nozzle-exit boundary layers. *Physics of Fluids* **24** (10), 105107.
- BRADSHAW, P. 1966 The effect of initial conditions on the development of a free shear layer. *Journal of Fluid Mechanics* **26** (2), 225–236.
- BRIDGES, J. & BROWN, C. A. 2004 Parametric testing of chevrons on single flow hot jets. NASA TM 2004-213107.
- BRIDGES, J. & HUSSAIN, F. 1992 Direct evaluation of aeroacoustic theory in a jet. *Journal of Fluid Mechanics* **240**, 469–501.
- BRIDGES, J. E. & HUSSAIN, A. K. M. F. 1987 Roles of initial condition and vortex pairing in jet noise. *Journal of Sound and Vibration* **117** (2), 289–311.
- BROWN, C. & BRIDGES, J. 2006 Small hot jet acoustic rig validation. NASA/TM 2006-214234.
- BROWN, G. L. & ROSHKO, A. 1974 On density effects and large structure in turbulent mixing layers. *Journal of Fluid Mechanics* **64** (4), 775–816.
- CAVALIERI, A. V. G., DAVILLER, G., COMTE, P., JORDAN, P., TADMOR, G. & GERVAIS, Y. 2011 Using large eddy simulation to explore sound-source mechanisms in jets. *Journal of Sound and Vibration* **330**, 4098–4113.
- CAVALIERI, A. V. G., JORDAN, P., GERVAIS, Y., WEI, M. & FREUND, J. B. 2010 Intermittent sound generation and its control in a free-shear flow. *Physics of Fluids* **22**, 115113.
- CHU, W. T. & KAPLAN, R. E. 1976 Use of a spherical concave reflector for jet-noise-source distribution diagnosis. *Journal of the Acoustical Society of America* **59** (6), 1268–1277.
- COLONIUS, T., LELE, S. K. & MOIN, P. 1997 Sound generation in a mixing layer. *Journal of Fluid Mechanics* **330**, 375–409.
- CONCEPT ENGINEERING LTD. 2011 *Concept ViCount 180 Smoke System*. Concept Engineering Ltd.
- CRIGHTON, D. G. & HUERRE, P. 1990 Shear-layer pressure fluctuations and superdirective acoustic sources. *Journal of Fluid Mechanics* **220**, 355–368.

- CROW, S. C. & CHAMPAGNE, F. H. 1971 Orderly structure in jet turbulence. *Journal of Fluid Mechanics* **48** (3), 547–591.
- CURLE, N. 1955 The influence of solid boundaries upon aerodynamic sound. *Proceedings of the Royal Society A* **231** (1187), 505–514.
- DAY, M. J., MANSOUR, N. N. & REYNOLDS, W. C. 1998 The structure of the compressible reacting mixing layer: Insights from linear stability analysis. *Physics of Fluids* **10** (4), 993–1007.
- DOTY, M. J. 2002 An experimental investigation of the aeroacoustic properties of high-speed, helium/air mixture axisymmetric jets. PhD thesis, The Pennsylvania State University.
- DOTY, M. J. & MCLAUGHLIN, K. K. 2003 Acoustic and mean flow measurements of high-speed, helium-air mixture jets. *International Journal of Aeroacoustics* **2** (3-4), 293–334.
- FAA Title 14 Part 36 2014 *Electronic Code of Federal Regulations*, title 14: aeronautics and space part 36-noise standards: aircraft type and airworthiness certification edn. National Archives and Records Administration.
- FFOWCS WILLIAMS, J. E. & KEMPTON, A. J. 1978 The noise from the large-scale structure of a jet. *Journal of Fluid Mechanics* **84** (4), 673–694.
- FREUND, J. B. 2001 Noise sources in a low-Reynolds-number turbulent jet at Mach 0.9. *Journal of Fluid Mechanics* **438**, 277–305.
- FREUND, J. B. 2011 Adjoint-based optimization for understanding and suppressing jet noise. *Journal of Sound and Vibration* **330**, 4114–4122.
- FREUND, J. B., LELE, S. K. & MOIN, P. 2000 Numerical simulation of a Mach 1.92 turbulent jet and its sound field. *AIAA Journal* **38** (11), 2023–2031.
- FREUND, J. B. & MOIN, P. 2000 Jet mixing enhancement by high-amplitude fluidic actuation. *AIAA Journal* **38** (10), 1863–1870.
- FUCHS, H. V. 1972 Space correlations of the fluctuating pressure in subsonic turbulent jets. *Journal of Sound and Vibration* **23** (1), 77–99.
- GASTER, M., KIT, E. & WYGNANSKI, I. 1985 Large-scale structures in a forced turbulent mixing layer. *Journal of Fluid Mechanics* **150**, 23–39.
- GOLDSTEIN, M. & ROSENBAUM, B. 1973 Effect of anisotropic turbulence on aerodynamic noise. *Acoustical Society of America* **54** (3), 630–645.
- GOLDSTEIN, M. E. 2003 A generalized acoustic analogy. *Journal of Fluid Mechanics* **488**, 315–333.
- GOLDSTEIN, M. E. & LEIB, S. J. 2005 The role of instability waves in predicting jet noise. *Journal of Fluid Mechanics* **525**, 37–72.

- GROPENGEISSER, H. 1970 Study of the stability of boundary layers in compressible fluids. NASA Report TT-F-12.
- GUDMUNDSSON, K. & COLONIUS, T. 2011 Instability wave models for the near-field fluctuations of turbulent jets. *Journal of Fluid Mechanics* **689**, 97–128.
- GUITTON, A., KERHERVÉ, F., JORDAN, P. & DELVILLE, J. 2008 The sound production mechanism associated with coherent structures in subsonic jets. 14th AIAA/CEAS Aeroacoustics Conference.
- HAMA, F. R. 1962 Streaklines in a perturbed shear flow. *Physics of Fluids* **5** (6), 644–650.
- HILEMAN, J. I., THUROW, B. S., CARABALLO, E. J. & SAMIMY, M. 2005 Large-scale structure evolution and sound emission in high-speed jets: real-time visualization with simultaneous acoustic measurements. *Journal of Fluid Mechanics* **544**, 277–307.
- HILL, JR, W. G., JENKINS, R. C. & GILBERT, B. L. 1976 Effects of the initial boundary-layer state on turbulent jet mixing. *AIAA Journal* **14** (11), 1513–1514.
- HUERRE, P. & CHRUGHTON, D. G. 1983 Sound generation by instability waves in a low Mach number jet. AIAA 8th Aeroacoustics Conference.
- HUMPHREYS, W. M. & BARTRAM, S. M. 2001 Measurement of separating flow structures using a multiple-camera DPIV system. pp. 82–93. Instrumentation in Aerospace Simulation Facilities. 19th International Congress on ICIASF.
- HUSAIN, Z. D. & HUSSAIN, A. K. M. F. 1979 Axisymmetric mixing layer: Influence of the initial and boundary conditions. *AIAA Journal* **17** (1), 48–55.
- HUSSAIN, A. K. M. F. & CLARK, A. R. 1977 Upstream influence on the near field of a plane turbulent jet. *Physics of Fluids* **20** (9), 1416–1426.
- HUSSAIN, A. K. M. F. & ZAMAN, K. B. M. Q. 1980 Vortex pairing in a circular jet under controlled excitation. part 2. coherent structure dynamics. *Journal of Fluid Mechanics* **101**, 449–492.
- HUSSAIN, A. K. M. F. & ZAMAN, K. B. M. Q. 1985 An experimental study of organized motions in the turbulent plane mixing layer. *Journal of Fluid Mechanics* **159**, 85–104.
- HUSSAIN, A. K. M. F. & ZEDAN, M. F. 1978*a* Effects of the initial condition on the axisymmetric free shear layer: Effects of the initial fluctuation level. *Physics of Fluids* **21** (9), 1475–1481.
- HUSSAIN, A. K. M. F. & ZEDAN, M. F. 1978*b* Effects of the initial condition on the axisymmetric free shear layer: Effects of the initial momentum thickness. *Physics of Fluids* **21** (7), 1100–1112.

- ISO 3745 2003 *Acoustics — Determination of Sound Power Levels of Noise Sources Using Sound Pressure – Precision Methods for Anechoic and Hemi-Anechoic Rooms*, iso 3745 edn. International Organization for Standardization.
- JANARDAN, B. A., HOFF, G. E., BARTER, J. W., MARTENS, S., GLIEBE, P. R., MEN-
GLE, V. & DALTON, W. N. 2000 Ast critical propulsion and noise reduction technologies
for future commercial subsonic engines separate-flow exhaust system noise reduction con-
cept evaluation. NASA CR 2000-210039.
- JIMÉNEZ, J. 2013 How linear is wall-bounded turbulence? *Physics of Fluids* **25** (11), 110814.
- JORDAN, P. & COLONIUS, T. 2013 Wave packets and turbulent jet noise. *Annual Review
of Fluid Mechanics* **45**, 173–195.
- JUBELIN, B. 1980 New experimental studies on jet noise amplification. AIAA 6th Aeroa-
coustics Conference.
- JUVÉ, D., SUNYACH, M. & COMTE-BELLOT, G. 1979 Filtered azimuthal correlations in
the acoustic far field of a subsonic jet. *AIAA Journal* **17** (1), 112–113.
- JUVÉ, D., SUNYACH, M. & COMTE-BELLOT, G. 1980 Intermittency of the noise emission
in subsonic cold jets. *Journal of Sound and Vibration* **71** (3), 319–332.
- KAPILAVAI, D. S. K., TAPEE, J., SULLIVAN, J. & MERKLE, C. L. 2012 Experimental
testing and numerical simulations of shrouded plug-nozzle flowfields. *Journal of Propulsion
and Power* **28** (3), 530–544.
- KARON, A. Z. & AHUJA, K. K. 2013 Effect of nozzle-exit boundary layer on jet noise.
51st Aerospace Sciences Meeting and Exhibit.
- KEARNEY-FISCHER, M., KIM, K. H. & SAMIMY, M. 2009 Control of a high Reynolds
number Mach 0.9 heated jet using plasma actuators. *Physics of Fluids* **21** (9), 095101.
- KERECHANIN, II, C. W. 2000 The effects of nozzle trailing edge modifications on the
acoustic far field of a Mach 2 rectangular jet. Master’s thesis, The Ohio State University,
Columbus, OH.
- KERHERVÉ, F., GUITTON, A., JORDAN, P., DELVILLE, J., FORTUNÉ, V., GERVAIS, Y.
& TINNEY, C. 2008 Identifying the dynamics underlying the large-scale and fine-scale jet
noise similarity spectra. 14th AIAA/CEAS Aeroacoustics Conference.
- KHAVARAN, A & BRIDGES, J. 2005 Modelling of fine-scale turbulence mixing noise. *Journal
of Sound and Vibration* **3-5**, 1131–1154.
- KIM, J., BODONY, D. J. & FREUND, J. B. 2014 Adjoint-based control of loud events in
a turbulent jet. *Journal of Fluid Mechanics* **741**, 28–59.
- KIM, J. H., KASTNER, J. & SAMIMY, M. 2009 Active control of a high Reynolds number
Mach 0.9 axisymmetric jet. *AIAA Journal* **47** (1), 116–128.

- KLEINMANN, R. R. & FREUND, J. B. 2008 The sound from mixing layers simulated with different ranges of turbulence scales. *Physics of Fluids* **20**, 101503.
- KNOTT, P. R., JANARDAN, B. A., MAJJIGI, R. K., BHUTIANI, P. K. & VOGT, P. G. 1984 Free-jet acoustic investigation of high-radius-ratio coannular plug nozzles. *Tech. Rep.*. NASA.
- LAUFER, J., SCHLINKER, R. & KAPLAN, R. E. 1976 Experiments on supersonic jet noise. *AIAA Journal* **14** (4), 489–497.
- LAZAR, E., DEBLAUW, B., GLUMAC, N., DUTTON, C. & ELLIOTT, G. 2010 A practical approach to PIV uncertainty analysis. 27th AIAA Aerodynamic Measurement Technology and Ground Testing Conference.
- LIGHTHILL, M. J. 1952 On sound generated aerodynamically. I. General theory. *Proceedings of the Royal Society* **211** (1107), 564–587.
- LIGHTHILL, M. J. 1954 On sound generated aerodynamically. II. Turbulence as a source of sound. *Proceedings of the Royal Society* **222**, 1–22.
- LILLEY, G. M. 1974 On the noise from jets. *AGARD Technical Report CP-131* .
- LILLEY, G. M. 1993 On the noise radiated from a turbulent high speed jet. In *Computational Aeroacoustics*, pp. 85–115. Springer.
- LU, H. Y. 1983 Effect of excitation on coaxial jet noise. *AIAA Journal* **21** (2), 214–220.
- LUSH, P. A. 1971 Measurements of subsonic jet noise and comparison with theory. *Journal of Fluid Mechanics* **46**, 477–500.
- MAESTRELLO, L. & MCDAID, E. 1971 Acoustic characteristics of high-subsonic jets. *AIAA Journal* **9** (6), 1058–1066.
- MANKBADI, R. & LIU, J. T. C. 1984 Sound generated aerodynamically revisited: Large-scale structures in a turbulent jet as a source of sound. *Philosophical Transactions of the Royal Society of London. Series A. Mathematical and Physical Sciences* **311** (1516), 183–217.
- MERKINE, L. & LIU, J. T. C. 1975 On the development of noise producing large-scale wavelike eddies in a plane turbulent jet. *Journal of FLuid Mechanics* **70** (2), 353–368.
- MICHALKE, A. 1984 Survey on jet instability theory. *Progress in Aerospace Science* **21**, 159–199.
- MICHALKE, A. & FUCHS, H. V. 1975 On turbulence and noise of an axisymmetric shear flow. *Journal of Fluid Mechanics* **70** (1), 179–205.
- MITCHELL, B. E., LELE, S. K. & MOIN, P. 1995 Direct computation of the sound generated by subsonic and supersonic axisymmetric jets. *Tech. Rep.*. Stanford University.

- MOLLO-CHRISTENSEN, E. 1967 Jet noise and shear flow instability seen from an experimenter's viewpoint. *Journal of Applied Mechanics* **34** (1).
- MORRIS, P. J., GIRIDHARAN, M. G. & LILLEY, G. M. 1990 On the turbulent mixing of compressible free shear layers. *Proceedings of the Royal Society of London A* **431**, 219.
- MORRIS, S. C. & FOSS, J. F. 2003 Turbulent boundary layer to single-stream shear layer: the transition region. *Journal of Fluid Mechanics* **494**, 187–221.
- NARAYANAN, S., BARBER, T. J. & POLAK, D. R. 2002 High subsonic jet experiments: Turbulence and noise generation studies. *AIAA Journal* **40** (3), 430–437.
- NICHOLS, J. W., LELE, S. K., MOIN, P., HAM, F. E. & BRIDGES, J. E. 2012 Large-eddy simulation for supersonic rectangular jet noise prediction: effects of chevrons. 18th AIAA/CEAS Aeroacoustics Conference(33rd AIAA Aeroacoustics Conference).
- OBRIST, D. 2009 Directivity of acoustic emissions from wave packets to the far field. *Journal of Fluid Mechanics* **640**, 165–186.
- PANDA, J. 2007 Experimental investigation of turbulent density fluctuations and noise generation from heated jets. *Journal of Fluid Mechanics* **591**, 73–96.
- PANDA, J. & SEASHOLTZ, G. 2002 Experimental investigation of density fluctuations in high-speed jets and correlation with generated noise. *Journal of Fluid Mechanics* **450**, 97–130.
- PAPAMOSCHOU, D. 2007 Acoustics simulation of coaxial hot air jets using cold helium-air mixture jets. *Journal of Propulsion and Power* **23** (2).
- PAPAMOSCHOU, D. 2011 Wavepacket modeling of the jet noise source. 17th AIAA/CEAS Aeroacoustics Conference.
- PAREKH, D. E., KIBENS, V., GLEZER, A., WILTSE, J. M. & SMITH, D. M. 1996 Innovative jet flow control — mixing enhancement experiments. AIAA 34th Aerospace Sciences Meeting and Exhibit.
- PETERSEN, R. A. & SAMET, M. M 1988 On the preferred mode of jet instability. *Journal of Fluid Mechanics* **194**, 153–173.
- PIERCE, A. 1989 *Acoustics: An Introduction to its Physical Principles and Applications*. Acoustical Society of America.
- POPE, A. & HARPER, J. J. 1966 *Low-Speed Wind Tunnel Testing*. Wiley.
- RESHOTKO, E., SARIC, W. S. & NAGIB, H. M. 1997 Flow quality issues for large wind tunnels. AIAA Aerospace Sciences Meeting & Exhibit.
- RIBNER, H. S. 1969 Quadrupole correlations governing the pattern of jet noise. *Journal of Fluid Mechanics* **38** (1), 1–24.

- RICOU, F. P. & SPALDING, D. B. 1961 Measurement of entrainment by axisymmetrical turbulent jets. *Journal of Fluid Mechanics* **11** (1), 21–32.
- ROSHKO, A. 1993 Instability and turbulence in shear flows. In *Theoretical and Applied Mechanics 1992* (ed. S. R. Bodner, J. Singer, A. Golan & Z. Hashin). Elsevier.
- SAE ARP866A 1975 *Aerospace Recommended Practice*. Society of Automotive Engineers.
- SAMIMY, M., ADAMOVICH, I., WEBB, B., KASTNER, J., HILEMAN, J., KESHAV, S. & PALM, P. 2004 Development and characterization of plasma actuators for high-speed jet control. *Experiments in Fluids* **37**, 577–588.
- SAMIMY, M., KIM, J. H., KASTNER, J., ADAMOVICH, I. & UTKIN, Y. 2007a Active control of a Mach 0.9 jet for noise mitigation using plasma actuators. *AIAA Journal* **45** (4), 890–901.
- SAMIMY, M., KIM, J. H., KASTNER, J., ADAMOVICH, I. & UTKIN, Y. 2007b Active control of high-speed and high-Reynolds-number jets using plasma actuators. *Journal of Fluid Mechanics* **578**, 305–330.
- SANDHAM, N. D. & REYNOLDS, W. C. 1990 Compressible mixing layer: Linear theory and direct simulation. *AIAA Journal* **28**, 618–624.
- SHIELDS, F. D. & BASS, H. E. 1977 Atmospheric absorption of high frequency noise and application to fractional-octave bands. *Tech. Rep.*. NASA.
- SIPPEL, D. 2011 Design rules & detail resolution for sls 3d printing. www.shapeways.com/tutorials/design_rules_for_3d_printing.
- STANLEY, S. A. & SARKAR, S. 2000 Influence of nozzle conditions and discrete forcing on turbulent planar jets. *AIAA Journal* **38** (9), 1615–1623.
- TAM, C. K. W. & AURIAULT, L. 1999 Jet mixing noise from fine-scale turbulence. *AIAA Journal* **37** (2), 145–153.
- TAM, C. K. W. & BURTON, D. E. 1984 Sound generated by instability waves of supersonic flows. Part 2. Axisymmetric jets. *Journal of Fluid Mechanics* **138**, 273–295.
- TAM, C. K. W., GOLEBIOWSKI, M. & SEINER, J. M. 1996 On the two components of turbulent mixing noise from supersonic jets. In *2nd AIAA and CEAS Aeroacoustics Conference*. 2nd AIAA and CEAS Aeroacoustics Conference.
- TAM, C. K. W., VISWANATHAN, K., AHUJA, K. K. & PANDA, J. 2008 The sources of jet noise: experimental evidence. *Journal of Fluid Mechanics* **615**, 253–292.
- TANNA, H. K., DEAN, P. D. & BURRIN, R. H. 1976 The generation and radiation of supersonic jet noise. volume 3: Turbulent mixing noise [final technical report, 6 nov. 1972-6 nov. 1975]. *Tech. Rep.*.

- THIRUMURTHY, DEEPAK, JONES, JESSE, LYRINTZIS, BLAISDELL & SULLIVAN 2010 Experimental investigation and computation of a supersonic ejector nozzle with clamshells. 40th AIAA Fluid Dynamics and Applied Aerodynamics Conference and Exhibit.
- UKEILEY, L. 2007 Spatial correlations in a transonic jet. *AIAA Journal* **45** (6).
- UTKIN, Y. G., KESHAV, S., KIM, J. H., KASTNER, J., ADMOVICH, I. V. & SAMIMY, M. 2007 Development and use of localized arc filament plasma actuators for high-speed flow control. *Journal of Applied Physics D: Applied Physics* **40** (3), 685–694.
- UZUN, A., BIN, J. & HUSSAINI, M. Y. 2011 High-fidelity numerical simulation of a chevron nozzle jet flow. *International Journal of Aeroacoustics* **10** (5-6), 531–564.
- UZUN, A. & HUSSAINI, M. Y. 2009 Simulation of noise generation in near-nozzle region of a chevron nozzle jet. *AIAA Journal* **47** (8), 1793–1810.
- VISWANATHAN, K. 2004 Aeroacoustics of hot jets. *Journal of Fluid Mechanics* **516**, 39–82.
- VISWANATHAN, K. 2006 Instrument considerations for accurate jet noise measurements. *AIAA Journal* **44** (6), 1137–1149.
- VISWANATHAN, K. 2008 Does a model-scale nozzle emit the same jet noise as a jet engine? *AIAA Journal* **46** (2), 336–355.
- VISWANATHAN, K. & CLARK, L. T. 2004a Effect of nozzle internal contour on jet aeroacoustics. 42nd Aerospace Sciences Meeting and Exhibit.
- VISWANATHAN, K. & CLARK, L. T. 2004b Effect of nozzle internal contour on jet aeroacoustics. *International Journal of Aeroacoustics* **3** (2), 103–135.
- VISWANATHAN, K. & MORRIS, P. J. 1992 Predictions of turbulent mixing in axisymmetric compressible shear layers. *AIAA Journal* **30**, 1529–1536.
- WANG, M., FREUND, J. B. & LELE, S. K. 2006 Computational prediction of flow-generated sound. *Annual Review of Fluid Mechanics* **38**, 483–512.
- WEI, M. & FREUND, J. B. 2006 A noise-controlled free shear flow. *Journal of Fluid Mechanics* **546**, 123–152.
- WHITE, F. M. 2005 *Viscous Fluid Flow*, 3rd edn. McGraw-Hill.
- ZAMAN, K. B. M. Q. 1985a Effect of initial condition on subsonic jet noise. *AIAA Journal* **23** (9), 1370–1373.
- ZAMAN, K. B. M. Q. 1985b Far-field noise of a subsonic jet under controlled excitation. *Journal of Fluid Mechanics* **152**, 83–111.
- ZAMAN, K. B. M. Q. 2012 Effect of initial boundary-layer state on subsonic jet noise. *AIAA Journal* **50** (8), 1784–1795.

- ZAMAN, K. B. M. Q. & HUSSAIN, A. K. M. F. 1980 Vortex pairing in a circular jet under controlled excitation. Part 1. General jet response. *Journal of Fluid Mechanics* **101**, 493–544.
- ZAMAN, K. B. M. Q. & HUSSAIN, A. K. M. F. 1981 Turbulence suppression in free shear flows by controlled excitation. *Journal of Fluid Mechanics* **103**, 133–159.
- ZUCKERWAR, A. J. & MEREDITH, R. W. 1985 Low-frequency absorption of sound in air. *J. Acoust. Soc. Am.* **78** (3), 946–955.